Novel Concepts in the PECVD Deposition of Silicon Thin Films : from Plasma Chemistry to Photovoltaic Device Applications

Junkang Wang

université PARIS-SACLAY

NNT : 2017SACLX079

Thèse de doctorat

Novel concepts in the PECVD of silicon thin films: from plasma chemistry to photovoltaic device applications

Thèse de doctorat de l'Université Paris-Saclay
préparée à L'Ecole Polytechnique

École doctorale n°573 Interface : approches interdisciplinaires, fondements, applications et innovation
Spécialité de doctorat: Physique

Thèse présentée et soutenue à Palaiseau, le 10/10/2017, par

M. Junkang Wang

Composition du Jury :

M. Patrick Le Quéré Directeur de Recherche, LIMSI Orsay (UPR 3251)	Président
M. Holger Kersten Professeur, Christian-Albrechts-Universität zu Kiel	Rapporteur
Mme. Agnès Granier Directeurice de Recherche, IMN Nantes (UMR 6502)	Rapporteur
M. Erik V. Johnson Chargée de Recherche, LPICM École Polytechnique (UMR7647)	Directeur de thèse
M. Jean-Paul Booth Directeur de Recherche, LPP École Polytechnique (UMR 7648)	Invité

Acknowledgements

Working in LPICM as PhD candidate would definitely be a precious experience in my life, but finishing the thesis means I have to put an ending to the story. Taking this opportunity, I thank all those who were along with me during these three years of time.

First, I would like to express my sincere gratitude to Erik Johnson, my supervisor, for providing this PhD research subject to me, and also thanks for his continuous support during work and study. I really enjoyed every discussion with him, and I appreciate that he could always be ready to give me insightful suggestions and guidance in the most logical way in front of new experimental results, or even just some preliminary ideas.

Then, I would like to mention Pere Roca i Cabarrocas, the lab director, who is always keeping enthusiastic to make the LPICM become a better place. It was really encouraging for the younger generations like us to see the lab director coming to the lab at 7am, making discussions, organizing meetings, and doing experiments. Moreover, many thanks for giving me a ride on my way to work and back from supermarket, so many times!

I would specially thank my mentor Pavel Victorovich Boulkine (I think this is his full name), for guiding me to the vacuum technology. Thanks for his rigorous attitude about work, so that I did not need "to use my whole year salary to pay for the turbopump" due to stupid mistakes, and also thanks for tolerating me come to his office directly any time I met technical troubles. Even though sometimes we might not be able to find the best solutions immediately, he could always come out with numbers of research references (even back to 1930s!).

My gratitude also goes to Ileana Florea and Jean-Luc Maurice for their help in the TEM samples preparation and experimental analysis, and also for their comments on papers and thesis writing. I also thank Dmitri Daineka for providing doped layers during the solar cells fabrication, especially running back and force between LPICM and Thales building.

I would also like thank Joaquim Nassar, who guided into LPICM as a master intern in 2013, and thank the previous successive PhD students Bastien Bruneau and Jean-Christophe Dornstetter for being my internship mentors.

I also appreciate many others from the lab (I will try to make it in the alphabetical order): Carine Roger-Roulling, Chiara Toccafondi, Cyril Jadaud, Denis Tondelier, Etienne Drahi, Fabien Lebreton, Fabienne Pandolf, Farah Haddad, Federico Ventosinos, François Silva, Frédéric Farci, Gabriela Medina, Guillaume Fischer, Hao Chen, Jacqueline Tran, Jeongmo Kim, Jérôme Charliac, Jian Tang, Laurence Gérot, Letian Dai, Martin Foldyna, Mutaz Al Ghzaiwat, Nacib Benmammar, Nada Habka, Patricia Prod'homme, Rasha Khoury, Ronan Léal, Wanghua Chen, Zeyu Li, Zheng Fan, for their tremendous help in administrative matters, equipments training, facilities maintenance, and fruitful discussions during these three years. I also have to say thank you to Mustapha El Yaakoubi and Emmanuel Stephanos from TFSC for the maintenance and update of

SSPG and EQE setups, to Christophe Longeaud from LGEP for the SSPC characterization, to Sandrine Tusseau-Nenez from LPMC for the XRD training, and to Patrick Chapon and Sofia Gaiaschi from HORIBA for the GD-OES measurements.

Besides, I am grateful of my defense jury members: Dr. Patrick Le Quéré, Prof. Holger Kersten, Dr. Agnes Granier, and Dr. Jean-Paul Booth for their insightful comments and suggestion, and also for the questions which incented me to widen my research from various perspectives.

Finally, I would like to acknowledge my parents for the endless support during these years, and my wife Han for always being by my side and inspiring me to do better. And last but not least, to my daughter Cholé-Luoyi, my best gift.

Abstract

This PhD thesis work is dedicated to exploring and understanding the growth of silicon thin film materials using different plasma-enhanced chemical vapour deposition (PECVD) techniques for applications in photovoltaics.

The first part of the work concerns combining a new process chemistry using an SiF_4/H_2 gas mixture with the matrix-distributed electron cyclotron resonance (MDECR) PECVD technique to obtain high growth rate microcrystalline silicon (µc-Si:H). Due to the particular design of the MDECR system, a careful investigation of the impact of the impinging ion energies on material deposition can be done. We find that moderate ion energy conditions are beneficial to achieve a significant drop in the density of nano-voids, and thus a higher quality material with better stability can be obtained. A two-step deposition method has been introduced as an alternative way to eliminate the formation of an amorphous incubation layer during film growth.

The second part of the work is dedicated to the exploration of the Tailored Voltage Waveforms (TVW) excitation technique for capacitively coupled plasma (CCP) processes. As an advantage over the conventional sinusoidal excitations, the TVW technique provides an elegant solution for ion flux-energy decoupling in CCP discharges through the electrical asymmetry effect. This makes it possible to independently study the impact of ion energy on material deposition at relatively high process pressure. Based on this insight, we have studied the deposition of µc-Si:H and amorphous silicon (a-Si:H) from the $SiF_4/H_2/Ar$ and SiH_4/H_2 plasma chemistries, respectively. From an analysis of the structural and electronic properties, we find that the variation of ion energy can be directly translated into the material quality. We have applied these results to photovoltaic devices and have established comprehensive links between the controllable plasma parameters via TVW, the deposited material properties, and, finally, the resulting device quality.

In the last part, as a further application of TVW, we discovered a set of "electrode-selective" CCP processes. In the case of silicon thin film deposition from the $SiF_4/H_2/Ar$ plasma chemistry when using *sawtooth* TVW, one can achieve a deposition process on one electrode, while at the same time either no deposition or an etching process on the counter electrode. This is due to two effects: the multi-precursor nature of the resulting surface process and the asymmetric plasma response caused by the slope asymmetry effect of *sawtooth* TVW. Moreover, such a deposition/etching balance can be directly controlled through the H_2 flow rate. We have further studied the impact of process pressure and reactor geometry on the asymmetric plasma response for both the single-gas and multi-gas plasmas using *sawtooth* TVW. The product of pressure and inter-electrode distance is deduced to be a crucial parameter in determine the plasma heating mode, so that a more flexible control over the discharge asymmetry as well as the resulting "electrode-selective" surface process can be expected.

Keywords: silicon thin film, photovoltaic, plasma-enhanced chemical vapour deposition, electron cyclotron resonance, ion energy, tailored voltage waveforms, electrical asymmetry effect, plasma heating

Résumé

Dans la première et la deuxième parties de ce manuscrit, grands efforts ont été consacrés à l'optimisation des processus de dépôt des couches minces de silicium et à la fabrication de dispositifs photovoltaïques basé sur des différents types des techniques de dépôt chimique en phase vapeur assisté par plasma (PECVD), et notamment l'influence de l'énergie ionique sur les résultats de traitement. Dans la troisième partie, en tant qu'application de la technique d'excitation multi-fréquence TVW, nous avons découvert un effet "electrode-selective" dans les processus plasma radiofréquence capacitivement couplé (RF-CCP).

Tout d'abord, afin d'réaliser de le dépôt de silicium microcristallin hydrogéné (μc-Si:H) à grande vitesse, nous avons couplé la technique plasmas distributés matriciellement à résonance cyclotronique électronique (MDECR) PECVD et un plasma halogéné en utilisant un mélange de SiF_4/H_2. Il a été démontré que la température du substrat est essentielle pour obtenir une fraction volumique cristalline élevée avec des conditions de plasma à grande densité et basse pression, en raison de l'augmentation thermiquement induite de la diffusion des espèces sur de surface. D'autre part, en raison de la conception spécifique du système MDECR, nous avons effectué une étude minutieuse de l'influence d'énergie ionique sur le dépôt de matériaux. Nous avons trouvé qu'une condition d'énergie ionique modérée est bénéfique pour obtenir une diminution significative de la densité des nano-vides, et ainsi nous pouvons obtenir un matériau de meilleure qualité avec une meilleure stabilité. En augmentant l'énergie ionique pendant le dépôt, deux seuils l'énergie de bombardement ionique IBE à ~12 eV et ~43 eV sont détectés, correspondant aux effets des déplacements atomiques en surface et en volume induits par SiF^+. Les plus petites tailles de grains et les couches de surface plus rugueuses observées sont qualitativement liées au déplacement de surface induit par SiF^+. À des énergies ioniques plus élevées, le déplacement en volume induit par SiF^+ peut sévèrement entraver le processus de nucléation, conduisant à un effet d'amorphisation local sur le film en croissance.

En outre, nous avons constaté que le processus d'incubation est l'étape la plus difficile de la croissance de μc-Si:H pour cette technologie. Une méthode de dépôt en deux étapes est présentée comme une alternative pour éliminer l'existence d'une couche d'incubation amorphe. En préparant une couche fortement cristallisé (peut être aussi mince que ~ 4 nm) à une pression de processus relativement faible, la couche principale de μc-Si:H à grande vitesse peut subir directement la croissance avec la phase cristalline. Ces résultats suggèrent tous que l'utilisation de la technique MDECR et du plasma SiF_4/H_2 pour le dépôt de μc-Si:H résulte en des exigences assouplies sur les paramètres du procédé pour le matériau de qualité du dispositif.

Nous avons exploré l'application de la technique d'excitation TVW pour les processus CCP. Comme avantage par rapport aux excitations classiques à fréquence unique, le TVW non sinusoïdales fournissent une solution élégante pour le découplage d'énergie ionique et de flux ionique dans les décharges de CCP par l'effet d'asymétrie électrique. Basé sur ce point, nous avons éffectué des études sur l'influence de l'énergie ionique sur le CCP-PECVD de μc-Si:H à partir de

plasma $SiF_4/H_2/Ar$. Un contrôle semi-indépendant de l'énergie ionique a été atteint, car un vitesse de dépôt du matériau peu variable nous a permis de concentrer sur l'effet des ions. Nous trouvons qu'une variation de l'énergie ionique, ou précisément le maximum IBE (IBE_{max}) avec des conditions de pression relativement élevée, peut être directement traduite dans la qualité du matériau. Les propriétés structurelles et électroniques des couches ont été analysées, et nous avons obtenu du matériau ayant des propriétés optimales avec des valeurs IBE_{max} modérées comprises entre ~45 et 55 eV. Au-delà de cette plage, nous avons observé une diminution des propriétés du matériau par la plus petite cristallite et la plus faible densité, ce qui correspond à l'effet du déplacement atomique en volume induit par les ions liés au silicium pendant le dépôt. Une telle efficacité de TVW pour le contrôle de processus est encore confirmée en étudiant le dépôt de silicium amorphe hydrogéné (a-Si:H) à partir de plasma SiH_4/H_2. Dans les conditions d'énergie ionique étudiées, nous avons trouvé que des valeurs modérées de IBE_{max} peuvent conduire à une densité de matériau améliorée ainsi qu'à une meilleure stabilité sous illumination. Un IBE_{max} threshold à ~12 eV, correspondant au déplacement de surface induit par SiH_x^+, a été déterminé comme étant responsable de la dégradation de la qualité du matériau. Nous avons ensuite appliqué ces résultats à des applications photovoltaïques (µc-Si:H et a-Si:H) et établi des liens complets entre les paramètres de plasma contrôlables par TVW et les propriétés des matériaux déposés, et finalement les performances du dispositif photovoltaïque correspondant.

Dans cette partie, l'effet d'asymétrie de pente causée par l'utilisation de *sawtooth* TVW a été étudié. En raison de la forte asymétrie de pente de montée et de descente dans la tension appliquée, la dynamique de gaine spatiale asymétrique et l'absorption de puissance électronique localisée à chaque électrode peuvent être générées, même dans un réacteur géométriquement symétrique. Par analogie avec les plasmas à un seul gaz, une telle asymétrie de décharge dépend du mécanisme de chauffage du plasma dominant et peut être simplement réfléchie par les mesures de la tension d'autopolarisation. En couplant cet effet avec le plasma $SiF_4/H_2/Ar$ à multi-précurseur, nous avons observé l'apparition d'un effet "electrode-selective" dans un processus CCP. Pour certains rapports de débit de gaz, nous pouvons obtenir le dépôt sur une électrode, tout en ne produisant pas de dépôt ou de gravure sur l'autre électrode. En outre, un tel équilibre dépôt/gravure peut être contrôlé par l'injection de H_2.

Nous avons analysé l'influence de la pression et de la géométrie du réacteur sur l'effet d'asymétrie de pente pour les plasmas mono- et multi-gaz. Le produit de la pression et de la distance inter-électrodes $P{\cdot}d_i$ est déduit comme un paramètre crucial pour déterminer le mode de chauffage du plasma, déduit par la tension d'autopolarisation obtenue expérimentalement, en particulier les valeurs relatives de *sawtooth-up* et *-down* TVW. Cela a également été observé dans la chimie du plasma SiH_4/H_2, avec des conclusions similaires. Cela signifie que l'asymétrie de décharge peut être commutée en changeant les conditions $P{\cdot}d_i$, et donc un contrôle plus flexible sur le processus "electrode-selective" peut être attendu.

Nous avons également identifié de tels processus "electrode-selective" lors de l'utilisation de *peaks* et *valleys* TVW, typiquement utilisés pour maximiser l'effet d'asymétrie d'amplitude (contrôle de l'énergie ionique). Nous proposons que cela soit dû au fait que l'une des gaines rétrécit rapidement et reste effondrée pendant la plus grande partie d'une période fondamentale. Une telle dynamique de gaine unique peut également provoquer un chauffage du plasma localisé à proximité d'un bord de la gaine qui s'effondre.

En résumé, ces résultats renforcent la flexibilité de la technique TVW pour l'optimisation des processus liés aux RF-CCP. La possibilité d'obtenir une asymétrie de décharge contrôlable et la découverte de processus "electrode-selective" encouragent la possibilité de choisir un ensemble de conditions de procédé pour réaliser une grande variété de dépôts désirés sur une électrode tout en laissant l'autre vierge.

Contents

List of Acronyms and Symbols

Acronyms	Definition
a-Si:H	Hydrogenated amorphous silicon
a-Si:H,F	Hydrogenated and fluorinated amorphous silicon
a-SiC:H	Hydrogenated amorphous silicon carbide
CCP	Capacitively coupled plasma
c-Si	Monocrystalline silicon
CVD	Chemical vapor deposition
EAE	Electrical asymmetry effect
ECR	Electron cyclotron resonance
EEDF	Electron energy distribution function
EQE	External quantum efficiency
FTIR	Fourier transform infrared spectroscopy
HAADF	High-angle annular dark field
ICP	Inductively coupled plasma
ITO	Indium tin oxide
LS	Light soaking
MDECR	Matrix-distributed electron cyclotron resonance
OES	Optical emission spectroscopy
PECVD	Plasma-enhanced chemical vapor deposition
PVD	Physical vapor deposition
RF	Radio frequency
RGA	Residual gas analyzer
SM	Stretching modes
SSPG	Steady state photocarrier grating
STEM	Scanning transmission electron microscopy
TEM	Transmission electron microscopy
TVW	Tailored voltage waveforms
µc-Si:Cl,F	Hydrogenated and chlorinated microcrystalline silicon
µc-Si:H	Hydrogenated microcrystalline silicon
µc-Si:H,F	Hydrogenated and fluorinated microcrystalline silicon
µc-SiO:H	Hydrogenated microcrystalline silicon oxide
ZnO:Al	Aluminum doped zinc oxide

Symbols	Unit	Definition
σ_d, σ_{ph}	S cm^{-1}	Dark conductivity, photoconductivity
d_i	mm	Inter-electrode distance
$\Delta\eta$	V	Sheath potential drop
ε		Symmetry parameter
ε_0	F m^{-1}	Vacuum permittivity
ε_i		Imaginary part of pseudo-dielectric function
E_g	eV	Optical band gap
FF	%	Fill factor
FWHM	cm^{-1}	Full width at half maximum
IBE (IBE_{max})	eV	(Maximum) Ion bombardment energy
J_0, J_{SC}	mA cm^{-2}	Dark saturation, short-circuit current
L_d	nm	Minority carrier diffusion length
λ	nm	Light wavelength
m, M	kg	Electron, ion mass
$\bar{n}_{sp}$, $\bar{n}_{sg}$	m^{-3}	Mean sheath ion density close to powered, ground electrode
P_{MW}, P_{RF}	W	Microwave, radio frequency power
P	Torr	Pressure
R_S, R_{SH}	Ω cm^2	Series, shunt resistance
R^*		Microstructure parameter
r_d	Å/s	Deposition rate
sccm	cm^3 min^{-1}	Standard cubic centimeter per minute
T_e	eV	Electron temperature
T_{rf}, T_{sub}	ºC	Powered, ground electrode (substrate) temperature
t, t_i	nm	Layer thickness, intrinsic absorber layer thickness
$\mu\tau_{min}$, $\mu\tau_{max}$	cm^2 V^{-1} s^{-1}	Minority, majority carrier mobility-lifetime product
V_{DC}	V	DC self-bias
V_{OC}	mV	Open-circuit voltage
V_{PP}	V	Peak-to-peak voltage
V_{min}, V_{max}	V	Minimum, maximum applied voltage
$\widetilde{V}_{pl}$	V	Time-averaged plasma potential
ω	s^{-1}	Angular frequency
ω_{pe}, ω_{pi}	s^{-1}	Electron, ion plasma angular frequency
X_c^{ES}, X_c^{Raman}	%	Ellipsometry, Raman crystalline volume fraction
η	%	Light conversion efficiency

Chapter 1 Introduction

Contents

1.1. Thin films and their deposition

A thin film is a layer of material applied onto a substrate surface and is usually used to achieve a wide variety of unattainable (or not easily attainable properties) by the substrate surface alone. Taking a simple case as an example, a thin layer of silver is often coated on glass to form a reflective interface for household mirrors. Thin film manufacturing processes are also at the heart of the semiconductor industry. Depending on their properties, thin film materials can be classified into different categories and can be applied in a broad range of areas, such as optical thin films for light filters, electrical thin films for optoelectronic devices, magnetic thin films for memories, chemical and thermal thin films for barriers or protection layers, etc. Furthermore, these thin films can also be multi-functional. For instance, titanium dioxide is the most widely used white pigment because of its brightness and high refractive index, but also has the potential to be used in energy production as a photocatalyst for hydrolysis.

"Thin" is a relative term and cannot be generally defined. While in most application cases, it means a layer having a thickness from a fraction of nanometer (a monolayer) up to several tens of micrometers. It is interesting to picture such a layer in a more intuitive way. For instance, a 100 nm thick silicon (atomic density of 5.0×10^{22} cm^{-3}) thin film with a 1×1 cm^2 area contains about 5×10^{17} silicon atoms. If we imagine each of these atoms as a grape with 2 cm diameter and pile them up one by one with no gap, they would form a stack as high as a three story building. To relativize this in the other dimension, this three-story high building would have an area of 1.6×10^8 km^2, which is ~24 times that of the French territory!

In practice, the synthesis of this 100 nm silicon thin film by a standard technique, often referred as deposition, needs only a "short" processing time from a couple of seconds to several tens of minutes. Although the deposition can be done within such a short time, depending on the function the film must serve, a certain level of material quality needs to be assured. This can therefore lead to extremely stringent requirements for the deposition techniques to be used. Depending on the process, these deposition techniques can fall into two main categories: physical vapor deposition (PVD) and chemical vapor deposition (CVD). The PVD process is based on the physical material transfer from a solid or liquid source to vapor phase and then onto a substrate as a condensed phase, while CVD is a process that relies on chemical reactions between gaseous or liquid precursors with other reactants. This thesis mainly focuses on the synthesis of silicon thin film materials using the CVD process (or more precisely, the plasma-enhanced CVD process), so a brief introduction about its general principles will be given subsequently.

1.1.1 Chemical vapor deposition (CVD)

Due to the ability to controllably produce a large variety of desired materials, the CVD process has been employed in diverse industrially relevant applications such as semiconductor and

microelectronic technologies, where the guarantee for high quality thin films and coatings is of crucial importance. In turn, this has served as a powerful driver spurring the development of the CVD technology. Many variants of CVD processing methods have therefore been proposed and developed. These methods fall in a variety of formats depending on the operating conditions like the operating pressure (atmospheric pressure, low pressure, ultrahigh vacuum, etc.), the state of growth precursor (gaseous, metalorganic, liquid, aerosol assisted, etc.), and the driving source (hot wire, plasma enhanced, laser assisted, photo assisted etc.). There are also some other types of methods like atomic layer CVD, or more commonly referred as atomic layer deposition. An exhaustive classification will not be listed here, further and more detailed information about these techniques can be found in handbooks such as the ones by Hitchman *et al*[1] or Ohring[2].

Nonetheless, regardless of this large variety of methods, the CVD processes share a general set of sequential steps, as shown in Figure 1.1: firstly, reactants and dilute gases (if present) are introduced from the inlets, and are transferred to the reaction region, where the growth precursors and by-products are produced in the gas phase; then the growth precursors and reactants approach the processing surface, and are physically or chemically adsorbed; after that, surface migration of these species towards the energetically favorable sites leads to the film growth (surface reaction can also occur during this step of the process); finally, volatile by-products desorb from the growing surface into the bulk gas flow region and are pumped away towards the reactor exit.

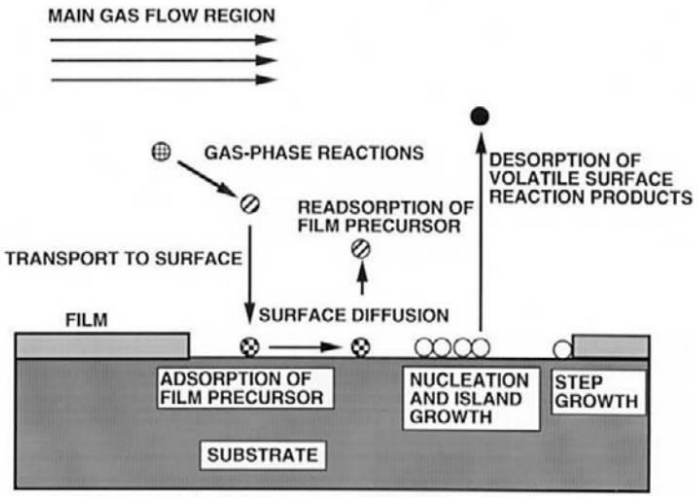

Figure 1.1 Schematic of transportation and reaction sequence in CVD process. Extracted from Ref. 1.

1.1.2 Plasma-enhanced CVD (PECVD)

The plasma-enhanced CVD (PECVD) process is derivation of CVD process, where all the gas phase and surface physical and chemical reactions described above are stimulated by the presence of a glow-discharge plasma. In addition to the solid, liquid, and gas state, plasma is often viewed as the fourth fundamental state of matter. It is an electrically neutral medium mainly consisting of

[1] *Chemical Vapor Deposition: Principles and Applications*, M. L. Hitchman and K. F. Jensen (Ed.). Academic Press (1993).
[2] M. Ohring, *Materials Science of Thin Films: Deposition and Structure*, 2nd ed., Academic Press (2002).

unbound neutral, positive, and negative particles (neutrals, ions, and electrons). In the majority of PECVD processes, plasmas are excited by energy coming from an external electrical field and providing a path for electron energy gain. As visualized in Figure 1.2, the energetic electrons then induce different types of electron-impact processes such as dissociation, excitation, ionization, and attachment. As a consequence, a large variety of plasma species (atoms, molecules and ions in the grounded and excited states, molecular fragments, free radicals) including the growth precursors for material deposition can be generated.

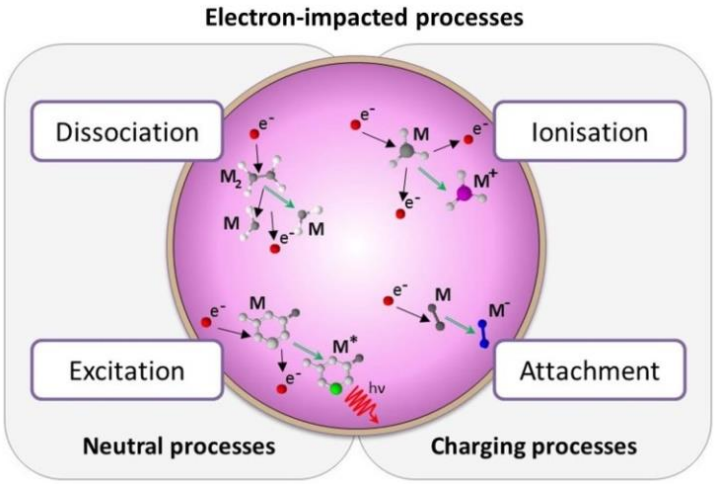

Figure 1.2 Schematic of electron-impact processes in a plasma. Extracted from Ref. 3.

The emergence of the PECVD technique also stems from the demands of the semiconductor industry for advances in process control, and a large amount of early commercial applications of PECVD were the low-temperature deposition of silicon nitride films for the passivation and encapsulation of completed microelectronic devices. Since the electron temperature is much higher than the gas temperature and substrate temperature, the PECVD process has the advantage to be able to operate under much lower temperature over the conventional thermally-activated CVD process not benefiting from the plasma activation. Therefore, previously unfeasible high-temperature reactions can be made to occur on temperature-sensitive substrates. Moreover, as has been extensively reported, the properties of the resulting material such as composition, stress, and morphology are strongly impacted by the elevated substrate temperature needed to dissociate precursors in standard CVD process. By operating at low temperature, the PECVD technique provides greater flexibility in process optimization.

1.2. Thin film silicon materials

1.2.1. Hydrogenated amorphous silicon (a-Si:H)

The preparation of pure silicon thin film is practically feasible by using the PVD method, and the resulting material can be either amorphous or microcrystalline. However, material prepared in

[3] C. Gerhard, et al., in *Plasma Science and Technology - Progress in Physical States and Chemical Reactions*, T. Mieno (Ed.), InTech (2016).

such a way contains a very high density of neutral threefold-coordinated Si dangling bonds (defect states) on the order of 10^{19} cm^{-3}, which prevent doping, carrier transport, and many other characteristics that are desirable for a useful optoelectronic device. Such material is therefore of little technical importance.

However, the situation can be largely improved by incorporating atomic hydrogen into the silicon network, thus producing hydrogenated amorphous silicon (a-Si:H). Concerning the deposition of a-Si:H, the first published work can be traced back to 1879 done by Ogier[4]. However, research into this type of material really started one century later. In the second half of the 1960s, Sterling, Chittick and coworkers from the Standard Telecommunication Laboratories group published the formation of a-Si:H thin film from silane (SiH_4) using glow discharge[5,6]. With the incorporation of hydrogen, they managed to decrease the Si dangling bonds density down to 10^{15}-10^{16} cm^{-3}.

However, the essential role of hydrogen was not recognized immediately. It was later suggested by Lewis *et al*[7] from the Harvard group in a study about sputtered amorphous germanium in 1974, that the high density of defect states can be suppressed by adding hydrogen (H_2) to the plasma during processing. Through the passivation of dangling bonds by hydrogen atoms, improved electronic properties were obtained for the resulting amorphous material. Afterwards, it was confirmed by means of a hydrogen evolution experiment that glow discharge deposited amorphous silicon from pure SiH_4 also contains hydrogen[8]. Ever since, it has been generally recognized that device-grade amorphous silicon material in fact should be hydrogenated. Later on, Spear and Le Comber reported that the a-Si:H deposited using glow discharge can be *n*-type and *p*-type doped by the addition of phosphine and diborane[9]. Shortly afterwards, the demonstration of a-Si:H *pn* junction[10] and the first practical a-Si:H *p-i-n* solar cell device were published in 1976[11]. All these observations lead to significant interest in a-Si:H material, and since then, a tremendous quantity of research activities have been performed on this topic.

Properties

In contrast to crystalline silicon (c-Si) material which possesses a well-ordered silicon network, the main feature for amorphous silicon material is the long-range disorder in the atomic structure. As shown in Figure 1.3, although it has a tetrahedral bonding configuration as in c-Si, amorphous silicon shows a large distribution in bond lengths and bond angles. Therefore, free electrons and holes can have a scattering length of about an interatomic spacing, and as a consequence, the mobility of free electrons and holes in amorphous silicon are much lower than those for c-Si.

[4] M. J. Ogier, *Bull. Société Chim. Fr.*, **116**: (1879).
[5] H. F. Sterling, et al., *Solid-State Electron.*, **8(8)**: 653 (1965).
[6] R. C. Chittick, et al., *J. Electrochem. Soc.*, **116(1)**: 77 (1969).
[7] A. J. Lewis, et al., *AIP Conf. Proc.*, **20(1)**: 27 (1974).
[8] A. Triska, et al., *Bull. Am. Phys. Soc.*, **20**: 392 (1975).
[9] W. E. Spear, et al., *Solid State Commun.*, **17(9)**: 1193 (1975).
[10] W. E. Spear, et al., *Appl. Phys. Lett.*, **28(2)**: 105 (1976).
[11] D. E. Carlson, et al., *Appl. Phys. Lett.*, **28(11)**: 671 (1976).

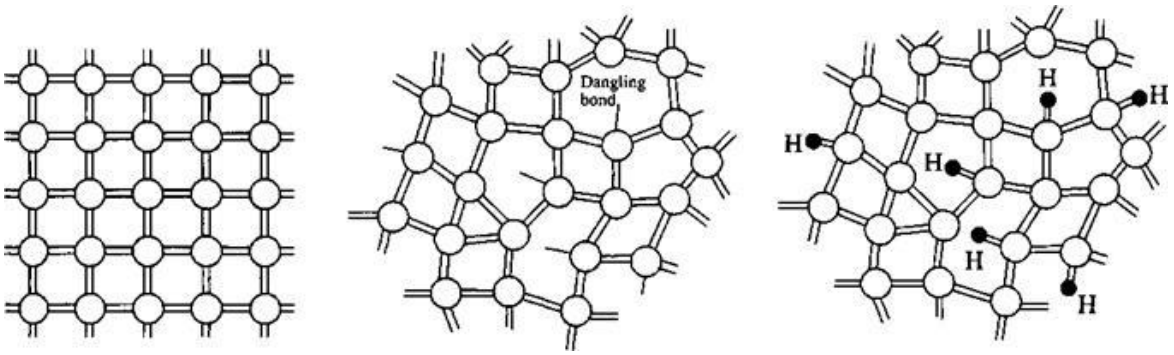

Figure 1.3 Schematic of c-Si (left), a-Si (medium), and a-Si:H (right).

Figure 1.4 depicts the density of states plot for a-Si:H, from which the electronic structure can be described. The bonding disorder causes exponential tails of localized states at the band edges extending into the forbidden gap, called band tails. Due to the frequent trapping and de-trapping from these localized states in band tails, the effective mobility of free electrons and holes in a-Si:H are further reduced. The energy level dividing the extended states and localized states is called the mobility edge[12]. To distinguish from the classical band gap, a mobility gap defined by the separation of the valence and conduction band mobility edges is used to describe the optical band gap for a-Si:H. On the other hand, despite the incorporation of hydrogen, the a-Si:H retains a considerable amount of dangling bonds. These dangling bonds can give rise to additional defect states near the center of mobility gap, and which are associated with carrier trapping and recombination processes, thus determining the material electronic properties.

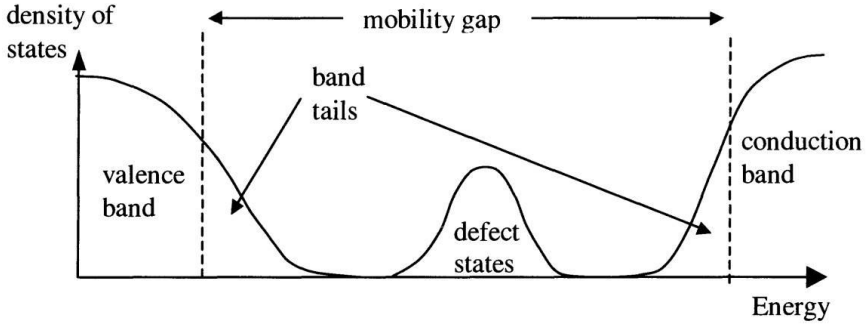

Figure 1.4 Schematic of density of states for a-Si:H. Extracted from Ref. 13.

Due to the presence of long-range disorder in the atomic network, the optical properties of a-Si:H are also different from c-Si. The rapid scattering of free carriers makes the momentum conservation law for electron excitation relaxed, thus making a-Si:H behave more like a material with a direct band gap. This is important for solar cell applications, as to absorb all the available above-band photons, a much lower active layer thickness (usually on the order of several hundred nanometers) is required for an a-Si:H solar cell than that for c-Si solar cell (usually on the order of several hundred microns).

[12] N. Mott, *J. Phys. C: Solid State Phys.*, **20(21)**: 3075 (1987).
[13] R. A. Street, *Hydrogenated Amorphous Silicon*, Cambridge University Press (1991).

Staebler-Wronski effect

The main challenge for the application of a-Si:H in photovoltaics is its light-induced degradation, as after prolonged illumination, additional metastable defects will be generated in the material. The exact nature and detailed explanation for this effect is still not well known, but it is generally thought to be associated with the breaking of weak or strained Si-Si bonds or the emission of mobile hydrogen from Si-H bonds. These metastable defects can act as recombination centers for free carriers in a similar fashion to dangling bonds, consequently giving reduced electronic properties. In fact, this light-induced degradation (LID) is a reversible process. By annealing the sample at suitable temperature with enough time, these metastable defects can be (partially) eliminated. As this effect was first reported by Staebler and Wronski shortly after the fabrication of the first practical a-Si:H solar cell, it is often referred as the *Staebler-Wronski Effect*[14].

Growth mechanism

Among the many preparation methods for a-Si:H thin films, the PECVD technique is most widely used. As previously stated, in such a plasma-based process, all the events are a consequence of electron-impact processes. Taking a commonly used SiH_4/H_2 plasma process for example, a rich variety of species are generated through the inelastic collisions between feed gas molecules and energetic electrons: hydrogen radicals, silicon radicals (neutral, positively or negatively charged, metastable), photons, etc., as shown by Figure 1.5-(a). Besides these primary reactions, those reactive products can make further reactions with each other, or with their parent SiH_4 and H_2 molecules, forming larger molecules, nanoparticles, or clusters.

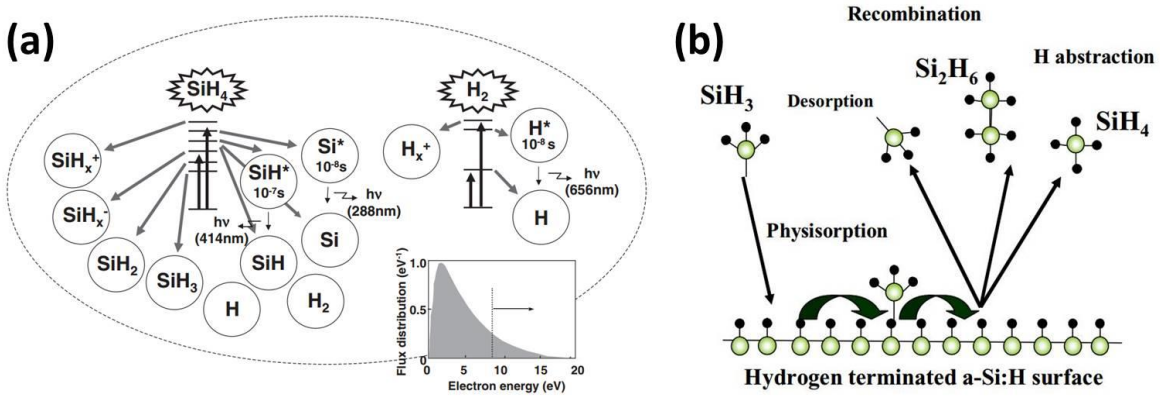

Figure 1.5 (a) Products from electron-impact processes in SiH_4/H_2 plasma. Extracted from Ref. 15. (b) Schematic of the a-Si:H film growth mechanism, assuming SiH_3 radicals as the main growth precursor. Extracted from Ref. 17.

Despite the richness of plasma species, the standard deposition model for a-Si:H is based on SiH_3 (which as a single unsaturated bond) as the main growth precursor[15,16,17]. Figure 1.5-(b)

[14] D. L. Staebler, et al., *Appl. Phys. Lett.*, **31(4)**: 292 (1977).
[15] A. Matsuda, *Jpn. J. Appl. Phys.*, **43(12R)**: 7909 (2004).
[16] W. M. M. Kessels, et al., *Thin Solid Films*, **383(1–2)**: 154 (2001).
[17] P. Roca. i Cabarrocas, in *Physics and Technology of Amorphous-Crystalline Heterostructure Silicon Solar Cells*, W. G. J. H. M. van Sark, L. Korte, and F. Roca (Eds.), Springer Berlin Heidelberg (2012).

schematically describes the most important processes on the film growth surface. During processing, the a-Si:H surface is almost fully terminated by hydrogen atoms at a relatively low substrate temperature (usually less than 200°C). The SiH_3 radicals produced in the gas phase will physisorb and start to diffuse on the hydrogen terminated surface. During the surface diffusion process, SiH_3 may experience various reactions: it could just simply desorb as SiH_3, since it has a low sticking coefficient of around 0.1; or it recombines with another SiH_3 to produce a larger radical like Si_2H_6; it could also abstract a surface-bonded hydrogen, forming SiH_4 and leaving behind a dangling bond on the surface. This dangling bond can act as a growth-site, to which another SiH_3 can adhere to form an Si-Si bond, leading to film growth.

1.2.2. Hydrogenated microcrystalline silicon (μc-Si:H)

μc-Si:H is a slight variant on a-Si:H, produced under similar conditions, but with dramatically different properties. The first detailed study about the fabrication of μc-Si:H was published by Vepřek *et al* in 1968[18]. In their process, they used a chemical vapor transport technique. By making use of a H_2 plasma, silicon material was etched from a solid-phase silicon source and then deposited as a microcrystalline phase on a substrate at another position. Following this, the first study about the deposition of μc-Si:H using PECVD was reported by Usui *et al* in 1979[19]. In the course of preparing doped a-Si:H, they accidently found that the material with a microcrystalline phase was obtained.

Thereafter, research activities on this topic grew explosively, including on the application of μc-Si:H in solar cells. The real breakthrough in this field came more than 10 years later. In 1993, the first working μc-Si:H solar cell was successfully fabricated at the IMT group (Neuchâtel) by applying the intrinsic μc-Si:H as the absorber layer[20]. This then stimulated further systematic research on all aspects of μc-Si:H material and devices for the following two decades and more.

Properties

μc-Si:H is a two-phase material consisting of crystalline grains and amorphous tissue, and as so is highly inhomogeneous. Shortly after the accident discovery of the formation of μc-Si:H by PECVD, it was found that the resulting material can be easily adjusted between pure amorphous phase and highly crystallized phases by modifying the processing parameters appropriately.

Taking the SiH_4/H_2 plasma chemistry for example, an easy way to achieve this variation is to control the hydrogen dilution ratio ($R = [H_2]/[SiH_4]$)[21,22,23]. The evolution of the material morphology with the change of ratio R is schematically depicted in Figure 1.6. A higher value of R usually gives a higher crystalline volume fraction, with a prominent conical morphology (see the left side of Figure 1.6). Upon the decrease of hydrogen dilution, a dramatic change of the microstructure can be observed. Initially, the resulting material tends to present reduced crystalline

[18] S. Vepřek, et al., *Solid-State Electron.*, **11(7)**: 683 (1968).
[19] S. Usui, et al., *J. Non-Cryst. Solids*, **34(1)**: 1 (1979).
[20] R. Flückiger, et al., *23th IEEE PVSC Proc.*, 839 (1993).
[21] A. Matsuda, *J. Non-Cryst. Solids*, **59**: 767 (1983).
[22] O. Vetterl, et al., *Sol. Energy Mater. Sol. Cells*, **62(1–2)**: 97 (2000).
[23] R. W. Collins, et al., *Sol. Energy Mater. Sol. Cells*, **78(1–4)**: 143 (2003).

column size with smaller grains. Then during the transition from highly crystallized material to amorphous phase dominant material, more amorphous tissue is incorporated between the crystalline grains, which prohibits the lateral growth of the columnar structure. As a result, at low *R* values, the material is characterized by the columnar growth of amorphous silicon with very fine crystalline domains embedded in the amorphous matrices (see the right side of Figure 1.6). Eventually, the crystalline phase growth completely disappears at further decreased hydrogen dilution conditions, giving a purely amorphous phase material.

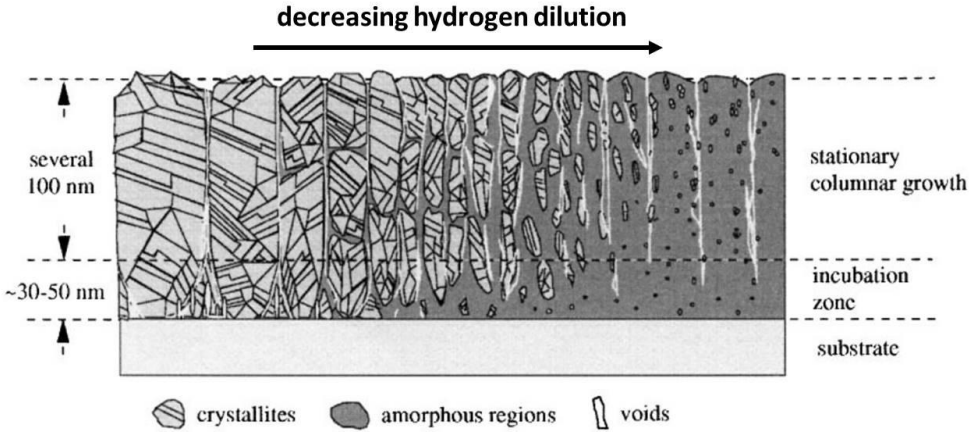

Figure 1.6 Evolution of structure of silicon thin films deposited with varying hydrogen dilution. Extracted from Ref. 22.

As in a-Si:H, one can also expect a large number of defects from dangling bonds and strained bonds in μc-Si:H, which can be active either as carrier traps or as recombination centers. However, a complication arises for μc-Si:H compared with a-Si:H from the fact that the local environment for these defects can vary; they may be inside a crystalline grain, on the surface of a grain boundary, or amongst the amorphous tissue. It is therefore not straightforward to distinguish these different defect states via only one experimental technique. Therefore, for the sake of simplicity, people usually concentrate on the characterization of the total defect density. For this, one frequently uses methods such as electron spin resonance[24], photothermal deflection spectroscopy[25], constant photocurrent method[26], or Fourier-transform photocurrent spectroscopy[27].

In view of the application of intrinsic μc-Si:H as the absorber layer in solar cells, the material optical absorption coefficient versus photon energy is a critical quantity. Figure 1.7 shows a typical optical absorption spectra for intrinsic μc-Si:H, and for comparison, the typical spectra for c-Si and a-Si:H are also presented. The band gap of μc-Si:H seems to be lower than that of c-Si, but if one considers light scattering by the rough surface of μc-Si:H[28], a similar band gap at ~1.1 eV for both μc-Si:H and c-Si is extracted[29]. On the other hand, although μc-Si:H material is highly inhomogeneous, its absorption curve closely follows that of c-Si over a wide range, especially for

[24] M. Vaněček, et al., *J. Non-Cryst. Solids*, **266**: 519 (2000).
[25] E. Sauvain, et al., *Solid State Commun.*, **85(3)**: 219 (1993).
[26] C. Main, et al., *J. Non-Cryst. Solids*, **338**: 228 (2004).
[27] M. Vaněček, et al., *Appl. Phys. Lett.*, **80(5)**: 719 (2002).
[28] A. Poruba, et al., *J. Appl. Phys.*, **88(1)**: 148 (2000).
[29] A. V. Shah, et al., *Sol. Energy Mater. Sol. Cells*, **78(1–4)**: 469 (2003).

photon energies below ~1.8 eV. The optical absorption in this range is mainly due to the crystalline phase material. This is true even for less crystallized µc-Si:H material, as absorption in this range may still be present (not shown here), and it will only disappear when the material is fully amorphous. On the other hand, for photon energies above ~1.8 eV, the optical absorption of µc-Si:H is more due to the amorphous phase, since it presents a absorption coefficient higher than c-Si but lower than a-Si:H in this range.

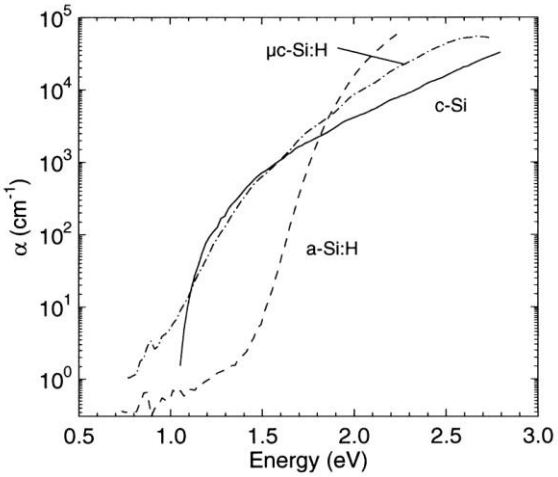

Figure 1.7 Typical optical absorption coefficient of µc-Si:H as a function of photon energy (compared to that of c-Si and a-Si:H). Extracted from Ref. 22.

Light-induced degradation also occurs for µc-Si:H material, but overall the degradation is lower when compared to a-Si:H. As a matter of fact, the extent of LID for µc-Si:H strongly depends on the content of amorphous phase in the material[30,31]. Usually, the lower the crystallinity, the stronger the degradation, while highly crystallized material is significantly more stable under illumination. As an example from Ref. 30, a single-junction µc-Si:H solar cell with highly crystallized intrinsic absorber layer shows almost no degradation in light conversion efficiency (within experimental error) after 1000 hours of light soaking.

Another important aspect for the material properties of µc-Si:H is the oxygen contamination. In certain cases, highly crystallized µc-Si:H presents a pronounced *n*-type character with a rather high dark conductivity. This has been suggested by Torres *et al*[32] to be linked to the extrinsic incorporation of oxygen atoms (at grain boundaries, voids surface, etc.), thus creating shallow donor states in the material. To avoid such donors, the authors have reported that it could be helpful to use a gas purifier for the feed gas and to have a better control over the out-gassing rate during the deposition process. In doing so, lower oxygen concentration was observed in the resulting intrinsic µc-Si:H layers, and the direct consequence was the decrease of dark conductivity; moreover, solar cells containing these less oxygen contaminated layers can have a considerable enhancement of the spectra response in the long wavelength range[33].

[30] F. Finger, et al., *IEEE Proc. - Circuits Devices Syst.*, **150(4)**: 300 (2003).
[31] F. Meillaud, et al., *31st IEEE PVSC Proc.*, 1412 (2005).
[32] P. Torres, et al., *Appl. Phys. Lett.*, **69(10)**: 1373 (1996).
[33] T. Matsui, et al., *Jpn. J. Appl. Phys.*, **42(8A)**: L901 (2003).

Growth mechanism

Three types of growth model have been proposed for the formation of μc-Si:H by PECVD: *surface diffusion models*, *etching models*, and *chemical annealing models*. In a review study[34], Matsuda has given a good summary for these models, as shown in Figure 1.8.

Figure 1.8-(a) describes the *surface diffusion model*. In this model, it is suggested that the high hydrogen dilution guarantees a sufficient flux of atomic hydrogen (H) towards the growing surface, which ensures a full surface coverage of bonded hydrogen. This can also produce great amount of local heating through the hydrogen recombination process on the surface. As a consequence, the surface diffusion of growth precursors is enhanced. This can help them to find energetically favorable sites for the formation of atomically flat surface, and subsequently, leading to the generation of crystalline nuclei and the growth of crystalline grains.

Figure 1.8-(b) describes the *etching model*. This model was proposed based on the experimental fact that the film deposition rate is reduced by an increase of hydrogen dilution. Atomic hydrogen on the growing surface breaks the energetically unfavorable weak Si-Si bonds, present preferentially in the amorphous network. In doing so, if one Si atom is removed from the surface, the next incoming growth precursor would move to this site to establish a more rigid Si-Si bond and give an ordered structure, i.e., the formation of crystalline grains.

Figure 1.8-(c) describes the *chemical annealing model*. This model was proposed based on the experimental observation that material with a crystalline phase was formed during H_2 plasma treatment of an a-Si:H layer using a layer-by-layer (LBL) deposition method (alternating sequence of a-Si:H deposition and H_2 plasma treatment). By performing the alternating LBL process for several ten times, it was found that the film thickness was essentially not reduced during the H_2 plasma treatment. This phenomenon cannot be explained by the atomic H etching effect through the *etching model*. To give a reasonable explanation, it was suggested that many of these hydrogen atoms penetrated into the "sub-surface" or "growth zone" below the top surface, which induced a certain extend of structural relaxation (exothermic) in this region. With sufficient flux density of atomic H, this interaction can give rise to the occurrence of crystallization of amorphous silicon network without removing a significant quantity of silicon atoms through the etching process.

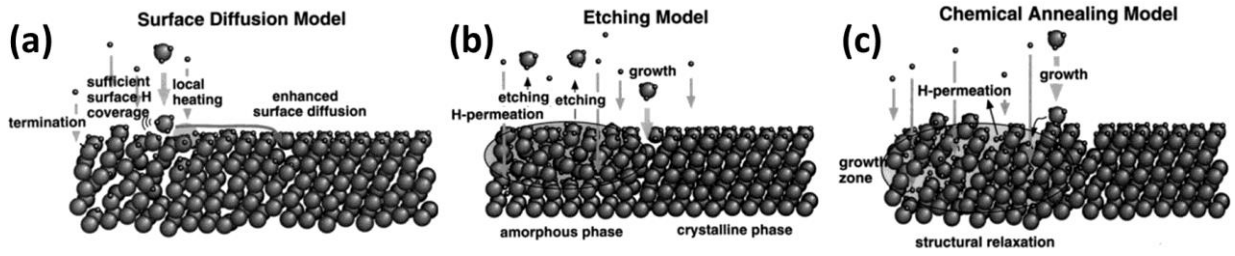

Figure 1.8 Schematic of surface process during μc-Si:H film growth based on a (a) *surface diffusion model*, (b) *etching model*, and (c) *chemical annealing model*. Extracted from Ref. 34.

In the same study, a detailed experimental verification for each of these models has also been carried out. The *surface diffusion model* was examined by studying the substrate temperature

[34] A. Matsuda, *Thin Solid Films*, **337(1–2)**: 1 (1999).

(impacting the radicals' surface diffusion) dependence of crystallinity for the resulting µc-Si:H as well as the film's initial growth behavior on a originally flat substrate. The *etching model* was discussed by comparing the relationship between radical generation rate in plasma through the corresponding optical emission and the resulting film deposition rate. The *chemical annealing model* was investigated through film growth using a similar LBL process. However, an improvement for the reaction apparatus was done by using a clean shutter in front of the cathode during the H_2 plasma treatment, in order to eliminate the possibility of material etched from the cathode acting as silicon source. The results showed that the *etching model* and *chemical annealing model* were insufficient to explain the growth of µc-Si:H, and the *surface diffusion model* was more supported by the experimental evidence.

Nevertheless, all these models are useful to condense knowledge about µc-Si:H from experimental observations, and each can be helpful in various cases. However, all these models converge on one general consensus concerning the plasma deposition of silicon thin films; in order to achieve high-quality material, any contribution from nanoparticles or nanocrystals generated in the plasma must be avoided. However, other work has led to a re-examination of this widely-held view. It was shown that plasma-generated nanoparticles or nanocrystals can also act as the building blocks for film growth. Moreover, unique optical and electrical properties for the resulting materials have been observed[17,35,36]. Overall, all these results suggest that a single, universal explanation for all process conditions may not exist, and a combinative consideration of these different models would be more appropriate to understand and evaluate thin film silicon growth processes.

1.3. Halogenated plasma chemistry

Halogenated amorphous silicon

As an alternative to SiH_4, research activities into using halogenated gases SiX_4 or SiH_2X_2 (here X can be chlorine or fluorine) as the silicon source for the deposition of silicon thin films have also been conducted over the last 40 years. Shortly after the observation of light-induced structural instability in a-Si:H, in 1978, the pioneering work of Ovshinsky and Madan was published in «*Nature*» about the preparation of a new type of amorphous silicon-based alloy having additive fluorine as one of its main structural components[37]. They showed that amorphous material resulting from a silicon tetrafluoride (SiF_4) and hydrogen plasma chemistry is superior to the previous SiH_4-based material for optoelectronic applications. The steric chemical and electronic properties for this type of Si-H-F alloy (a-Si:H,F) were described in detail in their subsequent work[38,39]. The author emphasized that the fluorine can act as a dangling bond terminator and its incorporation in the silicon network leads to low density of defect states, in particular lower than that of a-Si:H without fluorine (compared to their own work in Ref. 40). Due to the inherently low density of defect states, the material can be doped (*n*-type by adding arsine) very effectively.

[35] P. Roca i Cabarrocas, et al., *J. Phys. D: Appl. Phys.*, **40(8)**, 2258 (2007).
[36] K.-H. Kim, et al., *Sci. Rep.*, **7**: 40553 (2017).
[37] S. R. Ovshinsky, et al., *Nature*, **276(5687)**: 482 (1978).
[38] A. Madan, et al., *Philos. Mag. Part B*, **40(4)**: 259 (1979).
[39] A. Madan, et al., *J. Non-Cryst. Solids*, **35**: 171 (1980).
[40] A. Madan, et al., *J. Non-Cryst. Solids*, **20(2)**: 239 (1976).

Furthermore, almost no light-induced structure modification was observed. Because of these highly desirable characteristics, the authors predicted that "*this material seems to have a potential for general semiconducting applications as well as for photovoltaics*"[37].

Quite soon, this intrinsic a-Si:H,F material was successfully implemented into Schottky-barrier metal/insulator/semiconductor solar cell devices, and conversion efficiencies of up to 6.3 % were reported[41,42]. This work was soon followed and validated by Japanese groups[43,44], and the first *p-i-n* structure a-Si:H,F solar cell with a conversion efficiency of 2.5 % was fabricated by *SANYO*, which presented less degradation compared to their reference a-Si:H (without fluorine) solar cell[45].

Halogenated microcrystalline silicon

In 1980, Matsuda *et al* obtained doped hydrogenated and fluorinated silicon material with a microcrystalline phase by introducing a dopant gas (phosphine or phosphorus pentafluoride) in the SiF_4/H_2 gas mixture[46]. From that work, it was suggested that the fluorine is of crucial importance in inducing the ordered structure, especially in the case of high *n*-type doping levels. In fact, the first report about the preparation of intrinsic halogenated microcrystalline silicon was based on another type of halogenated gas – silicon tetrachloride ($SiCl_4$), thus giving a hydrogenated and chlorinated microcrystalline silicon (µc-Si:H,Cl)[47]. As for fluorine, the chlorine in the resulting material also act as a dangling bond terminator. Later on, the deposition of intrinsic hydrogenated and fluorinated microcrystalline silicon (µc-Si:H,F) was also achieved from an SiF_4/H_2 plasma chemistry by using a hydrogen-radical chemical vapor deposition (HRCVD) method, where the SiF_4 gas was exposed to the H_2 plasma generated in a microwave discharge[48]. From the HRCVD process, it was shown that the regulation of H_2 flow is a critical factor not only for determining the film deposition rate, but also for controlling the material structure, ranging from pure amorphous to varying amount of crystalline volume fraction.

Subsequently, µc-Si:H:F from PECVD using both $SiF_4/SiH_4/H_2$[49,50] or $SiF_4/Si_2H_6/H_2$[51] plasma chemistries was also reported. However, in those cases the silicon growth precursors are supposed to be from SiH_4 and Si_2H_6, as their binding energy is lower than that for SiF_4. The PECVD of µc-Si:H,F using SiF_4 as the silicon source was later reported using an SiF_4/H_2/He plasma chemistry in 1990s[52], and the role of He dilution in such a process was discussed in Ref. 53. Through the correlation of experimental results with *in-situ* optical emission spectroscopy measurements, it was suggested that the additive He can give an additional flexibility on the control over the film nucleation process and eventually its microstructure.

[41] M. Shur, et al., *International Electron Devices Meeting*, **26**: 545 (1980).
[42] A. Madan, et al., *Appl. Phys. Lett.*, **37(9)**: 826 (1980).
[43] M. Konagai, et al., *Appl. Phys. Lett.*, **36(7)**: 599 (1980).
[44] K. Nishihata, et al., *Jpn. J. Appl. Phys.*, **20(S2)**: 151 (1981).
[45] Y. Kuwano, et al., *Jpn. J. Appl. Phys.*, **20(S2)**: 157 (1981).
[46] A. Matsuda, et al., *Jpn. J. Appl. Phys.*, **19(6)**: L305 (1980).
[47] Z. Iqbal, et al., *Thin Solid Films*, **87(1)**: 43 (1982).
[48] N. Shibata, et al., *Jpn. J. Appl. Phys.*, **26(1A)**: L10 (1987).
[49] Y. Okada, et al., *J. Non-Cryst. Solids*, **114(2)**: 816 (1989).
[50] T. Nagahara, et al., *Jpn. J. Appl. Phys.*, **31(12S)**: 4555 (1992).
[51] D. Kim, et al., *J. Vac. Sci. Technol. A: Vac. Surf. Films*, **14(2)**: 478 (1996).
[52] J. I. Woo, et al., *Appl. Phys. Lett.*, **65(13)**: 1644 (1994).
[53] G. Cicala, et al., *Thin Solid Films*, **337(1–2)**: 59 (1999).

Work in the LPICM

In the late 1990s, such a fluorinated plasma chemistry was introduced in the LPICM for the PECVD of µc-Si:H[§] material[54], and the target is mainly for optoelectronic device applications[55]. Instead of helium, another noble gas, argon, was chosen (giving an $SiF_4/H_2/Ar$ gas mixture). In the early stages, the research activities were focused on the application of the material in thin film transistors[56]. Based on those studies, a better understanding was obtained for the growth mechanism[57] as well as the electronic properties[58, 59] of the resulting µc-Si:H material. Furthermore, more insights about the correlation between dusty plasma chemistry and the resulting surface processes were clarified by studying the gas-phase generated nanoparticles and their role in material deposition[60]. As research trends switched towards renewable energy, the research focus was transferred to photovoltaics since the late 2000s, such as the fabrication of the intrinsic absorber layer for thin film solar cells[61,62,63], and the epitaxial growth of the emitter for c-Si solar cells[64].

In recent PhD thesis work, a *phenomenological model*[65] was proposed to understand the material deposition from such an $SiF_4/H_2/Ar$ plasma chemistry. First of all, besides its similar function to He in the $SiF_4/H_2/He$ plasma chemistry, it was experimentally determined that Ar can act as a catalyzer of the gas dissociation. Accepting this, the model consists of two kinetic reactions, as shown by Equation (1.1) and (1.2). The first one simplistically accounts for the dissociation process of SiF_4 by assuming SiF_3 and atomic fluorine (F) as the by-products. The second one is the reaction of H_2 with atomic F.

$$SiF_4 \leftrightarrow SiF_3 + F \tag{1.1}$$

$$H_2 + F\bullet \leftrightarrow HF + H\bullet \tag{1.2}$$

In this model, the prominent process happening in the plasma is the removal of fluorine. Atomic fluorine species generated from the dissociation of SiF_4 (Equation (1.1)) are thought to be scavenged by molecular H_2 in the form of HF during processing (Equation (1.2)). The resulting surface process can be easily illustrated by Figure 1.9.

When no hydrogen is injected, there will be no deposition from the pure SiF_4/Ar plasma despite the presence of SiF_x. This is because that the SiF_4 dissociation process is always associated with the generation of fluorine atoms, which can result in a strong etching effect either in the gas phase

[§] All the microcrystalline silicon material fabricated in this thesis work is based on the $SiF_4/H_2/Ar$ plasma chemistry. For the sake of simplicity, we will use the abbreviation of µc-Si:H instead of µc-Si:H,F in the following content.

[54] R. Brenot, *PhD thesis*, École Polytechnique (2000).
[55] S. Kumar, et al., *Solid State Phenom.*, **80–81**: 237 (2001).
[56] S. Kasouit, et al., *Thin Solid Films*, **427(1–2)**: 67 (2003).
[57] A. Abramov, et al., *J. Non-Cryst. Solids*, **352**: 964 (2006).
[58] R. Vanderhaghen, et al., *J. Non-Cryst. Solids*, **299–302**: 365 (2002).
[59] S. K. Ram, et al., *Thin Solid Films*, **515(19)**: 7469 (2007).
[60] S. Kasouit, et al., *J. Non-Cryst. Solids*, **338–340**: 86 (2004).
[61] Q. Zhang, et al., *Phys. Status Solidi (RRL) – Rapid Res. Lett.*, **2(4)**: 154 (2008).
[62] M. Moreno, et al., *Sol. Energy Mater. Sol. Cells*, **100**: 16 (2012).
[63] J.-C. Dornstetter, et al., *IEEE J. Photovolt.*, **3(1)**: 581 (2013).
[64] R. Léal, et al., *AIP Adv.*, **7(2)**: 025006 (2017).
[65] J.-C. Dornstetter, *PhD thesis*, École Polytechnique (2014).

or on the substrate. Therefore, whatever the growth precursor, the film deposition requires both SiF_x as well as the removal of corresponding fluorine atoms through the formation of HF.

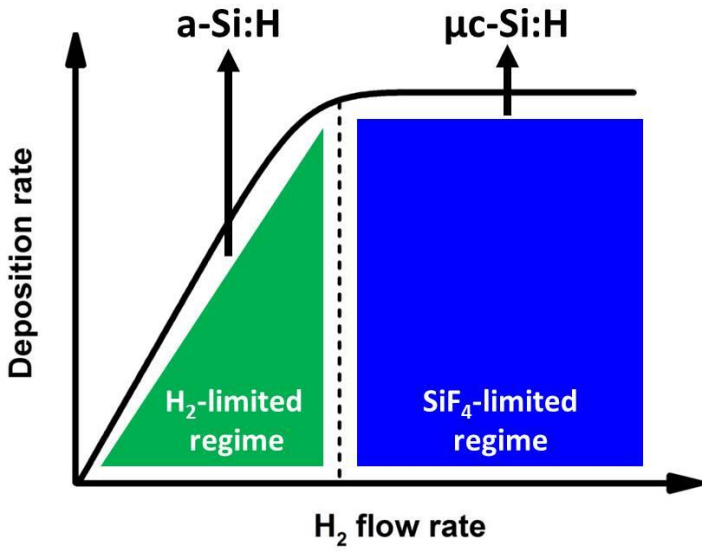

Figure 1.9 General description of variation of film deposition rate as a function of H_2 flow rate for $SiF_4/H_2/Ar$ plasma chemistry.

Once hydrogen is added into the gas mixture, the etching effect can be reduced and the deposition process appears. At low H_2 flows (see the green region), there is insufficient H_2 to scavenge the fluorine present, and a depletion of H_2 molecules will occur. Due to the remaining atomic fluorine, the etching process is still dominant. Therefore, in this case, hydrogen is the factor limiting the film deposition rate, and any increase in the hydrogen flow will result in an increase of deposition rate. This is called the H_2-limited regime.

When hydrogen is further increased, after a certain threshold the deposition rate will be no longer limited by the available hydrogen, but in turn by the dissociation of SiF_4, i.e., the available growth precursors. This is called the SiF_4-limited regime (see the blue region), where the depletion of hydrogen decreases as the relative concentration of available hydrogen increases and all fluorine is scavenged as HF. As a consequence, the film deposition rate stays high but constant in this region.

In addition, the transition between these two regimes while adding hydrogen is usually accompanied by a material phase transition from amorphous to microcrystalline. In the H_2-limited regime, amorphous material is obtained due to insufficient hydrogen being present for crystalline growth to occur. In the SiF_4-limited regime, the atomic hydrogen is in excess, favoring the crystallization process, either in the gas phase or on the growing surface, leading to the formation of microcrystalline phase material. In addition, such an amorphous-to-microcrystalline transition depends on the level of SiF_4 dissociated during the process, and thus increases with power injection and with SiF_4 flow rate. In such cases, more hydrogen is required to scavenge the fluorine by-product, and thus to trigger the transition.

It should be noted that this model does not mean to detail the otherwise complex chemical

processes in the plasma, but nevertheless providing a more intuitive link between the controllable processing parameters (power, pressure, gas flow ratio) and the experimental trends (deposition rate, material category).

In contrast to μc-Si:H films deposited from the SiH_4-based plasma chemistry, films deposited from the SiF_4-based plasma chemistry can have larger grain sizes and a rather small faction of amorphous content (sometimes even fully crystallized). Despite such low amorphous fractions, the material can still have a well-passivated grain boundaries and crystallites. For example, a defect density as low as 5.1×10^{14} cm^{-3} was achieved for a fully crystallized layer, and this was correlated with an excellent open-circuit voltage (V_{OC}) for the resulting μc-Si:H solar cell[65]. This upsets the paradigm that to obtain high efficiency devices, a material at the transition region between amorphous and microcrystalline silicon must be used as the active absorber layer to avoid the decrease of V_{OC}[66]. In addition, excellent carrier transport properties in the materials and less collection issue in the resulting devices allow one to use thicker absorber layers to obtain higher short-circuit current (I_{SC}).

[66] C. Droz, et al., *Sol. Energy Mater. Sol. Cells*, **81(1)**: 61 (2004).

1.4. Structure of this thesis

This PhD thesis work is dedicated to understanding the growth of silicon thin film materials using differing PECVD techniques and/or plasma chemistries, always with photovoltaic applications in mind. In addition to this first chapter, this manuscript consists of five main parts.

In chapter 2, we briefly describe the general background of experimental and characterization techniques.

In chapter 3, a halogenated plasma chemistry based on SiF_4 is combined with the matrix-distributed electron cyclotron resonance (MDECR) PECVD technique to obtain high growth rate µc-Si:H. The film growth dynamics under such low process pressure and high plasma density conditions is investigated, and the impact of different process parameters on the material quality is discussed.

In chapter 4, we explore the application of a recently developed radio frequency (RF) excitation source – Tailored Voltage Waveforms (TVW) – for capacitively coupled plasma (CCP). Through the use of the TVW technique, one can achieve a semi-independent control over the RF plasma parameters, even at a relatively high process pressure. Therefore, the study of their impact on RF-PECVD silicon thin film quality can be done for both µc-Si:H and a-Si:H. We apply the results to solar cell devices and establish a comprehensive link from the control over plasma parameters via TVW to the properties of deposited materials, and eventually to the performance of the resulting devices.

In chapter 5, the slope asymmetry effect observed when using *sawtooth* TVW (until now mainly studied in single-gas plasmas) is applied for the first time to more process-relevant, multi-gas plasmas. When combined with the multi-precursor nature of the deposition/etching process of the SiF_4-based plasma chemistry, an "electrode-selective" effect is observed in the resulting CCP process.

Finally, the whole work is summarized in the chapter 6, which also gathers some future perspectives.

Reference

[1] *Chemical Vapor Deposition: Principles and Applications*, M. L. Hitchman and K. F. Jensen (Ed.), London: Academic Press, 1993.

[2] M. Ohring, *Materials Science of Thin Films: Deposition and Structure* (second edition), San Diego: Academic Press, 2002.

[3] C. Gerhard, W. Viöl, and S. Wieneke, "*Plasma-Enhanced Laser Materials Processing*", in *Plasma Science and Technology - Progress in Physical States and Chemical Reactions*, T. Mieno (Ed.), InTech, 2016.

[4] M. J. Ogier, "Sur la formation thermique de l'hydrogène silicié", *Bull. Société Chim. Fr.*, p. 116, 1879.

[5] H. F. Sterling and R. C. G. Swann, "Chemical vapour deposition promoted by r.f. discharge", *Solid-State Electron.*, vol. 8, no. 8, p. 653, 1965.

[6] R. C. Chittick, J. H. Alexander, and H. F. Sterling, "The Preparation and Properties of Amorphous Silicon", *J. Electrochem. Soc.*, vol. 116, no. 1, p. 77, 1969.

[7] A. J. Lewis, G. A. N. Connell, W. Paul, J. R. Pawlik, R.J. Temkin, H.C. Wolfe, M.H. Brodsky, S. Kirkpatrick, and D. Weaire, "Hydrogen Incorporation in Amorphous Germanium", *AIP Conf. Proc.*, vol. 20, no. 1, p. 27, 1974.

[8] A. Triska and D. Dennison, "Hydrogen content in amorphous Ge and Si prepared by r.f. decomposition of GeH_4 and SiH_4", *Bull. Am. Phys. Soc.*, vol. 20, p. 392, 1975.

[9] W. E. Spear and P. G. Le Comber, "Substitutional doping of amorphous silicon", *Solid State Commun.*, vol. 17, no. 9, p. 1193, 1975.

[10] W. E. Spear, P. G. Le Comber, S. Kinmond, and M. H. Brodsky, "Amorphous silicon p-n junction", *Appl. Phys. Lett.*, vol. 28, no. 2, p. 105, 1976.

[11] D. E. Carlson and C. R. Wronski, "Amorphous silicon solar cell", *Appl. Phys. Lett.*, vol. 28, no. 11, p. 671, 1976.

[12] N. Mott, "The mobility edge since 1967", *J. Phys. C: Solid State Phys.*, vol. 20, no. 21, p. 3075, 1987.

[13] R. A. Street, *Hydrogenated Amorphous Silicon*. Cambridge: Cambridge University Press, 1991.

[14] D. L. Staebler and C. R. Wronski, "Reversible conductivity changes in discharge-produced amorphous Si", *Appl. Phys. Lett.*, vol. 31, no. 4, p. 292, 1977.

[15] A. Matsuda, "Thin-Film Silicon – Growth Process and Solar Cell Application –", *Jpn. J. Appl. Phys.*, vol. 43, no. 12R, p. 7909, 2004.

[16] W. M. M. Kessels, A. H. M. Smets, D. C. Marra, E. S. Aydil, D. C. Schram, and M. C. M. van de Sanden, "On the growth mechanism of a-Si:H", *Thin Solid Films*, vol. 383, no. 1–2, p. 154, 2001.

[17] P. Roca i Cabarrocas, "Deposition Techniques and Processes Involved in the Growth of Amorphous and Microcrystalline Silicon Thin Films", in *Physics and Technology of*

Amorphous-Crystalline Heterostructure Silicon Solar Cells, W. G. J. H. M. van Sark, L. Korte, and F. Roca, Eds. Springer Berlin Heidelberg, p. 131, 2012.

[18] S. Vepřek and V. Mareček, "The preparation of thin layers of Ge and Si by chemical hydrogen plasma transport", *Solid-State Electron.*, vol. 11, no. 7, p. 683, 1968.

[19] S. Usui and M. Kikuchi, "Properties of heavily doped GD-Si with low resistivity", *J. Non-Cryst. Solids*, vol. 34, no. 1, p. 1, 1979.

[20] R. Flückiger, J. Meier, H. Keppner, M. Götz, and A. Shah, "Preparation of Undoped and Doped Microcrystalline Silicon (μc-Si:H) by VHF-GD for p-i-n Solar Cells", *Proceedings of the 23th IEEE Photovoltaic Specialists Conference*, Louisville, p. 839, 1993.

[21] A. Matsuda, "Formation kinetics and control of microcrystallite in μc-Si:H from glow discharge plasma", *J. Non-Cryst. Solids*, vol. 59, p. 767, 1983.

[22] O. Vetterl, F. Finger, R. Carius, P. Hapke, L. Houben, O. Kluth, A. Lambertz, A. Mück, B. Rech, and H. Wagner, "Intrinsic microcrystalline silicon: A new material for photovoltaics", *Sol. Energy Mater. Sol. Cells*, vol. 62, no. 1–2, p. 97, 2000.

[23] R. W. Collins, G. M. Ferreira, C. Chen, J. Koh, and Y. Lee, "Evolution of microstructure and phase in amorphous, protocrystalline, and microcrystalline silicon studied by real time spectroscopic ellipsometry", *Sol. Energy Mater. Sol. Cells*, vol. 78, no. 1–4, p. 143, 2003.

[24] M. Vaněček, A. Poruba, Z. Remeš, J. Rosa, S. Kamba, V. Vorlíček, J. Meier, and A. Shah, "Electron spin resonance and optical characterization of defects in microcrystalline silicon", *J. Non-Cryst. Solids*, vol. 266, p. 519, 2000.

[25] E. Sauvain, A. Mettler, N. Wyrsch, and A. Shah, "Subbandgap absorption spectra of slightly doped a-Si:H measured with constant photocurrent method (CPM) and photothermal deflection spectroscopy (PDS)", *Solid State Commun.*, vol. 85, no. 3, p. 219, 1993.

[26] C. Main, S. Reynolds, I. Zrinščak, and A. Merazga, "Comparison of AC and DC constant photocurrent methods for determination of defect densities", *J. Non-Cryst. Solids*, vol. 338, p. 228, 2004.

[27] M. Vaněček and A. Poruba, "Fourier-transform photocurrent spectroscopy of microcrystalline silicon for solar cells", *Appl. Phys. Lett.*, vol. 80, no. 5, p. 719, 2002.

[28] A. Poruba, A. Fejfar, Z. Remeš, J. Špringer, M. Vaněček, J. Kočka, J. Meier, P. Torres, and A. Shah, "Optical absorption and light scattering in microcrystalline silicon thin films and solar cells", *J. Appl. Phys.*, vol. 88, no. 1, p. 148, 2000.

[29] A. V. Shah, J. Meier, E. Vallat-Sauvain, N. Wyrsch, U. Kroll, C. Droz, and U. Graf, "Material and solar cell research in microcrystalline silicon", *Sol. Energy Mater. Sol. Cells*, vol. 78, no. 1–4, p. 469, 2003.

[30] F. Finger, R. Carius, T. Dylla, S. Klein, S. Okur, and M. Gunes, "Stability of microcrystalline silicon for thin film solar cell applications," *IEE Proc. - Circuits Devices Syst.*, vol. 150, no. 4, p. 300, 2003.

[31] F. Meillaud, E. Vallat-Sauvain, X. Niquille, M. Dubey, J. Bailat, A. Shah, and C. Ballif, "Light-induced degradation of thin film amorphous and microcrystalline silicon solar

cells", *Proceeding of the 31st IEEE Photovoltaic Specialists Conference*, Lake Buena Vista, p.1412, 2005.

[32] P. Torres, J. Meier, R. Flückiger, U. Kroll, J. A. A. Selvan, H. Keppner, A. Shah, S. D. Littelwood, I. E. Kelly, and P. Giannoulès, "Device grade microcrystalline silicon owing to reduced oxygen contamination", *Appl. Phys. Lett.*, vol. 69, no. 10, p. 1373, 1996.

[33] T. Matsui, M. Kondo, and A. Matsuda, "Origin of the Improved Performance of High-Deposition-Rate Microcrystalline Silicon Solar Cells by High-Pressure Glow Discharge", *Jpn. J. Appl. Phys.*, vol. 42, no. 8A, p. L901, 2003.

[34] A. Matsuda, "Growth mechanism of microcrystalline silicon obtained from reactive plasmas", *Thin Solid Films*, vol. 337, no. 1–2, p. 1, 1999.

[35] P. Roca i Cabarrocas, T. Nguyen-Tran, Y. Djeridane, A. Abramov, E. Johnson, and G. Patriarche, "Synthesis of silicon nanocrystals in silane plasmas for nanoelectronics and large area electronic devices", *J. Phys. D: Appl. Phys.*, vol. 40, no. 8, p. 2258, 2007.

[36] K.-H. Kim, E. V. Johnson, A. G. Kazanskii, M. V. Khenkin, and P. R. i Cabarrocas, "Unravelling a simple method for the low temperature synthesis of silicon nanocrystals and monolithic nanocrystalline thin films", *Sci. Rep.*, vol. 7, p. 40553, 2017.

[37] S. R. Ovshinsky and A. Madan, "A new amorphous silicon-based alloy for electronic applications", *Nature*, vol. 276, no. 5687, p. 482, 1978.

[38] A. Madan, S. R. Ovshinsky, and E. Benn, "Electrical and optical properties of amorphous Si:F:H alloys", *Philos. Mag. Part B*, vol. 40, no. 4, p. 259, 1979.

[39] A. Madan and S. R. Ovshinsky, "Properties of amorphous Si:F:H alloys", *J. Non-Cryst. Solids*, vol. 35, p. 171, 1980.

[40] A. Madan, P. G. Le Comber, and W. E. Spear, "Investigation of the density of localized states in a-Si using the field effect technique", *J. Non-Cryst. Solids*, vol. 20, no. 2, p. 239, 1976.

[41] M. Shur, W. Czubatyj, J. McGill, J. Yang, and A. Madan, "Experimental and theoretical studies of high efficiency a-Si:F:H MIS solar cells", *International Electron Devices Meeting*, vol. 26, p. 545, 1980.

[42] A. Madan, J. McGill, W. Czubatyj, J. Yang, and S. R. Ovshinsky, "Metal-insulator-semiconductor solar cells using amorphous Si:F:H alloys", *Appl. Phys. Lett.*, vol. 37, no. 9, p. 826, 1980.

[43] M. Konagai and K. Takahashi, "Amorphous Si-F-H solar cells prepared by dc glow discharge", *Appl. Phys. Lett.*, vol. 36, no. 7, p. 599,1980.

[44] K. Nishihata, K. Komori, M. Konagai, and K. Takahashi, "Effect of Fluorine on the Photovoltaic Properties of Amorphous Silicon Prepared by DC Glow Discharge", *Jpn. J. Appl. Phys.*, vol. 20, no. S2, p. 151, 1981.

[45] Y. Kuwano, M. Ohnishi, H. Nishiwaki, S. Tsuda, and H. Shibuya, "Properties of Amorphous Si:F:H Film and Its Photovoltaic Characteristics", *Jpn. J. Appl. Phys.*, vol. 20, no. S2, p. 157, 1981.

[46] A. Matsuda, S. Yamasaki, K. Nakagawa, H. Okushi, K. Tanaka, S. Iizima, M. Matsumura,

and H. Yamamoto, “Electrical and Structural Properties of Phosphorous-Doped Glow-Discharge Si:F:H and Si:H Films”, *Jpn. J. Appl. Phys.*, vol. 19, no. 6, p. L305, 1980.

[47] Z. Iqbal, P. Capezzuto, M. Braun, H.R. Oswald, S. Vepřek, G. Bruno, F. Cramarossa, H. Stüssi, J. Brunner, and M. Schärli, “Structural and some other properties of silicon deposited in an $SiCl_4$-H_2 r.f. discharge”, *Thin Solid Films*, vol. 87, no. 1, p. 43, 1982.

[48] N. Shibata, K. Fukuda, H. Ohtoshi, J. Hanna, S. Oda, and I. Shimizu, “Preparation of Polycrystalline Silicon by Hydrogen-Radical-Enhanced Chemical Vapor Deposition”, *Jpn. J. Appl. Phys.*, vol. 26, no. 1A, p. L10, 1987.

[49] Y. Okada, J. Chen, I. H. Campbell, P. M. Fauchet, and S. Wagner, “Mechanism of microcrystalline silicon growth from silicon tetrafluoride and hydrogen”, *J. Non-Cryst. Solids*, vol. 114, no. Part 2, p. 816, 1989.

[50] T. Nagahara, K. Fujimoto, N. Kohno, Y. Kashiwagi, and H. Kakinoki, “In-Situ Chemically Cleaning Poly-Si Growth at Low Temperature”, *Jpn. J. Appl. Phys.*, vol. 31, no. 12S, p. 4555, 1992.

[51] D. Kim and S. Rhee, “Particle formation in the remote plasma enhanced chemical vapor deposition of Si films from Si_2H_6–SiF_4–H_2”, *J. Vac. Sci. Technol. A: Vac. Surf. Films*, vol. 14, no. 2, p. 478, 1996.

[52] J. I. Woo, H. J. Lim, and J. Jang, “Polycrystalline silicon thin film transistors deposited at low substrate temperature by remote plasma chemical vapor deposition using SiF_4/H_2”, *Appl. Phys. Lett.*, vol. 65, no. 13, p. 1644, 1994.

[53] G. Cicala, P. Capezzuto, and G. Bruno, “Plasma enhanced chemical vapor deposition of nanocrystalline silicon films from SiF_4-H_2-He at low temperature”, *Thin Solid Films*, vol. 337, no. 1–2, p. 59, 1999.

[54] R. Brenot, “Corrélation entre mode de croissance et propriétés de transport du silicium microcristallin, établie par réflectométrie micro-onde et ellipsométrie”, *PhD thesis*, École Polytechnique (2000).

[55] S. Kumar, R. Brenot, B. Kalache, V. Tripathi, R. Vanderhaghen, B. Drevillon, and P. Roca i Cabarrocas, “Highly Crystalline Intrinsic Microcrystalline Silicon Films Using SiF_4/Ar/H_2 Glow Discharge Plasma”, *Solid State Phenom.*, vol. 80–81, p. 237, 2001.

[56] S. Kasouit, P. Roca i Cabarrocas, R. Vanderhaghen, Y. Bonassieux, M. Elyaakoubi, I. French, J. Rocha, and B. Vitoux, “Effect of deposition conditions and dielectric plasma treatments on the electrical properties of microcrystalline silicon TFTs”, *Thin Solid Films*, vol. 427, no. 1–2, p. 67, 2003.

[57] A. Abramov, Y. Djeridane, R. Vanderhaghen, and P. Roca i Cabarrocas, “Large grain μc-Si:H films deposited at low temperature: Growth process and electronic properties”, *J. Non-Cryst. Solids*, vol. 352, no. 9–20, p. 964, 2006.

[58] R. Vanderhaghen, S. Kasouit, R. Brenot, V. Chu, J. Conde, F. Liu, A. de Martino, and P. Roca i Cabarrocas, “Electronic transport in microcrystalline silicon controlled by trapping and intra-grain mobility”, *J. Non-Cryst. Solids*, vol. 299–302, p. 365, 2002.

[59] S. K. Ram, S. Kumar, and P. Roca i Cabarrocas, “Role of microstructure in electronic transport behavior of highly crystallized undoped microcrystalline Si Films”, *Thin Solid*

Films, vol. 515, no. 19, p. 7469, 2007.

[60] S. Kasouit, R. Brenot, V. Chu, J. Conde, F. Liu, A. de Martino, and P. Roca i Cabarrocas, "Contribution of plasma generated nanocrystals to the growth of microcrystalline silicon thin films", *J. Non-Cryst. Solids*, vol. 338–340, p. 86, 2004.

[61] Q. Zhang, E. V. Johnson, Y. Djeridane, A. Abramov, and P. Roca i Cabarrocas, "Decoupling crystalline volume fraction and V_{OC} in microcrystalline silicon pin solar cells by using a μc-Si:F:H intrinsic layer", *Phys. Status Solidi RRL*, vol. 2, no. 4, p. 154, 2008.

[62] M. Moreno, R. Boubekri, and P. Roca i Cabarrocas, "Study of the effects of different fractions of large grains of μc-Si:H:F films on the infrared absorption on thin film solar cells", *Sol. Energy Mater. Sol. Cells*, vol. 100, p. 16, 2012.

[63] J.-C. Dornstetter, S. Kasouit, and P. Roca i Cabarrocas, "Deposition of High-Efficiency Microcrystalline Silicon Solar Cells Using SiF_4/H_2/Ar Mixtures", *IEEE J. Photovolt.*, vol. 3, no. 1, p. 581, 2013.

[64] R. Léal, F. Haddad, G. Poulain, J.-L. Maurice, and P. Roca i Cabarrocas, "High quality boron-doped epitaxial layers grown at 200°C from SiF_4/H_2/Ar gas mixtures for emitter formation in crystalline silicon solar cells", *AIP Adv.*, vol. 7, no. 2, p. 025006, 2017.

[65] J.-C. Dornstetter, "Microcrystalline silicon deposited from SiF_4/H_2/Ar plasmas and its application to photovoltaics", *PhD thesis*, École Polytechnique, 2011.

[66] C. Droz, E. Vallat-Sauvain, J. Bailat, L. Feitknecht, J. Meier, and A. Shah, "Relationship between Raman crystallinity and open-circuit voltage in microcrystalline silicon solar cells", *Sol. Energy Mater. Sol. Cells*, vol. 81, no. 1, p. 61, 2004.

Chapter 2 Fundamental and experimental background

Contents

2.1. Capacitively coupled plasma (CCP)

A CCP reactor is generally composed of two electrodes in parallel with a spacing between them. After plasma ignition and for voltage excitation frequencies above a few MHz, only the electrons can respond to the instantaneous electric field produced by the applied voltage due to their lower mass and therefore higher mobility compared to other charged species. As well, they will be more quickly lost to the electrodes. On the contrary, the ions are characterized by a considerable lower mobility due to their much higher mass. As a consequence, such difference in mobility leads to the stratification of the discharge volume.

Figure 2.1-(a) generally shows an electropositive plasma (ions are only positively charged) operated in a geometrically symmetric system, where the electrons and ions density (n_e and n_i) profiles are depicted. The central part of the discharge, i.e., the bulk plasma, is essentially quasi-neutral since the amount of electrons and ions is comparable. However, such quasi-neutrality is no longer respected for the regions close to the electrodes. Because of the quick electrons loss, these regions always contain an excess of ions compared to electrons ($n_i > n_e$). As one can note in the figure, the closer one is to the electrodes, the greater this charge imbalance. Such space charge regions are named the plasma sheaths.

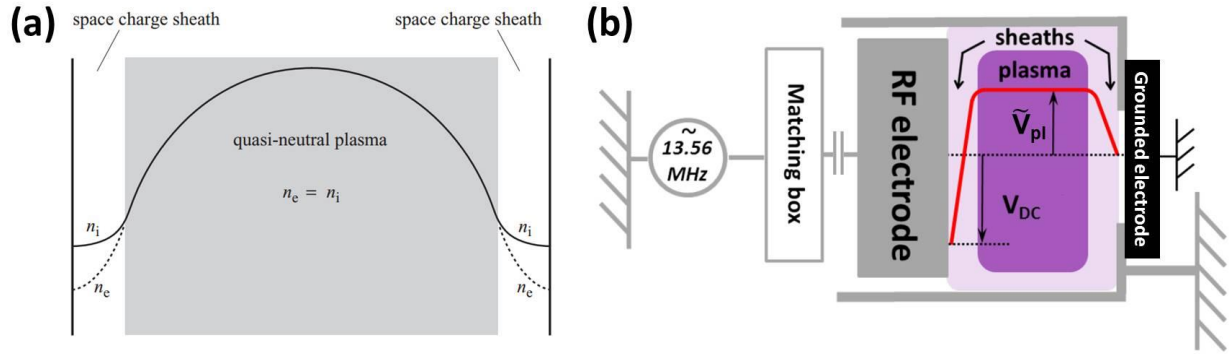

Figure 2.1 (a) Schematic of plasma density distribution in a CCP process. Extracted from Ref. 1. (b) Schematic of a typical RF-PECVD system. The red line denotes the plasma potential profile. Extracted from Ref. 2.

To quantify the difference of mobility between electrons and ions, one can define a plasma frequency representing the highest frequency to which one species can respond. For example, the electron plasma frequency and the ion plasma frequency[3] can be given by

[1] P. Chabert, et al., *Physics of Radio-Frequency Plasmas*, Cambridge: Cambridge University Press (2011).
[2] M. Labrune, *PhD thesis*, École Polytechnique (2011).
[3] M. A. Lieberman, et al., *Principles of Plasma Discharges and Materials Processing*, New Jersey: Wiley (2005).

$$\omega_{pe} = q\sqrt{\frac{n_e}{m\varepsilon_0}} \quad \text{and} \quad \omega_{pi} = q\sqrt{\frac{n_i}{M\varepsilon_0}} \tag{2.1}$$

respectively, where q is the elementary charge, m and M are the mass of the electron and ion respectively, and ε_0 is the vacuum permittivity. Considering a commonly used 13.56 MHz RF excitation source, we have the following relationship

$$\omega_{pi} \ll \omega \ll \omega_{pe} \tag{2.2}$$

Here ω corresponds to the excitation frequency. This means that the light electrons can respond to the oscillating excitation source instantaneously, while the heavy ions can only see the time-averaged quantities.

2.1.1. RF-PECVD processing system

A typical RF-PECVD processing system is the capacitively coupled configuration, as depicted in Figure 2.1-(b). The process chamber consists of a vacuum vessel surrounding the two electrodes. An oscillating voltage signal is applied to one of the electrodes, called the powered electrode (or RF electrode). The other electrode is usually grounded. A matching network is employed between the powered electrode and the voltage source to maximize the delivered power. The processing substrate can be placed on the electrode, which can be heated. In systems with typical inter-electrode distances (several cm down to a few mm), a plasma can be sustained in a pressure range from several tens of mTorr to several Torr. Depending on the excitation frequency and power, the resulting plasma densities are usually in the range of 10^9-10^{11} cm^{-3} and electron temperature is on the order of several eV.

For most RF-PECVD reactors, the lateral walls are also grounded, which in fact gives a larger surface area for the grounded electrode than that of the powered electrode. This is called a geometrical asymmetry. If an external blocking capacitor is present between the voltage source and the powered electrode, this asymmetry will lead to the presence of a DC self-bias voltage V_{DC} on the powered electrode. This is can be understood by assuming the plasma as an equivalent circuit model composing of two series-connected capacitive sheaths (much lower capacitance than the external blocking capacitor) and a resistive plasma bulk[4]. These two capacitive sheaths can be viewed as a voltage divider in the RF domain. Supposing the impact of the sheath thickness is small, the larger area of the grounded electrode will lead to a larger capacitance for its adjacent sheath than that in front of the powered electrode. As a consequence, the time-averaged potential drops across the two sheaths are different, and such difference results in the formation of V_{DC}.

The red line in Figure 2.1-(b) represents the time-averaged potential profile within the plasma chamber. As previously stated, the plasma bulk is quasi-neutral, so the potential in this region is characterized by a nearly constant value (for electropositive plasma), and this time-averaged value is called the plasma potential $\tilde{V}_{pl}$. In most cases, this $\tilde{V}_{pl}$ is higher than the potential at the two electrodes, although in very specific conditions[5] the opposite situation – sheath reversal – can also

[4] C. B. Zarowin, *J. Vac. Sci. Technol. A: Vac. Surf. Films*, **2(4)**: 1537 (1984).
[5] O. Leroy, et al., *J. Phys. D: Appl. Phys.*, **28(3)**: 500 (1995).

be observed. Due to the presence of a potential drop, ions moving into the sheaths can be accelerated to a high kinetic energy, thus leading to a bombardment effect on the electrodes.

In practice, such ion bombardment plays a vital role in determining the processing results. Therefore, it is necessary to make estimation of the $\tilde{V}_{pl}$, as it is directly linked to the maximum kinetic energy that an ion may acquire before arriving on the electrode. Despite the technical challenges in measuring the $\tilde{V}_{pl}$ directly (usually by Langmuir probes) in some processes, for a sinusoidal voltage source, it can still be estimated by knowing V_{DC} via the well-known formula[6,7]

$$\tilde{V}_{pl} = \frac{1}{2}\left(\frac{1}{2}V_{PP} + V_{DC}\right) \tag{2.3}$$

where V_{PP} denotes the peak-to-peak voltage. Note that several preconditions have to be assumed concerning the estimation of $\tilde{V}_{pl}$ by Equation (2.3): i) the potential of bulk plasma is linearly related to the applied voltage; ii) no potential drop in the bulk plasma (time-averaged); iii) complete sheaths collapse in each fundamental period; iv) no sheath reversal. Therefore, the maximum kinetic energy for ions arriving at the powered electrode IBE_{max}^{p} and at the grounded electrode IBE_{max}^{g} can be approximately expressed as

$$IBE_{max}^{p} = \tilde{V}_{pl} - V_{DC} \tag{2.4}$$

and

$$IBE_{max}^{g} = \tilde{V}_{pl} \tag{2.5}$$

As the substrates (samples) are always positioned on the grounded electrode throughout this work, we simply express the maximum ion bombardment energy during processing (IBE_{max}^{g}) as IBE_{max}.

2.1.2. Description of RF-PECVD reactors

In this work, two RF-PECVD reactors were extensively used: PHILIX and NEXTRAL.

PHILIX is a monochamber reactor used for the deposition of intrinsic a-Si:H and µc-Si:H films from SiH_4- and SiF_4-based plasma chemistries respectively. The general schematic of the processing system is shown in Figure 2.2. The deposition chamber comprises a cylindrical confinement plasma box surrounding two 100 mm diameter parallel electrodes with adjustable inter-electrode distance. The plasma box is grounded, thus making the chamber geometrically asymmetric. The two electrodes are vertically positioned during processing to minimize the impact from powders formed in the gas phase on the material deposition. Both electrodes are heated by resistive coils controlled via feedback loops, with temperatures monitored by embedded thermocouples. The gases are injected behind the powered electrode, which is pierced by a number of small holes, as shown in Figure 2.2-(a). There are several viewports on the chamber sidewall

[6] O. Christensen, et al, *LeVide Couches Minces*, **165**: 37 (1973).
[7] B. Chapman, *Glow Discharge Processes: Sputtering and Plasma Etching*, New York: Wiley, (1980).

available for *in-situ* spectroscopic ellipsometry, optical emission spectroscopy, and residual gas analysis measurements. Note that there is no load-lock in this system, and a fairly long pumpdown time is required before each deposition to achieve the desired base pressure (below 2×10^{-6} mTorr in this work).

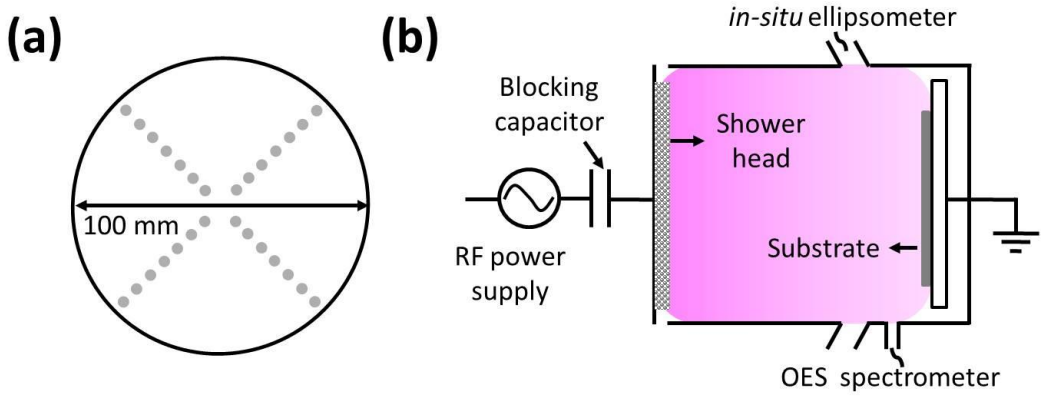

Figure 2.2 Schematics of PHILIX CCP-PECVD processing system: (a) top view of the powered electrode with shower head for gas injection and (b) cross-sectional view of the deposition chamber (not to scale).

NEXTRAL is also a monochamber reactor (located in the Thales building cleanroom). It was used for the deposition of *n*-a-SiC:H and *p*-a-Si:H layers for the single junction a-Si:H solar cells, and the *n*-a-Si:H and *p*-µc-Si:H layers for the single junction µc-Si:H solar cells. A detailed description of that processing system can be found in Ref. 8.

2.2. High density plasma source

In some particular applications, high density plasma is preferred to the more common RF-CCP process in order to achieve less processing time. This greatly motivates the development of plasma sources with higher ionization efficiency, i.e., higher plasma density. Such requirements could be satisfied by referring to more efficient power coupling schemes than the "classical" capacitive coupling, by using much higher excitation frequencies, or by employing magnetic confinement and resonant effects. Accordingly, different excitation sources like the inductively coupled plasma sources, helicon sources, electron cyclotron resonance plasma sources, and some other plasma sources have been developed.

Here, some typical instances of these high-density plasma systems will be briefly introduced, whereas a detailed study of the plasma processes is beyond the scope of this work. For a comprehensive understanding of these techniques, one is referred to the handbooks by Lieberman and Lichtenberg[3] and by Popov[9].

[8] A. Dommann, et al., *Microsyst. Technol.*, **7(4)**: 161 (2001).
[9] O. A. Popov, *High Density Plasma Sources Design, Physics and Performance*, William Andrew (1995).

2.2.1. Inductively coupled plasma source

In its simplest form, an inductively coupled plasma (ICP) source consists of a vacuum chamber and a non-resonant inductive coil. By applying an RF voltage (commonly with a frequency at 13.56 MHz or below) to the adjacent coil, the plasma can be created. From an electromagnetic point of view, the oscillating magnetic field associated with the time-varying coil current induces a current in the ionized gas.

As shown by the schematics in Figure 2.3, ICP systems usually have a cylindrical or a planar configuration. In the former case (see Figure 2.3-(a)), the plasma is generated by wrapping the spiral inductor around the outside (or inside) of the process chamber. In the latter case (see Figure 2.3-(b)), the inductive coil is a flat helix wound mounted on one side of the process chamber from the center to the outer radius, and is usually separated from the vacuum region by a dielectric window. In some applications, it is also possible to place it inside the chamber, but special design is required to avoid the issues of contamination due to sputtering. In addition, an array of multipolar magnets is sometimes placed around the discharge region to improve the radial plasma uniformity. Unlike the electron cyclotron resonance plasma sources introduced below, there is no resonance between electron motion and the frequency of the excitation source.

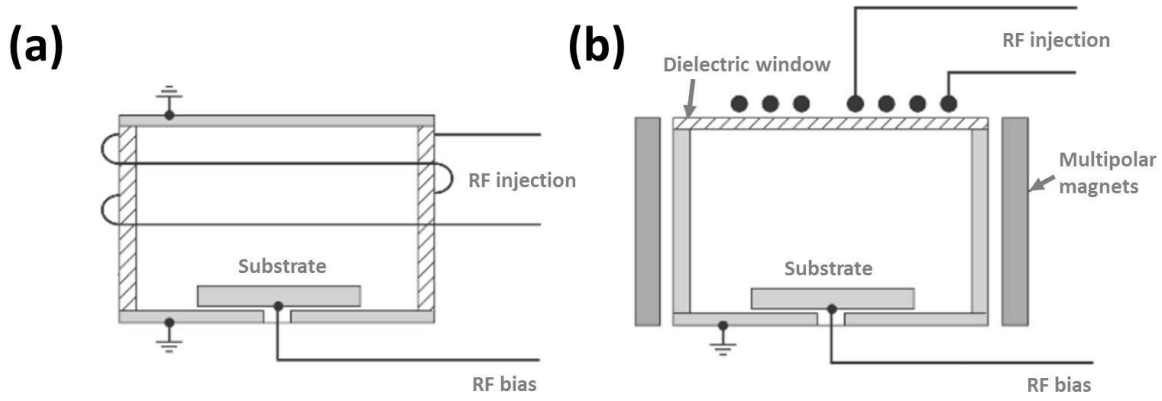

Figure 2.3 Schematic of ICP sources in (a) cylindrical and (b) planar configurations. Extracted from Ref. 3.

2.2.2. Helicon source

When low-frequency whistler waves are confined to a cylinder, their purely electromagnetic character cannot be maintained and they become partly electrostatic, and as a result, their propagation and polarization characteristics will also change. These bounded whistler waves are known as helicon waves. These waves have frequencies between the lower hybrid frequency and the ion plasma frequency, which is much lower than the electron cyclotron frequency that will be introduced later. In the early 1970s, Boswell found that the helicon waves can be unusually efficient in producing high density RF plasmas[10]. As a matter of fact, the experimentally measured ionization rate was about three orders of magnitude higher than that predicted by the theoretical calculation. It was later pointed out by Chen that Landau damping could be the cause for such

[10] R. W. Boswell, *Phys. Lett. A*, **33(7)**: 457 (1970).

efficient power absorption[9].

The general schematic of a typical helicon source is shown in Figure 2.4-(a). The main difference between a helicon discharge and an inductively coupled discharge is the presence of a weak (typically 50-200 G) magnetic field along the axis of source region. This magnetic field together with an RF-driven antenna placed around the chamber wall lead to the generation of helicon wave within the source region. The presence of the magnetic field can have several functions[9]. Firstly, the skin depth is increased, so that the inductive field can penetrate into the entire plasma; secondly, it is beneficial to have better electrons confinement; and finally it can also give extra flexibility to control the plasma uniformity via the magnetic field intensity.

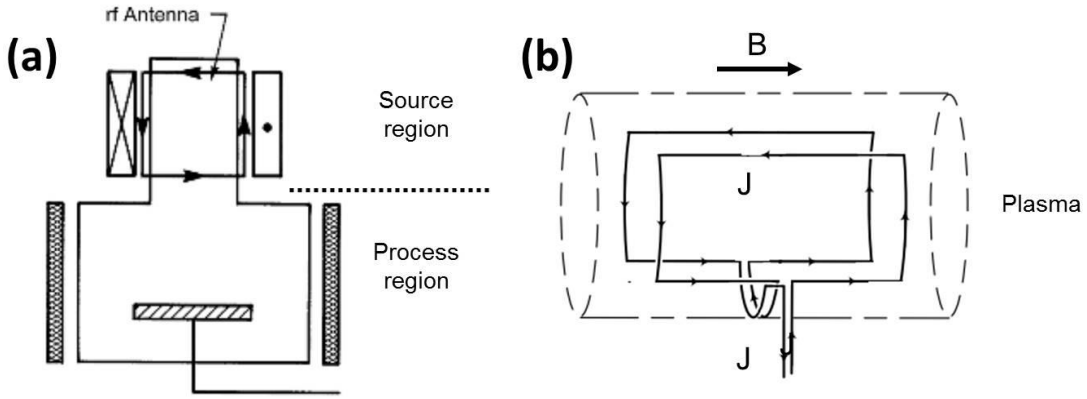

Figure 2.4 Schematics of (a) a typical helicon plasma source and (b) a Boswell antenna. Extracted from Ref. 3 and Ref. 9.

2.2.3. Electron resonance plasma (ECR) source

ECR plasmas are another type of magnetized plasma, but in contrast to ICP and helicons, the excitation source for an ECR plasma is in the microwave range. By setting the microwave frequency to be synchronous with the gyration frequency of the electrons defined by the magnetic field intensity, a resonant condition for the electrons can be obtained.

In this case, the electrons are accelerated continuously along the direction perpendicular to the magnetic field. Since the ECR-PECVD process has been extensively used in this work, we make a further description about this technique, mainly about the generalities and different types of reactor designs.

2.2.3.1. ECR plasma heating

Under the circumstance of a static and uniform magnetic field B, electrons experience a circular or helical (if the initial axial velocity is non-zero) motion along the magnetic field due to the Lorentz force, as shown in Figure 2.5-(a). The electron rotation has an angular frequency ω_c given by

$$\omega_c = \frac{qB}{m} \tag{2.6}$$

with a radius r_c given by

$$r_c = \frac{mv}{qB} \tag{2.7}$$

where v is the electron velocity in the direction perpendicular to the magnetic field. However, such circular or helical motion does not provide any energy gain for these electrons, even in a vacuum, without any collisions.

When a microwave electric field with an angular frequency ω

$$E = E_0 \cos(\omega t) \tag{2.8}$$

is superimposed on the magnetic field (see Figure 2.5-(b)), trajectory of the electron motion will be modified. If the condition of $\omega = \omega_c$ is satisfied, a resonance effect would occur. Then the electrons will move in phase with the electric field and will be accelerated continuously. This effect is known as the ECR effect. For the commonly used 2.45 GHz microwave excitation, the resonance effect occurs when magnitude of the magnetic field is at the specific value of 875 Gauss.

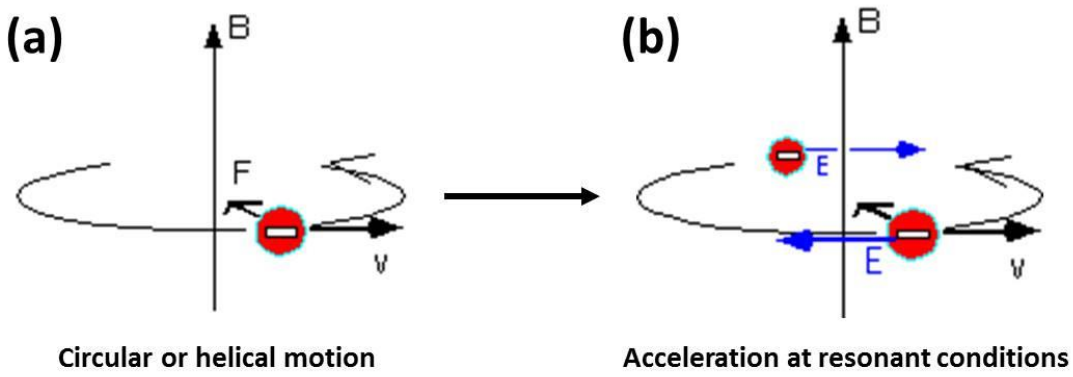

Figure 2.5 (a) The circular or helical motion of an electron in a static and uniform magnetic field. (b) Continuous acceleration of the electron in a superimposed magnetic field and electric field.

To understand the ECR effect, one can decompose a polarized microwave beam as a sum of a right-hand polarized component and a left-hand polarized component, referred as *R* wave and *L* wave respectively[11]. The geometry is shown in Figure 2.6-(a). The electric field for the *R* wave (E_R) rotates anti-clockwise in time as viewed from the magnetic field direction. Considering an electron experiencing a circular or helical motion around the magnetic field line, the vector of E_R is in the same direction of the gyrating electrons. To make it simplified, we can divide one microwave oscillating period into four stages, as shown in Figure 2.6-(b). If $\omega = \omega_c$, *R* wave can be in resonance with the electrons, and it loses its energy by continuously accelerating the electrons in all the stages. However, the situation for *L* wave is different, of which the oscillating vector is opposite as the gyrating electrons, and it does not have a resonance effect with electrons. As seen in Figure 2.6-(c), the electrons are accelerated in the first and third stages, but then are decelerated in the second and fourth stages. As a consequence, the overall kinetic energy gain is zero.

[11] F. F. Chen, *Introduction to Plasma Physics and Controlled Fusion*, 3rd ed. Springer (2016).

Therefore, the "pure" ECR plasma heating can only exist for the *R* wave. The electrons within the ECR coupling region are continuously accelerated. Those fast electrons then lose their energy via collisions with neutral particles, resulting in ionization and momentum transfer. Since ECR plasmas essentially operate at very low pressures (lower than 10 mTorr), the long mean free path make it possible for electrons to gain rapidly enough kinetic energy to achieve high ionization efficiency and high plasma density.

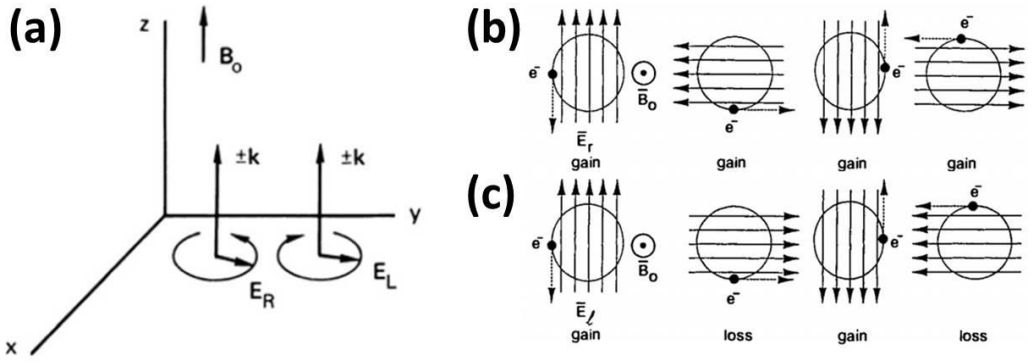

Figure 2.6 (a) Geometry of right-hand polarized (*R*) and left-hand polarized (*L*) waves propagating along the magnetic field. Extracted from Ref. 3. (b) Continuous electrons acceleration by *R* wave. Extracted from Ref. 11. (c) Alternating electrons acceleration and deceleration by *L* wave. Extracted from Ref. 11.

2.2.3.2. ECR-PECVD processing system

Influence of magnetic field on the value of breakdown electric field at microwave frequencies, that eventually led to the development of ECR plasma sources, was initially studied in the 1950s by Lax *et al*[12] as a method for bounded plasma diagnostics, and the idea of using this technique for plasma generation was implemented in the early 1960s for plasma fusion and plasma acceleration research [13,14,15,16]. The first attempts to apply ECR plasmas for surface processes were conducted in the middle of the 1970s and early 1980s. Results were published for silicon oxidation[17], plasma etching[18], ion implantation[19], and dielectric material deposition[20].

Since then, ECR plasma processing has become an active area, and has been applied to various PECVD processes, like the deposition of silicon (alloys), carbon coatings, metal oxides, as well as passivation coatings. Along with the development of these thin film deposition processes using the ECR-PECVD technique, the methods of plasma excitation and the engineering of processing systems have also experienced a remarkable development. Here, we will make a brief overview of several typical designs.

[12] B. Lax, et al., *J. Appl. Phys.*, **21(12)**: 1297 (1950).
[13] R. J. Kerr, et al., *Bull. Am. Phys. Soc.*, **7**: 290 (1962).
[14] D. B. Miller, et al., *Third Annual Symposium on the Engineering Aspects of MHD*, Univ. of Rochester (1962).
[15] R. Geller, *Appl. Phys. Lett.*, **16**: 401 (1970).
[16] J. Musil, et al., *Plasma Phys.*, **13**: 471 (1971).
[17] L. Bardos, et al., *J. Phys. D: Appl. Phys.*, **8**: L195 (1975).
[18] K. Suzuki, et al., *Jpn. J. Appl. Phys.*, **16**: 1979 (1977).
[19] N. Sakudo, et al., *Rev. Sci. Instrum.*, **48**: 762 (1977).
[20] S. Matsuo, et al., *Jpn. J. Appl. Phys.*, **22**: L210 (1983).

Divergent ECR type

The most commonly used ECR plasma reactor is the divergent (magnetic) field system – also often referred as the Hitachi/NTT-type[9]. This is a "pioneer" type of design for the ECR plasma source, and was first employed by Musil and Suzuki in their early plasma oxidation experiments. As shown in Figure 2.7, the system often consists of a microwave coupler, a source chamber, and a process chamber. The microwave power is transferred by a cylindrical or rectangular waveguide terminated by a dielectric (quartz, alumina, etc) window, and is then introduced into the source chamber via this window by a coupling structure to ignite the plasma. By adjusting the electromagnetic coils appropriately, strong ECR coupling region can be obtained in the source chamber. The plasma species created in the region then diffuse together with the remaining gas molecules towards the downstream, realizing various surface processes depending on the operation conditions.

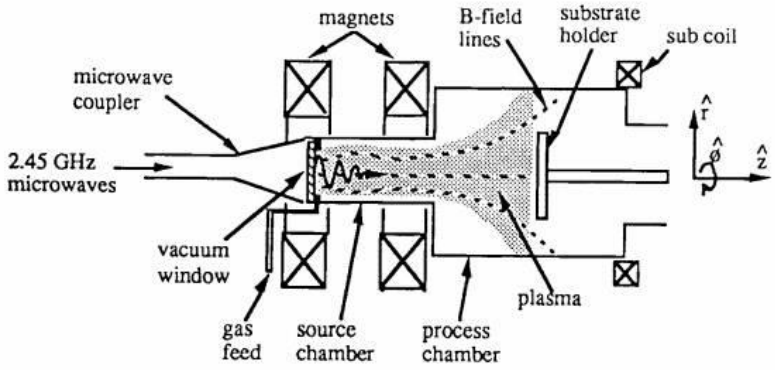

Figure 2.7 Schematic of a typical divergent ECR plasma processing system. Extracted from Ref. 9.

However, due to the limited number of the electromagnetic coils, the magnetic field is solenoidal along the axial direction. In some application processes, this diverging axial magnetic field would induce non-uniformity issues, since the microwave excitation non-uniformities are directly transferred along magnetic field lines into the process chamber and onto the substrate. Additionally, since the diverging magnetic field lines cut through the substrate with varying angles at the radial direction, the ions will arriving on the substrate surface with varying angles of incidence. This could become problematic in an etching application, where a high aspect ratio for the processed material is often required. Therefore, in some cases additional electromagnetic coils are placed downstream at the same level of the substrate to correct the diverging magnetic lines.

Multipolar ECR Cavity-Type

Figure 2.8-(a) shows the general schematic of a typical multipolar ECR cavity type of reactor, or also referred as the microwave plasma disk reactor. The system consists of a cylindrical cavity applicator, a disk-shaped quartz source chamber and a process chamber. During the operation, the discharge is formed inside the source chamber enclosed by the cylindrical cavity walls and the sliding short. The length of the sliding short is adjustable to allow the cavity applicator to resonate in different electromagnetic mode. One important feature of this cavity applicator is its ability to provide a high-strength tangential electric field to the quartz discharge chamber, without reflecting

power from the applicator[21]. Thus, even for high density discharges, microwave energy is coupled into the discharge with a rapidly decaying evanescent electric field.

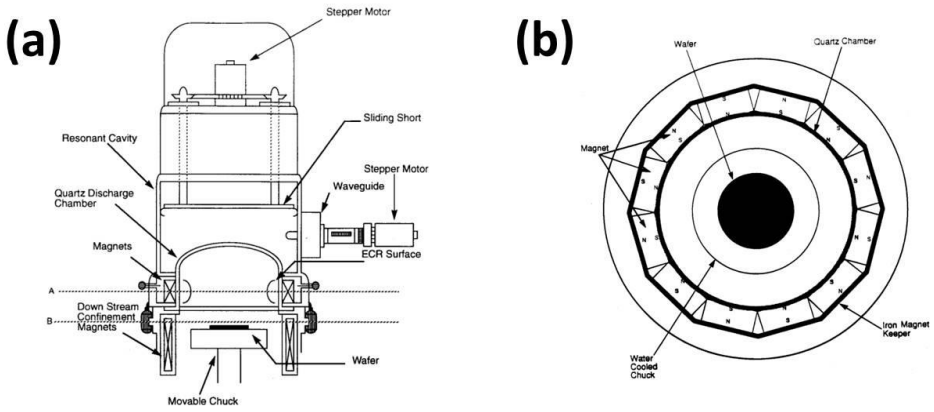

Figure 2.8 (a) Schematic of a typical multipolar ECR cavity-type plasma processing system. (b) Top view of the circularly arranged magnets adjacent to the quartz source chamber. Extracted from Ref. 22.

A set of permanent magnets with alternating polarities are equally spaced adjacent to the source chamber in a circular arrangement, as shown in Figure 2.8-(b). With this configuration, the magnetic field strength produced by these magnets is zero at the center and increases along the radial direction. Therefore, a three-dimensional ECR region is confined along the inner circumference of the chamber wall close to the magnets (indicated as "ECR surface" in Figure 2.8-(a)). Following the similar concept as in the divergent ECR reactors, another set of multipolar magnets are located downstream around the process chamber to reduce the species radial diffusion and improve plasma uniformity near the substrate. Since the ECR region exists only at the source chamber circumference and the process chamber is almost field free, another feature of this design is that any plasma non-uniformities present in the discharge region can be largely smoothed out when they arrive the processing surface.

Distributed ECR type

The development of the distributed ECR (DECR) type of reactor was based on the concept of magnetic multipolar plasma confinement[23,24] and the design of linear antennas running close to the magnet rows[25]. As shown in Figure 2.9-(a), a typical DECR reactor consists of a cylindrical vacuum chamber, a row of magnets and a row of antennas along the length of chamber wall. Microwave power supply is introduced to the discharge through the coaxial feedthroughs, and the substrate is placed at the bottom center of the chamber. Figure 2.9-(b) shows the schematic representative of an elementary excitation source for the DECR reactor. Multipolar permanent magnets are circularly arranged adjacent to chamber outer circumference, giving a closed magnetic field between every two contiguous units. By then applying microwave power through

[21] P. Mak, et al., *J. Vac. Sci. Technol. A: Vac. Surf. Films*, **10(4)**: 1281 (1992).
[22] J. Asmussen, et al., *IEEE Trans. Plasma Sci.*, **25(6)**: 1196 (1997).
[23] M. Sadowski, *Phys. Lett. A*, **25(9)**: 695 (1967).
[24] R. Limpaecher, et al., *Rev. Sci. Instrum.*, **44(6)**: 726 (1973).
[25] M. Pichot, et al., *Rev. Sci. Instrum.*, **59(7)**: 1072 (1988).

the linear antenna placed inside close to the chamber wall and along the magnetic rods, an ECR region (indicated as "lobes" in the figure) is then created along the full antenna length. Therefore, there is no clear-cut boundary between discharge region and processing region. The central part of chamber is almost magnetic field free, so that the processing region is free of high-energy electrons and the plasma therein is mainly obtained by diffusion.

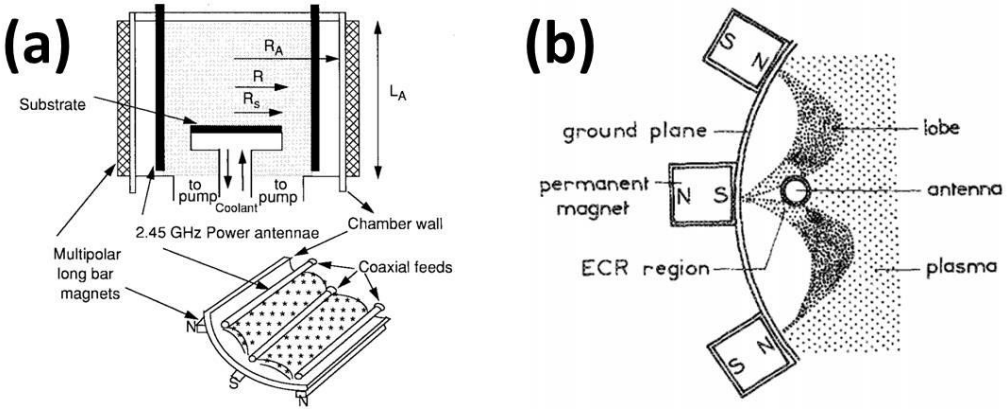

Figure 2.9 (a) Schematic of a typical DECR plasma processing system. Extracted from Ref. 22. (b) Top view of an elementary excitation source showing different plasma regions. Extracted from Ref. 25.

The cylindrical design of the DECR fits well with application processes with similar dimensions as the plasma sources. However, due to the presence of a magnetic field gradient, it will become inadequate when the processes need to be performed in larger areas. Furthermore, the presence of a high density plasma can lead to the damping of microwaves propagating through the antennas, thus inducing plasma non-uniformity along the axial direction. To improve the situation, a planar configuration named uniform DECR (UDECR) was proposed by Pelletier *et al*[26,27]. Differing from the DECR, wherein the antennas are inserted adjacent to the magnets, the UDECR design places the antennas between contiguous magnets, as shown in Figure 2.10.

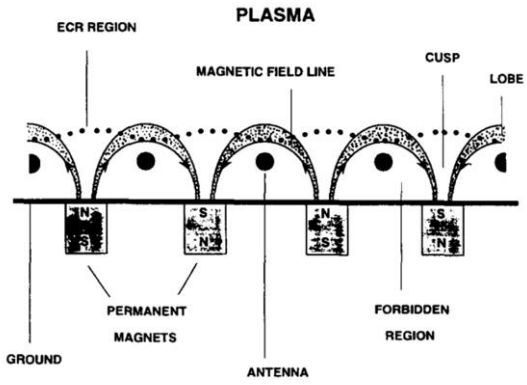

Figure 2.10 Top view of a UDECR excitation source. Extracted from Ref. 27.

Clearly, this design makes it possible to scale processes from a small to a large area without any

[26] J. Pelletier, US patent 5 216 329 A (1993).
[27] J. Pelletier, et al., *Thin Solid Films*, **241(1-2)**: 240 (1994).

alteration in the characteristics. In addition, the antennas (i.e., the microwave propagation paths) are well-separated from the power-absorbing ECR regions, so that the issue of microwave damping can be greatly released. Due to the same reason, such arrangement can also effectively reduce the metal contamination from the sputtering of the antenna material.

Integrated DECR type

As a next step of development of the initial concept of DECR plasma sources, the design of integrated DECR (IDECR) was proposed by integrating the microwave supply with the magnets, to make more effective power coupling[28,29]. The microwave power supply is introduced via microwave applicators positioned across the process chamber. Permanent magnets are fixed inside the microwave applicators and the whole structure is water cooled. A detailed illustration of the system is shown in Figure 2.11.

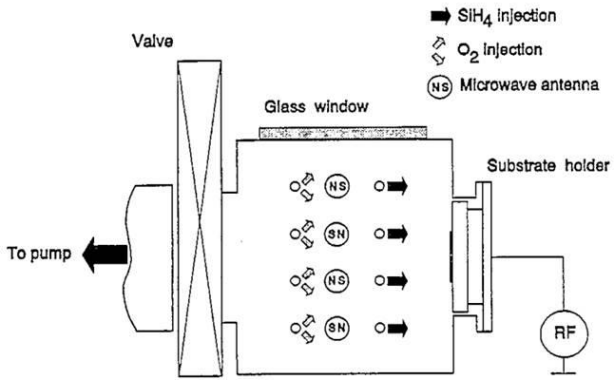

Figure 2.11 Cross-sectional view of a typical IDECR reactor. Extracted from Ref. 28.

It has separate gases injection, which present a symmetric configuration together with the excitation sources. For deposition processes using multiple precursors, this configuration allows for the option to generate background plasma species by injecting the gas close to the ECR regions where the most intensive power absorption occurs. Then, to make a better utilization of the feed gas, the growth precursors are subsequently injected close to the substrate. In some special cases, additional propagators can be inserted between the antennas and the precursor gases injection to enhance the discharge in front of the substrate. Since the extension of the length of each single microwave applicator and their arrangements is rather flexible, this design make the ECR plasma source easy to scale up and adjust for variant shapes of processing requirements.

Matrix-distributed ECR type

A more recent concept of the DECR plasma source - the matrix-distributed or multi-dipolar ECR (MDECR) - has been developed by Lacoste *et al*[30] in the early 2000s. In this design, elementary microwave applicators are arranged in an array to be the excitation source. As shown in Figure

[28] P. Bulkin, et al., *Thin Solid Films*, **296(1-2)**: 66 (1997).
[29] P. Bulkin, et al., *J. Non-Cryst. Solids*, **231(3)**: 268 (1998).
[30] A. Lacoste, et al., *Plasma Sources Sci. Technol.*, **11(4)**: 407 (2002).

2.12-(a)[31], each microwave applicator is composed of two main parts: a coaxial microwave feedthrough with an azimuthal symmetry around along its axial direction and a cylindrical permanent magnet at the rod end. The magnet is completely encapsulated in a metallic envelope, and water is circulating through the whole structure to keep the magnet cold. The microwave applicator terminated with magnet is inserted into vacuum chamber, with an adjustable insertion depth. Strong ECR coupling occurs in proximity to the 875 Gauss region close to the magnet of each individual unit or between two adjacent magnets with opposite polarities. An example of such design is shown in Figure 2.12-(b) (an earlier reactor in our group), where 25 microwave applicators are arranged in a 5×5 matrix[32]. The substrate is placed in the opposite end of the process chamber, and the surface processing is realized by the plasma species diffused from the source region.

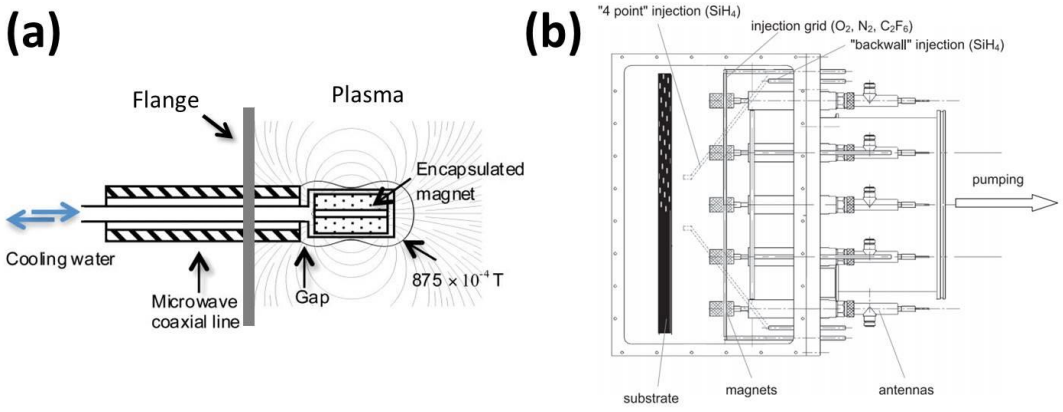

Figure 2.12 (a) Schematic of an elementary plasma excitation unit. Extracted from Ref. 31. (b) Cross-sectional view of a typical MDECR reactor. Extracted from Ref. 32.

The use of MDECR plasma sources has several advantages over the conventional DECR plasma sources: i) the simplicity of the elementary microwave applicator makes it easy for scaling-up simply by inserting as many such elementary units as necessary; ii) as the insertion depth of the elementary unit into the vacuum can be adjusted, different processing requirements in terms of the surface shape can be realized by engineering the antenna configuration; iii) as most of the length of applicator is coaxially shielded, there is little possibility for microwaves to be absorbed by the plasma before reaching the corresponding ECR regions. This leads to perfect fast electron confinement, so that considerably lower power is required to sustain stable plasma. In addition, this design reduces microwaves propagation towards the adjacent elementary unit, so microwave interferences between different sources are greatly reduced.

2.2.3.3. Description of MDECR-PECVD reactor

A large portion of the work in this thesis was carried out on one MDECR-PECVD reactor: ATOS. It is a monochamber reactor designed for the study of intrinsic µc-Si:H film deposition at high rate from the SiF_4-based plasma chemistry. The 2.45 GHz microwave power is introduced by an

[31] S. Béchu, et al., *Phys. Plasmas*, **20(10)**: 101601 (2013).
[32] D. Daineka, et al., *Eur. Phys. J. Appl. Phys.*, **26(01)**: 3 (2004).

excitation array consisting of seven microwave applicators, which are all terminated with permanent samarium cobalt magnets. In order to form a closed magnetic field configuration, these elementary units are equally spaced and arranged in a hexagonal shape with one in the center and the rest on the border having alternate polarities, as shown in Figure 2.13-(a).

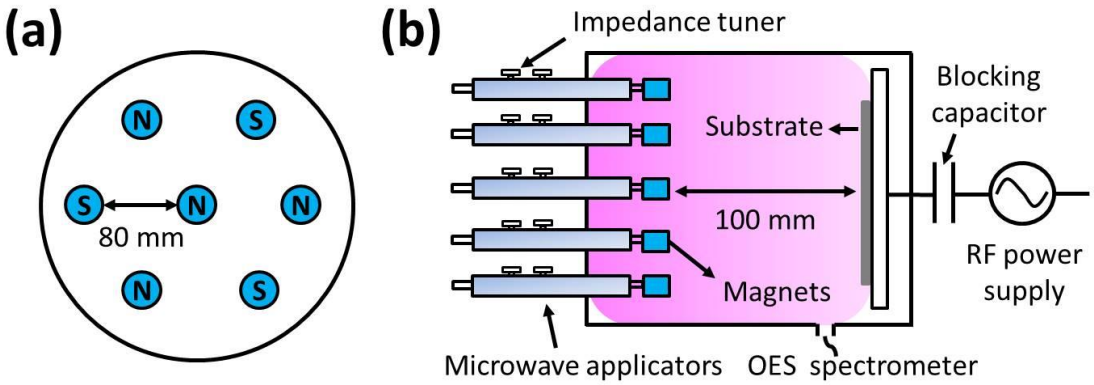

Figure 2.13 Schematics of ATOS MDECR-PECVD processing system: (a) top view of the microwave applicators array and (b) cross-sectional view of the deposition chamber (not to scale).

The cross-sectional schematic of the deposition system is shown in Figure 2.13-(b). It comprises a cylindrical plasma chamber with the excitation array mounted on one side and the substrate holder on the opposite side. By using a microwave power divider (patented by Pelletier *et al*[33]), the total excitation power is equally split into eight channels. Seven of these channels are connected to the corresponding seven microwave applicators for the power injection, and the last one is thermally dissipated by a 50 Ω water-cooled dummy resistor, with a maximum power dissipation of 250 W. For each of the elementary plasma source, the impedance matching is achieved by manually tuning a coaxial impedance adaptor. The substrate holder has a maximum 10×10 cm^2 active area, and is placed 10 cm away from the ECR coupling region. The system is equipped with a load-lock to prevent exposure of the main chamber to the air during sample loading. A base pressure below 5×10^{-7} mTorr is achieved before each deposition. There are also viewports on the sidewall of the chamber available for *in-situ* diagnostics, although only optical emission spectroscopy measurements have been performed in this work.

For an ECR plasma process typically operated under a very low pressure, the thermal transfer by convection in the gas phase is rather weak. As well, the substrate is usually not perfectly attached to the substrate holder (or electrode), therefore substrate heating via thermal conduction can also be poor. For these reasons, substrate heating for the ECR plasma process is more challenging than that for the high-pressure plasma processes. Moreover, in our experiments, the thermocouple used to measure the substrate temperature is embedded in the substrate holder. This configuration may lead to a large error in determining the real substrate temperature, since the poor thermal transfer would always produce a much lower temperature on the substrate surface than within the substrate holder, which is directly connected to the heating source. Therefore, to have a better determination of the substrate temperature, we have employed the method of Pyrometry[34].

[33] J. Pelletier, et al., US Patent, 6 727 656 (2004).
[34] *Theory and Practice of Radiation Thermometry*, D. P. DeWitt and G. D. Nutter (Eds.), Wiley (1988).

An “Infratherm IN 5/5 plus” pyrometer is installed on the plasma source flange and placed among the microwave applicator arrays, with a direction parallel to the substrate normal. The thermal irradiation at 5.14 µm is recorded *in-situ*. However, since the CaF_2 window through which the irradiation signal collected by the pyrometer is not 100 % transparent to the 5.14 µm irradiation and the thermal emissivity of the glass substrate is also not unity, a calibration of the Pyrometry measurements should be taken. As shown in Figure 2.14, a piece of glass was mounted on the substrate holder, with a PT 100 thermocouple glued on the surface by Kapton® tape to quantify the real surface temperature.

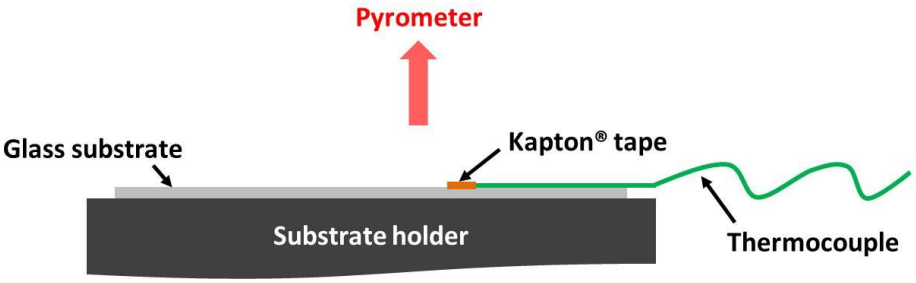

Figure 2.14 Cross-sectional view of the substrate holder during substrate temperature calibration.

Firstly, a temperature evolution test has been conducted. The temperature of heating source was preset to be 450 ºC, and the evolution of substrate surface temperature over 60 min was recorded. The experimental results are shown in Figure 2.15-(a). The two methods present similar evolution trends, and it takes about 40 min for the surface temperature to be stabilize. A large discrepancy around 250 ºC is observed between the preset temperature and the surface temperature. This can be explained by the above-mentioned poor thermal transfer in such a low-pressure condition. Apart from this point, one can note from the results that the real surface temperature given by the thermocouple is slightly (~3-4 %) higher than the one given by the pyrometer.

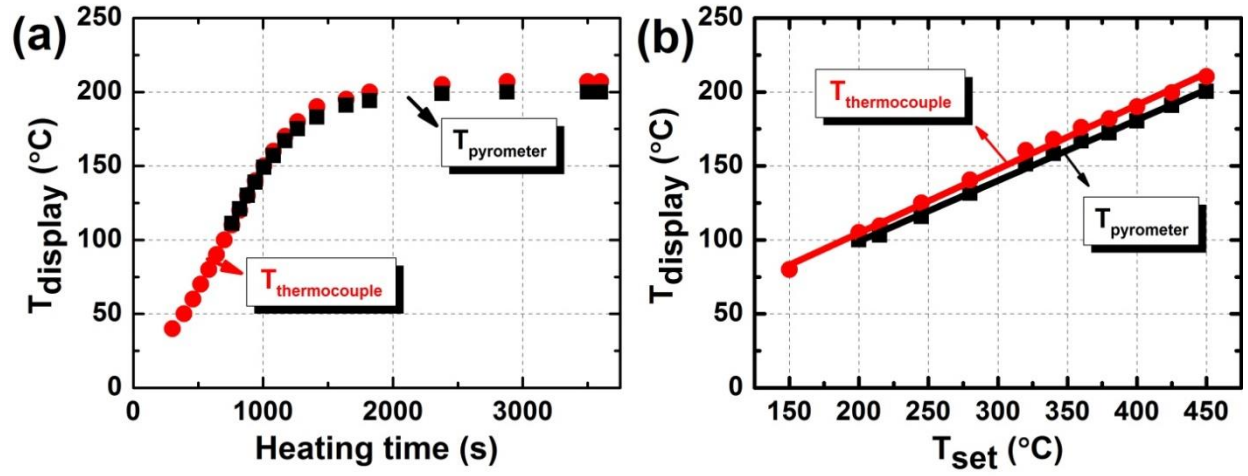

Figure 2.15 Substrate temperature calibration for ATOS by comparing measurement results from thermocouple (red) and pyrometer (black): (a) evolution of temperature over time with preset temperature at 450 ºC, (b) variation of temperature with increasing preset values.

In a second test, the temperature of the heating source was scanned from 150 to 450 ºC, and we

compared the measured values from pyrometer and thermocouple. Figure 2.15-(b) shows the results with increasing preset temperature. The small discrepancies between the results from pyrometer and thermocouple exist for the whole temperature range. Therefore, for all the subsequent MDECR-PECVD processes, the determination of substrate temperature has taken such discrepancies into account.

However, one should also keep in mind the universal issue in a practical PECVD process (even in the case of CCP processes) that, due to the presence of ion bombardment, the real surface temperature is always higher than any measured value. The impact of this effect on silicon thin film deposition has been discussed by van den Donker *et al*[35] and quantified in a related paper[36].

2.3. Other deposition methods

2.3.1. Magnetron sputtering

Sputtering is the process of moving particles from a solid target to another substrate. It involves the physical material ejection from the target surface (either an element or an alloy compound) by momentum transfer via the bombardment of energetic ions. During processing, ions arriving on the target surface with a kinetic energy greater than the surface binding energy can lead to the ejection of atoms from the target, leading to the deposition on substrate. Generally, magnetrons are employed to confine the plasma close to the target surface, so this technique is also often referred as magnetron sputtering. As an advantage, such kind of asymmetric plasma confinement can effectively avoid the resputtering of the deposited material.

In this work, the magnetron sputtering depositions were performed using an Alliance concept DP 650, which consists of one load lock with a transfer arm, and a vacuum chamber equipped with planar targets of different materials. Each target is protected by a blocking shutter and is kept closed before deposition (a detailed description can be found in Ref. 37). The system is used to deposit aluminum doped zinc oxide (ZnO:Al), indium tin oxide (ITO), and silver (Ag) as contacts or back reflectors for solar cells. A base pressure below 4.5×10^{-7} mTorr is achieved before each deposition, and the process conditions are shown in Table 2.1.

Table 2.1 Process conditions for the magnetron sputtering of ZnO:Al, ITO, and Ag.

Sample	Ar	Ar/O_2	P	P_{RF}	T_{sub}	V_{DC}	r_d
	sccm	sccm	mTorr	W	°C	V	nm/min
ZnO:Al	30	-	3.2×10^{-3}	250	RT[§] or 325	140	~36
ITO	43	3	4.6×10^{-3}	200	RT	200	~40
Ag	41	-	4.3×10^{-3}	50	RT	200	~33

[35] M. N. van den Donker, et al., *Thin Solid Films*, **511–512**: 562 (2006).
[36] Y. Yasuhiro, et al., *Energy*, **56(266)**: 46 (2006).
[37] C. Charpentier, *PhD thesis*, École Polytechnique (2012).
[§] RT: room temperature.

2.3.2. Thermal evaporation

Thermal evaporation is based on the boiling off (or sublimating) of a heated material onto a substrate in vacuum. In laboratory scale setups, the material is usually evaporated by passing a high current through a highly refractory metal containment structure, e.g., a tungsten crucible, or by high energy electron beam (e-beam) heating of the source material itself. In order to reduce the impact of radiant heating by the vaporization source, the substrate is usually placed at an appreciable distance away from the heated material.

In this work, the thermal evaporation depositions are performed using a laboratory-made evaporator, which consists of a vacuum chamber covered by a glass bell jar. The system is used to deposit aluminum (Al) as the coplanar contacts for the electrical characterizations in the material studies, and shadow masks are used to obtain desired contacts. A base pressure below 5×10^{-6} mTorr is achieved before each deposition, and a quartz crystal is position at the same height as the substrate holder to monitor the thickness of the evaporated films.

2.4. Characterization techniques

2.4.1. Plasma diagnostics

2.4.1.1. Optical emission spectroscopy

Optical emission spectroscopy (OES), as a simple and fundamental plasma diagnostic technique, has been widely used for qualitative and quantitative analysis in plasma science. Because of the contactless configuration, this method can be used for various plasma conditions. Within the plasma, the interactions between electrons and species are responsible for almost all the excitation processes (note that ion bombardment, chemical reactions, and metastable energy transfer also contribute). As a result, part of the plasma species can be electronically excited into optically emitting states, giving light emission at different characteristic wavelength depending on the composition. Therefore, spectroscopic measurements of the emission allow one to make a qualitative determination of species concentrations in the plasma.

However, the densities of plasma species in their optically emitting states are not necessarily linearly proportional to their total densities, and the probability of these excitation processes are also determined by the electron energy distribution function (EEDF). It is always not easy to make a quantification of the plasma species densities by monitoring the emission intensities, since any variation in process conditions can lead to the change in both species densities and EEDF. Therefore, an actinometric approach[38] (deliberately adding a small amount of a noble gas) should be employed to make appropriate correlation between the emission intensities and species densities. However, as we will use this only as a comparative tool, this is out of the scope of this work.

In our experiments, the OES measurements were performed using an Ocean Optics Maya 2000 Pro spectrometer. A spectral range of 200-1100 nm was monitored during processing via a viewport in the vacuum chamber. This technique was used to study the evolution of the emission intensity for species of interest when varying process conditions.

2.4.1.2. Residual gas analysis

The residual gas analyzer (RGA) is also a very powerful diagnostic tool for plasma processes, by which the gas species present in a vacuum system can be monitored. This can be an extremely valuable measurement as it allows one to easily make a fast determination about the features of the gas phase reactions as well as the stability of the gas environment during processing.

Figure 2.16 shows a basic layout of the RGA detection system, of which the general operating principle is based on the detection of positive ions with specific mass-to-charge ratios m/q. As depicted in Figure 2.16-(b), it consists of an ion source, a mass spectrometer, and a measurement section. On the left side, the residual gas from the plasma is connected to an ionizer, in which the neutral gas molecules are positively ionized via electron-impact collisions. These electrons are continuously discharged from a high-temperature filament and accelerated to a certain preset energy level. The so-generated ions then diffuse into the quadrupole mass spectrometer, which

[38] J. W. Coburn, et al., *J. Appl. Phys.*, **51(6)**: 3134 (1980).

acts as an ion filter. In the mass spectrometer, oscillating electric fields are generated by applying time-varying voltages to the four cylindrical electrodes, and this allows the ions to be separated by their m/q values. At a given oscillating frequency, ions with a specific m/q value can pass through the four electrodes and reach the detection system – usually a Faraday cup or a secondary electron multiplier – on the right side. The signal is collected as electric current, which is converted to a corresponding partial pressure. Assuming the amount of a certain detected ionized species is proportional to that of in its non-ionized state, the latter can then be determined from the signal intensity.

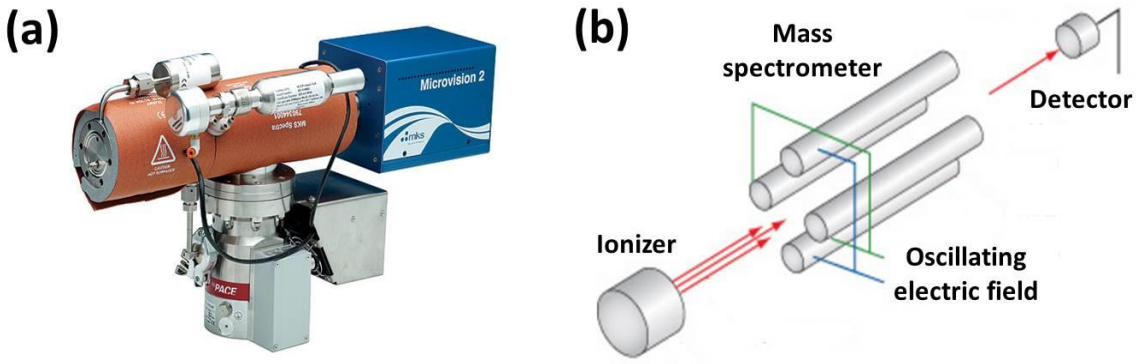

Figure 2.16 (a) Picture of RGA setup and (b) simplified schematic identifying the major components.

In practice, RGA measurements are often performed in two ways: 1) by presetting the m/q value individually and then making a sweep of the whole range of the molecules present in the process, the full range of chemical composition (concentration) in the plasma can be deduced; 2) by monitoring the evolution of several certain m/q values (certain species) in time, the impact of changes in process conditions on the plasma composition can be deduced. In our experiments, the second scheme has been preferentially used. The setup is a Microvision 2 from MKS Instruments, and is connected to the plasma chamber via a viewport. The measurement is always started before igniting the plasma, and the signal is recorded as P_X^{off} (X corresponds to the detected species). After the plasma ignition, the signal begins to decrease and becomes stable again at a lower level, which is recorded as P_X^{on}. Considering the relative change in signal intensity, the gas depletion can be estimated through

$$D_X = \frac{P_X^{off} - P_X^{on}}{P_X^{off}} \times 100\ \% \tag{2.9}$$

Accordingly, the absolute amount of consumed gas molecules per time unit can be calculated by

$$C_X = D_X \times F_X \tag{2.10}$$

It should be noticed that as the species can only reach the detection system by diffusion, some delay should be expected before the signal re-stabilizes. Moreover, due to differences in the sticking coefficients on the walls, such delay will differ from one species to the next. For example, a lesser delay can be observed for H_2^+ than that for SiF_4^+, since it has a higher diffusion coefficient and a lower sticking coefficient.

2.4.2. Material characterization

2.4.2.1. Spectroscopic ellipsometry

Spectroscopic ellipsometry is a fast, non-destructive optical measurement technique, and is widely used for the study of thin films, including the determination of material composition, optical constants, surface roughness, as well as the monitoring of *in-situ* growth, etc. This technique is based on detecting the change of polarization of a light beam after interacting with the sample. Generally, the measurement is carried out in the ultraviolet/visible region, but measurement in the infrared region can also be performed.

The spectroscopic ellipsometer used in this work is an *ex-situ* phase modulated UVISEL from Horiba Jobin-Yvon, and the measurements are performed in the spectral range from 1.5 eV (826.6 nm) to 4.5 eV (275.5 nm) with an energy step of 0.02 eV. The picture of the setup and its simplified schematic are shown in Figure 2.17.

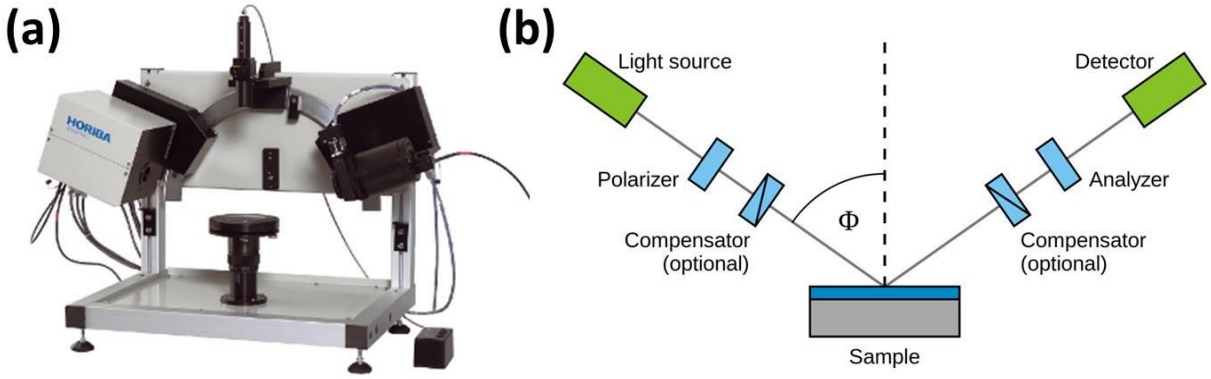

Figure 2.17 (a) Picture of *ex-situ* UVISEL phase shift modulated ellipsometer and (b) schematic view.

The main parts consist of a light source, a polarizer, a photoelastic modulator, an analyzer, a monochromator, and a detection system. By passing through the polarizer, the light beam is linearly polarized, with two components that are parallel (*p*-polarized) and perpendicular (*s*-polarized) to the incidence plane. After interacting with the sample, the complex reflection coefficients for the *p*- and *s*-polarized components at the air/surface interface can be expressed as

$$r_p = |r_p| e^{i\delta_p} \tag{2.11}$$

$$r_s = |r_s| e^{i\delta_s} \tag{2.12}$$

where the $|r_p|$, δ_p and $|r_s|$, δ_s represent the amplitude attenuation and the absolute phase change upon reflection for the two components, respectively. The change of the polarization state can then be characterized by the ratio ρ defined as

$$\rho = \frac{r_p}{r_s} = \frac{|r_p|}{|r_s|} e^{i(\delta_p - \delta_s)} = tan\,\Psi\, e^{i\Delta}, \text{ with } tan\,\Psi = \frac{|r_p|}{|r_s|} \text{ and } \Delta = \delta_p - \delta_s \tag{2.13}$$

where $tan\,\Psi$ stands for the ratio of amplitude attenuation and Δ the phase change difference. We

can then obtain the pseudo-dielectric function $\langle\varepsilon\rangle$ of the sample by

$$\langle\varepsilon\rangle = sin^2\,\theta\left[1+\frac{(1-\rho)^2}{(1+\rho)^2}tan^2\,\theta\right] \tag{2.14}$$

where θ is the incidence angle. In fact, the pseudo-dielectric function is a complex quantity that can be divided into the real $\langle\varepsilon_r\rangle$ and imaginary $\langle\varepsilon_i\rangle$ parts: $\langle\varepsilon\rangle = \langle\varepsilon_r\rangle + i\langle\varepsilon_i\rangle$. The two parameters herein, i.e., $\langle\varepsilon_r\rangle$ and $\langle\varepsilon_i\rangle$ are usually used to interpret the characteristics of the thin film materials.

The experimental results obtained by ellipsometry are a sum of contributions from different parts of the sample. Taking the low photon energy part, for example, the spectra usually shows some interference fringes because the light penetration length is greater than the sample thickness, leading to the interaction between the light reflected at the air/sample interface and that from the sample/substrate interface. Generally, these interference fringes depend on the substrate material, and their amplitude is linked to the contrast in the refraction index between the sample and substrate. For silicon thin films, stronger interference fringes can be observed for samples deposited on glass than for those deposited on a silicon wafer, as seen in Figure 2.18-(a). From these interference fringes, information about the sample/substrate interface and the sample thickness can be qualitatively determined. However, with increasing photon energy, the film gradually becomes "opaque" and the incoming light will just interact with the sample without the interference from substrate reflection.

To interpret the ellipsometric spectra, one can model the measured sample by regarding it as a multilayer stack, with each layer's thickness, volume fraction and dielectric function as the input parameters. By fitting the dielectric function of the modeled complex material stack to the experimental spectra, one can determine more useful information concerning the measured sample. Practically, this process can be done by using the Bruggeman effective medium approximation (BEMA) method, which calculates the dielectric function ε_b for a layer from the combination of the dielectric functions of different materials that constitute the layer, by solving

$$0 = \sum_i f_i \frac{\varepsilon_i-\varepsilon_b}{\varepsilon_i+2\varepsilon_b} \tag{2.15}$$

where ε_i is the dielectric function of the i^{th} material with a volume fraction of f_i. Usually, the input dielectric function of the materials used in the model can be described by dispersion laws or simply by taking the dielectric function of well-known reference materials[39].

For example, the fitting for an a-Si:H film is usually done using a two-layer model including a bulk layer (100 % of a-Si:H) and the surface roughness (usually consists of 50 % of a-Si:H and 50 % of void). The amorphous material is described by a single Tauc-Lorentz dispersion formula. Figure 2.18-(b) shows a typical a-Si:H ellipsometry spectra compared with the fitted spectra. In addition to the layers' thicknesses, an estimation of the optical band gap (E_g) of the sample can also be obtained. This fitting process was performed with the software platform DeltaPsi 2.

[39] D. A. G. Bruggeman, *Annalen der Physik* **416**, 636 (1935).

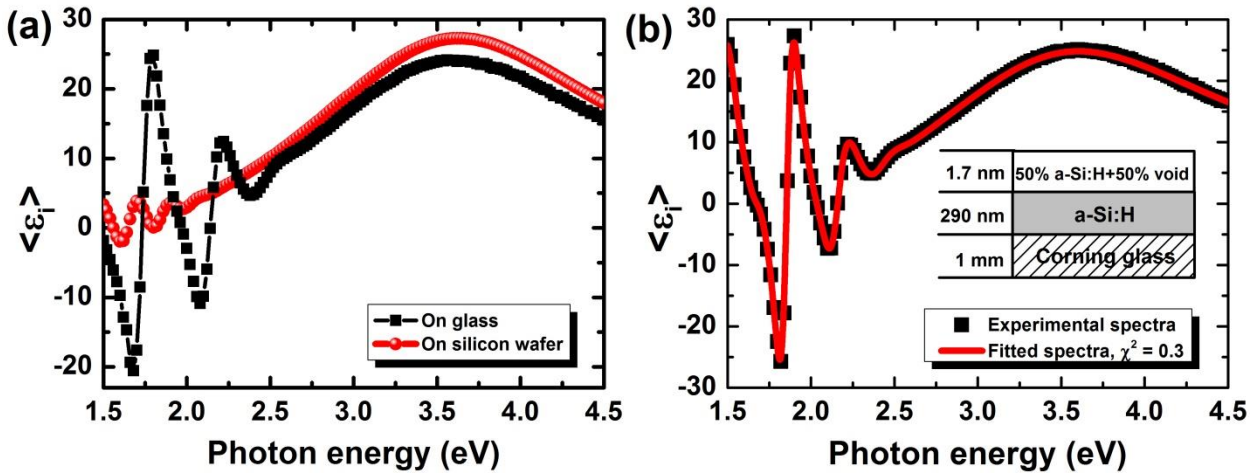

Figure 2.18 (a) Imaginary part of the pseudo-dielectric function $\langle \varepsilon_i \rangle$ for the a-Si:H films deposited on silicon wafer and Corning glass. (b) Example of fitting of typical a-Si:H film using DeltaPsi 2.

In contrast to a-Si:H material, a two-layer model might be insufficient for the case of µc-Si:H because of the anisotropy of material composition along the growth direction (as introduced in Section 1.2.2). A set of layers with gradient in material composition could be the more appropriate choice, and even in some more cases, a subsurface layer should be added to describe the local crystallization process within the region just below the growing surface[40]. However, for the sake of simplicity, we use a model with a single homogeneous bulk layer but with one more layer added at the sample/substrate interface to describe the transition (incubation) region. In doing so, as shown in Figure 2.19, a four-layer model (interface layer, bulk layer, subsurface and surface roughness) is employed to fit the spectra of µc-Si:H sample, and dielectric functions of reference materials, e.g., amorphous silicon[41], polycrystalline silicon (small and large grain) can be found in the publication of Jellison[42].

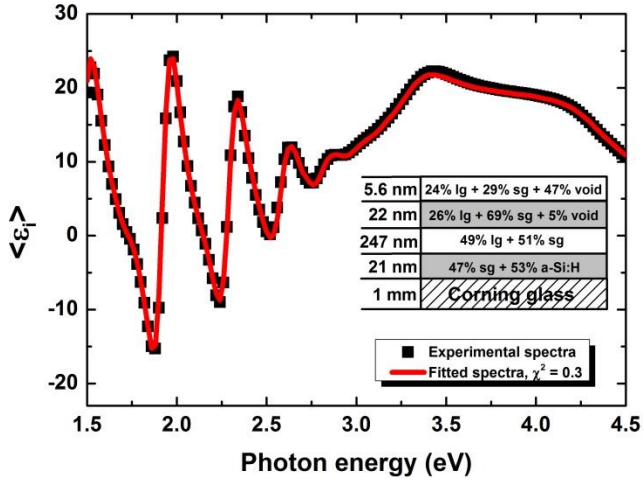

Figure 2.19 Example of fitting of typical µc-Si:H film using DeltaPsi 2.

[40] P. Roca i Cabarrocas, et al., *Solid State Phenom.*, **93**: 257 (2003).
[41] D. E. Aspnes, et al., *Phys. Rev. B*, **27(2)**: 985 (1983).
[42] G. E. Jellison, *Opt. Mater.*, **1(1)**: 41 (1992).

2.4.2.2. Raman spectroscopy

Raman spectroscopy is also a non-destructive optical characterization technique based on the observation of the inelastic scattering of photons by elementary vibrational excitations in the material. It can provide detailed information about chemical structure, polymorphology, crystallinity, etc. in a material.

As depicted in Figure 2.20, this technique relies on the inelastic scattering of a high intensity monochromatic light, usually in the range of near infrared, visible, or near ultraviolet, with the sample. When a thin film sample is illuminated with incident laser, most of the photons will be elastically scattered without any energy exchange. This is called Rayleigh scattering and does not provide useful information. However, depending on the structure of the sample, a small amount of light can be scattered with a shift in frequency after their interaction with the vibrating atoms of the film through the absorption or creation of phonons. This is called Raman scattering, and if the final vibrational state of the sample is more energetic than the initial state, then the emitted photon will be shifted to a lower frequency in order to keep the total energy of the system balanced. This shift in energy (wavelength) is designated as a Stokes shift. If the final vibrational state is less energetic than the initial state, then the emitted photon will be shifted to a higher frequency, and this is designated as Anti-Stokes shift. Using Raman spectroscopy, we obtain a spectra of the allowed Raman-active phonons in the sample.

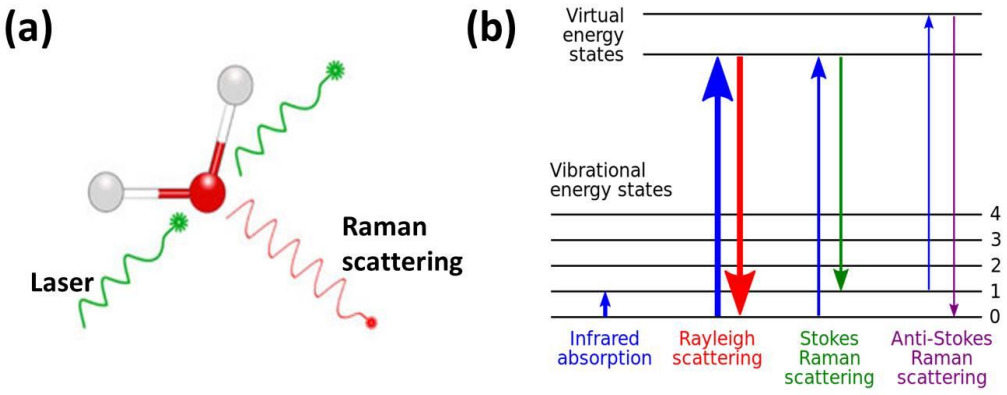

Figure 2.20 (a) Raman scattering from a molecule, from *www.horiba.com*. (b) Energy level diagram of states involved in Raman signal, from *wikipedia.org*.

The Raman spectrometer used in this work is a LabRAM ARAMIS from Horiba Jobin-Yvon. The measurements are performed with laser sources emitting at 486 nm, 633 nm and 785 nm, each with different light penetration depth, and chosen depending on the sample thickness. The Raman signal (i.e., the phonon spectra) is determined by the chemical and structural composition of the measured sample, and it is sensitive to a number of factors such as the material phase, defect states, impurities, and internal stresses. Therefore, Raman spectroscopy allows one to make a fast assessment of the sample.

Figure 2.21-(a) shows a comparison of the Raman spectra for silicon materials consisting of a pure crystalline phase, a mixed-phase, and an amorphous phase. c-Si has highly uniform bond angles and bond lengths, and the phonon spectra possesses a limited number of Raman active

modes. This leads to the sharp Raman peak with a characteristic Transverse Optical (TO) band centered at ~521 cm^{-1}. The a-Si material is less orderly in its arrangement with a wider distribution of bond angles, bond energies and bond lengths in addition to dangling bonds. This leads to all four modes being Raman active, and thus in a broad TO band centered at ~480 cm^{-1} that is readily distinguishable from that of c-Si. Accordingly, for the mixed-phase µc-Si material, the Raman spectra typically consist of a sharp crystalline phase peak with the broad shoulder-like peak reflecting the amorphous content.

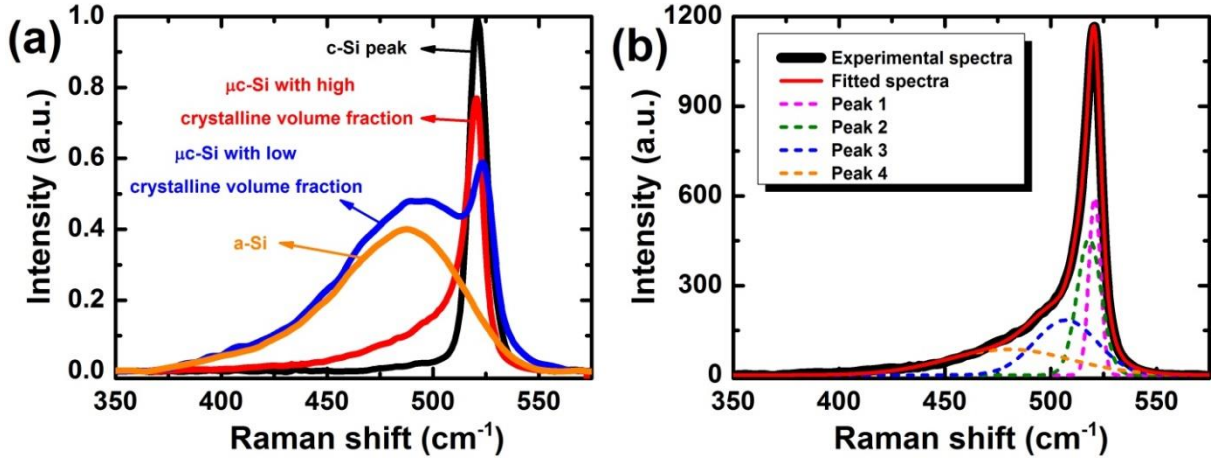

Figure 2.21 (a) Comparison of Raman spectra for silicon materials from pure crystalline to those containing different amounts of amorphous content. (b) Fitting of Raman spectra for typical µc-Si:H film.

By then deconvoluting the Raman spectra, one can quantify the relative amounts of amorphous and crystalline phase in the layer. As described in Ref. 43, the Raman spectra of µc-Si:H film can be deconvoluted into four Gaussian peaks located at ~520 cm^{-1}, ~507-517 cm^{-1}, ~490-505 cm^{-1}, and ~480 cm^{-1}, corresponding to the crystalline phase, smaller crystallites or a distribution of grain sizes, grain boundaries, and amorphous phase, respectively. By fitting these four peaks, it is possible to calculate the Raman crystalline volume fraction X_c^{Raman} through

$$X_c^{Raman} = \left(\frac{I_b+I_{sc}+I_c}{I_a+I_b+I_{sc}+I_c}\right) \times 100\ \% \tag{2.16}$$

where I_a, I_b, I_{sc} and I_c are the integrated peak intensities of the amorphous, grain boundaries, small crystallites and crystalline phase, respectively. In addition, further material properties like lattice disorder, averaged crystallite sizes, and stress in the layer can also be extracted from the Raman spectra. These will be discussed individually for specific samples in the following studies.

2.4.2.3. Fourier transform infrared spectroscopy

Fourier Transform Infrared (FTIR) Spectroscopy is a method of obtaining the absorption spectra in the infrared region for a sample. When passing through a sample, infrared irradiation is absorbed due to the vibration of certain functional groups in molecules, as well as by free carrier absorption. As a result, for a non-conducting sample, the recorded absorption signal is a spectra denoting the

[43] J.-C. Dornstetter, et al., *IEEE J. Photovolt.*, **3(1)**: 581 (2013).

molecular information in the material.

The FTIR spectrometer used in this work is a Nicolet 6700 from Thermo Fisher Scientific, and measurements are performed in the transmission mode for a spectral range of 650-4000 cm^{-1}. Since it is operated in the infrared range, the substrate has to be infrared transparent. To meet the requirement of measurement, the samples are co-deposited on the highly resistive (10000-20000 Ω cm), double side polished float-zone c-Si wafer (with low oxygen content). Before the measurements, the chamber is purged with nitrogen to minimize the artefacts from H_2O and CO_2 absorption. The usefulness of FTIR spectroscopy arises from the fact that different chemical structures can give different spectral response. Since hydrogen plays a crucial role in determining the quality of silicon thin film material, the quantification of silicon-hydrogen bonding configurations by FTIR measurements can be of great interest. In particular, the absorption due to the stretching modes of hydrides (SiH_x) at ~1850-2200 cm^{-1} can provide fruitful information about a film's microstructural properties[44,45,46]. Detailed analysis for a-Si:H and μc-Si:H materials will be discussed in the following studies.

2.4.2.4. Hydrogen exodiffusion

Another characterization technique to assess the hydrogen bonding information is temperature-dependent exodiffusion[47,48,49]. During this measurement, the sample is gradually heated to high temperature, and during the process the effused gases are detected. For hydrogenated-silicon thin film material, this method provides a fast approach to estimate the hydrogen incorporation and its stability, since the gas effusion strongly depends on the local environment of the hydrogen in the sample, such as nano-sized voids, internal surfaces, and in the amorphous matrices. In our experiments, the measurements are carried out in a vacuum chamber (with a base pressure below 2×10^{-7} mbar) surrounded by a furnace. A heating range from room temperature up to 700 °C, with a fixed heating rate of 10 °C/min is used. The partial pressure of hydrogen molecules is detected by a quadrupole mass spectrometer.

2.4.2.5. Transmission electron microscopy

Transmission electron microscopy (TEM) is a very powerful tool for material science. Basically, the measurements are operated along the same basic principles as an optical microscope, but instead of light, an energetic electron beam with uniform density is used as the excitation source. The interactions between electrons and atoms can be used to observe microscopic information about the material such as phase composition, crystalline features, defects, etc. Since the wavelength of electrons is much smaller than that of light, the resolution attainable for TEM images is several orders of magnitude better than that of an optical light microscope. Therefore, high resolution analysis revealing the finest details of the internal structure (even at the atomic

[44] M. H. Brodsky, et al., *Phys. Rev. B*, **16(8)**: 3556 (1977).
[45] G. Lucovsky, *Solid State Commun.*, **29(8)**: 571 (1979).
[46] W. Beyer, in *Tetrahedrally-Bonded Amorphous Semiconductors*, D. Adler and H. Fritzsche (Eds.), Springer (1985)
[47] P. A. Redhead, *Vacuum*, **12(4)**: 203 (1962).
[48] L. A. Pétermann, *Prog. Surf. Sci.*, **3**: 1 (1972).
[49] W. Beyer, et al., in *Advanced Characterization Techniques for Thin Film Solar Cells*, D. Abou-Ras, T. Kirchartz, and U. Rau (Eds.), Wiley (2011).

level in some cases) is achievable. Due to such great advantages, TEM has been widely used to reveal the evidence of microstructural features in a large variety of materials, including the silicon thin films studied in our work. Taking µc-Si:H for instance, the direct observation of the conical shape of crystalline grains as well as the surrounding amorphous matrices in the material were first reported by using TEM analysis in the early 1990s[50]. Later on, a large number of follow-up studies were conducted to detail the microstructure of µc-Si:H and to witness the impact of process conditions on material properties.

Typically, a TEM characterization setup consists of an electron emission source for the generation of the electron beam, a vacuum system through which the electrons travel, a series of electromagnetic lens to condense the beam, an objective lens to form the diffraction in the back focal plane with an objective aperture, and an imaging system. As schematically depicted in Figure 2.22-(a), when illuminating a thin sample, the condensed electrons may simply pass through without being scattered or may be diffracted off the optic axis by interaction with atoms. By then choosing the position of the objective aperture on the back focal plane, one can get two different types of imaging modes: the bright field (BF) image and the dark field (DF) image, as seen in Figure 2.22-(b) and Figure 2.22-(c) respectively. In the former case, the objective aperture is placed on the optic-axis, which only allows the direct-beam electrons passing through. The contrast in a TEM-BF image comes from the material having differing thicknesses or densities. Thicker or denser regions with a higher atomic number can block more electrons and will appear to be darker in the image. In contrast, thinner or lower atomic number regions will appear to be brighter, since the electrons' travel is less hindered. In the case of the DF image, more scattered electrons are allowed to be collected. Due to the fact that these electrons have strongly interacted with the sample, more detailed information can be extracted from the resulting TEM-DF image like crystalline features, defects, stacking faults, etc.

In contrast to the "conventional" TEM, which uses a parallel incident electron beam, the scanning transmission electron microscopy (STEM) mode employs a fine and convergent electron beam, as shown in Figure 2.22-(d). With the addition of scanning coils that scan the electron beam over a defined surface area of the sample (keeping parallel to the optic axis), highly localized information from the sample can be obtained. In the STEM mode, the direct or scattered electron beams are collected in an equivalent way as in the TEM mode, but using an electron detector rather than an objective aperture. In analogy with TEM mode, a BF electron detector is positioned on-axis to get the STEM-BF image. This BF detector only collects the direct-beam electrons falling on each point of the sample scanned by the beam. Then, for the STEM-DF imaging, a disk-shape annular dark-field (ADF) detector centered on the optic axis is used. It has a hole in the middle where the BF detector is located, and so the image formed using the ADF detector comes only from the scattered electrons. This gives rise to a fundamental difference between the TEM-DF and STEM-DF modes, as the TEM-DF image is formed by allowing only a fraction of the scattered electrons to enter the objective aperture, whereas STEM-DF image is formed by collecting most of the scattered electrons on the ADF detector. Therefore, STEM-DF image usually has a greater contrast with less noise in comparison with TEM-DF image. Moreover, one can also use another type of detector named high-angle annular dark field (HAADF) positioned around the ADF detector, which picks up the signal coming from the electrons scattered out to even higher angles, and leading to the formation of the so-called STEM-HAADF (or Z-contrast)

[50] Y. L. Chen, et al., *J. Vac. Sci. Technol. A: Vac. Surf. Films*, **10(4)**: 874 (1992).

image. Since high-angle electron scattering is associated with the nucleus of atoms in the sample, STEM-HAADF imaging maximizes Rutherford scattering effects and suffers little or no diffraction effects, which is rather favorable in indicating atomic-number (material density) contrast and can bring a great improvement in signal to noise ratio. Together with the incoherent nature of the imaging, this mode enables a better characterization of the material microstructure, useful to verify the presence of nanosized voids or "nanoporous" regions.

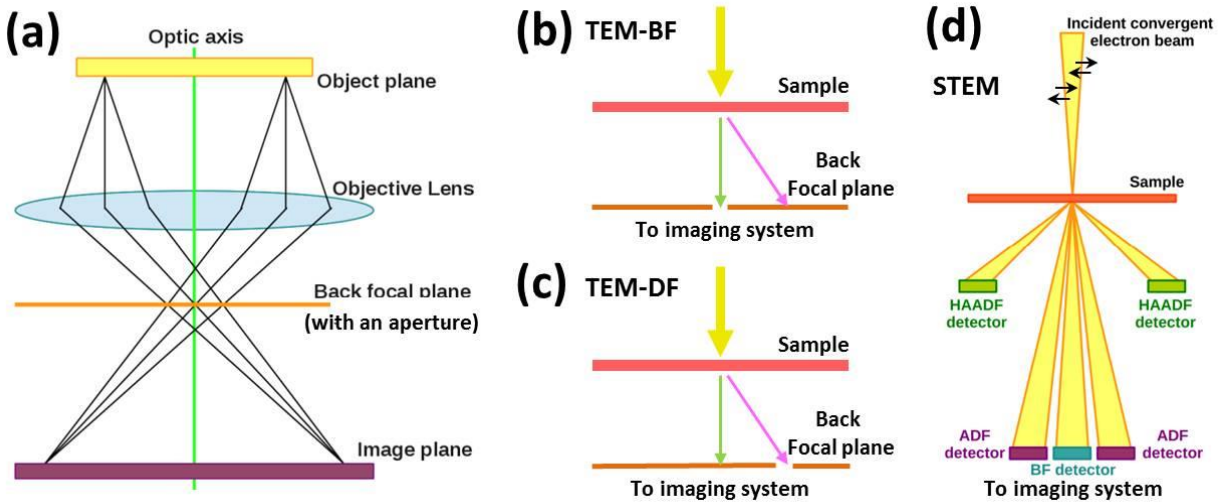

Figure 2.22 (a) Simplified representation of electron beam path in TEM characterization process. (b)/(c) Comparison of the use of objective aperture in TEM to select direct/scattered electron beams for the BF/DF imaging. (d) Simplified representation of the electron beam path as well as different types of electron detector in a STEM characterization process. Extracted from Ref. 51.

In this work, image acquisition has been performed using a Jeol 2010 FEG (field emission gun) electron microscope operating at 200 kV acceleration voltage. Prior to the TEM analysis, the focused ion beam (FIB) technique is used in order to obtain very thin cross-sectional lamellas for all the considered samples. Moreover, to bring into evidence the presence of "nanoporous" regions within the films, Fresnel contrast experiments have been carried out in the BF imaging mode with images acquired under slightly defocused conditions (both under- and over- focused).

2.4.2.6. Steady state photocarrier grating

The steady state photocarrier grating (SSPG) method was first proposed by Ritter, Zeldov, and Weiser (hereafter referred as RZW) to determine the minority carrier transport properties of a-Si:H material[52]. This method is based on the measurement of current flowing through a sample illuminated by an interference pattern created by the superimposition of two coherent laser beams, as illustrated in Figure 2.23-(a). The result of this light pattern is the presence of a spatially modulated photocarrier generation rate within the sample – this is the so-called photocarrier grating. The trapping of minority carriers will result in a periodic space charge distribution,

[51] S. Gaiaschi, *PhD thesis*, Université Paris Sud (2014).
[52] D. Ritter, et al., *Appl. Phys. Lett.*, **49(13)**: 791 (1986).

leading to the creation of an internal electrical field pattern. By then setting different grating periods and measuring the corresponding photocurrents, the ambipolar diffusion length, i.e., the hole diffusion length in the case of silicon thin films, can be determined by assuming ambipolar transport and charge neutrality.

The SSPG setup used in this work is a SSPG-230 from TFSC-Instrument, and the general schematic is shown in Figure 2.23-(b). A laser source is split into two components L_1 and L_2, which are then incident onto the same area of the sample surface. The laser source is deviated by two mirrors M_1 and M_2 before splitting, and two polarizers P_1 and P_2 are position in the light path: the former can be rotated to adjust the global light flux and the latter gives the light source a polarization perpendicular to the plane of the figure. As can be seen, L_1 is reflected directly on the sample by mirror M_3. The situation is different for L_2, which is first attenuated by a filter, giving a much lower intensity than L_1. It is then modulated by a chopper, and reflects off a movable mirror M_4. By changing the position of M_4, L_2 can be sent to a series of fixed mirrors ($M_{5\text{-}1}$ to $M_{5\text{-}10}$), and eventually reflected towards the sample surface with different angles θ with L_1.

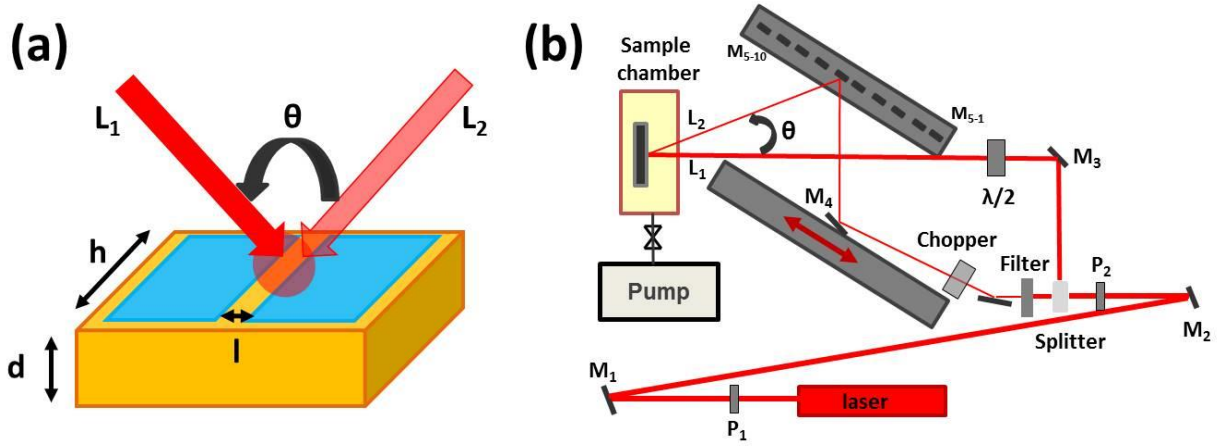

Figure 2.23 (a) Schematic of the sample with coplanar electrodes illuminated by two coherent laser beams L_1 and L_2, where *d*, *h*, and *l* are sample thickness, electrode width, and electrodes gap, respectively. (b) Schematic of the SSPG measurement system (not scale), from *www.tfscinstrument.com*.

If the two components have the same polarization, an interference pattern will be formed within the illuminated area with a grating period Λ given by

$$\Lambda = \frac{\lambda}{2\,sin(\theta/2)} \tag{2.17}$$

where λ is the wavelength of the laser beam, and θ is the angle between them. One can note from Equation (2.17) that, by changing θ, the grating period can be modified continuously. Assuming low absorption so that there is negligible decay of photon flux, the photocarrier generation rate $G(x, y, z)$ can be considered uniform along the vertical direction as[52]

$$G(x, y, z) \approx G(x) = G_1 + G_2 + 2\gamma_0 (G_1 G_2)^{1/2} cos(2\pi x/\Lambda) \tag{2.18}$$

where $G(x)$ is the photocarrier generation rate along the horizontal direction x, and G_1 and G_2 are

the corresponding generation rate from the two components. The additional parameter γ_0 has been introduced in Ref. 52 as a grating-quality factor to account for a non-ideal grating because of optical scattering, non-ideal coherence, or mechanical vibrations. The ideal value of γ_0 is unity.

As one can see in Figure 2.24, the photocarrier generation is sinusoidally-modulated, with the light and dark areas corresponding to regions with high and low carrier generation rates. Due to the density gradient, the carriers generated within the light regions will diffuse towards the dark regions and will also drift due to the presence of the internal electrical field. If a half-wave plate is inserted between M_3 and the sample (see Figure 2.23-(b)), leading to a 90º delay for B_1, the two components will not be coherent anymore, and the inference pattern disappears.

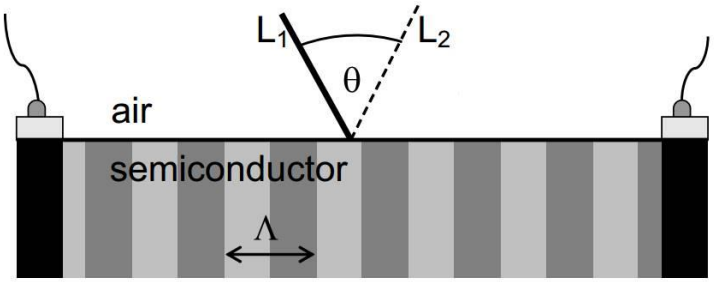

Figure 2.24 Schematic of interference pattern generated within sample between the coplanar electrodes. Extracted from Ref. 53.

During measurement, a DC voltage is applied to two coplanar electrodes made by evaporated aluminum, and the current is measured with and without interference (I_{coh} and I_{incoh}). For a grating period Λ smaller than the ambipolar diffusion length L_d, i.e., $\Lambda < L_d$, an effectively homogenous distribution of carriers between the two electrodes will be achieved due to carrier diffusion, and no difference will be observed between I_{coh} and I_{incoh}. However, if $\Lambda > L_d$, and carrier diffusion is insufficient to lead to a homogenous distribution, the collected current will therefore be different. According to the RZW analysis, the measured photocurrent can be related to the diffusion length by defining a parameter β as

$$\beta = \frac{I_{coh}}{I_{incoh}} = 1 - \frac{2\phi}{(1+(2\pi L_d/\Lambda)^2)^2} \tag{2.19}$$

where ϕ is related to the grating-quality factor γ_0. This ratio β can be obtained for different Λ values (different positions of M_4), therefore the experimental results can be plotted as a function of Λ, from which the ambipolar diffusion length can be deduced based on Equation (2.19).

The measurements are performed at room temperature, and an He-Ne laser with a total flux of 6.7×10^{16} cm^{-2} s^{-1} is used as the excitation source. The DC voltage applied to the electrodes is set to 9 V. The mirror M_4 can be moved between ten different positions, which corresponds to a variation of the grating period Λ in the range between 0.85 µm and 19.4 µm. Figure 2.25-(a) illustrates the $\beta(\Lambda)$ curve for a µc-Si:H film. By using ϕ and L_d as the fitting parameters, a non-linear fitting of the data is conducted (red curve), from which L_d is deduced to be of 184 nm.

[53] R. Brüggemann, in *Advanced Characterization Techniques for Thin Film Solar Cells*, D. Abou-Ras, T. Kirchartz, and U. Rau (Eds.), Wiley (2011).

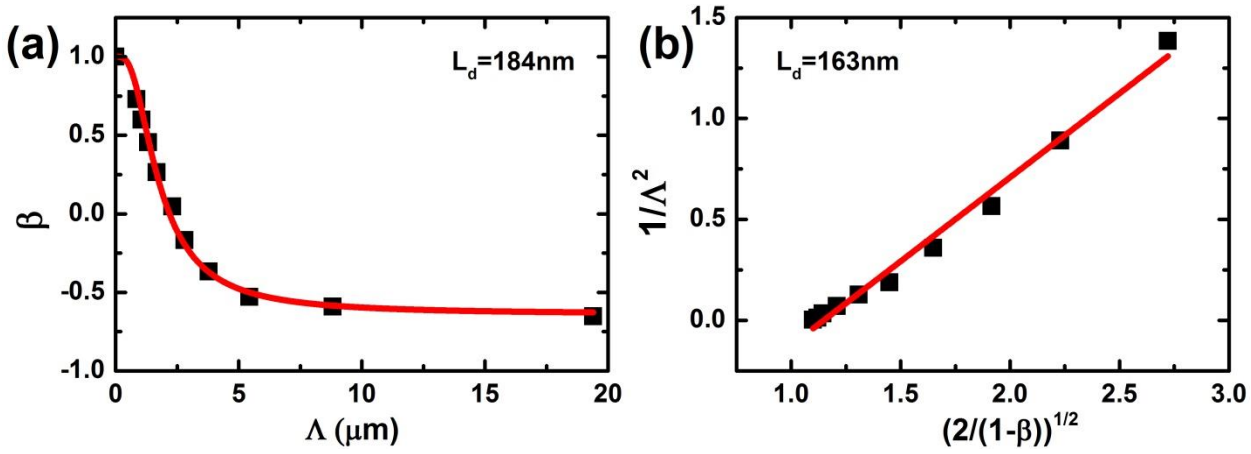

Figure 2.25 (a) $\beta(\Lambda)$ plot and (b) Balberg plot of SSPG experimental data for a µc-Si:H film.

Moreover, as suggested by Balberg *et al*[54], the results can also be plotted in a form as

$$\frac{1}{\Lambda^2} = \frac{\sqrt{\phi}}{2\pi L_d^2}\sqrt{\frac{2}{1-\beta}} - \frac{1}{(2\pi L_d)^2} \tag{2.20}$$

with $1/\Lambda^2$ and $(2/(1-\beta))^{1/2}$ as the ordinate axis and abscissa axis, respectively. This formula usually gives a straight line, and the fitting results give a L_d of 163 nm, which is in good agreement as the result from Equation (2.19) (see Figure 2.25-(b)). The main advantage of using a linear plot is that it can help to easily identify the disagreement of experimental results and theoretical expectation. However, a comparison of these two evaluation methods is discussed in Ref. 55, and it has been pointed out that the abscissa values $(2/(1-\beta))^{1/2}$ suffer from a very large error when β is close to one, since $(1-\beta)$ is the denominator of the linear plots.

Based on the RZW analysis, the ambipolar diffusion length can also be connected to the carrier mobilities and lifetimes through the following expression

$$L_d = \sqrt{2\frac{kT}{q}\frac{\mu\tau_{min}\mu\tau_{maj}}{\mu\tau_{min}+\mu\tau_{maj}}} \tag{2.21}$$

where $\mu\tau_{min}$ and $\mu\tau_{maj}$ are the mobility-lifetime products for the minority and majority carriers, respectively. Since in our case, $\mu\tau_{min} \ll \mu\tau_{maj}$, Equation (2.21) can be simplified as

$$L_d \approx \sqrt{2\frac{kT}{q}(\mu\tau)_{min}} \tag{2.22}$$

This allows one to make a quantification of $\mu\tau_{min}$, and as an example, the above µc-Si:H film with a L_d = 184 nm should have a $\mu\tau_{min}$ value of 6.8×10^{-9} cm^2 V^{-1}s^{-1}.

[54] I. Balberg, *Appl. Phys. Lett.*, **53(11)**: 992 (1988).
[55] R. Brüggemann, *Appl. Phys. Lett.*, **73(4)**: 499 (1998).

2.4.2.7. Dark conductivity and steady state photoconductivity

Dark conductivity and steady state photoconductivity measurements were also performed, with the goal of obtaining complementary information concerning the material transport properties. To do so, the same coplanar electrodes as depicted in Figure 2.23-(a) have been used.

Assuming a transport model consisting only of free carriers above the mobility edge, the thermally activated dark conductivity σ_d can be given by

$$\sigma_d = e\mu_n n_0 + e\mu_p p_0 \tag{2.23}$$

where μ_n and μ_p are the mobilities of majority and minority carriers, respectively, and μ_0 and p_0 are the densities of free majority and minority carriers in the dark, respectively. As previously stated, in the case of silicon thin film materials, electrons are the majority carriers, having much larger mobility than the minority carrier holes, i.e., $\mu_n \gg \mu_p$. The value of σ_d can therefore be approximately expressed as

$$\sigma_d = e\mu_n n_0 \tag{2.24}$$

Considering an electron density distribution given by

$$\mathrm{n(T)} = N_C exp\left(-\frac{E_C - E_F}{kT}\right), \text{ with } N_C = 2\frac{(2\pi m^* kT)^{3/2}}{h^3} \tag{2.25}$$

where T is the temperature, E_C is the conduction band edge, E_F is the Fermi level, k is the Boltzmann constant, N_C is the effective density of states in the conduction band, m^* is the effective mass of electron, and h is the Planck constant. Then σ_d can be rewritten as

$$\sigma_d(T) = \sigma_0 exp\left(-\frac{E_a}{kT}\right), \text{ with } \sigma_0 = e\mu_n N_C \tag{2.26}$$

Here σ_0 is a pre-exponential factor, and $E_a = E_C - E_F$ is the activation energy.

In our experiments, knowing the applied voltage V, the electrode width h, the electrodes gap l, and the sample thickness d, the dark conductivity at a certain temperature is determined through Equation (2.27) by measuring the dark current. Moreover, one can note from Equation (2.26) that, the activation energy can also be extracted by performing the temperature-dependent dark conductivity measurements via the Arrhenius method.

$$\sigma_d(T) = \frac{I_d(T)}{V}\frac{l}{hd} \tag{2.27}$$

When the sample is illuminated by a monochromatic constant photon flux with energy higher than the bandgap, the free carrier density can be greatly increased. The carrier generation rate at a depth z will be given by

$$\mathrm{G(z)} = F_{dc}(1-R)\eta'\alpha exp(-\alpha z) \tag{2.28}$$

where F_{dc} is the photon flux, R, η', and α are respectively the sample reflectance, quantum

efficiency, and absorption coefficient at the irradiation wavelength. As a consequence, the conductivity also becomes depth-dependent, and Equation (2.24) is then modified as

$$\sigma_{ph}(z) = e\mu_n \Delta n(z) \tag{2.29}$$

Using the carrier generation rate in Equation (2.28), the excess electrons can be given by

$$\Delta \mathrm{n(z)} = \mathrm{G(z)}\tau_\mathrm{n}(\mathrm{z}) - n_0 \tag{2.30}$$

where $\tau_\mathrm{n}(\mathrm{z})$ is the free electrons lifetime. Accordingly, the photocurrent can be calculated by

$$I_{ph}(T) - I_d(T) = \int_0^d d\sigma_{ph}(z)\xi h \tag{2.31}$$

where ξ is the applied electric field defined by $\xi = V/l$. Substituting $\Delta n(z)$ from Equation (2.30), the photocurrent can be rewritten as

$$I_{ph}(T) - I_d(T) = e\mu_n \tau_\mathrm{n} \xi h F_{dc}(1-R)\eta' exp(-\alpha z) \tag{2.32}$$

and thus the $\mu\tau_{maj}$, i.e., the mobility-lifetime product for electrons

$$\mu\tau_{maj} = \frac{I_{ph}(T) - I_d(T)}{\xi h F_{dc}(1-R)\eta' exp(-\alpha z)} \tag{2.33}$$

In our experiments, the current under illumination I_{ph} is measured, and by then using the dark current measured at the same temperature, the photoconductivity can be determined as

$$\sigma_{ph}(T) = \frac{I_{ph}(T) - I_d(T)}{V} \frac{l}{hd} \tag{2.34}$$

2.4.2.8. Modulated photocurrent

Modulated photocurrent (MPC) measurements allow one to study the density of states (DOS) within the band gap for a semiconductor material. The theory of this technique is based on the continuity equations of the free carriers and the Shockley-Read statistics, in which it is assumed that localized states can lead to a process of carrier trapping-and-release, resulting in the exchange of electrons and holes between the conduction and valence bands.

By illuminating a sample with modulated monochromatic irradiation, a photocurrent consisting of one DC component and one AC (modulated) component can be generated. Due to the interactions of the photo-generated carriers with the localized states, the phase of the AC photocurrent will be shifted from the original excitation, and this phase shift φ can be modified by changing the modulation frequency. By then analyzing the frequency-dependent phase shift, one can quantitatively derive information on the energetic distribution of the localized states in the band gap.

One of the advantageous aspects of this method is that it does not require any assumption about the distribution of the localized states before analyzing experimental data, and it was first proposed

by Oheda[56] to infer the DOS distribution for a CdS crystal. An alternative treatment of the experimental data was proposed by Brüuggemann *et al*[57] using both the phase shift and the modulus of the AC photocurrent, which can omit the recursive procedure required in the previous approach.

However, these treatments can only give the relative values of DOS, and knowledge of the capture cross-section is required to determine the absolute values of DOS. This situation was later improved by Kleider and Longeaud[58,59]. Practically, both types of carriers can contribute to the photocurrent, therefore the DOS obtained cannot distinguish between electron-traps and hole-traps. However, the MPC technique probes the states that lead to the lower signals. Therefore, assuming there is a predominant contribution of one type of carrier to the photocurrent, the absolute values of DOS can be determined through

$$\frac{N(E_\omega)\mu}{c} = \frac{2}{\pi kT}\left(\frac{Se\xi G_{AC}\sin\varphi}{|I_{AC}|} - \omega\right), \text{ with } \left|E_\mu - E_\omega\right| = kT\,ln(\upsilon/\omega) \tag{2.35}$$

where $N(E_\omega)$ is the DOS at energy level E_ω, υ is the attempt-to-escape frequency defined by $\upsilon = ckTN(E_\mu)$, E_μ is the mobility edge, $N(E_\mu)$ is the DOS at the mobility edge, μ is the free carrier mobility, c is the capture cross section, S is the conduction surface area,G_{AC} is the AC component of the photo-carriers generation rate, I_{AC} is the AC photocurrent, and ω is the angular frequency of the excitation that can negligible compared to the first term on the right side.

2.4.3. Solar cell device characterization

2.4.3.1. Current-voltage characteristic

In the dark, the current-voltage (*I-V*) characteristic of a solar cell can be described by the Shockley diode equation as follows

$$\mathrm{I(V)} = I_0\left[exp\left(\frac{qV}{nkT}\right) - 1\right] \tag{2.36}$$

where I_0 is the dark saturation current, and *n* is the ideality factor of the diode. Figure 2.26-(a) shows the typical dark *I-V* curve for a solar cell device. From this result, some important parameters can be extracted. In Equation (2.36), the first term in the brackets will dominate. Thus, a semi-log plot of the data following Equation *(2.37)* should show a linear proportionality in the positive-biased region.

$$\ln\big(\mathrm{I(V)}\big) = \frac{q}{nkT}V + \ln(\mathrm{I_0}) \tag{2.37}$$

From such plots, the ideality factor *n* and the value of I_0 can be determined. Here, I_0 is an extremely important parameter to evaluating the quality of a solar cell device. It is related to free

[56] H. Oheda, *J. Appl. Phys.*, **52(11)**: 6693 (1981).
[57] R. Brüuggemann, et al., *Philos. Mag. Part B*, **62(1)**: 29 (1990).
[58] J. P. Kleider, et al., *J. Non-Cryst. Solids*, **137**: 447 (1991).
[59] C. Longeaud, et al., *Phys. Rev. B*, **45(20)**: 11672 (1992).

carrier recombination, and usually a lower value of I_0 suggests a less significant recombination effect.

When the solar cell is exposed to light, the *I-V* characteristic will be superimposed on a photo-generated current I_{ph} flowing in the opposite direction as

$$\mathrm{I(V)} = I_{ph} - \mathrm{I_0}\left[exp\left(\frac{qV}{nkT}\right) - 1\right] \tag{2.38}$$

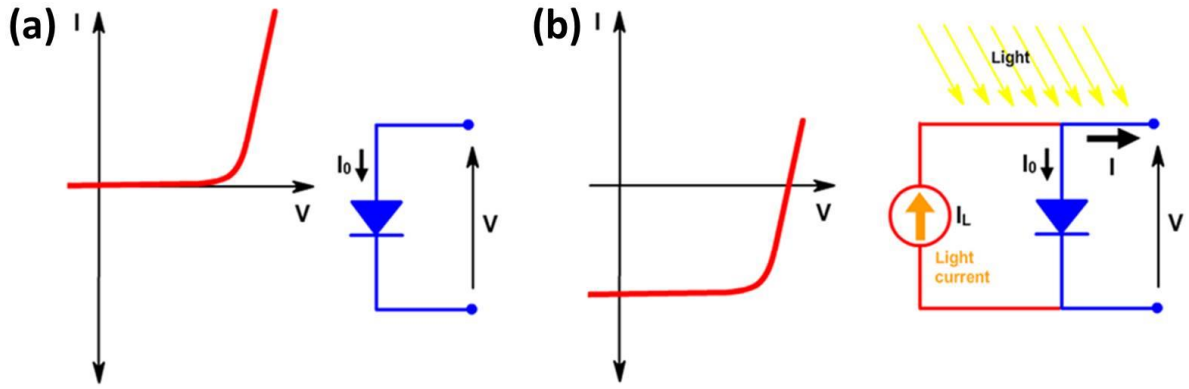

Figure 2.26 Current-voltage characteristic of solar cell (a) in the dark and (b) under illumination. The right side of each figure shows the corresponding simplified equivalent circuit, from *pveducation.org*.

Figure 2.27 shows a light *I-V* curve with the important performance parameters highlighted. The maximum current I_{SC} is obtained when the voltage is zero. The maximum voltage V_{OC} is obtained when no current flows through the device. However, at these two operating points, the converted power from the solar cell device is zero. The maximum converted power P_{max} is obtained when the product of current and voltage is maximum, i.e., at the maximum power point $MPP\ (V_{mp}, I_{mp})$. Practically, a parameter called fill factor FF that describes the solar cell device performance at MPP is commonly used. The FF is defined as

$$FF = \frac{V_{mp} \times I_{mp}}{V_{OC} \times I_{SC}} \tag{2.39}$$

Graphically, the FF is a measure of the "squareness" of the *I-V* curve and is also the area of the largest rectangle which fits in the *I-V* curve.

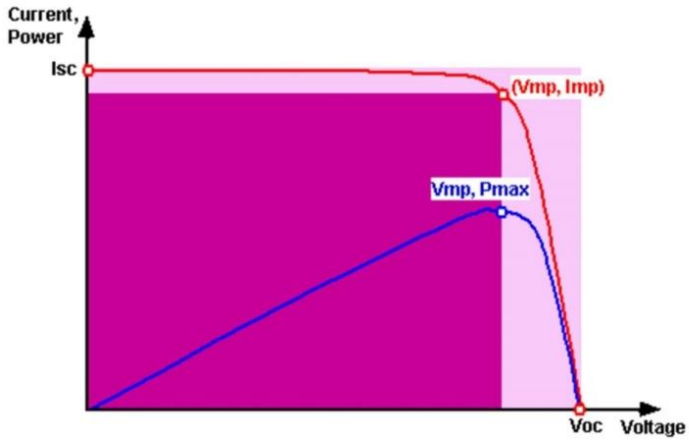

Figure 2.27 Current-voltage characteristic of a solar cell under illumination with short-circuit current, open-circuit voltage, and maximum power point highlighted, from *pveducation.org*.

However, during operation, parasitic resistances in the device should be taken into account, as shown by the equivalent circuit in Figure 2.28-(a), since they reduce the light conversion efficiency by dissipating power. Accordingly, a more general expression for the *I-V* characteristic is given by

$$\mathrm{I(V)} = I_{ph} - I_0 \left[exp\left(\frac{q(V - I(V)R_S)}{nkT}\right) - 1 \right] - \frac{V - I(V)R_S}{R_{SH}} \tag{2.40}$$

where R_S and R_{SH} are the series resistance and the shunt resistance respectively. R_S typically arises from the bulk resistance of device, contact resistance between the semiconductor and metal contacts, and the resistance of metal contacts or conductive oxide layers. Since it only impacts the device when a photocurrent flows through the junction, R_S does not affect the device performance at all at open-circuit voltage. However, near open-circuit, the *I-V* curve is strongly affected by R_S, as shown in Figure 2.28-(b).

R_{SH} is mainly related to the leakage current of the device (defects, junction edge, pinholes). Low R_{SH} causes power losses in the device by providing an alternate path for the photocurrent. Such a diversion of current reduces the amount of photocurrent flowing through the junction and reduces the power obtainable from the device. This effect is particularly severe at low illumination levels when a lesser photocurrent is generated, and therefore the current loss to the shunt has a larger impact.

Note that such model is indeed valid and can be theoretically justified for crystalline solar cells, consisting of *pn*-diodes[60]. However, one needs to take further considerations for the other types of designs. For instance, Merten *et al*[61] proposed an improved model for the case of a-Si:H solar cells in a *p-i-n* configuration, namely introducing an additional term relating with the current losses, as indicated by the dashed lines in Figure 2.28-(a). This term takes into account the recombination

[60] M. A. Green, *Solar cells : operating principles, technology and system*. University of New South Wales, Kensington (1992).
[61] J. Merten, et al., *IEEE Trans. Electron Devices*, **45(2)**, 423 (1998).

effect in the intrinsic layer of the device, which strongly depends on the working voltage[62].

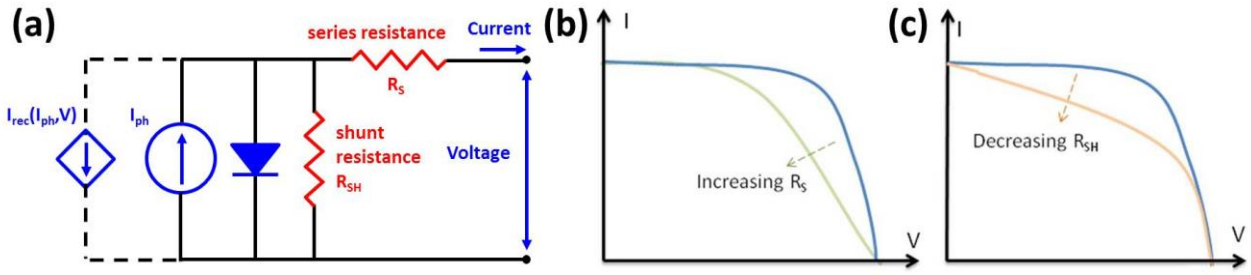

Figure 2.28 (a) Equivalent circuit for solar cell device under illumination taking into account parasitic resistances R_S and R_{SH}. The dashed lines represent current losses due to the recombination in *i*-layer (proposed by Merten *et al* for the case of a-Si:H solar cell in a *p-i-n* configuration). The effect of non-negligible (b) R_S and (c) R_{SH}.

To evaluate the device performance, the power conversion efficiency η is the most commonly used parameter, which can be determined from the device *I-V* characteristic and is given by:

$$\eta = \frac{P_{max}}{P_{in}} = \frac{V_{OC} \times I_{SC} \times FF}{P_{in}} \tag{2.41}$$

Since the η of a solar cell device depends on the operating spectra and temperature, in this work, the *I-V* characteristic measurements are all performed under the same conditions: with AM1.5 solar spectra and at a temperature of 25°C.

2.4.3.2. External quantum efficiency

Second only to the *I-V* characteristic, the quantum efficiency (QE) measurement is also a fundamental characterization tool for solar cells. The QE measurement allows one to quantify the light conversion efficiency as a function of wavelength, so it can be viewed as an indicator of how good the solar cell is at converting sun light to electrical energy. It is defined by the ratio of the number of charge carriers that are collected by the solar cell to the number of impinging photons at a given wavelength, and two types of QE are often considered:

- The external QE (EQE) including the effect of all optical losses such as the light transmitted through the cell and the light reflected back from the cell.
- The internal QE (IQE) that refers to the efficiency under exclusion of transmitted or reflected light.

In this work, only the EQE given by Equation (2.42) is measured,

$$EQE(\lambda) = \frac{I_{ph}(\lambda)}{q\Phi_{ph,\lambda}} \tag{2.42}$$

where $I_{ph}(\lambda)$ is the photocurrent generated at a wavelength λ, and $\Phi_{ph,\lambda}$ is the photon flow

[62] J. Hubin, et al., *Philos. Mag. Part B*, **72(6)**, 589 (1995).

incident on the solar cell at that wavelength. The measurements are performed in the spectral range of 350-1100 nm. Providing all the photons of a certain wavelength are absorbed and the resulting charge carriers are successfully collected, the EQE at that particular wavelength may have a value of 100%. Thus, the EQE spectra for an ideal solar cell device has a square shape as shown in Figure 2.29 by the dashed line. However, due to the presence of optical and electrical losses, such as parasitic absorption and recombination losses, respectively, the EQE will be below 100 % for almost all types of solar cells. Figure 2.29 shows typical EQE spectra for single junction a-Si:H (red) and µc-Si:H (black) solar cells.

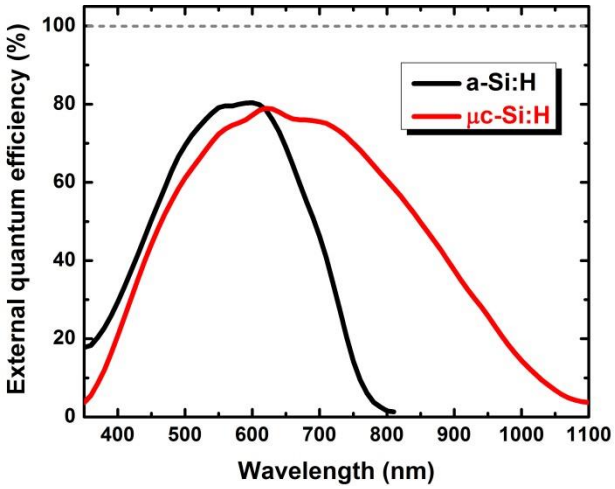

Figure 2.29 Typical EQE spectra for single-junction a-Si:H (black) and µc-Si:H (red) solar cells.

As one can see, for the a-Si:H cell, photons with energies larger than the band gap, i.e., with the wavelength lower than 750-800 nm, are typically absorbed, and photons with energy smaller than the band gap are not. For the µc-Si:H cell, which has an active layer with a lower band gap, the absorption range is extent to above 1100 nm. If the EQE measurement is performed under short circuit conditions, the short-circuit current density J_{SC} can be determined through

$$J_{SC} = q \int EQE(\lambda)\Phi_{ph,\lambda} d\lambda \tag{2.43}$$

In contrast to the *I-V* measurement, the determination of J_{SC} via the EQE measurement has the advantage that it is independent of the spectral shape of the light source. Moreover, on lab scale the real contact area of solar cell is not accurately determined during *I-V* measurements. However, the EQE measurement is independent of the contact area. Hence, for accurate measurement of J_{SC}, it is not sufficient to rely on *I-V* measurements only, but an EQE setup has to be used.

Reference

[1] P. Chabert and N. Braithwaite, *Physics of Radio-Frequency Plasmas*, Cambridge: Cambridge University Press, 2011.

[2] M. Labrune, "Silicon surface passivation and epitaxial growth on c-Si by low temperature plasma processes for high efficiency solar cells", *PhD thesis*, École Polytechnique, 2011.

[3] M. A. Lieberman and A. J. Lichtenberg, *Principles of Plasma Discharges and Materials Processing* (second edition), New Jersey: Wiley, 2005.

[4] C. B. Zarowin, "Relation between the RF discharge parameters and plasma etch rates, selectivity, and anisotropy", *J. Vac. Sci. Technol. A: Vac. Surf. Films*, vol. 2, no. 4, p. 1537, 1984.

[5] O. Leroy, P. Stratil, J. Perrin, J. Jolly, and P. Belenguer, "Spatiotemporal analysis of the double layer formation in hydrogen radio frequency discharges," *J. Phys. D: Appl. Phys.*, vol. 28, no. 3, p. 500, 1995.

[6] O. Christensen and M. Brunot, *LeVide Couches Minces*, vol. 165, p. 37, 1973.

[7] B. Chapman, *Glow Discharge Processes: Sputtering and Plasma Etching*. New York: Wiley, 1980.

[8] A. Dommann, N. Herres, M. Krink, J. J. Galiano, and B. Stämpfli, "Internal stresses and lifetime evaluation of PECVD isolating layers", *Microsyst. Technol.*, vol. 7, no. 4, p. 161, 2001.

[9] O. A. Popov, *High Density Plasma Sources Design, Physics and Performance*, Park Ridge: William Andrew, 1995.

[10] R. W. Boswell, "Plasma production using a standing helicon wave", *Phys. Lett. A*, vol. 33, no. 7, p. 457, 1970.

[11] F. F. Chen, *Introduction to Plasma Physics and Controlled Fusion* (third edition), Springer, 2016.

[12] B. Lax, W. P. Allis, and S. C. Brown, "The Effect of Magnetic Field on the Breakdown of Gases at Microwave Frequencies", *J. Appl. Phys.* vol. 21, no. 12, p. 1297, 1950.

[13] R. J. Kerr, R. A. Dandl, H. O. Eason, A. C. England, M. C. Becker, and W. B. Ord, *Bull. Am. Phys. Soc.* vol. 7, p. 290, 1962.

[14] D. B. Miller, P. Gloersen, E. F. Gibbons, and D. J. BenDaniel, *3rd Symposium on Engineering Aspects of Magnetohydrodynamics (MHD)*, Rochester, New York, 1962.

[15] R. Geller, "NEW HIGH INTENSITY ION SOURCE WITH VERY LOW EXTRACTION VOLTAGE", *Appl. Phys. Lett.* vol. 16, p. 401, 1970.

[16] J. Musil and F. Zacek, "Penetration of a strong electromagnetic wave in an inhomogeneous plasma generated by ECR using a magnetic beach", *Plasma Phys.*, 13, p. 471, 1971.

[17] L. Bardos, G. Loncar, I. Stoll, J. Musil, and F. Zacek, "A method of formation of thin oxide films on silicon in a microwave magnetoactive oxygen plasma", *J. Phys. D: Appl. Phys.*, vol. 8, no. 16, p. L195, 1975.

[18] K. Suzuki, S. Okudaira, N. Sakudo, and I. Kanomata, “Microwave Plasma Etching”, *Jpn. J. Appl. Phys.*, vol. 16, no. 11, p. 1979, 1977.

[19] N. Sakudo, K. Tokiguchi, H. Koike, and I. Kanomata, “Microwave ion source”, *Rev. Sci. Instrum.*, vol. 48, no. 7, p. 762, 1977.

[20] S. Matsuo and M. Kiuchi, “Low Temperature Chemical Vapor Deposition Method Utilizing an Electron Cyclotron Resonance Plasma”, *Jpn. J. Appl. Phys.*, vol. 22, no. 4A, p. L210, 1983.

[21] P. Mak, G. King, T. A. Grotjohn, and J. Asmussen, “Investigation of the influence of electromagnetic excitation on electron cyclotron resonance discharge properties”, *J. Vac. Sci. Technol. A: Vac. Surf. Films*, vol. 10, no. 4, p. 1281, 1992.

[22] J. Asmussen, T. A. Grotjohn, P. Mak, and M. A. Perrin, “The design and application of electron cyclotron resonance discharges”, *IEEE Trans. Plasma Sci.*, vol. 25, no. 6, p. 1196, 1997.

[23] M. Sadowski, “Plasma confinement with spherical multipole magnetic field”, *Phys. Lett. A*, vol. 25, no. 9, p. 695, 1967.

[24] R. Limpaecher and K. R. MacKenzie, “Magnetic Multipole Containment of Large Uniform Collisionless Quiescent Plasmas”, *Rev. Sci. Instrum.*, vol. 44, no. 6, p. 726, 1973.

[25] M. Pichot, A. Durandet, J. Pelletier, Y. Arnal, and L. Vallier, “Microwave multipolar plasmas excited by distributed electron cyclotron resonance: Concept and performance”, *Rev. Sci. Instrum.*, vol. 59, no. 7, p. 1072, 1988.

[26] J. Pelletier, “Device for distributing a microwave energy for exciting a plasma”, US Patent 5 216 329 A, 1993.

[27] J. Pelletier and T. Lagarde, “Chemical vapor deposition in high-density low-pressure plasmas: reactor scale-up and performance”, *Thin Solid Films*, vol. 241, no. 1–2, p. 240, 1994.

[28] P. Bulkin, N. Bertrand, and B. Drévillon, “Deposition of SiO_2 in integrated distributed electron cyclotron resonance microwave reactor”, *Thin Solid Films*, vol. 296, no. 1–2, p. 66, 1997.

[29] P. Bulkin, R. Brenot, B. Drévillon, and R. Vanderhaghen, “Structure and transport properties of integrated distributed electron cyclotron resonance grown micro-crystalline silicon”, *J. Non-Cryst. Solids*, vol. 231, no. 3, p. 268, 1998.

[30] A. Lacoste, T. Lagarde, S. B. Chu, Y. Arnal, and J. Pelletier, “Multi-dipolar plasmas for uniform processing: physics, design and performance”, *Plasma Sources Sci. Technol.*, vol. 11, no. 4, p. 407, 2002.

[31] S. Béchu, A. Soum-Glaude, A. Bès, A. Lacoste, P. Svarnas, S. Aleiferis, A.A. Ivanov Jr., and M. Bacal, “Multi-dipolar microwave plasmas and their application to negative ion production”, *Phys. Plasmas*, vol. 20, no. 10, p. 101601, 2013.

[32] D. Daineka, P. Bulkin, G. Girard, J.-E. Bourée, and B. Drévillon, “High density plasma enhanced chemical vapor deposition of optical thin films”, *Eur. Phys. J. Appl. Phys.*, vol. 26, no. 1, p. 3, 2004.

[33] J. Pelletier, A. Lacoste, T. L. Lagarde, M. Moisan, Y. Arnal, and Z. Zakrzewski, "PCT WO01/20710", US Patent 6 727 656, 2004.

[34] *Theory and Practice of Radiation Thermometry,* D. P. DeWitt and G. D. Nutter (Eds.), Wiley, 1988.

[35] M. N. van den Donker, R. Schmitz, W. Appenzeller, B. Rech, W. M. M. Kessels, and M. C. M. van de Sanden, "The role of plasma induced substrate heating during high rate deposition of microcrystalline silicon solar cells", Thin Solid Films, vol. 511–512, p. 562, 2006.

[36] Y. Yasuhiro, T. Hiromu, T. Yoshiaki, F. Masayuki, K. Keisuke, and Y. Nobuyuki, "Development of a-Si/microcrystalline-Si tandem-type photovoltaic solar-cells", Energy, vol. 56, no. 266, p. 46, 2006.

[37] C. Charpentier, "Investigation of deposition conditions and annealing treatments on sputtered ZnO:Al thin films: Material properties and application to microcrystalline silicon solar cells", *PhD thesis*, École Polytechnique, 2012.

[38] J. W. Coburn and M. Chen, "Optical emission spectroscopy of reactive plasmas: A method for correlating emission intensities to reactive particle density", *J. Appl. Phys.*, vol. 51, no. 6, p. 3134, 1980.

[39] D. A. G. Bruggeman, "Berechnung verschiedener physikalischer Konstanten von heterogenen Substanzen. I. Dielektrizitätskonstanten und Leitfähigkeiten der Mischkörper aus isotropen Substanzen", *Ann. Phys.*, vol. 416, p. 636, 1935.

[40] P. Roca i Cabarrocas, A. Fontcuberta i Morral, B. Kalache, and S. Kasouit, "Microcrystalline Silicon Thin-Films Grown by Plasma Enhanced Chemical Vapour Deposition - Growth Mechanisms and Grain Size Control", *Solid State Phenom.*, vol. 93, p. 257, 2003.

[41] D. E. Aspnes and A. A. Studna, "Dielectric functions and optical parameters of Si, Ge, GaP, GaAs, GaSb, InP, InAs, and InSb from 1.5 to 6.0 eV", *Phys. Rev. B*, vol. 27, no. 2, p. 985, 1983.

[42] G. E. Jellison, "Optical functions of silicon determined by two-channel polarization modulation ellipsometry", *Opt. Mater.*, vol. 1, no. 1, p. 41, 1992.

[43] J.-C. Dornstetter, B. Bruneau, P. Bulkin, E. V. Johnson, and P. Roca i Cabarrocas, "Understanding the amorphous-to-microcrystalline silicon transition in SiF_4/H_2/Ar gas mixtures", *J. Chem. Phys.*, vol. 140, no. 23, p. 234706, 2014.

[44] M. H. Brodsky, M. Cardona, and J. J. Cuomo, "Infrared and Raman spectra of the silicon-hydrogen bonds in amorphous silicon prepared by glow discharge and sputtering", *Phys. Rev. B*, vol. 16, no. 8, p. 3556, 1977.

[45] G. Lucovsky, "Chemical effects on the frequencies of Si-H vibrations in amorphous solids", *Solid State Commun.*, vol. 29, no. 8, p. 571, 1979.

[46] W. Beyer, "Hydrogen Incorporation in Amorphous Silicon and Processes of Its Release", in *Tetrahedrally-Bonded Amorphous Semiconductors,* D. Adler and H. Fritzsche (Eds.), Springer US, p. 129, 1985.

[47] P. A. Redhead, “Thermal desorption of gases”, *Vacuum*, vol. 12, no. 4, p. 203, 1962.

[48] L. A. Pétermann, “Thermal desorption kinetics of chemisorbed gases”, *Prog. Surf. Sci.*, vol. 3, p. 1, 1972.

[49] W. Beyer and F. Einsele, “Hydrogen Effusion Experiments”, in *Advanced Characterization Techniques for Thin Film Solar Cells*, D. Abou-Ras, T. Kirchartz, and U. Rau (Eds.), Wiley-VCH Verlag GmbH & Co. KGaA, p. 449, 2011.

[50] Y. L. Chen, C. Wang, G. Lucovsky, D. M. Maher, and R. J. Nemanich, “Transmission electron microscopy and vibrational spectroscopy studies of undoped and doped Si,H and Si,C:H films”, *J. Vac. Sci. Technol. A: Vac. Surf. Films*, vol. 10, no. 4, p. 874, 1992.

[51] S. Gaiaschi, “Fabrication, characterization and modeling of microcrystalline silicon-carbon alloys thin films”, *PhD thesis*, Université Paris Sud (2014).

[52] D. Ritter, E. Zeldov, and K. Weiser, “Steady-state photocarrier grating technique for diffusion length measurement in photoconductive insulators”, *Appl. Phys. Lett.*, vol. 49, no. 13, p. 791, 1986.

[53] R. Brüggemann, “Steady-State Photocarrier Grating Method”, in *Advanced Characterization Techniques for Thin Film Solar Cells*, D. Abou-Ras, T. Kirchartz, and U. Rau (Eds.), Wiley-VCH Verlag GmbH & Co. KGaA, p. 177, 2011.

[54] I. Balberg, A. E. Delahoy, and H. A. Weakliem, “Self-consistency and self-sufficiency of the photocarrier grating technique”, *Appl. Phys. Lett.*, vol. 53, no. 11, p. 992, 1988.

[55] R. Brüggemann, “Improved steady-state photocarrier grating in nanocrystalline thin films after surface-roughness reduction by mechanical polishing”, *Appl. Phys. Lett.*, vol. 73, no. 4, p. 499, 1998.

[56] H. Oheda, “Phase-shift analysis of modulated photocurrent: Its application to the determination of the energetic distribution of gap states”, *J. Appl. Phys.*, vol. 52, no. 11, p. 6693, 1981.

[57] R. Brüuggemann, C. Main, J. Berkin, and S. Reynolds, “An evaluation of phase-shift analysis of modulated photocurrents”, *Philos. Mag. Part B*, vol. 62, no. 1, p. 29, 1990.

[58] J. P. Kleider, C. Longeaud, and O. Glodt, “Study of the density of states of hydrogenated amorphous silicon from time-of-flight and modulated photocurrent experiments”, *J. Non-Cryst. Solids*, vol. 137, p. 447, 1991.

[59] C. Longeaud and J. P. Kleider, “General analysis of the modulated-photocurrent experiment including the contributions of holes and electrons”, *Phys. Rev. B*, vol. 45, no. 20, p. 11672,1992.

[60] M. A. Green, *Solar cells : operating principles, technology and system*. University of New South Wales, Kensington, 1992.

[61] J. Merten, J. M. Asensi, C. Voz, A. V. Shah, R. Platz, and J. Andreu, “Improved equivalent circuit and analytical model for amorphous silicon solar cells and modules”, *IEEE Trans. Electron Devices*, vol. 45, no. 2, p. 423, 1998.

[62] J. Hubin and A. V. Shah, “Effect of the recombination function on the collection in a p-i-n solar cell”, *Philos. Mag. Part B*, vol. 72, no. 6, p. 589, 1995.

Chapter 3 MDECR-PECVD growth of μc-Si:H film from SiF_4/H_2 plasma chemistry

Contents

In this chapter, the high-rate deposition of µc-Si:H films is studied by combining the SiF_4-based plasma chemistry and the MDECR-PECVD technique. Firstly, we will focus on the effect of process parameters such as substrate temperature and ion energy on the film growth under such low process pressure and high plasma density conditions. Secondly, aiming to use the material as the absorber layer for photovoltaic applications, approaches to achieve µc-Si:H film without any amorphous incubation layer and to broaden the deposition process window are further explored.

3.1. Plasma optical emission spectra

For silicon thin film deposition from the SiF_4-based plasma using MDECR-PECVD, the first thing to be noted is that the noble gas Ar is not necessarily required to assist gas dissociation, as it is in the case of RF-PECVD. Therefore, the work presented in this chapter is based on an SiF_4/H_2 plasma chemistry alone.

To get a general idea about the plasma composition under such conditions, OES measurements were performed through a viewport in the chamber. The spectra was monitored at a position about 3 cm above the substrate holder. Figure 3.1-(a) shows a typical OES spectra (only the range of 200-700 nm is shown) for the SiF_4/H_2 MDECR plasma operated in the ATOS reactor. The measurement was performed with the process conditions shown in Table 3.1. As a comparison, the spectra obtained from an $SiF_4/H_2/Ar$ RF plasma operated at high pressure in PHILIX is depicted in Figure 3.1-(b). During measurements, the following species of interest were detected: Si^* at 288 nm, SiF^* at 440 nm, SiF_2^* at 385 nm, SiF_3^* at 235 nm, H_β^* at 486 nm and H_α^* at 656 nm[1,2].

Table 3.1 Process conditions of the SiF_4/H_2 MDECR plasma and the $SiF_4/H_2/Ar$ RF plasma.

Plasma source	P_{MW}	P	SiF_4	H_2	Ar
	W	mTorr	sccm	sccm	sccm
MDECR	1250	7	10	60	-
RF	15	3000	3.6	5.3	88

As one can see, the two spectra present intense hydrogen emission peaks, which suggest an abundance of excited hydrogen in plasmas excited by both MDECR and RF sources. However, the results also underline the huge difference between these two sources. In contrast to the OES spectra of the RF plasma, wherein all the SiF_x^* (x = 0-3) species can be detected, the elevated dissociation of SiF_4 in the MDECR plasma process leads to the fact that SiF^* dominates the SiF_x^*

[1] G. Bruno, et al., *J. Appl. Phys.*, **69**: 7256 (1991).
[2] S. K. Ram, et al., *Phys. Status Solidi A*, **207**: 591 (2010).

species, and SiF_3^* and SiF_2^* are barely observable. Such a high level of dissociation of the feed gas has also been reported in an earlier study about the MDECR-PECVD of μc-Si:H from a pure SiH_4 plasma chemistry[3]. In that work, except for the presence of the SiH_x^* (x = 0,1) emission peaks, the SiH_4 MDECR plasma showed an almost identical OES spectra to a pure H_2 MDECR plasma, underlining the fact that the elevated gas dissociation gives enough concentration of H species to allow for the deposition of μc-Si:H film. Therefore, two things are clear for the MDECR-PECVD of μc-Si:H films from the SiF_4/H_2 plasma chemistry: the H_2 flow is sufficient to provide the necessary atomic H, and Si and SiF are probably the most dominant growth precursors.

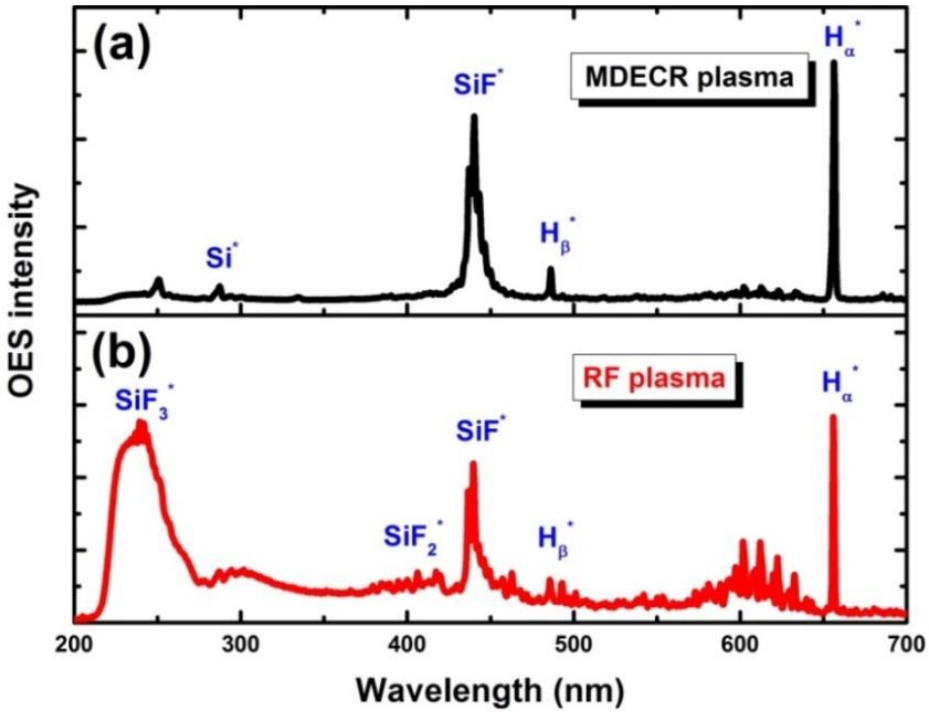

Figure 3.1 OES spectra obtained from (a) an SiF_4/H_2 MDECR plasma and (b) an SiF_4/H_2/Ar RF plasma.

3.2. Effect of substrate temperature

To study the impact of substrate temperature on the growth of μc-Si:H, a series of films were deposited on Corning "Eagle" glass with different substrate temperatures. Considering the high extent of gas dissociation in the MDECR-PECVD process, a higher proportion of H_2 is required to sufficiently eliminate fluorine for the μc-Si:H film growth, in contrast to the values just less than unity for the SiF_4/H_2 ratio in the RF plasma process[4]. The process conditions for this series of films are given in Table 3.2. To make a fair comparison, deposition times were adjusted to ensure that all the films are around 150 nm thick.

[3] P. Roca i Cabarrocas, et al., *Thin Solid Films*, **516**: 6834 (2008).
[4] J.-C. Dornstetter, et al., *IEEE J. Photovolt.*, **3(1)**: 581 (2013).

Table 3.2 Process conditions for studying effect of substrate temperature.

P_{MW}	P_{RF}	P	T_{sub}	SiF_4	H_2
W	W	mTorr	°C	sccm	sccm
1250	10	7	110-190	10	60

Ellipsometry

The deposited films were first examined by ellipsometry, and Figure 3.2 shows the data of $\langle \varepsilon_i \rangle$ in the high energy region of the spectra. As one can see, the spectra of films deposited at low substrate temperatures present a wide bump around 3.7 eV – a characteristic of amorphous silicon. Shoulder-like peaks at 3.4 eV and 4.2 eV characteristic of microcrystalline silicon appear at 140 ºC, and become more pronounced for temperatures higher than 175 ºC.

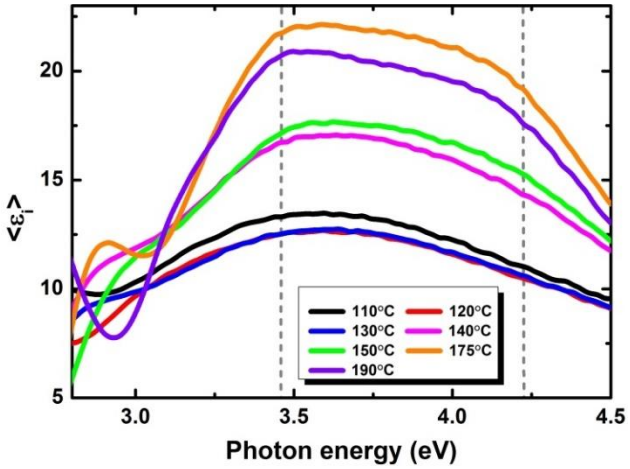

Figure 3.2 Ellipsometry spectra in high energy region for films deposited at different temperatures.

Raman spectroscopy

Raman spectra for these films are presented in Figure 3.3-(a), and the results confirm the observations from ellipsometry measurements. At low substrate temperatures, the films are all a-Si:H, as indicated by the single broad peak around 480 cm^{-1}. With increasing temperature, a transition from amorphous to microcrystalline is notably seen. The signature of crystalline silicon peak detected at 520 cm^{-1} shows up at 140 ºC, but is still accompanied by a considerable amount of amorphous phase with a broad shoulder in the spectra. For further increased temperatures, the amorphous silicon peak merges into the crystalline silicon peak, which indicates the deposition of a typical µc-Si:H layer.

In Figure 3.3-(b), the extracted values of X_c^{Raman} are plotted as a function of substrate temperature, and show a monotonic increase above 140 ºC. Up to 190°C, µc-Si:H films with X_c^{Raman} on the order of 60 % are obtained. Figure 3.3-(b) also includes the deposition rates (r_d), and shows a global trend of decreasing r_d with substrate temperature. A r_d of 8.5 Å/s is observed for amorphous material at 110 °C going down to 5.7 Å/s for microcrystalline material at 190 °C.

It is well known that the variation of substrate temperature can lead to complex consequences for the PECVD of μc-Si:H film under standard growth conditions. At low temperature, the species arriving on the growing surface are assumed to be unable to diffuse to energetically favorable sites for the formation of crystalline nuclei. Accordingly, a greater thickness of the underlying a-Si:H tissue is needed for crystallite nucleation to occur, or the film even remains in the a-Si:H regime. In general, for the temperature range lower than ~300 °C (not a universal value, could be slightly different for different cases), increasing substrate temperature is favorable for enhancing the thermally-induced adatom motion process[5], leading to an increase of the thermal diffusion coefficient D_S of species on the growing surface[6]. Thus, for μc-Si:H film, a faster crystallization process and a more rigid silicon network can be attained. However, above ~300 °C, a degradation in material quality will be observed due to the elimination of H during deposition. Deficient coverage of H on the growing surface leads to the loss of etching effectiveness and dangling bond passivation. Meanwhile, the thermal dissociation of Si-H bonds at high temperature can even lead to the creation of dangling bonds. These mechanisms have all been proposed to explain why excessive substrate temperature is detrimental for material quality[7].

From the results above, one can note that the substrate temperature is of crucial importance to achieve μc-Si:H films with high crystalline volume fraction under such low pressure, high deposition rate conditions. Considering substrate temperatures that range from 110 °C to 190 °C, the observed enhancement of the crystallization process likely arises from a gain in thermally-induced adatom motion at higher substrate temperature. Ideally, at very low species arrival rates, the thermally-induced adatom motion continues indefinitely, or in deposition cases, for a time limited by burial under the subsequent layer.

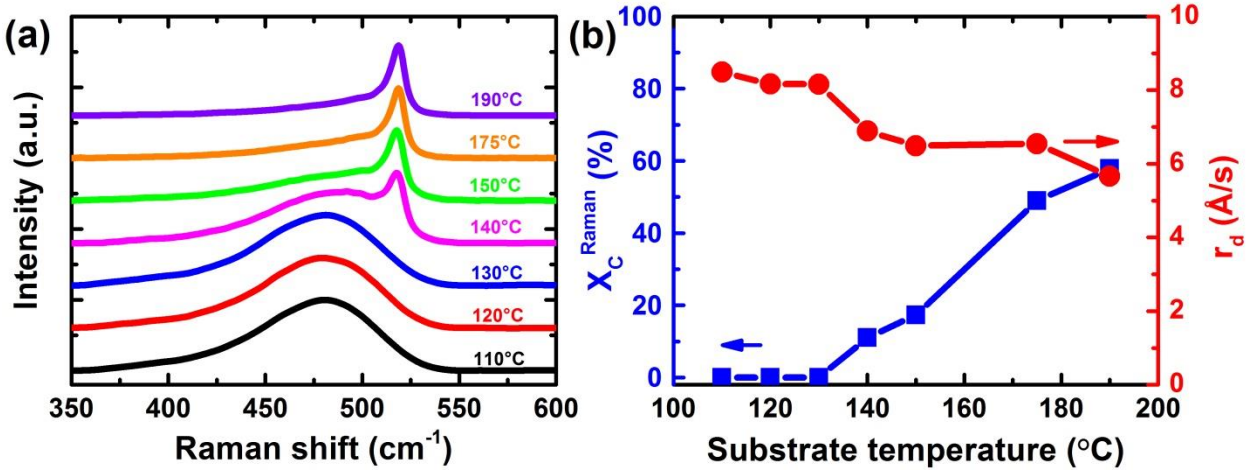

Figure 3.3 (a) Raman spectra for films deposited at different temperatures. (b) Variation of X_c^{Raman} (left axis, blue square) and r_d (right axis, red circle) for these films deposited with varying temperature.

For the case of a MDECR plasma deposition, species migration on the growing surface is greatly restricted due to the high deposition rate. Therefore, an appropriately higher substrate temperature is even more essential for the crystallization process of μc-Si:H film deposited by

[5] D. Smith, *Thin-Film Deposition: Principles and Practice*, McGraw Hill Professional (1995).
[6] A. Matsuda, *Jpn. J. Appl. Phys.*, **43**: 7909 (2004).
[7] A. Matsuda, *Thin Solid Films*, **337**: 1 (1999).

MDECR-PECVD. This is consistent with published results on the deposition of μc-Si:H film from a pure SiH_4 MDECR plasma, wherein the substrate temperature was required to be increased up to 268 ºC to achieve a X_c^{Raman} of 63 %[3]. It should be mentioned that the μc-Si:H film thickness therein was around 300 nm, which is twice as thick as the films in our case. As the most common process temperatures to fabricate μc-Si:H solar cells are below 200 ºC, such high substrate temperatures (above 260 ºC) may have been the origin of the poor performance of the resulting devices[8]. Interestingly, the substrate temperature needed to obtain highly crystallized μc-Si:H material from an SiF_4/H_2 plasma is much lower than that required for SiH_4/H_2. This can be explained by the fact that compared to atomic H, atomic F usually has a stronger etching activity on silicon[9]. Furthermore, the stronger "etching selectivity" of the amorphous phase silicon by atomic F at lower temperatures[10] can also partially contribute to the crystallization process.

3.3. Growth dynamics

The results given in the previous section were for films all having a similar thickness. To investigate the time evolution of the material microstructure during growth, another series of μc-Si:H films deposited at 140 ºC but with different deposition times (60-900 s) were prepared. These times corresponded to films' thicknesses ranging from ~40 nm to ~600 nm.

Ellipsometry and Raman spectroscopy

Figure 3.4 present the evolution of the ellipsometry spectra and Raman spectra for these films. As verified by both techniques, a μc-Si:H film deposited using MDECR-PECVD proceeds through the same evolution as in the case of RF-PECVD; both undergo the stages of amorphous incubation, crystallite nucleation, mixed phase growth, and microcrystalline phase steady state growth.

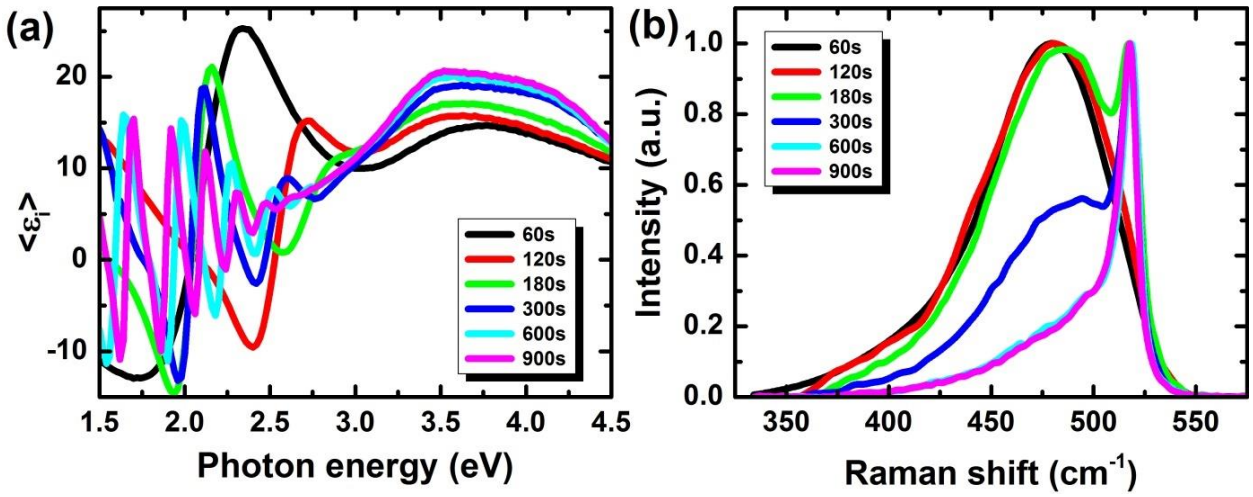

Figure 3.4 (a) Ellipsometry and (b) Raman (normalized) spectra for films with different thicknesses.

[8] L. Kroely, *PhD thesis*, École Polytechnique (2010).
[9] D. Humbird, et al., *J. Appl. Phys.*, **96**: 791 (2004).
[10] G. Bruno, et al., *Philos. Mag.*, **89**: 2469 (2009).

TEM characterization

This is also confirmed by the cross-sectional TEM image for the film with 600 s deposition time, as shown in Figure 3.5. As one can see, at the initial stage of growth, almost no nucleation sites can be observed at the interface with the substrate. Then, as explained in Ref. 3 (or by the *surface diffusion model*), the exothermal recombination of hydrogen provides energy to reorganize the silicon network, the crystalline nuclei starts to show up when the amorphous layer is several tens of nanometers thick. Ultimately, the conical growth of crystalline grains is observed.

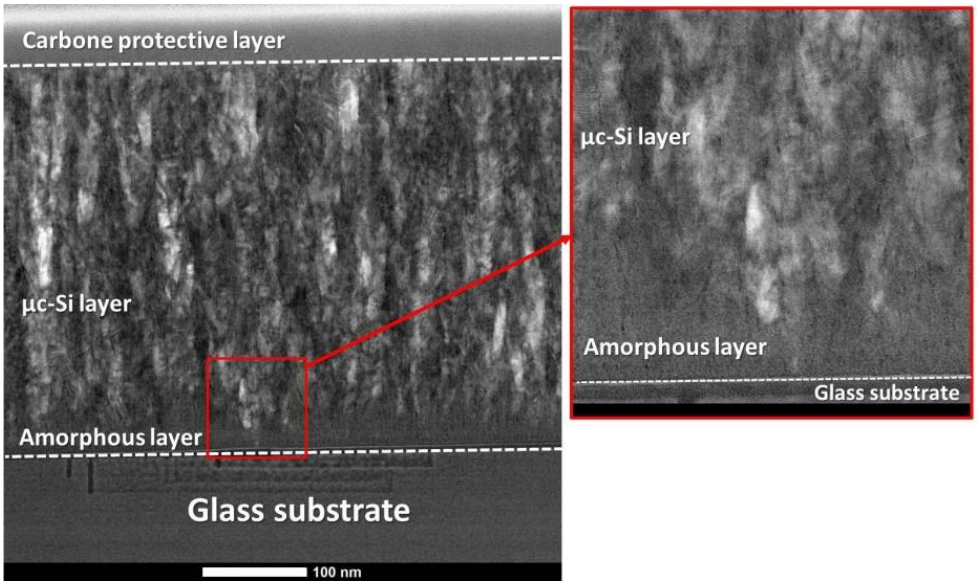

Figure 3.5 STEM-DF image of μc-Si:H film after 600 s of deposition.

3.4. Effect of ion energy

3.4.1. Estimation of ion energy

One should note that the efficient gas dissociation in the MDECR plasma process is attributed to the high-energy electrons trapped in tori around the permanent magnets. At the same time, it is the low-energy electrons that diffuse away from the multipolar magnetic confinement which determine the sheath potential drop ($\Delta\eta$)[11].

Therefore, as depicted in Figure 3.6, a low $\Delta\eta$ is expected for the MDECR plasma under electrically floating conditions (with no RF power injection to the substrate holder, here noted as $\Delta\eta_{float}$), which can be estimated by

$$\Delta\eta = \frac{T_e}{2q} \ln\left(\sqrt{2\pi\frac{m}{M}}\right) \tag{3.1}$$

where q, m, and M are the elementary charge, the electron mass, and the ion mass, respectively.

[11] A. Lacoste, et al., *Plasma Sources Sci. Technol.*, **11**: 407 (2002).

Considering the electron temperature T_e measured by Godyak [12] under similar plasma conditions on the same reactor that is used in our case, the $\Delta\eta_{float}$ herein is deduced to be about 1.5 V. This low value is due to high density of the low temperature electrons in the vicinity of the substrate holder. Accordingly, knowing the value of the drop in self-bias DC voltage ΔV_{DC}, which can be expressed by

$$\Delta V_{DC} = V_{DC}^{float} - V_{DC}^{rf} \tag{3.2}$$

where V_{DC}^{float} and V_{DC}^{rf} are the self-bias DC voltage under electrically floating conditions and with certain amount of RF power injection respectively (see Figure 3.6). Therefore, with the knowledge of the change in self-bias DC voltage, the IBE[§] during film deposition can be determined by

$$IBE = \Delta\eta_{float} + \Delta V_{DC} \tag{3.3}$$

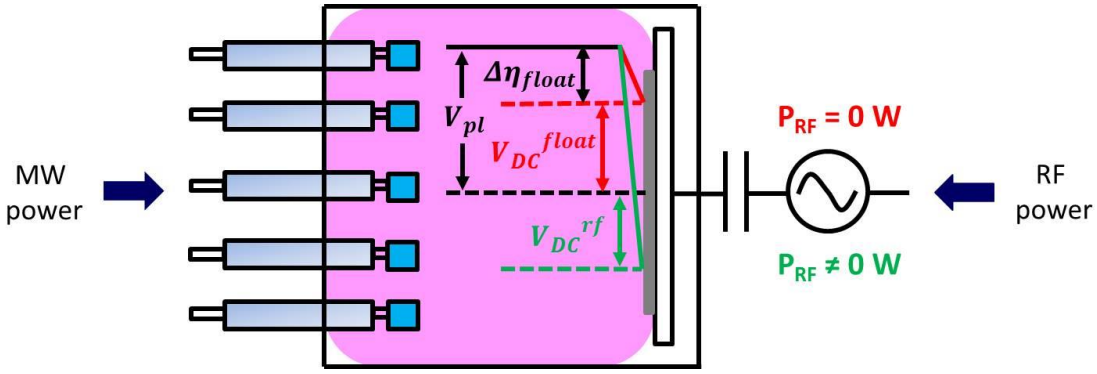

Figure 3.6 General description of difference in self-bias DC voltage under electrically floating conditions and with certain amount of RF power injection (not to scale).

Based on this point, the impact of ion energy has been studied by carrying out depositions for which the RF power supply on the substrate side was changed. A series of µc-Si:H films were deposited using the same process conditions shown in Table 3.1, except with varying RF power. While increasing the RF power from 0 W to 25 W, a decrease in the value of the self-bias DC voltage from +69 V (floating potential) down to +4 V is observed. Therefore, using the assumptions above, IBE ranging from 1.5 eV to 66.5 eV has been attained during processing. The deposition times were adjusted to keep the films' thicknesses around 450 nm.

3.4.2. Structural properties

Raman spectroscopy

The deposited films were first characterized by Raman spectroscopy. Figure 3.7-(a) shows the variation of X_c^{Raman} as a function of IBE. One can see that a sharp increase of X_c^{Raman} is observed

[12] V. A. Godyak, et al., *J. Phys. D: Appl. Phys.*, **44**: 233001 (2011).

[§] Due to the rather lower working pressure compared to the RF-PECVD process, the plasma sheath for the MDECR-PECVD process can be assumed to be collisionless. So here we use IBE instead of IBE_{max}.

(from 35 % up to 59 %) as the IBE increases just slightly from floating conditions (IBE = 1.5 eV) to 4.5 eV. With further increase in ion energy, the films continue to be crystalline phase dominant, and only a small and smooth further increase in X_c^{Raman} is seen, up to the film deposited with IBE = 41.5 eV, which shows an X_c^{Raman} of 70 %. However, once the IBE increases above this certain value, a local amorphization effect is observed, indicated by the dramatic reduction of X_c^{Raman} down to 24 % at IBE = 46.5 eV and below 20 % at IBE = 66.5 eV.

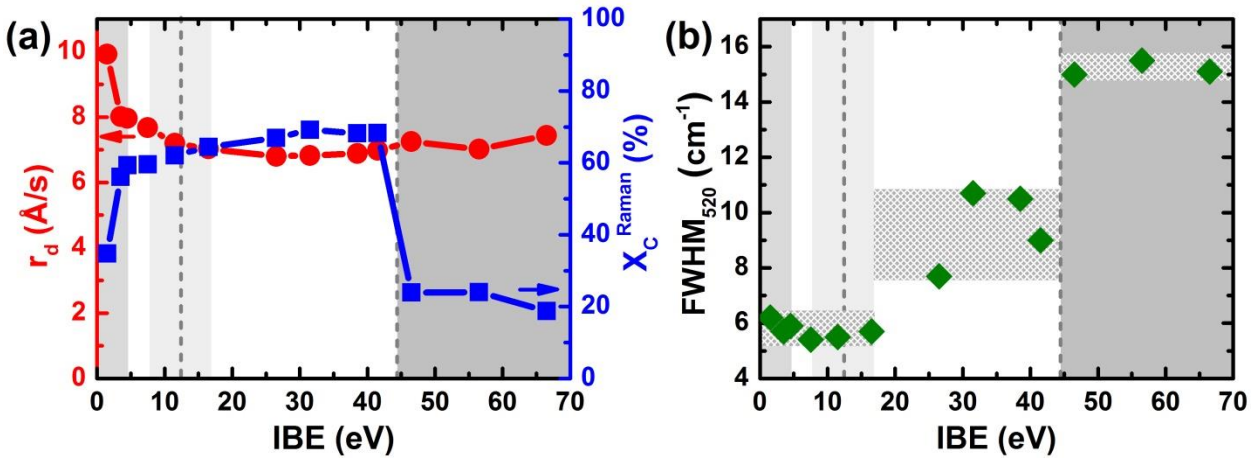

Figure 3.7 (a) Variation of r_d (left axis, red circle), X_c^{Raman} (right axis, blue square) and (b) $FWHM_{520}$ for μc-Si:H films deposited under different ion energy conditions.

Another effect of ion energy is observed in the variation of the full width at half maximum of the Raman crystalline peak at 520 cm^{-1} ($FWHM_{520}$). It can be noted from Figure 3.7-(b) that with increasing IBE, the $FWHM_{520}$ increases from 6 cm^{-1} at IBE = 1.5 eV to 9 cm^{-1} at IBE = 41.5 eV, suggesting a smaller crystalline grain size[13]. This indicates that although there is a higher X_c^{Raman}, smaller grained material results.

When further increasing the ion energy, the resulting films show $FWHM_{520}$ values up to around 15 cm^{-1}. For reasons explained in the discussion to follow, this variation can be viewed as two stepwise increases, with the second transition occurring simultaneously with a rapid decrease in X_c^{Raman} under high ion energy conditions. Interestingly, a moderate increase in ion energy up to IBE = 11.5 eV leads to an increase in X_c^{Raman}, while the $FWHM_{520}$ remains at a relative stable value over this range.

Ellipsometry

Figure 3.8-(a) shows the ellipsometry spectra in the high photon energy range for these films. Looking simply at the maximum magnitude of the spectra, one can see that this value changes with IBE, and again, a two stepwise changes can be observed.

The variation of the maximum value of $\langle \varepsilon_i \rangle$ in this high energy portion ($\langle \varepsilon_i \rangle_{max}$) with IBE is presented in Figure 3.8-(b). Generally, the $\langle \varepsilon_i \rangle_{max}$ of a μc-Si:H film depends on a number of

[13] M. N. Islam, et al., *Appl. Phys. Lett.*, **78**: 715 (2001).

factors: the crystalline volume fraction, crystallite size, density, as well as surface roughness. Regardless of the reason, a greater $\langle \varepsilon_i \rangle_{max}$ is commonly considered to be associated with improved material properties[14].

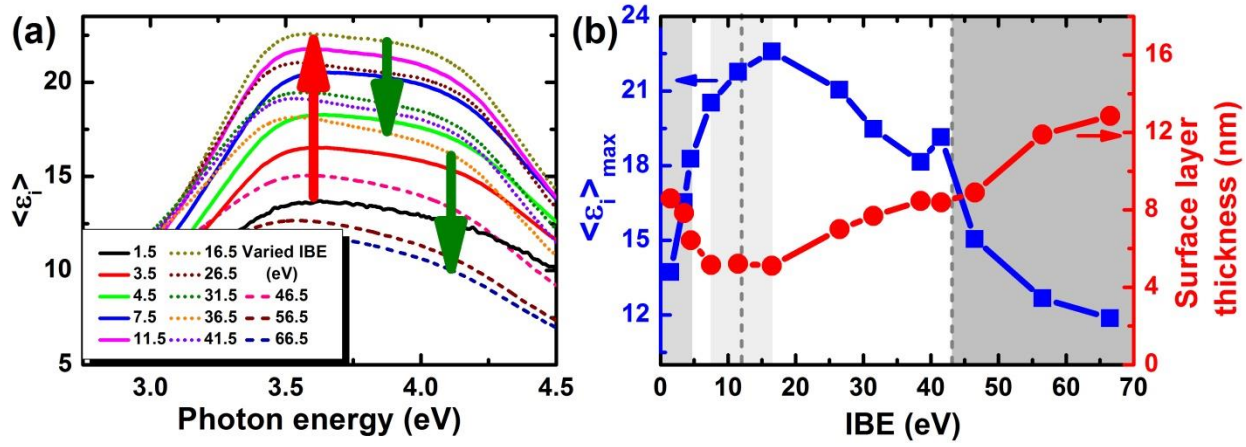

Figure 3.8 (a) Ellipsometry spectra for high photon energies for µc-Si:H films deposited under different ion energy conditions. (b) Variation of $\langle \varepsilon_i \rangle_{max}$ (left axis, blue square) and surface roughness layer thickness (right axis, red circle) deducing from ellipsometry modeling.

From Figure 3.8-(b), $\langle \varepsilon_i \rangle_{max}$ increases monotonically until an IBE value of 16.5eV, and then decreases continuously for higher ion energy conditions. This maximum coincides with the first transition of the $FWHM_{520}$ as shown in Figure 3.7-(b). For films deposited with IBE higher than 41.5 eV, the collapse in $\langle \varepsilon_i \rangle_{max}$ together with the gradually disappearing shoulder-like peaks suggests the dominance of an amorphous silicon phase, which is also in line with the Raman measurements.

In addition, deduced from the complete modeling of the films, the surface roughness of these films is also depicted in Figure 3.8-(b). Benefiting from the moderate ion energy condition, the film surface roughness decreases from 8.6 nm at IBE = 1.5 eV down to 5 nm at IBE = 11.5 eV and remains so until 16.5eV. When the ion energy is further increased, films with higher surface roughness are obtained, regardless of whether they are crystalline or amorphous silicon phase dominant material.

Infrared absorption

Based on the results shown above, one can note that a moderate ion energy condition (with IBE lower than 20 eV) during processing can lead to µc-Si:H films with improved structural properties, including crystalline grain features, material density as well as surface morphology.

To further explore the properties of these films, FTIR analyses were performed on co-deposited films grown on undoped c-Si wafers and with IBE at 1.5 eV (electrically floating), 6.5 eV and 16.5 eV. The measurements have been done right after deposition, and after exposure to ambient air for 5 days, 15 days, 30 days and 120 days. Figure 3.9 depicts the evolution of the FTIR spectra for the

[14] A. Abramov, et al., *Jpn. J. Appl. Phys.*, **47**: 7308 (2008).

film deposited at IBE = 1.5 eV. In this figure, details about the hydride (SiH_x) stretching modes (SMs) absorption are also presented.

The assignments of the SMs frequency positions for a μc-Si:H film will be discussed in Chapter 4. The focus of this study is on the films' stability in the ambient air. As one can see from the figure, the film shows a decreased absorption intensity by the SiH_x SMs after air exposure, while new peaks appear around 2200 cm^{-1} and 2250 cm^{-1}. These new peaks are attributed to the vibrational absorptions of a silicon atom bonding with different numbers of oxygen and hydrogen atoms (SiH_xO_y)[15,16,17]. Regardless of the SiH_xO_y bonding configuration, the result reflects that the SiH_x bonds located at least on the crystalline grain boundaries are attacked by oxidants present in the air, leading to oxygen atom substitution for hydrogen and the formation of SiH_xO_y bonds at internal surfaces[18,19].

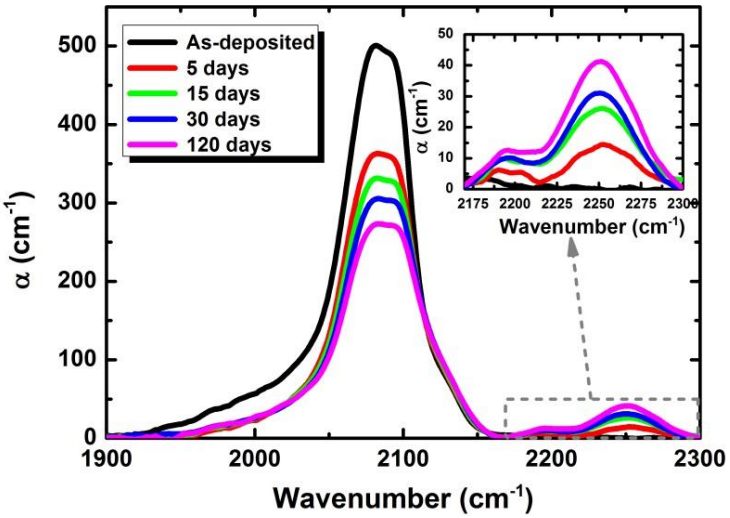

Figure 3.9 Evolution of FTIR spectra for μc-Si:H film deposited with IBE of 1.5 eV.

This considerable post-deposition oxidation can be greatly reduced by using a moderate ion energy condition during growth. To illustrate, Figure 3.10 presents a comparison of FTIR spectra for films deposited under different ion energies. Two absorption regions are shown: the dihydride ($(SiH_2)_n$) scissoring modes at ~840-880 cm^{-1}, and the SiO_x stretching modes at ~950-1200 cm^{-1}[19].

A significant increase of the SiO_x stretching mode absorption intensity in the film deposited at IBE = 1.5 eV is observed after four months of air exposure (Figure 3.10-(a)), consistent with a strong post-deposition oxidation effect. With increasing ion energy during deposition, a reduced oxidation effect is observed at IBE = 6.5 eV (Figure 3.10-(b)), indicated by the reduced intensity of the SiO_x and SiH_xO_y absorption peaks, and further reduced when the IBE is increased to 16.5 eV (Figure 3.10-(c)).

[15] G. Lucovsky, *J. Vac. Sci. Technol.*, **16**: 1225 (1979).
[16] G. Lucovsky, *Solid State Commun.*, **29**: 571 (1979).
[17] J. A. Schaefer, et al., *Surf. Sci. Lett.*, **139**: L209 (1984).
[18] M. Niwano, et al., *J. Appl. Phys.*, **76**: 2157 (1994).
[19] A. H. M. Smets, et al., *Appl. Phys. Lett.*, **92**: 33503 (2008).

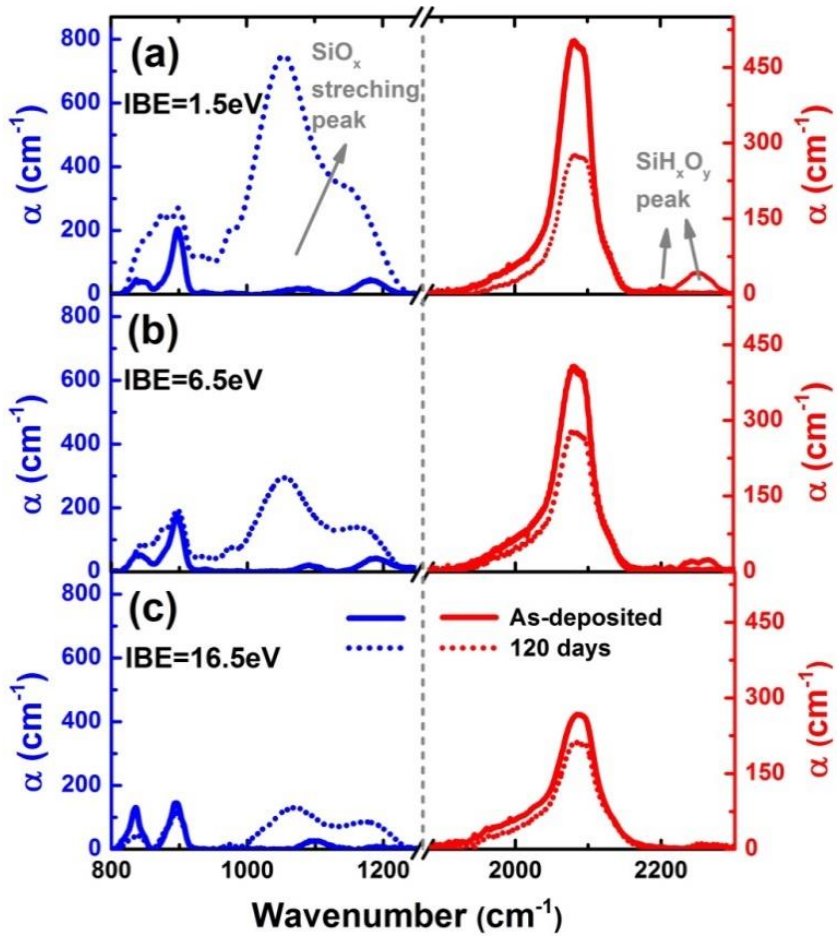

Figure 3.10 Comparison of FTIR spectra for co-deposited µc-Si:H films on c-Si wafer with IBE of (a) 1.5 eV, (b) 6.5 eV and (c) 16.5 eV in their initial state and after exposure to ambient air for 120 days.

Hydrogen exodiffusion

For the same series of films deposited on c-Si wafers, temperature-dependent exodiffusion experiments have also been carried out. Figure 3.11 shows the detected partial pressure of hydrogen molecules P_{H_2} (normalized to the maxima) as a function of temperature, for these films. In practice, the hydrogen effusion peak position depends on the local environments of the hydrogen in the material bulk, as well as the bonding configuration, and it is not easy to assign all the peaks from a single effusion spectra. However, for comparison, one can still define several peaks of interests. Under electrically floating conditions (IBE = 1.5 eV), the film exhibits a broad peak around 500-600 °C, which is representative of hydrogen effusion from an amorphous phase. However, a considerable decrease of this broad peak intensity is observed when the ion energy during processing is moderately increased. This can be attributed to a reduction of the amorphous phase in the deposited film, which is consistent with the aforementioned results from Raman measurements that an increased X_c^{Raman} is found with increasing IBE.

Moreover, several other effusion peaks can be identified in the lower temperature range, of which a weak one around 200-250 °C and a shoulder-like one centered around 350-450 °C are also

strongly influenced by the increasing ion energy. The presence of these two peaks can be attributed to hydrogen effusion from the desorbed water attached to the film surface and to internal "cracks"[20] (see more discussion in the following paragraphs), as well as to SiH_x bonds located on the surface of internal cavities or crystalline grain boundaries[21,22]. The drop in P_{H_2} for the former peak suggests less water incorporation after deposition, and therefore that a denser film is obtained under the moderate ion energy condition.

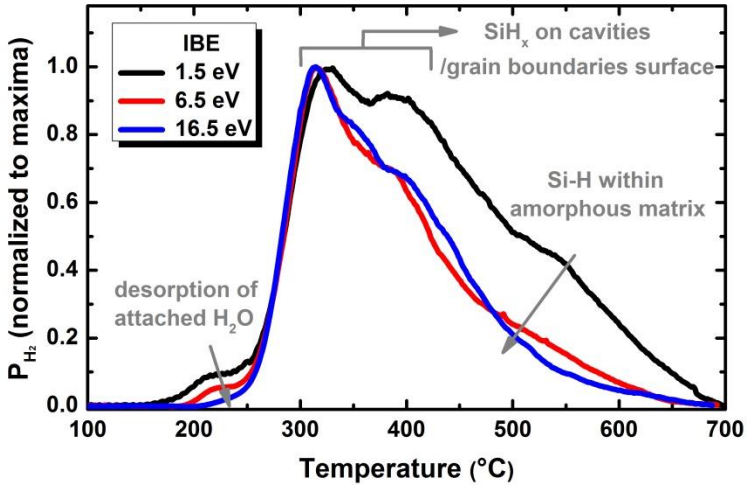

Figure 3.11 Comparison of hydrogen effusion spectra for co-deposited μc-Si:H films on c-Si wafers with IBE of 1.5 eV, 6.5 eV and 16.5 eV.

TEM characterization

To further investigate the impact of ion energy on the μc-Si:H film microstructure, TEM characterization has also been performed. Figure 3.12 and Figure 3.13 show results obtained for the two films deposited at IBE = 1.5 eV and 16.5 eV, respectively. As seen in Section 3.3, almost no nucleation sites can be observed at the early stage of growth for either film. The appearance of crystalline nuclei and then conical growth of crystalline grains are observed on top of an amorphous phase incubation layer.

The analyses are also performed under conditions of slight under-focus (Figure 3.12-(b) and (e)) and over-focus (Figure 3.12-(c) and (f)). It can be seen that under a low ion energy condition (IBE = 1.5 eV), the deposited film contains a rather high density of nanosized voids, which appear as white dots in the image, and have nanometric sizes (1-3nm). These "nanoporous" regions appear at grain boundaries in the deposited film, as also observed in Ref. 23. Some of them are even inter-connected, and appear as white lines along the grain boundaries, leading to the formation of "cracks" in the material bulk. Correspondingly, these "cracks" are characterized as black lines under the over-focused condition, as shown in Figure 3.12-(c). When the higher ion energy condition (IBE = 16.5 eV) is used for the deposition, a significant decrease of the nanosized voids

[20] N. Pham, *PhD thesis*, Université de Reims Champagne-Ardenne (2009).
[21] A. H. Mahan, et al., *Philos. Mag. Lett.*, **80**: 647 (2000).
[22] B. C. Pan, et al., *J. Non-Cryst. Solids*, **333**: 44 (2004).
[23] S. N. Agbo, et al., *Prog. Photovolt. Res. Appl.*, **22**: 346 (2014).

density is seen, (Figure 3.12-(e) and (f)). Moreover, the existing nanosized voids are characterized as having smaller sizes, and few inter-connections are observed.

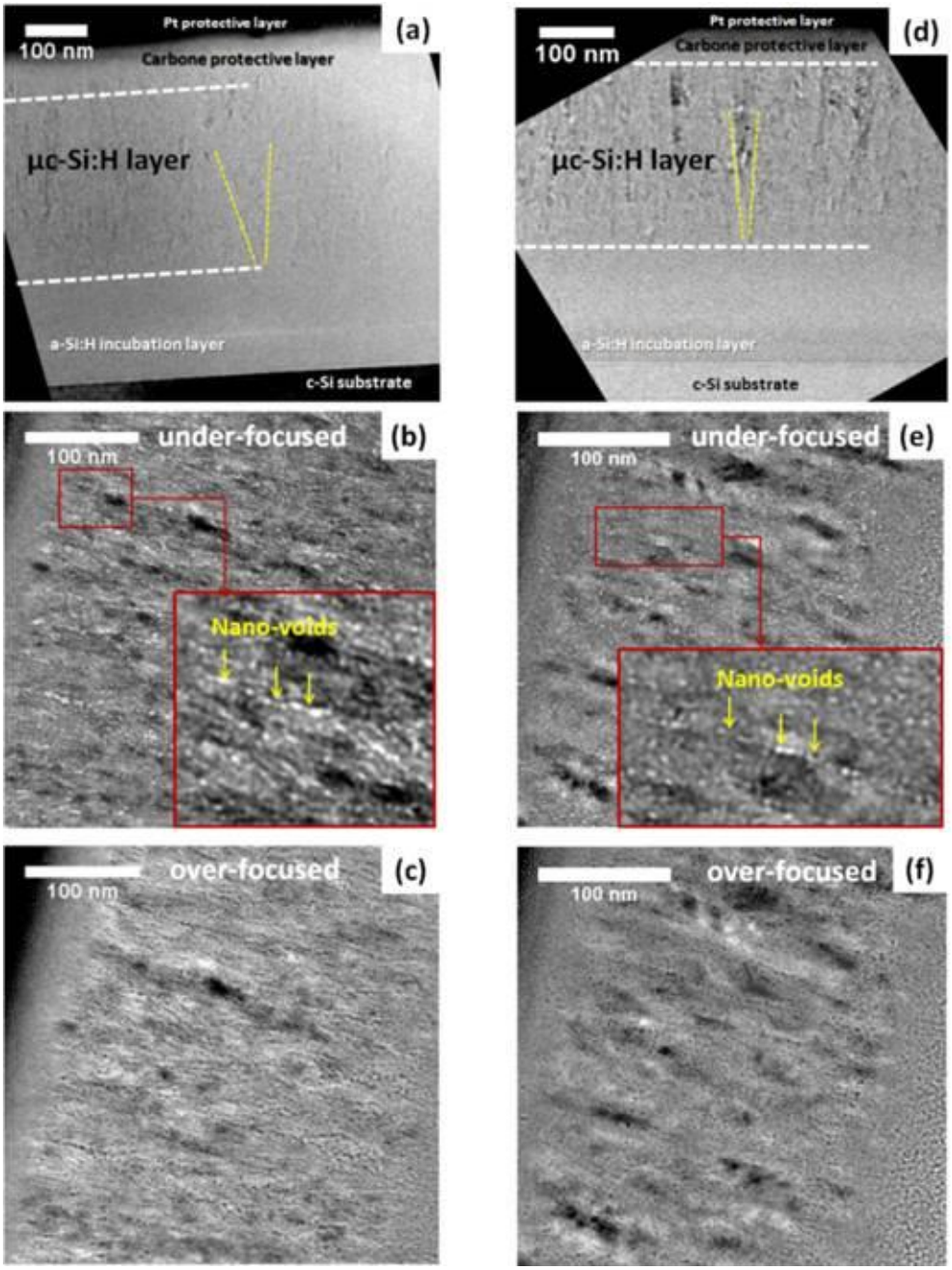

Figure 3.12 TEM-BF images of µc-Si:H films deposited with IBE of 1.5 eV/16.5 eV in (a)/(d) focused, (b)/(e) under-focused, and (c)/(f) over-focused conditions.

Consistent results are observed through STEM-HAADF analysis, as shown in Figure 3.13-(c) and (d). For the film with IBE = 1.5 eV, the inter-connected "cracks" appear right after crystallite nucleation and extend through the entire layer. However, for the case of IBE = 16.5 eV, the nanosized voids are considerably reduced, and few "cracks" are observed.

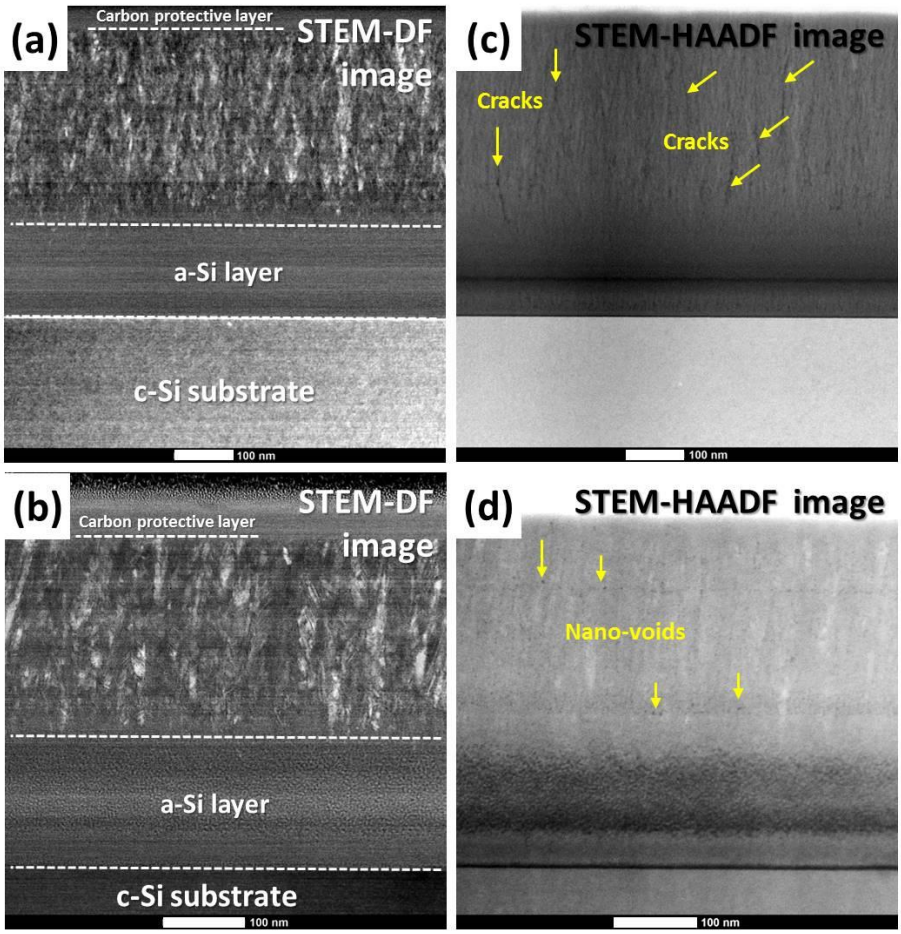

Figure 3.13 Cross-sectional (a)/(b) STEM-DF and (c)/(d) STEM-HADDF images of µc-Si:H films deposited with IBE of 1.5 eV/16.5 eV.

Along with the FTIR and hydrogen exodiffusion analyses, these results suggest that these "cracks" are responsible for the post-deposition oxidation effect observed for films deposited under low ion energy conditions. As introduced in Section 1.2.2, oxygen contamination in µc-Si:H material can create shallow donor states, leading to a reduced material quality and a poor spectral response in the red for the resulting solar cell devices. Therefore, for the high-rate deposition of µc-Si:H film in the MDECR-PECVD system, the suppression of the formation of "cracks" is essential to achieve high material quality, and the moderate ion energy condition during processing can be beneficial.

3.4.3. Ion-related interactions

In this section, we attempt to reveal the role of ion energy in µc-Si:H film growth for the low process pressure and high growth rate conditions of the MDECR-PECVD system. Links between the ion energy conditions and the properties of the resulting material will therefore be proposed throughout this chapter.

In contrast to neutrals, ions within the plasma can have a considerable amount of kinetic energy

due to their acceleration in the plasma sheath. A great deal of studies have shown that such energetic ions can play a vital role in determining the properties of PECVD-deposited μc-Si:H films. This should be evident from the fact that ions can contribute up to ~70 % of film growth in some cases[24], but also by the wide variety of effects induced by ion-surface and ion-bulk interactions, as demonstrated in both theoretical and experimental work. Energetic ions impinging on the growing surface can produce a local thermal spike and/or induce surface or bulk atomic displacements. The extent to which the deposited material will be affected depends on a number of factors: the ion kinetic energy, the mass ratio between the ions and the target atoms, as well as the ion incidence angle (angle between the ion trajectory and the target surface normal)[5]. Indeed, μc-Si:H film growth behavior, microstructure[25,26,27,28], as well as optoelectronic properties[2,29,30] are all influenced by these ion-related processes.

One is usually prevented from directly investigating the effect of ion energy in RF-PECVD systems, as any variation in ion energy is always coupled to changes in other plasma parameters (ion flux, plasma chemistry) which also impact μc-Si:H film growth[31,32,33]. However, this is not the case for a MDECR-PECVD system, since it has been mentioned that the gas dissociation is determined by the microwave power injection with the magnetic confinement effect (for electrons), and the ion energy condition during processing can be independently controlled through the RF power injection at the substrate. Practically, the sheath can be assumed to be collisionless for a MDECR plasma due to the low process pressure, so that a large proportion of ions will arrive the growing surface with maximum IBE as expressed by Equation (3.3). Moreover, it has been suggested by the results of Figure 3.1 that SiF^* dominates the SiF_x^* species in the SiF_4/H_2 MDECR plasma, allowing one to precisely investigate the impact of ion energy on μc-Si:H film growth for this simple plasma composition[8]. Doing so will allow us to make some conclusions concerning the above experimental results.

As explained in Ref. 5, the effective energy transfer between impinging ions and target atoms can generate an ion-induced adatom motion[13]. Although this is different in principle from the thermally-induced adatom motion mentioned in Section 3.2, it will have a similar effect on the growing surface, i.e., an enhancement of D_S. This is coherent with the results in our work, and as shown in Figure 3.7-(a) and Figure 3.8-(b), a highly promoted crystallization process and a smoother surface are obtained for films deposited with moderate ion energy conditions compared to those under floating conditions. With a further increase in ion energy, μc-Si:H films deposited by MDECR plasma show some distinct trends; from both Raman and ellipsometry analyses, sharp variations in the crystalline volume fraction, crystalline grain size, and surface roughness are observed at well-defined IBE thresholds. This stands in contrast to the case of RF-CCP processes under high pressure conditions, where such interactions just lead to a greater a-Si:H/μc-Si:H

[24] E. A. G. Hamers, et al., *J. Appl. Phys.*, **88**: 3674 (2000).
[25] B. Kalache, et al., *Solid State Phenom.*, **80**: 71 (2001).
[26] B. Kalache, et al., *J. Non-Cryst. Solids*, **299**: 63 (2002).
[27] B. Kalache, et al., *J. Appl. Phys.*, **93**: 1262 (2003).
[28] S. Lebib, et al., *J. Appl. Phys.*, **97**: 104334 (2005).
[29] G. Bugnon, et al., *33rd IEEE PVSC Proc.*, **1** (2008).
[30] A. C. Bronneberg, et al., *J. Vac. Sci. Technol. A: Vac. Surf. Films*, **30**: 061512 (2012).
[31] A. C. Bronneberg, et al., *J. Appl. Phys.*, **114**: 063305 (2013).
[32] J. Palmans, et al., *J. Phys. D: Appl. Phys.*, **47**: 224003 (2014).
[33] A. Michelmore, et al., *Front. Phys.*, **3**: 3 (2015).

transition thickness[34].

To understand the mechanism behind the existence of these thresholds, we consider the mass-dependent ion-related interactions with the growing surface. Figure 3.14 shows the theoretical minimum energy needed to induce surface and bulk atomic displacement on a silicon substrate as a function of impinging ion mass[35]. In our conditions, the most likely ions in the plasma are SiF_x^+ (x = 0-3), H_x^+ (x = 0-3). Although it has been proposed that the energetic impinging H_3^+ ion can induce considerable impact to the μc-Si:H film growth using RF-PECVD[36], it is not the case for the deposition using MDECR-PECVD in our work. It can be noted from Figure 3.14 that neither the *IBE* threshold of the H_3^+-induced surface atomic displacement (~30 eV), nor the bulk atomic displacement (~65 eV) matches the experimentally obtained values.

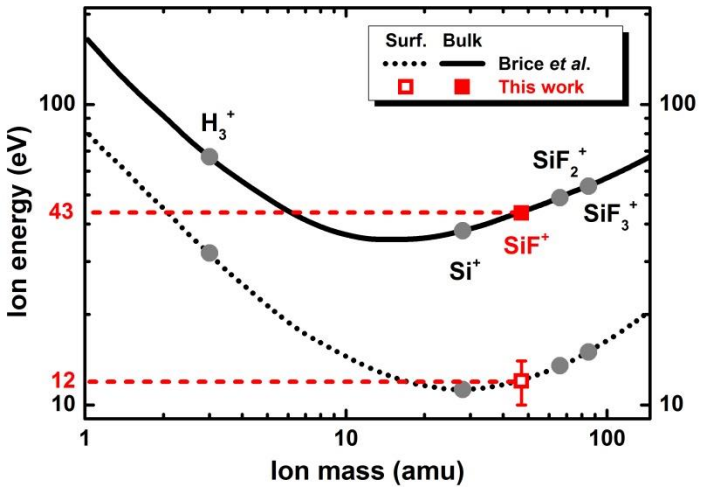

Figure 3.14 Energy threshold for ion-induced surface (dashed line) and bulk (solid line) atomic displacement on a silicon substrate versus impinging ion mass (by Brice *et al*[35]). The SiF_x^+ and H_3^+-induced displacements are highlighted (solid circles). The squares correspond to the experimental values for SiF^+ found in this work.

For the possible SiF_x^+ ions (i.e., Si^+, SiF^+, SiF_2^+ and SiF_3^+) in the MDECR plasma, the *IBE* thresholds for effective bulk atomic displacement are 36 eV, 43 eV, 50 eV and 55 eV respectively (indicated by the dots). As one can see, the value of 43 eV given by SiF^+ corresponds very well with the experimental transition values deduced from the Raman (Figure 3.7, wherein the transition is indicated by the third shaded region) and ellipsometry measurements (Figure 3.8-(b)). This is particularly true if one considers that the transition energies for Si^+, SiF_2^+ or SiF_3^+ will be far from the observed thresholds. In combination with the OES spectra shown in Figure 3.1 which indicated that SiF^* dominates the SiF_x^* species, we can reasonably consider that SiF^+ is the most abundant SiF_x^+ ion in the MDECR plasma, a fact that has also been observed by using quadrupole mass spectrometer under similar process conditions on the same reactor in Ref. 37.

However, the threshold energy of 12 eV given by Figure 3.14 for SiF^+-induced surface atomic

[34] B. Bruneau et al., *J. Appl. Phys.*, **115**: 084901 (2014).
[35] D. K. Brice, et al., *Nucl. Instrum. Methods Phys. Res.*, **44**: 68 (1989).
[36] B. Bruneau, et al., *IEEE J. Photovolt.*, **4**: 1354 (2014).
[37] S. Kasouit, et al., *63rd GEC*, **55**: 7 (2010).

displacement (indicated by the bottom dashed line) is less clearly defined. Due to the aforementioned ion-induced enchantment of D_S under moderate ion energy conditions, the change in X_c^{Raman} in the μc-Si:H films shows a first threshold closer to 4-5 eV of IBE (in Figure 3.7-(a), shown by the first shaded region), after which X_c^{Raman} grows more slowly. Consistently, very low IBE enhances the surface smoothness until a plateau between 7-17 eV is observed (in Figure 3.8-(b), shown by the second shaded region), presumably as the ions with energies above 12 eV begin to dislodge surface growth species from their lowest energy positions. Furthermore, $FWHM_{520}$ indicates a sharp decrease in crystal size, but only starting around 18-24 eV (see Figure 3.7-(b)). This last result can be understood by considering the renucleation process explained in Ref. 34. Through the reorganization by the impinging ions of the atoms around the impinging sites, new grains can appear on the already existing grains but with locally distinct crystalline orientations, thus resulting in smaller grain sizes.

In contrast with the unclear results at low IBE values, under much higher ion energy conditions, the SiF^+-induced bulk displacement is more dramatic. It can be argued that although the surface renucleation process could still be happening, the atomic displacement near the subsurface seriously hinders the formation of crystalline nuclei or even breaks up small crystallites. Consequently, a local amorphization effect starts to appear, resulting in lower crystalline volume fraction as well as even smaller crystalline domains.

In conclusion, all these results show that the control of ion energy is of crucial importance for the growth of μc-Si:H films from an SiF_4/H_2 plasma chemistry using the MDECR-PECVD technique. Very low IBE during processing can lead to the existence of inter-connected nanosized voids through the entire film thickness, which is responsible for less compact material and strong post-deposition oxidation after air exposure. However, high IBE can also be detrimental to the material properties. The bulk atomic displacement induced by the impinging SiF^+ can severely suppress the nucleation process, leading to a local amorphization effect on the growing film. A moderate ion energy condition is beneficial to achieve a significant drop in the density of voids, and a higher quality μc-Si:H film with better stability can be obtained.

3.5. Two-step process

3.5.1. Seed layer

As seen in Section 3.3, a μc-Si:H film deposited using MDECR-PECVD proceeds through the same evolution as does one grown using RF-PECVD: amorphous phase incubation, crystallite nucleation, mixed phase growth, and microcrystalline phase steady state growth. However, it has been extensively reported that this amorphous incubation layer within μc-Si:H film is detrimental to the performance of the resulting solar cells devices[38,39], especially on the transport properties at the *p*/*i* interface.

Thinning or elimination of this amorphous incubation layer to obtain device quality μc-Si:H material from the start of growth has always been a major research and industrial challenge. Van

[38] J. Koh, et al., *Appl. Phys. Lett.*, **75**: 2286 (1999).
[39] H. Fujiwara, et al., *Phys. Rev. B*, **63**: 115306 (2001).

den Donker *et al*[40] proposed that by applying a H_2 background prior to plasma ignition to suppress the SiH_4 back diffusion during the initial growth stage, one can avoid the formation of incubation layer. This method has been successfully implemented into the μc-Si:H solar cell fabrication, and an enhancement of device performance (blue response) was achieved. However, this technique is still limited by difficulties such as a narrow process window and long deposition times.

Another way to eliminate the amorphous incubation layer is to prepare a highly crystallized thin seed layer providing enough nucleation sites for the crystalline phase growth, for which approaches like hydrogen dilution "grading"[41,42] or H_2 plasma treatment for the amorphous under-layer before the main layer deposition[43] have been employed. However, by applying these hydrogen rich plasma methods for the initial growth of μc-Si:H film, one may need to consider the risk of damaging the *p*/*i* interface due to the H-related etching[44]. In addition, a major challenge of these methods is that the extra process procedures make them less attractive to industry.

3.5.2. Amorphous incubation layer free μc-Si:H film

In our case, in order to avoid the amorphous incubation layer, we propose introducing a two-step method. Very simply, the whole deposition was split into two steps using identical conditions except for process pressure. Figure 3.15-(a) depicts the material phase evolution in a normal continuous one-step deposition. In contrast, in the two-step process shown by Figure 3.15-(b), the highly crystallized seed layer is first deposited at a lower pressure, and is then followed by the deposition of the main layer at a higher pressure. The process conditions are given in Table 3.3.

Table 3.3 Process conditions for deposition of μc-Si:H films using two-step method.

Step	P_{MW}	P_{RF}	*IBE*	*P*	T_{sub}	SiF_4	H_2
	W	W	eV	mTorr	°C	sccm	sccm
I	1250	10	16.5	1.67	140	10	60
II				7			

Advantageously, there is no need to stop the plasma between these two steps. For an ECR plasma process, deposition rate is proportional to the process pressure (in a reasonable range)[45], so the thickness of the seed layer can be easily controlled. During the lower pressure step, ~20 nm of μc-Si:H was deposited in 15 min (~0.22 Å/s), and as deduced from Raman measurements, X_c^{Raman} is estimated to be around 70 %, which means that it can serve as the seed layer.

[40] M. N. van den Donker, et al., *Appl. Phys. Lett.*, **87**: 263503 (2005).
[41] J. H. Zhou, et al., *Appl. Phys. Lett.*, **71**: 1534 (1997).
[42] O. Vetterl, et al., *Thin Solid Films*, **427**: 46 (2003).
[43] H. Yue, et al., *J. Cryst. Growth*, **322**:1 (2011).
[44] Y. M. Li, et al., *Thin Solid Films*, **483**: 84 (2005).
[45] X. H. Zhu, et al., *Vacuum*, **83**: 386 (2008).

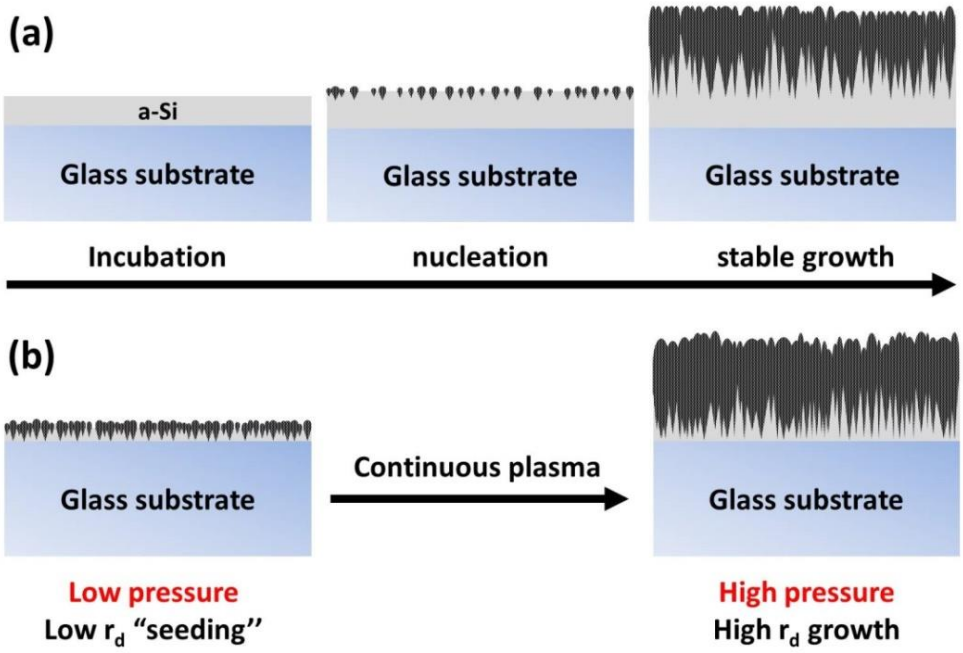

Figure 3.15 (a) Conventional continuous one-step deposition and (b) two-step deposition with seed layer growth at low process pressure and main layer growth at high process pressure.

Figure 3.16 presents the evolution of X_c^{Raman} for the two-step process deposited films with increasing thickness, as well as for the films deposited by a one-step deposition, as studied in Section 3.3. For the films with an underlying seed layer, a high density of nucleation sites provides the possibility to get over the a-Si/µc-Si transition and to proceed directly to the crystalline phase growth. As a result, for the whole deposition process, the crystalline volume fraction of the film varies little from a value on the order of 70 %, which is greater than the 58 % achieved at the stable stage for the case of a one-step deposition.

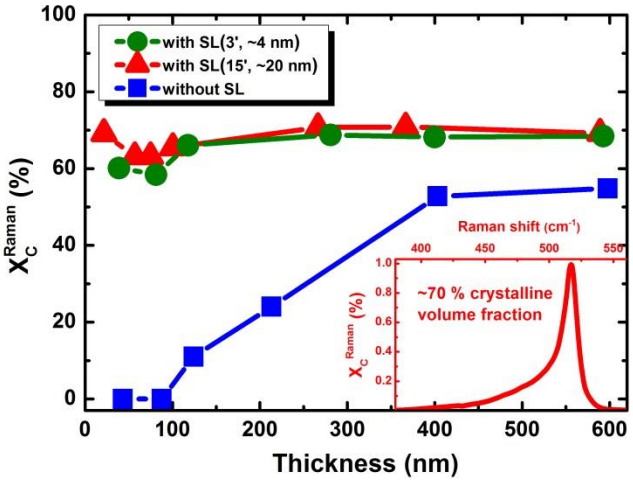

Figure 3.16 Evolution of X_c^{Raman} during growth process for µc-Si:H films with ~4 nm (green circles) and ~20 nm seed layer (red triangles) deposition compared to one-step process deposited films (blue squares). The inset shows the Raman spectra of the ~20 nm seed layer.

Surprisingly, even with only 3 min (~4 nm) of seed layer deposition, similar results can also be achieved (see the green data in Figure 3.16). It should be noted that demonstrating a thinner effective seed layer thickness not only means less process time, but also minimizes the probability of any amorphous incubation layer existing within the seed layer itself, as well as minimizing the exposure of any doped layer to this plasma condition in the case of device fabrication.

The microstructure of the two-step films incorporating a 15 min deposition of seed layer were analyzed by STEM. In Figure 3.17-(a), the DF image shows no amorphous incubation layer at the bottom part of the deposited film. Highly crystallized material is immediately obtained at the initial growth stage. However, by using the HAADF mode, more details about the microstructure are revealed. As indicated by the yellow lines in Figure 3.17-(b), the well-defined seed layer can be observed in the HAADF image, while it cannot be distinguished in the DF image. Moreover, a considerable amount of pores are present in the transition region between the seed layer and the main layer. During film growth, these pores extend further into the material bulk, leading to the formation of stacking faults among the crystalline grains.

This is even more obvious in a second experiment, in which we stopped the plasma and broke the vacuum after the seed layer deposition, as shown in Figure 3.17-(c) and (d). Although the nucleation process for the following main layer with high growth rate can still happen right above the seed layer, the interface is rather rough and a layer of voids can be observed.

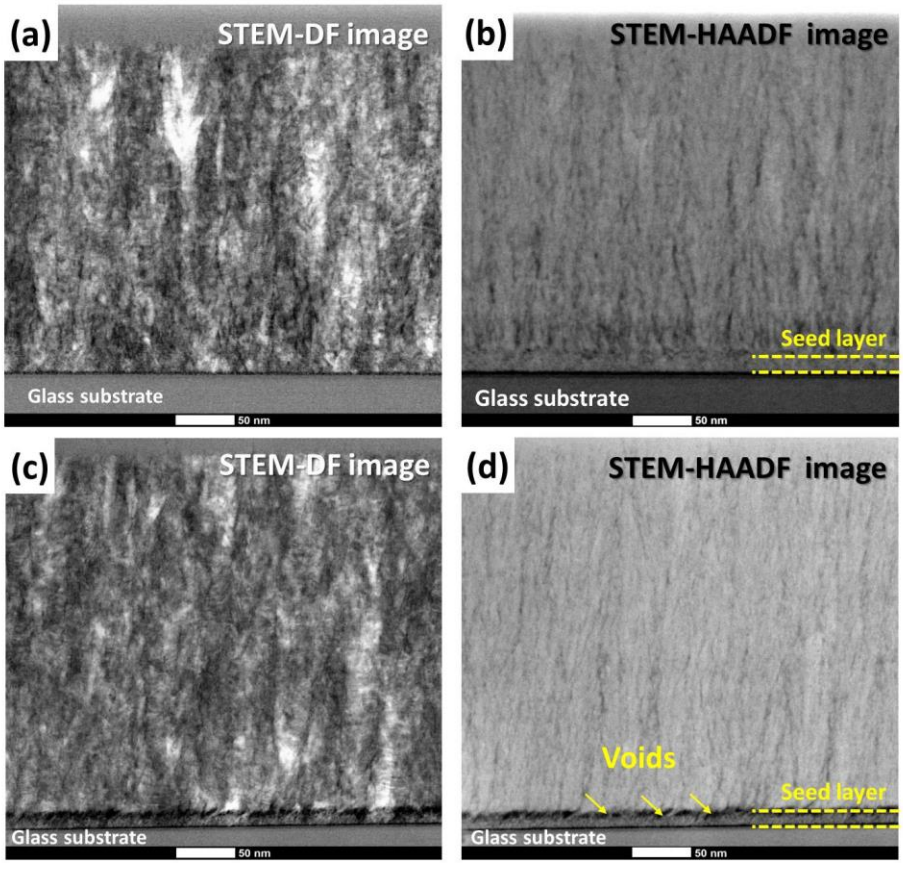

Figure 3.17 (a)/(c) STEM-DF and (b)/(d) STEM-HADDF images of the two-step process deposited μc-Si:H films without/with vacuum break after the seed layer deposition.

The presence of such a porous region should be attributed to the sharp change in deposition rate, as the transition in process pressure between two steps is rather fast (several seconds) in our experiments. Although the highly crystallized seed layer promotes the crystallization process during the main layer growth, the opportunity for surface diffusion for the incoming species will be impacted by the high precursor flux at (relatively) high pressure conditions. Therefore, instead of a continuous and uniform growth occurring, a renucleation process will occur, and preferentially at existing crystalline grains. In this case, rapid conical growth can be observed, leaving behind porous material among these "cones". A higher resolution image of this porous region is presented in Figure 3.18. However, one could reasonably assume that a more compact interface layer and thus less stacking faults in the main layer could be achieved if a "graded" variation in the process pressure between the two steps is applied.

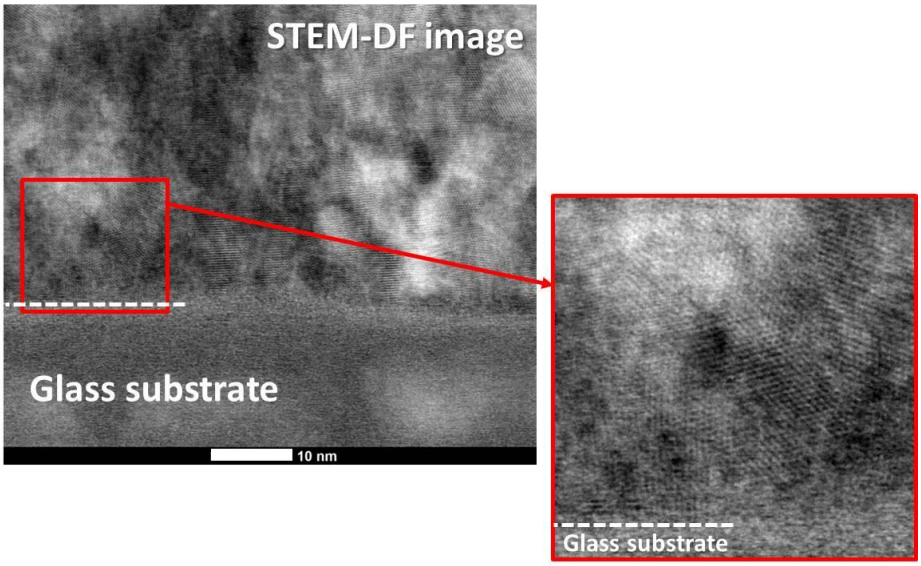

Figure 3.18 STEM-DF image (magnified at porous interface region) of µc-Si:H film deposited by two-step process without vacuum break after seed layer deposition.

3.5.3. Effect of gas pressure

To understand the origin and find the process window for this highly crystallized seed layer, the optical emission of plasmas operated under various pressures (ranging from 1.67 mTorr to 8 mTorr) were investigated.

Figure 3.19 presents the variation of H_α^* and SiF^* emission intensity as a function of gas pressure, which qualitatively indicates the variation of atomic H and growth precursor concentration within the plasma. As gas pressure increases, a continuous increase of the SiF^* intensity is observed. However, the situation is different for H_α^*. It just shows a slight increase up to a pressure of 3 mTorr and then decreases continuously for higher pressures

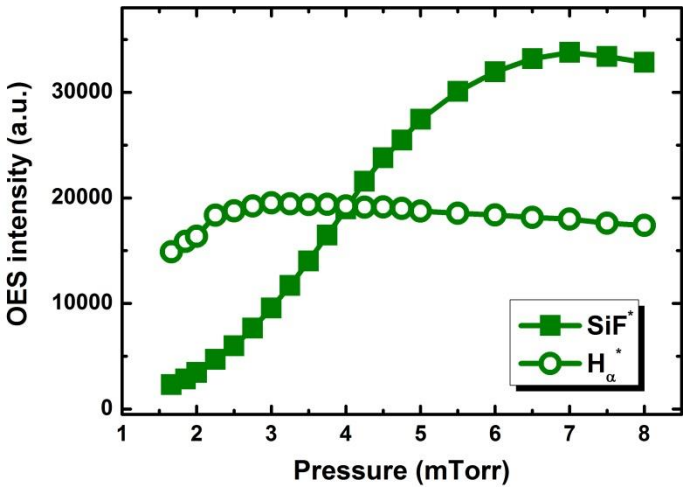

Figure 3.19. Evolution of SiF* (blue) and H_α* (red) emission intensity as a function of pressure, as obtained from OES measurements.

To establish the link between the variation of plasma properties and the material processing results, another series of depositions have been carried out with the same process pressures as in the above series. The process conditions are shown in Table 3.4. All the films have a thickness of ~20-30 nm.

Table 3.4 Process conditions for studying the effect of gas pressure.

P_{MW}	P_{RF}	P	T_{sub}	SiF_4	H_2
W	W	mTorr	°C	sccm	sccm
1250	10	1.67-8	140	10	60

The results are presented in Figure 3.20, where the corresponding variation of relative emission intensity of H_α^* and SiF^* (as detected by OES measurements, $R_{OES} = H_\alpha^*/SiF^*$) is also plotted. The value of R_{OES} decreases rapidly with increasing pressure, and then holds a certain value (in this experimental setup, close to unity) above a pressure of 3 mTorr. One can also note two other clear trends from Figure 3.20. Firstly, the deposition rate increases continuously from 0.24 Å/s at 1.67 mTorr to 7.2 Å/s at 7.2 mTorr. Secondly, X_c^{Raman} falls with increasing pressure, and tracks the value of R_{OES} (with an offset).

These trends in material properties can be correlated with the OES data. The increase in growth rate correlates with the SiF^* emission, as aforementioned that SiF is the dominant SiF_x growth precursor in the plasma. The connection with X_c^{Raman} is more subtle. It is generally believed that the atomic H concentration within the plasma (or the ion flux arriving at the growing surface) plays a crucial role in the crystallization process during μc-Si:H film growth[7,46,47]. In the growth processes from the SiF_4/H_2 plasma chemistry, this role is easily quantifiable. As it has been described in Section 1.3, for film growth to occur, sufficient atomic H is needed to abstract the F

[46] K. Nakamura, et al., *Jpn. J. Appl. Phys.*, **34**: 442 (1995).
[47] S. Sriraman, et al., *Nature*, **418**: 62 (2002).

atoms generated by the precursors for film growth, and the leftover radicals contribute to the chemistry required for the crystallization process[48]. This has been experimentally confirmed by detecting the HF molecules concentration using RGA, which linearly increases with the H_2 depletion under different process conditions (not shown).

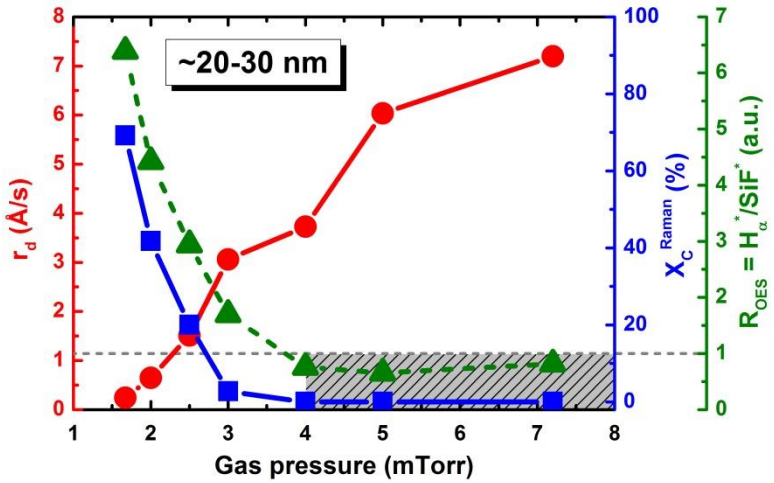

Figure 3.20 Variation of r_d (left axis, red) and X_c^{Raman} (right axis, blue) for films deposited with different pressures. Second right axis presents the corresponding relative emission intensity of H_α^* and SiF^* expressed by the ratio of H_α^*/SiF^* (green).

As indicated by the shaded region in Figure 3.20, films deposited with R_{OES} lower than one (> 3 mTorr) are amorphous. For pressures below 3 mTorr, all additional H not consumed through the elimination of F atoms can interact with weak Si-Si bonds and favor the crystallization process. It should be noted that without knowledge of the electron energy distribution function, it is difficult to estimate the concentration of corresponding radicals (like H_x and SiF_x) within the plasma from the optical emission intensity alone. This experimental ratio R_{OES} is therefore not a universal reference value. However, together with the results of material analysis, the process window defined may still be valid when processing in similar type of reactor. In short, due to the low deposition rate resulting from the lower SiF flux under low pressures, the thermally-induced adatom motion is allowed to play its normal role in enhancing surface species diffusion. In addition to the atomic H reactivity, both lead to a promotion of crystallization in these films.

3.5.4. Broader process window

To further investigate the benefit of a seed layer for MDECR-PECVD μc-Si:H film growth from the SiF_4/H_2 plasma chemistry, another series of films were deposited with various substrate temperatures using the two-step process. Table 3.5 shows the process conditions. Deposition times are adjusted to keep the seed layer and total thickness around 20 nm and 150 nm, respectively.

[48] J.-C. Dornstetter, et al., *J. Chem. Phys.*, **140**: 234706 (2014).

Table 3.5 Process conditions for studying the effect of substrate temperature using the two-step process.

Step	P_{MW}	P_{RF}	IBE	P	T_{sub}	SiF_4	H_2
	W	W	eV	mTorr	°C	sccm	sccm
I	1250	10	16.5	1.67	110-190	10	60
II				7			

The seed layers deposited with different substrate temperatures have been characterized individually, and the results are presented in Figure 3.21, which shows that X_c^{Raman} increases monotonically with substrate temperature up to 140 °C, at which point it reaches a relative stable value around 70 % (as also seen in Figure 3.20). In addition, the deposition rates of seed layers are also provided. A slow decrease with increasing substrate temperature is observed initially, and then deposition rate stays roughly constant around 0.22 Å/s for temperatures above 140 °C.

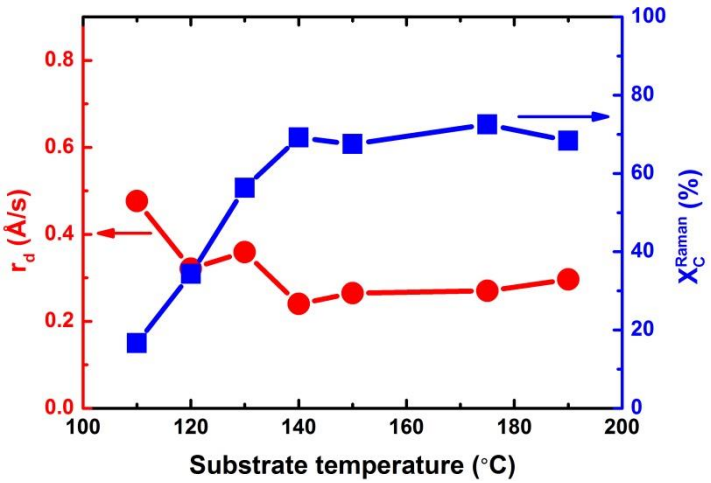

Figure 3.21 Variation of r_d (left axis, red) and X_c^{Raman} (right axis, blue) for seed layers deposited with different temperatures.

To make a complete comparison between the one-step process (see Section 3.2) and the two-step process, Raman spectra of films deposited using both methods are shown in Figure 3.22. At low temperatures, the one-step films show only a large peak around 480 cm^{-1} (Figure 3.22-(a) ~ (c)) and the crystalline phase only starts to appear with increasing temperature (Figure 3.22-(d)). However, for the two-step films, a small shoulder of the crystalline peak can already be observed for substrate temperatures as low as 110 °C (Figure 3.22-(a)). A dominant crystalline phase is seen for temperatures above 120 °C (Figure 3.22-(b)). Figure 3.23 shows the variation of X_c^{Raman} with substrate temperature for the two sets of films. In contrast with the one-step films, an X_c^{Raman} of 17 % is deduced for the two-step film deposited at a substrate temperature of 110 °C, and then a sharp increase up to 68 % at 120 °C is seen. With further increase in temperature, the films continue to be crystalline phase dominant, but only show a small and smooth further increase in X_c^{Raman}. In the end, a value of 70 % is obtained at 190 °C for the two-step films, as compared to a value of 58 % for the one-step films.

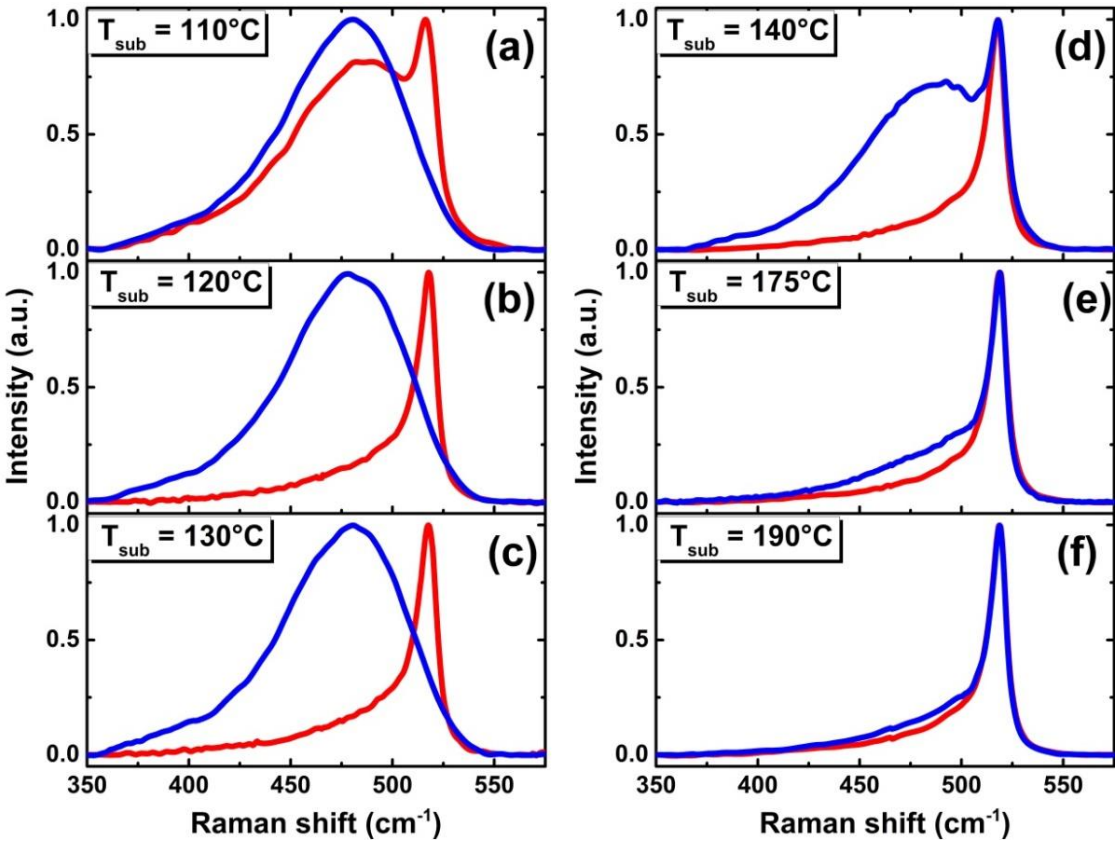

Figure 3.22 Comparison between Raman spectra of films deposited using one-step process (blue) and two-step process (red) with different temperatures.

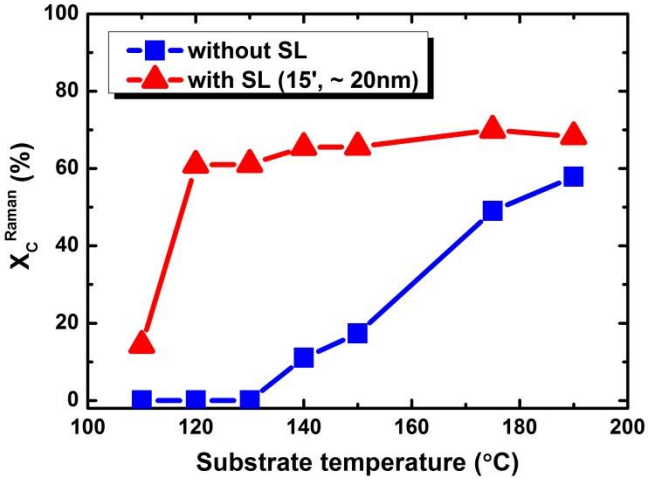

Figure 3.23 Comparison between X_c^{Raman} of films deposited using one-step process (blue) and two-step process (red) with different temperatures.

All these results remind one that the easily prepared highly crystallized seed layer does not only eliminate the amorphous incubation layer, but is also beneficial to achieve a much broader process window for μc-Si:H film deposition by MDECR-PECVD.

In addition, it is worth noting that for all the μc-Si:H films deposited using MDECR-PECVD in our work, regardless of the processing parameters (ion energy condition, substrate temperature, deposition rate, the presence of thin/thick seed layer or not, film thickness), the highest value of X_c^{Raman} is always on the order of 70 %. This is also true for the seed layer itself deposited at a rather low rate. However, much higher values of X_c^{Raman} are usually obtained for the μc-Si:H films deposited using RF-PECVD, and sometimes, even "fully-crystallized" material can be achieved[4]. This naturally leads one to ask:

- Are there any "build-in" limitations for the MDECR-PECVD technique that prevent more crystallized materials (by using the SiF_4-based plasma chemistry)?
- Would any other process parameters like gas flow ratio, the distance between substrate and the plasma source region, etc. change the situation?
- What would be the best choice of the μc-Si:H material deposited by this technique for photovoltaic applications?

To answer these questions, further experimental work should be carried out.

3.6. Summary

In this chapter, we have studied μc-Si:H film deposition from an SiF_4/H_2 plasma chemistry by MDECR-PECVD under low pressure conditions. Due to the high plasma density achievable in a MDECR system, a much higher deposition rate for the μc-Si:H films (~7 Å/s) is achieved compared to RF-PECVD.

Substrate temperature is demonstrated to be an essential parameter for achieving high crystalline volume fraction, presumably due to the thermally-induced enhancement of surface species diffusion. On the other hand, ion energy is also of crucial importance. Insufficient ion bombardment during processing can lead to the existence of inter-connected nanosized voids ("cracks") through the entire film thickness, which are responsible for a less compact film and strong post-deposition oxidation after air exposure. At moderate ion energies, the ion-induced enhancement of surface species diffusion produces a noticeable enhancement in material properties, namely lower void density and better stability. With further increased ion energies, two well-defined IBE thresholds at ~12 eV and ~43 eV are detected, corresponding to the effects of SiF^+-induced surface and bulk atomic displacements, respectively. The smaller grain sizes and rougher surface layers observed are qualitatively linked to SiF^+-induced surface atomic displacement. At higher energies, bulk atomic displacement by SiF^+ can severely suppress the nucleation process, leading to a local amorphization effect on the growing film.

Furthermore, it has been shown that the incubation process is the most challenging step of μc-Si:H growth for this technology. Due to poor surface diffusion for growth species (limited by the high deposition rate), other process parameters such as substrate temperature and ion energy must be carefully controlled to obtain high quality μc-Si:H material.

Finally, we demonstrate that through the use of a seed layer, a two-step process in the MDECR-PECVD system offers the possibility to obtain a μc-Si:H film free from any amorphous incubation layer. By igniting the plasma at a rather low process pressure, a highly crystallized seed layer with well controlled thickness can be easily prepared. The subsequently deposited μc-Si:H main layer, deposited at high deposition rate under high process pressure, can proceed into the crystalline phase growth directly. Based on this method, highly crystallized μc-Si:H films without any amorphous incubation layer are obtained with substrate temperature as low as 120 °C. Moreover, even ~4 nm of seed layer is shown to be effective in obtaining similar results. These results all suggest that the use of MDECR-PECVD and the SiF_4/H_2 plasma chemistry for the growth of μc-Si:H films result in relaxed requirements on process parameters for device quality films. High quality films can be deposited at temperatures as low as 120 °C, which provides a broadened deposition window well-adapted for the fabrication of μc-Si:H thin film solar cells.

Reference

[1] G. Bruno, P. Capezzuto, and G. Cicala, "rf glow discharge of SiF_4-H_2 mixtures: Diagnostics and modeling of the a-Si plasma deposition process", *J. Appl. Phys.*, vol. 69, no. 10, p. 7256, 1991.

[2] S. K. Ram, L. Kroely, P. Bulkin, and P. Roca i Cabarrocas, "Effect of ion energy on structural and electrical properties of intrinsic microcrystalline silicon layer deposited in a matrix distributed electron cyclotron resonance plasma reactor", *Phys. Status Solidi A*, vol. 207, no. 3, p. 591, 2010.

[3] P. Roca i Cabarrocas, P. Bulkin, D. Daineka, T. H. Dao, P. Leempoel, P. Descamps, T. K. D. Meerendré, and J. Charliac, "Advances in the deposition of microcrystalline silicon at high rate by distributed electron cyclotron resonance", *Thin Solid Films*, vol. 516, no. 20, p. 6834, 2008.

[4] J.-C. Dornstetter, S. Kasouit, and P. Roca i Cabarrocas, "Deposition of High-Efficiency Microcrystalline Silicon Solar Cells Using SiF_4/H_2/Ar Mixtures", *IEEE J. Photovolt.*, vol. 3, no. 1, p. 581, 2013

[5] D. Smith, *Thin-Film Deposition: Principles and Practice*. McGraw Hill Professional, 1995.

[6] A. Matsuda, "Thin-Film Silicon -Growth Process and Solar Cell Application-", *Jpn. J. Appl. Phys.*, vol. 43, no. 12R, p. 7909, 2004.

[7] A. Matsuda, "Growth mechanism of microcrystalline silicon obtained from reactive plasmas", *Thin Solid Films*, vol. 337, no. 1-2, p. 1, 1999.

[8] L. Kroely, "Process and material challenges in the high rate deposition of microcrystalline silicon thin films and solar cells by Matrix Distributed Electron Cyclotron Resonance plasma", *PhD thesis*, École Polytechnique, 2010.

[9] D. Humbird and D. B. Graves, "Atomistic simulations of spontaneous etching of silicon by fluorine and chlorine", *J. Appl. Phys.*, vol. 96, no. 1, p. 791, 2004.

[10] B. Giovanni, C. Pio, G. Maria M., and L. Maria, "From amorphous to microcrystalline silicon: Moving from one to the other by halogenated silicon plasma chemistry", *Philos. Mag.*, vol. 89, no. 28-30, p. 2469, 2009.

[11] A. Lacoste, T. Lagarde, S. B Chu, Y. Arnal, and J. Pelletier, "Multi-dipolar plasmas for uniform processing: physics, design and performance", *Plasma Sources Sci. Technol.*, vol. 11, no. 4, p. 407, 2002.

[12] V. A. Godyak and V. I. Demidov, "Probe measurements of electron-energy distributions in plasmas: what can we measure and how can we achieve reliable results?", *J. Phys. D: Appl. Phys.*, vol. 44, no. 23, p. 233001, 2011.

[13] M. N. Islam and S. Kumar, "Influence of crystallite size distribution on the micro-Raman analysis of porous Si", *Appl. Phys. Lett.*, vol. 78, no. 6, p. 715, 2001.

[14] A. Abramov, P. Roca i Cabarrocas, K. Girotra, H. Chen, S. Park, K. Park, J. Huh, J. Choi, C. Kim, and J. H. Souk, "Reliable Characterization of Microcrystalline Silicon Films for Thin

Film Transistor Applications", *Jpn. J. Appl. Phys.*, vol. 47, no. 9R, p. 7308, 2008.

[15] G. Lucovsky, "Relation of Si-H vibrational frequencies to surface bonding geometry", *J. Vac. Sci. Technol.*, vol. 16, no. 5, p. 1225, 1979.

[16] G. Lucovsky, "Chemical effects on the frequencies of Si-H vibrations in amorphous solids", *Solid State Commun.*, vol. 29, no. 8, p. 571, 1979.

[17] J. A. Schaefer, D. Frankel, F. Stucki, W. Göpel, and G. J. Lapeyre, "Chemical shifts of Si-H stretching frequencies at Si(100) surfaces pre-exposed to oxygen in the submonolayer range", *Surf. Sci. Lett.*, vol. 139, no. 2-3, p. L209, 1984.

[18] M. Niwano, J. Kageyama, K. Kurita, K. Kinashi, I. Takahashi, and N. Miyamoto, "Infrared spectroscopy study of initial stages of oxidation of hydrogen-terminated Si surfaces stored in air", *J. Appl. Phys.*, vol. 76, no. 4, p. 2157, 1994.

[19] A. H. M. Smets, T. Matsui, and M. Kondo, "Infrared analysis of the bulk silicon-hydrogen bonds as an optimization tool for high-rate deposition of microcrystalline silicon solar cells", *Appl. Phys. Lett.*, vol. 92, no. 3, p. 33503, 2008.

[20] N. Pham, "Contribution à l'étude des effets liés au transport de l'hydrogène dans les couches minces et les dispositifs à base de silicium amorphe et microcristallin", *PhD thesis*, Université de Reims Champagne-Ardenne, France, 2009.

[21] A. H. Mahan, W. Beyer, D. L. Williamson, J. Yang, and S. Guha, "An explanation for the low-temperature H evolution peak in hydrogenated amorphous silicon films deposited 'on the edge of crystallinity'", *Philos. Mag. Lett.*, vol. 80, no. 9, p. 647, 2000.

[22] B. C. Pan and R. Biswas, "Simulation of hydrogen evolution from nano-crystalline silicon", *J. Non-Cryst. Solids*, vol. 333, no. 1, p. 44, 2004.

[23] S. N. Agbo, S. Dobrovolskiy, G. Wegh, R. A. C. M. M. van Swaaij, F. D. Tichelaar, P. Sutta, and M. Zeman, "Structural analyses of seeded thin film microcrystalline silicon solar cell", *Prog. Photovolt. Res. Appl.*, vol. 22, no. 3, p. 346, 2014.

[24] E. A. G. Hamers, A. Fontcuberta i Morral, C. Niikura, R. Brenot, and P. Roca i Cabarrocas, "Contribution of ions to the growth of amorphous, polymorphous, and microcrystalline silicon thin films", *J. Appl. Phys.*, vol. 88, no. 6, p. 3674, 2000.

[25] B. Kalache, R. Brenot, V. Tripathi, S. Kumar, R. Vanderhaghen, and P. Roca i Cabarrocas, "Effects of Ion Bombardment upon Microcrystalline Silicon Growth", *Solid State Phenom.*, vol. 80-81, p. 71, 2001.

[26] B. Kalache, A. I. Kosarev, R. Vanderhaghen, and P. Roca i Cabarrocas, "Ion bombardment effects on the microcrystalline silicon growth mechanisms and structure", *J. Non-Cryst. Solids*, vol. 299-302, p. 63, 2002.

[27] B. Kalache, A. I. Kosarev, R. Vanderhaghen, and P. Roca i Cabarrocas, "Ion bombardment effects on microcrystalline silicon growth mechanisms and on the film properties", *J. Appl. Phys.*, vol. 93, no. 2, p. 1262, 2003.

[28] S. Lebib and P. Roca i Cabarrocas, "Effects of ion energy on the crystal size and hydrogen bonding in plasma-deposited nanocrystalline silicon thin films", *J. Appl. Phys.*, vol. 97, no. 10, p. 104334, 2005.

[29] G. Bugnon, A. Feltrin, F. Sculati-Meillaud, J. Bailat, and C. Ballif, "Influence of ion bombardment on microcrystalline silicon material quality and solar cell performances", *Proceeding of the 33rd IEEE Photovoltaic Specialists Conference*, San Diego, p. 1, 2008.

[30] A. C. Bronneberg, N. Cankoy, M. C. M. van de Sanden, and M. Creatore, "Ion-induced effects on grain boundaries and a-Si:H tissue quality in microcrystalline silicon films", *J. Vac. Sci. Technol. A: Vac. Surf. Films*, vol. 30, no. 6, p. 061512, 2012.

[31] A. C. Bronneberg, X. Kang, J. Palmans, P. H. J. Janssen, T. Lorne, M. Creatore, and M. C. M. van de Sanden, "Direct ion flux measurements at high-pressure-depletion conditions for microcrystalline silicon deposition", *J. Appl. Phys.*, vol. 114, no. 6, p. 063305, 2013.

[32] J. Palmans, W. M. M. Kessels, and M. Creatore, "Plasma–surface interaction during low pressure microcrystalline silicon thin film growth", *J. Phys. D: Appl. Phys.*, vol. 47, no. 22, p. 224003, 2014.

[33] A. Michelmore, J. D. Whittle, and R. D. Short, "The importance of ions in low pressure PECVD plasmas", *Plasma Phys.*, vol. 3, p. 3, 2015.

[34] B. Bruneau, J. K. Wang, J.-C. Dornstetter, and E. V. Johnson, "Growth mechanisms study of microcrystalline silicon deposited by SiH_4/H_2 plasma using tailored voltage waveforms", *J. Appl. Phys.*, vol. 115, p. 084901, 2014.

[35] D. K. Brice, J. Y. Tsao, and S. T. Picraux, "Partitioning of ion-induced surface and bulk displacements", *Nucl. Instrum. Methods Phys. Res. Sect. B Beam Interact. Mater. At.*, vol. 44, no. 1, p. 68, 1989.

[36] B. Bruneau, M. Lepecq, J. Wang, J.-C. Dornstetter, J.-L. Maurice, and E. V. Johnson, "Effect of Ion Energy on Microcrystalline Silicon Material and Devices: A Study Using Tailored Voltage Waveforms", *IEEE J. Photovolt.*, vol. 4, no. 6, p. 1354, 2014.

[37] S. Kasouit, P. Bulkin, L. Kroely, and P. Roca i Cabarrocas, "SiH_4 and SiF_4 dissociation in MDECR plasmas and consequences for material properties", in *Bulletin of the American Physical Society (63rd GEC, Paris)*, vol. 55, no. 7, 2010.

[38] J. Koh, A. S. Ferlauto, P. I. Rovira, C. R. Wronski, and R. W. Collins, "Evolutionary phase diagrams for plasma-enhanced chemical vapor deposition of silicon thin films from hydrogen-diluted silane", *Appl. Phys. Lett.*, vol. 75, no. 15, p. 2286, 1999.

[39] H. Fujiwara, M. Kondo, and A. Matsuda, "Real-time spectroscopic ellipsometry studies of the nucleation and grain growth processes in microcrystalline silicon thin films", *Phys. Rev. B*, vol. 63, no. 11, p. 115306, 2001.

[40] M. N. van den Donker, B. Rech, F. Finger, W. M. M. Kessels, and M. C. M. van de Sanden, "Highly efficient microcrystalline silicon solar cells deposited from a pure SiH_4 flow", *Appl. Phys. Lett.*, vol. 87, no. 26, p. 263503, 2005.

[41] J. H. Zhou, K. Ikuta, T. Yasuda, T. Umeda, S. Yamasaki, and K. Tanaka, "Growth of amorphous-layer-free microcrystalline silicon on insulating glass substrates by plasma-enhanced chemical vapor deposition", *Appl. Phys. Lett.*, vol. 71, no. 11, p. 1534, 1997.

[42] O. Vetterl, M. Hülsbeck, J. Wolff, R. Carius, and F. Finger, "Preparation of microcrystalline silicon seed-layers with defined structural properties", *Thin Solid Films*,

vol. 427, no. 1-2, p. 46, 2003.

[43] H. Yue, A. Wu, X. Zhang, and T. Li, “New two-step growth of microcrystalline silicon thin films without incubation layer”, *J. Cryst. Growth*, vol. 322, no. 1, p. 1, 2011.

[44] Y. M. Li, L. Li, J. A. A. Selvan, A. E. Delahoy, and R. A. Levy, “Effects of seeding methods on the fabrication of microcrystalline silicon solar cells using radio frequency plasma enhanced chemical vapor deposition”, *Thin Solid Films*, vol. 483, no. 1-2, p. 84, 2005.

[45] X. H. Zhu, G. H. Chen, and M. S. Zheng, “Influence of the deposition pressure on the preparation of μc-Si:H thin films in hot-wire-assisted MWECR-CVD system”, *Vacuum*, vol. 83, no. 2, p. 386, 2008.

[46] K. Nakamura, K. Yoshino, S. Takeoka, and I. Shimizu, “Roles of Atomic Hydrogen in Chemical Annealing”, *Jpn. J. Appl. Phys.*, vol. 34, no. 2R, p. 442, 1995.

[47] S. Sriraman, S. Agarwal, E. S. Aydil, and D. Maroudas, “Mechanism of hydrogen-induced crystallization of amorphous silicon”, *Nature*, vol. 418, no. 6893, p. 62, 2002.

[48] J.-C. Dornstetter, B. Bruneau, P. Bulkin, E. V. Johnson, and P. Roca i Cabarrocas, “Understanding the amorphous-to-microcrystalline silicon transition in SiF_4/H_2/Ar gas mixtures”, *J. Chem. Phys.*, vol. 140, no. 23, p. 234706, 2014.

Chapter 4 Novel process control for silicon thin film deposition using Tailored Voltage Waveforms

Contents

In this chapter, a novel RF excitation technique – Tailored Voltage Waveforms – has been applied for the deposition of silicon thin films (a-Si:H and μc-Si:H). Benefiting from the semi-independent control over the plasma properties (ion flux and ion energy) via the electrical asymmetry effect, the impact of ion energy on material deposition is investigated, even under relatively high process pressure. Based on the experimental results, we attempt to relate the modification of the surface processes, as well as the quality of the resulting materials and photovoltaic devices, to the plasma properties controlled through the utilization of Tailored Voltage Waveforms.

4.1. Tailored voltage waveforms (TVW)

4.1.1. Ion flux-energy coupling in CCP processes

RF-CCP discharges are currently widely applied for semiconductor processing in industry. In many of these applications, the plasma properties (such as concentrations of precursors, fluxes of radicals, impact energies of impinging ions, etc.) are of crucial importance in influencing the plasma-surface interactions. Obviously then, the surface processes governed by these interactions can be considerably impacted by the variations of those plasma properties. In particular, in the cases of thin film deposition and etching, the ion flux (determined by the plasma density) towards the substrate and the distribution of ion energy are two key issues in determining the resulting material and device properties, and many of them have contradictory plasma requirements[1,2,3]. Specifically, selective etching process typically requires anisotropic impinging ions with high kinetic energies[4,5]. On the other hand, for deposition process, high ion flux (or neutral radical flux) is usually preferable for achieving high deposition rate and reducing process time, but the ion energy should be necessarily kept low to prevent material sputtering[6]. Therefore, knowledge and control over the plasma properties are highly desirable for the optimization of such surface processes.

This leads to a dilemma for industrially relevant CCP processes. Variations in controllable process conditions like gas pressure and power injection usually result in a global changes in many plasma parameters.

As a demonstration of this, Figure 4.1 shows the relationship between ion flux and ion energy for an Ar plasma operated at 15 mTorr using different excitation frequencies[7], where the

[1] L. Martinu, et al., *J. Vac. Sci. Technol. A: Vac. Surf. Films*, **12(4)**: 1360 (1994).
[2] B. Kalache, et al., *J. Non-Cryst. Solids*, **299-302, Part 1**: 63 (2002).
[3] J. Palmans, et al., *J. Phys. D: Appl. Phys.*, **47(22)**: 224003 (2014).
[4] M. A. Lieberman, et al., *Principles of Plasma Discharges and Materials Processing*, Wiley (2005).
[5] P. Chabert, et al., *Physics of Radio-Frequency Plasmas*, Cambridge University Press (2011).
[6] A. Matsuda, *Thin Solid Films*, **337(1-2)**: 1 (1999).
[7] A. Perret, et al., *Appl. Phys. Lett.*, **86(2)**: 021501 (2005).

experimental data (solid symbols) shows a good agreement with the theoretical values deduced from the transmission line model (solid lines) proposed by Chabert *et al*[8]. Indeed, for a given frequency, higher ion flux can be achieved by increasing the power injection (applied voltage), but the ion energy is also increased accordingly. As an example, considering a process that requires the ion energy below 500 eV (indicated by the top dashed line), the ion flux would be limited below 0.15 mA/cm^2 when using the 13.56 MHz excitation. However, at higher frequency of 81.36 MHz, this limitation would be largely relaxed, as higher ion flux can be achieved while still keeping the ion energy low. However, if an etching process is considered, ion energies in excess of 100 eV become necessary, and the single high frequency excitation turns to be not appropriate since the ion energy always stays at low values. In addition, non-uniformity issues become significant for high frequency discharges, especially for large area applications[9], due to the significant electromagnetic effects such as standing waves and skin effects[4,10,11]. In short, independent parameter control in single-frequency discharges is intrinsically difficult due to such strong ion flux-energy coupling.

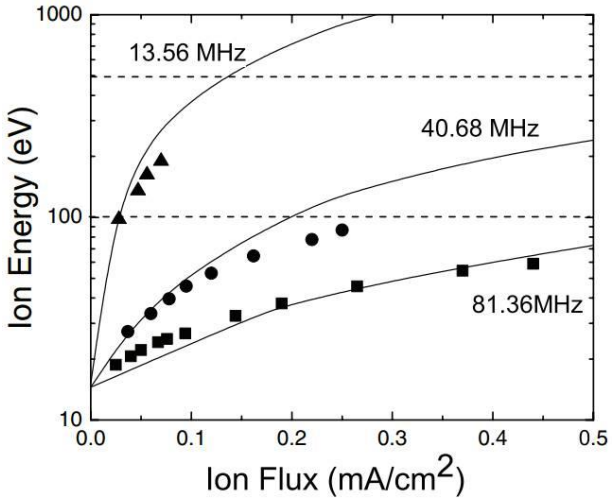

Figure 4.1 Evolution of ion energy as function of ion flux for an Ar plasma (15 mTorr), at discharge center, for three different excitation frequencies. Solids lines represent the theoretical values deduced from the transmission line model described by Chabert *et al*[8]. Extracted from Ref. 7.

Complementing single-frequency discharges, the utilization of "classical" dual-frequency excitation sources offers a solution. In this case, the voltage supply is injected at two widely separated frequencies (such as 2 MHz/50 kHz, 27.12 MHz/2 MHz, 160 MHz/13.56 MHz, etc.). The high frequency component is often responsible for the electron heating via the sheath motion, as it can indeed produce a much higher plasma density compared to that achievable through the lower frequency excitation (see Figure 4.1). Since the ion energy at the substrate is generally determined by the time-averaged voltage drop within the plasma sheath, it can therefore be semi-independently controlled by an appropriate choice of the voltage amplitude for the low-frequency source. Usually, a much higher amplitude for the low frequency voltage source is

[8] P. Chabert, et al., *Phys. Plasmas*, **11(5)**: 1775 (2004).
[9] A. Shah, et al., *MRS Online Proc. Libr. Arch.*, **258** (1992).
[10] A. Perret, et al., *Appl. Phys. Lett.*, **86(2)**: 021501 (2005).
[11] L. Sansonnens, et al., *Plasma Sources Sci. Technol.*, **6(2)**: 170 (1997).

used, although this has a limited impact on the plasma density due to the lower frequency.

This idea was first proposed by Goto *et al*[12] in a study of SiO_2 plasma etching. In their work, the authors found that by combining low and high frequency excitations, the IBE at the substrate can be effectively controlled without affecting the plasma density. To obtain further control over the plasma properties, one can also introduce a phase shift between the two frequencies. In a study of $Ar/CF_4/N_2$ plasma excited by a 27.12 MHz/2 MHz dual frequency voltage source[13], it was found that the peak position of the ion energy distribution functions for CF_3^+ can be varied with the low frequency component phase.

Such dual-frequency excitation sources provide a practical solution for the independent control of ion flux and ion energy, as has been extensively reported in literature and widely used in industrial applications[14,15,16]. However, this technique still has its limitations, as the issue of frequency coupling between the two components (particularly the electron heating and temporal ionization dynamics) has been identified by both analytical modeling [17] and numerical simulations[15,18,19], and also confirmed by experimental studies[20,21]. Furthermore, the emission of secondary electrons could make the frequency coupling effect more significant[18]. Therefore, a more elegant solution is needed to meet all given process requirements. A more recent excitation technique using the multi-frequency TVW has been proposed to do so, and it will be introduced in detail in the next section.

4.1.2. Electrical asymmetry effect

In contrast to the "classical" dual-frequency excitation source that necessarily requires the two components to be widely separated, better control over the plasma properties can be realized through the utilization of TVW excitation, wherein the voltage waveform consists of a series of consecutive harmonics with individually adjustable amplitudes and phases. This idea was first proposed by the group at the Ruhr-Universität Bochum in 2008 to achieve the separate control over the ion flux and ion energy in CCP discharges[22]. By making use of voltage waveforms with two phase-shifted frequencies:

$$\mathrm{V(t)} = V_1\, cos(\omega t + \varphi) + V_2\, cos(2\omega t) \tag{4.1}$$

where V_1 and V_2 are the voltage amplitudes for the applied frequencies, ω is the angular frequency corresponding to the fundamental frequency, and φ is the phase shift between the two components, the authors found that an electrically asymmetric plasma response can be formed, regardless of the

[12] H. Goto, et al., *Jpn. J. Appl. Phys.*, **29(12A)**: L2395 (1990).
[13] V. Georgieva, et al., *Phys. Rev. E*, **69(2)**: 026406 (2004).
[14] H. Löwe, et al., *J. Vac. Sci. Technol. A: Vac. Surf. Films*, **9(6)**: 3090 (1991).
[15] P. C. Boyle, et al., *J. Phys. D: Appl. Phys.*, **37(5)**: 697 (2004).
[16] Z. Donkó, et al., *Jpn. J. Appl. Phys.*, **45(10S)**: 8151 (2006).
[17] M. M. Turner, et al., *Phys. Rev. Lett.*, **96(20)**: 205001 (2006).
[18] Z. Donkó, et al., *Appl. Phys. Lett.*, **97(8)**: 081501 (2010).
[19] A. Derzsi, et al., *J. Phys. D: Appl. Phys.*, **46(48)**: 482001 (2013).
[20] D. O'Connell, et al., *Appl. Phys. Lett.*, **93(8)**: 081502 (2008).
[21] J.-P. Booth, et al., *Plasma Sources Sci. Technol.*, **19(1)**: 015005 (2010).
[22] B. G. Heil, et al., *J. Phys. D: Appl. Phys.*, **41(16)**: 165202 (2008).

reactor geometry. Simply speaking, a V_{DC} can be generated in such discharge even if it is operated in a geometrically symmetric reactor. Moreover, as a first approximation, an almost continuous scanning of V_{DC} can be achieved just by tuning φ, while at the same time, other process parameters are influenced very little. This is known as the Electrical Asymmetry Effect. Herein, we will give a brief description about the generation of V_{DC}; for a comprehensive understanding about this effect, one is referred to the original theoretical work[22] and extensive reviews[23,24].

According to Kirchhoff's voltage law for a CCP discharge[23], whatever the voltage waveform applied, the requirement of voltage balance should be satisfied as

$$\mathrm{V(t) + V_{DC} - V_{sp}(t) - V_{sg}(t) - V_b(t) = 0} \tag{4.2}$$

where $\mathrm{V(t)}$ is the applied voltage, $\mathrm{V_{sp}(t)}$ and $\mathrm{V_{sg}(t)}$ are the time-dependent sheath voltage drops close to the powered and grounded electrode, and $\mathrm{V_b(t)}$ is the time-dependent voltage drop across the bulk plasma. In general, changes in the two sheath potentials are 180º out of phase, i.e., when the voltage drop across one sheath is at a maximum, a floating potential will be observed on the counter electrode. In this case, when the maximum voltage $\mathrm{V_{max}}$ or minimum voltage $\mathrm{V_{min}}$ is applied to the powered electrode, the voltage balance in Equation (4.2) can be expressed as

$$\mathrm{V_{max} + V_{DC} = V_{sp}^{f} + V_{sg}^{max} + V_b} \tag{4.3}$$

and

$$\mathrm{V_{min} + V_{DC} = V_{sp}^{max} + V_{sg}^{f} - V_b} \tag{4.4}$$

where $\mathrm{V_{sp}^{max}}$ and $\mathrm{V_{sg}^{max}}$ are the maximum voltage drops across the powered and grounded sheaths, and $\mathrm{V_{sp}^{f}}$, $\mathrm{V_{sg}^{f}}$, and $\mathrm{V_b}$ are the corresponding floating potentials and voltage drop in the bulk plasma. To better illustrate such voltage balance in the system, Figure 4.2 shows the potential profiles corresponding to Equation (4.3) and (4.4). Although the waveform is assumed to be a sinusoid, these schematics would hold whatever the waveform considered.

By introducing a symmetry parameter ε defined by the ratio of sheath drop maxima

$$\varepsilon = \left| \frac{\mathrm{V_{sg}^{max}}}{\mathrm{V_{sp}^{max}}} \right| \tag{4.5}$$

and combining Equation (4.3) and (4.4), $\mathrm{V_{DC}}$ can analytically expressed as

$$\mathrm{V_{DC}} = -\frac{\mathrm{V_{max}} + \varepsilon \mathrm{V_{min}}}{1+\varepsilon} + \frac{\mathrm{V_{sp}^{f}} + \varepsilon \mathrm{V_{sg}^{f}}}{1+\varepsilon} + \frac{1-\varepsilon}{1+\varepsilon}\mathrm{V_b} \tag{4.6}$$

Equation (4.6) gives the general formula for $\mathrm{V_{DC}}$, in which the second and third terms, i.e., the floating potential and bulk plasma voltage drop, can be very small in many practical cases. In such cases, the expression can be simplified as

[23] J. Schulze, et al., *Plasma Sources Sci. Technol.*, **20(1)**: 015017 (2011).
[24] T. Lafleur, *Plasma Sources Sci. Technol.*, **25(1)**: 013001 (2016).

$$V_{DC} = -\frac{V_{max} + \varepsilon V_{min}}{1+\varepsilon} \tag{4.7}$$

The remaining issue is how to quantify the relationship between the symmetry parameter ε with the physical properties of the discharge. Based on the analytical model described in the original work[22], the symmetry parameter ε in many practical cases can be expressed as

$$\varepsilon = \left(\frac{A_p}{A_g}\right)^2 \frac{\bar{n}_{sp}}{\bar{n}_{sg}} \tag{4.8}$$

where A_p and A_g are the surface areas of the powered and grounded electrodes, respectively, and $\bar{n}_{sp}$ and $\bar{n}_{sg}$ are the corresponding mean sheath ion densities. This means that the symmetric parameter is related with the electrode surface area ratio and the relative sheath ion density. From Equation (4.8), one can note that V_{DC} can be generally derived by considering the waveform shape and the reactor geometry.

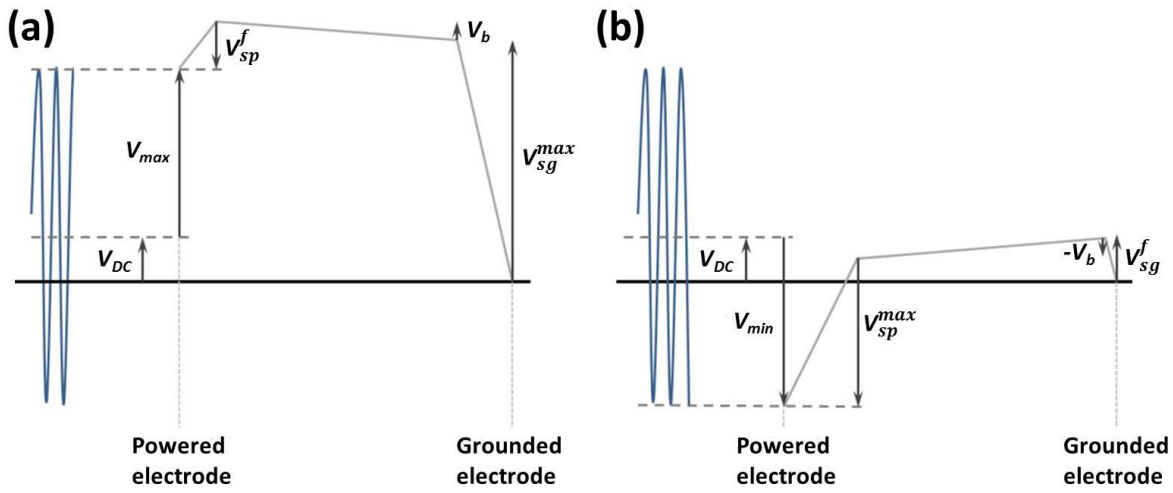

Figure 4.2 Schematic of potential profile in CCP system when applied voltage is at its (a) maximum and (b) minimum. The position of the powered and grounded electrodes are indicated. The up-, or down-arrows indicate that the quantity is positive or negative, respectively. Extracted from Ref. 25.

4.1.3. Ion flux-energy decoupling

For a single-frequency discharge where the electrode surface ratio is close to unity (as is often the case in industry), V_{DC} is determined by the relative sheath ion densities. In practice, any single-frequency discharge is essentially symmetric in terms of spatial distribution, i.e., $\bar{n}_{sp} \approx \bar{n}_{sg}$, thus giving a symmetry parameter $\varepsilon \approx 1$. Therefore, independent control over the absolute value of V_{DC} is very limited, and equally so for IBE_{max}, during processing.

The use of TVW can provide an opportunity in this situation. Figure 4.3-(a) shows two examples of two-frequency excitation as described by Equation (4.1). As one can see, the

[25] B. Bruneau, *PhD thesis*, École Polytechnique (2015).

maximum and minimum excursions of the applied voltage are different for these waveforms ($V_{max} \neq |V_{min}|$). Therefore, according to Equation (4.7), **a non-zero V_{DC} can be formed even in a geometrically symmetric reactor**. It can also be noted from Figure 4.3-(a) that the relative magnitude between V_{max} and V_{min} differs from one waveform to another. This amplitude asymmetry allows one to control the absolute value of V_{DC}. Indeed, a continuous variation of V_{DC} is achieved via the change of φ in Equation (4.1), as shown in Figure 4.3-(b). Therefore, this original theoretical work successfully demonstrated the existence of the electrical asymmetry effect, and predicted the independent control over the ion energy while leaving other plasma parameters effectively untouched. However, these analytical models gave no direct evidence that the ion fluxes towards the electrodes are necessarily constant when φ is varied.

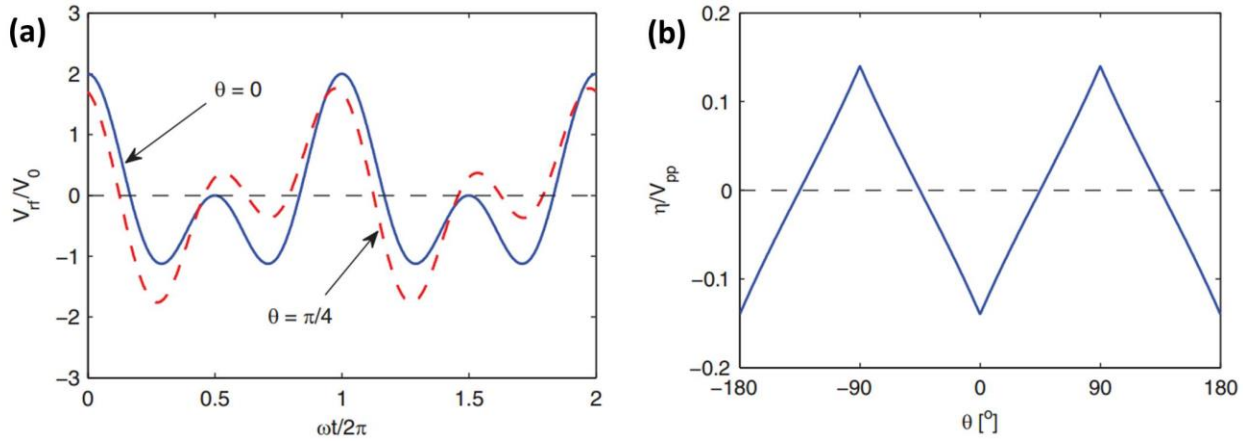

Figure 4.3 (a) Example of two-frequency voltage waveforms (normalized) in one fundamental period based on Equation (4.1) with φ equaling to 0 (blue solid) and π/4 (red dash). (b) Normalized V_{DC} plotted as a function of φ with ε = 1. Extracted from Ref. 24.

In turn, this was first verified by a self-consistent particle-in-cell (PIC) simulation done by Donkó *et al* in Ref. 26, where an Ar plasma excited by the voltage waveform based on Equation (4.1) with a fundamental frequency of 13.56 MHz was investigated. The results presented a good agreement with previous results[22], in that a (linearly) controllable V_{DC} can be formed in a geometrically symmetric reactor. More importantly, the authors found that the ion flux stayed roughly constant within ±5 % when φ was varied. This clearly demonstrated that ion flux-energy decoupling can be achieved using TVW via the electrical asymmetry effect. In the same year, this work was quickly followed by the first experimental demonstration for this effect published by Schulze *et al* in Ref. 27, where similar results were obtained for the Ar plasma operated under different process pressures.

All the above description about the electrical asymmetry effect are all based on two-frequency excitations, whereas such effects still hold true for voltage waveforms containing any number of consecutively harmonics of the fundamental frequency, as expressed by

$$V(t) = V \sum_{k=1}^{n} cos(k\omega t + \varphi) \tag{4.9}$$

[26] Z. Donkó, et al., *J. Phys. D: Appl. Phys.*, **42(2)**: 025205 (2009).
[27] J. Schulze, et al., *J. Phys. D: Appl. Phys.*, **42(9)**: 092005 (2009).

here n is the number of frequencies, and each frequency has an identical voltage amplitude of V. However, by further tuning the voltage amplitude of each frequency, the optimized voltage waveform giving the maximum electrical asymmetry effect was found to be

$$\mathrm{V(t)} = A\sum_{k=1}^{n}\frac{n-k+1}{n}cos(k\omega t + \varphi) \tag{4.10}$$

where A is the voltage amplitude prefactor (first proposed by Schulze *et al* in Ref. 23). The voltage waveforms with optimized amplitudes present globally greater differences in the relative magnitudes of positive and negative excursions. As a consequence, the control over the DC self-bias in a greater range can be achieved. Figure 4.4 shows some examples for such voltage waveforms with n set to four: a phase shift φ = 0 gives a *peaks* type waveform, while φ = 0.5π gives a *sawtooth* type and φ = π gives a *valleys* type. One can further increase it above π up to 2π. In that case, another set of voltage waveforms having the same waveshape will be obtained, but the positive and negative excursions are reversed.

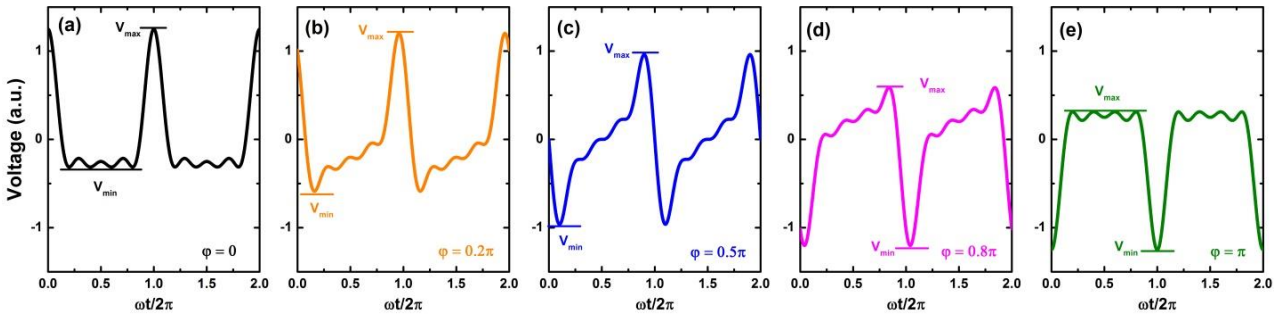

Figure 4.4 Voltage waveforms according to Equation (4.10) at different φ (in the range of 0- π), with n set to four. V_{min} and V_{max} represent the minimum and maximum applied voltage.

All the above early stage studies, including analytical models, numerical simulations as well as experimental demonstrations, have shown the great potential of TVW in providing an elegant solution for the ion flux-energy decoupling in the CCP discharges. By making use of the amplitude asymmetry in the applied voltage, a semi-independent control over the ion energy can be achieved. These observations have subsequently attracted a considerable research interest, and have brought a great helpfulness in understanding the plasma physics.

Nevertheless, recalling that the aim of proposing such a novel approach is to control the plasma properties, this approach must be verified for industrially relevant plasma processes. Towards this goal, a number of studies on the deposition of silicon thin films for photovoltaic applications were carried out by the LPICM and LPP groups at the École Polytechnique (Palaiseau) by using the multi-frequency TVW based on Equation (4.10)[28,29,30,31,32]. In those studies, it was found that control over the ion energy via the amplitude asymmetry effect can be helpful to understand and control µc-Si:H film growth morphology, material properties, and the resulting solar cell device

[28] E. V. Johnson, et al., *J. Phys. D: Appl. Phys.*, **43(41)**: 412001 (2010).
[29] E. V. Johnson, et al., *MRS Online Proc. Libr. Arch.*, **1339** (2011).
[30] E. V. Johnson, et al., *Appl. Phys. Lett.*, **100(13)**: 133503 (2012).
[31] E. V. Johnson, et al., *Jpn. J. Appl. Phys.*, **51(8S1)**: 08HF01 (2012).
[32] E. V. Johnson, et al., *J. Non-Cryst. Solids*, **358(17)**: 1974 (2012).

performance. This work was followed by results from other groups[33,34,35] using two-frequency excitations (Equation (4.9)). These works additionally argued that the electrical asymmetry effect could also be helpful to solve the issue of deteriorated uniformity in the deposition process with increasing excitation frequencies.

4.2. Deposition of μc-Si:H film using SiF_4/H_2/Ar plasma chemistry

To further advance our understanding of the TVW technique when applied to deposition processes, in this section, we first present the study of μc-Si:H film deposition using TVW (Equation (4.10)), wherein the material structural and electronic characteristics are studied. In the second part of this chapter, the performance of the resulting single-junction μc-Si:H solar cells in a *n-i-p* configuration is examined.

TVW excitation setup

The control system for supplying TVW to the powered electrode is shown in Figure 4.5. The ideal voltage waveshape is set by the computer and then produced by the programmable arbitrary function generator (AFG). After amplification via the broadband amplifier, the voltage waveform is sent to a low-pass filter, and then passes through a coupling capacitor (allowing a DC self-bias voltage to form). At the powered electrode feedthrough, the voltage waveform is monitored using a high-voltage probe with an oscilloscope.

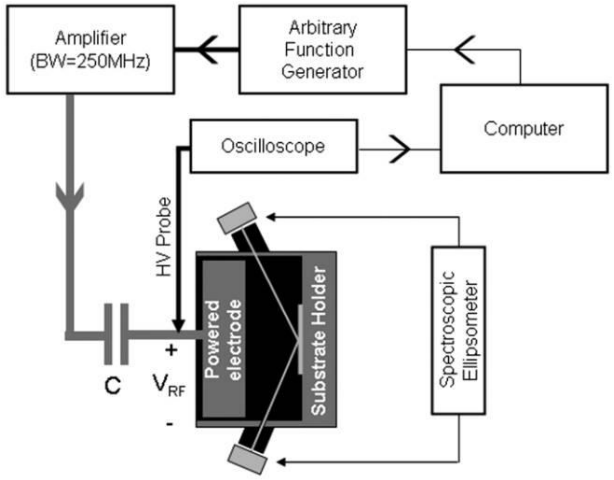

Figure 4.5 Diagram of TVW excitation control system. Extracted from Ref. 28.

Because of the dispersion of RF cables, the frequency dependent gain of amplifier, and the plasma nonlinearities, in practice, the voltage waveform will be different from the desired signal. Therefore, a corrective feedback system similar as described by Patterson *et al* in Ref. 36 is

[33] D. Hrunski, et al., *Thin Solid Films*, **532**: 56 (2013).
[34] D. Hrunski, et al., *Vacuum*, **87(0)**: 114 (2013).
[35] E. Schüngel, et al., *Thin Solid Films*, **574**: 60 (2015).
[36] M. M. Patterson, et al., *Plasma Sources Sci. Technol.*, **16(2)**: 257 (2007).

applied. The Fourier transform for each individual frequency component is performed and compared with the desired signal. Accordingly, adjustments of both amplitude and phase shift in initial signal are done to so that the target voltage waveform at the electrode is achieved.

Matching units

Note that no matching network has been used in our experiments, which means that a large fraction of the power is reflected (90-95%)[37] during processing. Indeed, the absence of suitable impedance matching would make the industrial application of this multi-frequency excitation source a technical non-starter.

In some early experimental work on the electrical asymmetry effect with the power supply based on Equation (4.1), a "classical" dual-frequency impedance matching network has been used[27,38,39]. However, the predicted performance gain for the electrical asymmetry effect by using multi-frequency (more than two) excitations was not clear[23,40]. A novel matching network was therefore proposed by Franek *et al*[41]. This system is based on a series of phase-locked RF generators corresponding to each consecutive harmonic. Each of these components is matched separately and then is combined together to excite the plasma. Based on this approach, an RF power supply with up to three frequencies has been tested experimentally[42,43]. However, the requirements of significant hardware (separate RF generators, filters, matching units) could be a big handicap to make this approach the one adopted by industry.

Another feasible solution using a simpler system with only one broadband RF generator has been proposed by our group[44]. However, further experimental work still need be performed. Therefore, we note that although no matching network was used to achieve the scientific results of this thesis, such a multi-frequency matching unit is indeed under development to enable the multi-frequency TVW excitation system in the future.

4.2.1. Estimation of ion energy

In contrast to the MDECR plasma discussed in Chapter 3, the RF source excited plasma has more collisional sheaths due to the higher process pressure, i.e., the mean free path is less than the sheath width. Consequently, a broad distribution of ion energies will be obtained, and only a small fraction of ions will arrive at the electrode with IBE_{max} during processing. This therefore prevents one from making precise conclusions concerning the impact of ion energy on the silicon thin film deposition in a RF-PECVD process. A preferable way has been proposed to conduct studies on this topic, namely using the concept of energy delivered per deposited Si atom (knowing the ion/atom

[37] T. Lafleur, et al., *Rev. Sci. Instrum.*, **84(1)**: 015001 (2013).
[38] U. Czarnetzki, et al., *J. Phys. Conf. Ser.*, **162(1)**: 12010 (2009).
[39] E. Schüngel, et al., *J. Appl. Phys.*, **112(5)**: 053302 (2012).
[40] A. Derzsi, et al., *Plasma Sources Sci. Technol.*, **22(6)**: 065009 (2013).
[41] J. Franek, et al., *Rev. Sci. Instrum.*, **86(5)**: 053504 (2015).
[42] B. Berger, et al., *J. Appl. Phys.*, **118(22)**: 223302 (2015).
[43] S. Brandt, et al., *Plasma Sources Sci. Technol.*, **25(4)**: 045015 (2016).
[44] E. V. Johnson, et al., *European patent*, EP 2675064 (A1) (2013).

arrival ratio)[45,46], or the mean kinetic energy of ions[3].

Nevertheless, it has been recently reported that the properties of RF-PECVD silicon thin film can still be largely influenced by the small fraction of ions arriving with IBE_{max}[47,48] (TVW have been used as the excitation source in such studies). For µc-Si:H films deposited from the SiH_4/H_2 plasma chemistry with a 850 mTorr process pressure, the ion-related interactions were found to be responsible for the modification of film growth dynamics as well as the surface morphology. Two well-defined IBE_{max} thresholds at 30 eV and 70 eV, corresponding to the SiH_x^+-induced bulk atomic displacement and H_3^+-induced surface atomic displacement, were detected. Similar conclusions were also obtained concerning low-temperature silicon epitaxy from the same plasma chemistry. A critical threshold of IBE_{max} at 30 eV (SiH_x^+-induced surface displacement) has also been observed, as the epitaxy can no longer be sustained once the IBE_{max} is above this value[49].

As previously stated, the TVW technique can provide an elegant solution for ion flux-energy decupling in an RF plasma; the remaining issue is how should one link the changes in the plasma properties with the processing results quality. Firstly, one must clearly quantify the value of $\tilde{V}_{pl}$. However, the estimation of $\tilde{V}_{pl}$ by Equation (2.3) is no longer suitable because of the non-sinusoidal waveforms. A more general approach to determine the $\tilde{V}_{pl}$ has been proposed in Ref. 47. Using the same assumptions as for Equation (2.3), the potential of the bulk plasma can be expressed as

$$V_{pl}(t) = aV(t) + \tilde{V}_{pl} \tag{4.11}$$

where a is positive and constant. Relating Equation (4.11) to Equation (4.3) and (4.4), we get

$$0 = aV_{min} + \tilde{V}_{pl} \tag{4.12}$$

$$V_{max} + V_{DC} = aV_{max} + \tilde{V}_{pl} \tag{4.13}$$

Solving Equation (4.13) with a from Equation (4.12),

$$\tilde{V}_{pl} = \frac{|V_{min}|}{|V_{min}|+V_{max}}\left(\frac{V_{max}}{|V_{min}|+V_{max}}V_{PP} + V_{DC}\right), \text{ with } V_{PP} = |V_{min}| + |V_{max}| \tag{4.14}$$

Therefore, $\tilde{V}_{pl}$ can be approximately estimated by knowing V_{PP}, V_{DC}, and the waveshape. Interestingly, if one considers a single-frequency discharge where $V_{max} = -V_{min}$, Equation (2.3) is actually a simplification of Equation (4.14). The validity of this expression for the estimation of $\tilde{V}_{pl}$, i.e., IBE_{max}, has been verified by PIC simulation for an Ar plasma. However, for the case of multi-gas plasmas like the SiH_4/H_2 plasma that is commonly used for silicon thin film deposition, the error made in the estimation remains at a relative low value (several volts). Further details can be found in Ref. 25.

[45] A. H. M. Smets, et al., *J. Non-Cryst. Solids*, **352(9)**: 937 (2006).
[46] A. C. Bronneberg, et al., *J. Vac. Sci. Technol. A: Vac. Surf. Films*, **30(6)**: 061512 (2012).
[47] B. Bruneau, et al., *J. Appl. Phys.*, **115**, 084901 (2014).
[48] B. Bruneau, et al., *IEEE J. Photovolt.*, **4(6)**: 1354 (2014).
[49] B. Bruneau, et al., *IEEE J. Photovolt.*, **4(6)**: 1361 (2014).

4.2.2. μc-Si:H deposition under different ion energy conditions

Now that it is possible to make a reasonable estimation of $\tilde{V}_{pl}$, we can try to study the impact of ion energy on the growth of μc-Si:H films. A series of films were deposited using TVW. Different types of voltage waveforms with constant V_{PP} of 250 V were used, and φ was varied in the range of 0-2π. For the sake of simplicity, hereafter, the films deposited with φ in the range of 0-π will be referred as the "0-π" films, and correspondingly, the films deposited with φ in the range of π-2π will be referred as the "π-2π" films.

The deposition has been performed on Corning "Eagle" glass, with co-deposited films on c-Si wafer for further characterization. The deposition times were adjusted to keep the films' thicknesses around 300 nm. The process conditions were chosen to lie in the "SiF_4-limited" regime to achieve the growth of μc-Si:H, as shown in Table 4.1. For the electrical characterizations, coplanar aluminum contacts with 1 mm gap were evaporated on top of the films deposited on glass substrate. All the samples were annealed at 125 ºC for one hour after contact deposition.

Table 4.1 Process conditions for μc-Si:H film deposition using TVW with varying φ.

φ	V_{PP}	P	d_i	T_{sub}	T_{rf}	SiF_4	H_2	Ar
π	V	Torr	cm	ºC	ºC	sccm	sccm	sccm
0-2	250	3	2	150	80	3.6	5	88

The value of V_{DC} was monitored during processing, and the corresponding IBE_{max} was estimated through Equation (4.17). Figure 4.6 shows the variation of V_{DC} and IBE_{max} as a function of φ. Due to the reactor geometrical asymmetry, large negative values of V_{DC} are usually observed (Figure 4.6-(a)). With φ increasing from 0 to π, V_{DC} presents an almost linear increase, whereas an opposite trend is observed for that with φ ranging from π to 2π. Accordingly, control over the IBE_{max} between ~20 eV and ~70 eV (with a similar trend as that for V_{DC}) is obtained, as shown in Figure 4.6-(b). Figure 4.6-(b) also provides the r_d of these films. On the whole, r_d shows a "W"-shape trend with two maxima at φ = 0 (or 2π, *peaks*) and φ = π (*valleys*). The reason for such a dependency on φ should originate from the φ-dependent power coupling when V_{PP} is kept constant[47], as it also been observed in previous experimental work and confirmed numerically.

However, upon close inspection, this "W"-shape is not actually symmetric. One can note that the "0-π" films always present higher deposition rates than their counterparts, as highlighted by the gray dashed line of Figure 4.6-(b). This is especially noticeable for the cases using the special group of *sawtooth* waveforms (φ = 0.5π or 1.5π)[50]. A r_d of 3.8 Å/s is at φ = 0.5π, while a significant lower value of 2.1 Å/s is observed at φ = 1.5π (with a waveform opposite to that at φ = 0.5π). The difference in ion energies cannot be the main reason for this, as similar IBE_{max} values (~40-50 eV) are found for both cases. To better understand this discrepancy in deposition rate, one should consider the slope asymmetry effect generated through the utilization of the special group of *sawtooth* waveforms. Further discussions along these lines will be presented in Chapter 5, and herein we will focus on the effect of ion energy on the process outcomes.

[50] B. Bruneau, et al., *Plasma Sources Sci. Technol.*, **23(6)**: 065010 (2014).

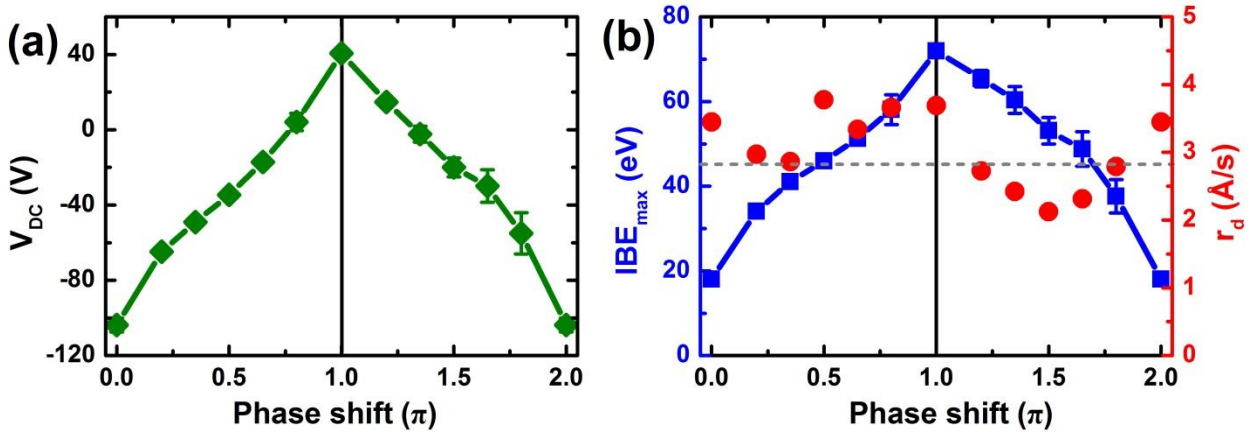

Figure 4.6 (a) Experimentally obtained V_{DC} as a function of φ during µc-Si:H films deposition. (b) Variation of the estimated IBE_{max} and r_d with varying φ.

4.2.3. Structural properties

Raman spectroscopy

To quantify the impact of ion energy, the films have been characterized by Raman spectroscopy, and the results are presented Figure 4.7. Upon initial inspection, the Raman spectra of these films are quite similar, as seen in Figure 4.7-(a) (only the "0-π" films are shown). Although the film deposited at φ = π (*valley*s) shows a shift of the peak position, (which may indicate stress in the material[51]) a pronounced Raman crystalline peak around 520 cm^{-1} is observed for all these films. After deconvolution, similar values of X_c^{Raman} on the order of ~70-75 % are obtained (Figure 4.7-(b)), regardless of any difference in process conditions.

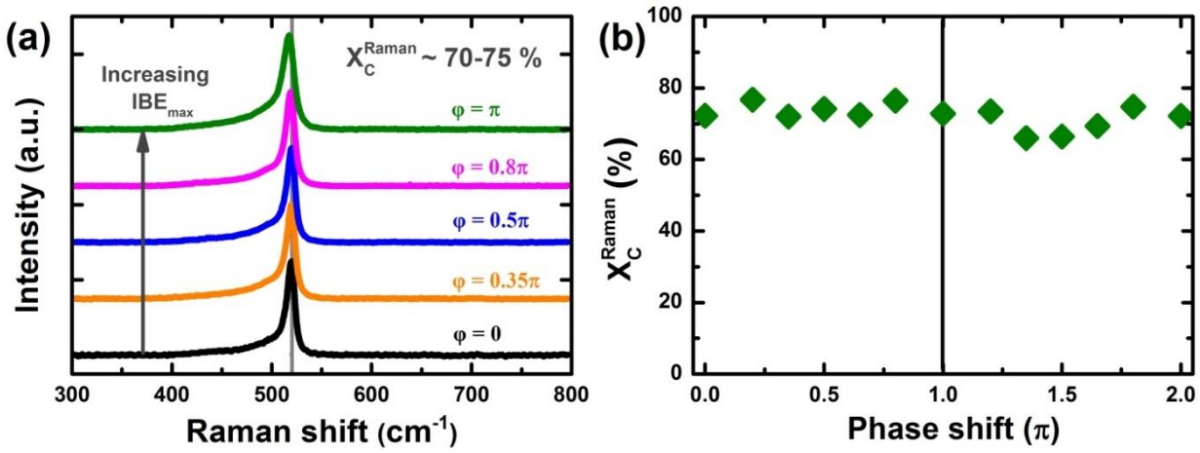

Figure 4.7 (a) Raman spectra for µc-Si:H films deposited using different types of TVW (only the "0-π" films are shown). (b) Variation of X_c^{Raman} with varying φ.

[51] *Physical problems in microelectronics: Proceedings of the Fourth International School, ISPPM*, J. Kassabov (Ed.), Varna, Bulgaria (1985).

Despite the small difference in crystalline volume fraction, a more significant effect of ion energy conditions can be revealed by looking at the extracted $FWHM_{520}$. Figure 4.8-(a) shows the variation of $FWHM_{520}$ as a function of φ. For the films deposited with φ closer to 0 (or 2π, *peaks*), relatively low values of $FWHM_{520}$ around 6.5 cm^{-1} are obtained. This quantity increases when using waveforms with φ closer to π (*valleys*), and a value of $FWHM_{520}$ around 8.7 cm^{-1} is observed at φ = π.

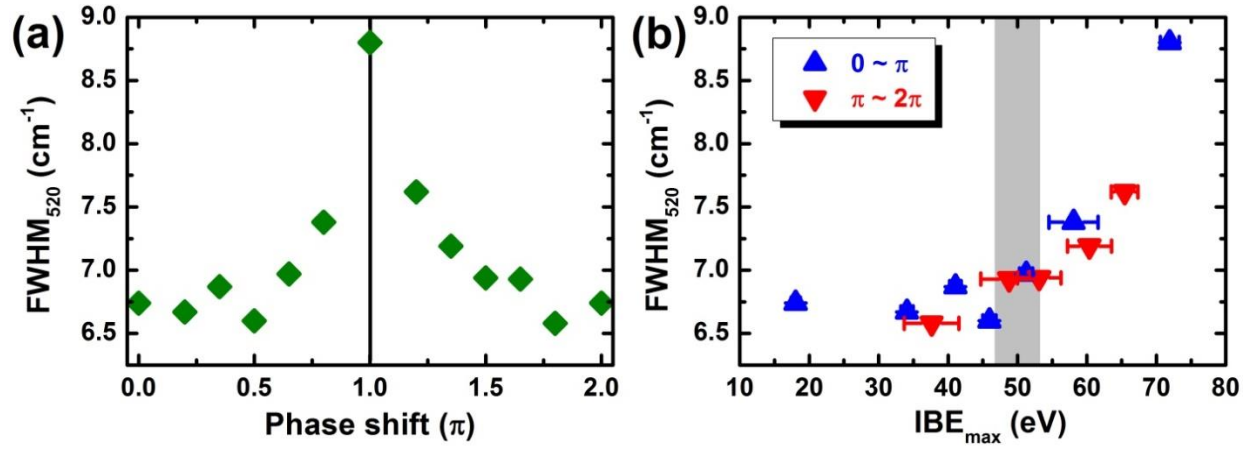

Figure 4.8 Variation of $FWHM_{520}$ with varying (a) φ and (b) IBE_{max}, where the up/down triangles correspond to the "0-π"/"π-2π" films, respectively.

From Figure 4.6-(b), voltage waveforms with φ closer to 0 (*peaks*) give lower ion energies during processing, and higher ion energies are obtained with φ closer to π (*valleys*). So, it could be more interesting to see the variation of $FWHM_{520}$ with IBE_{max}. Such results are presented in Figure 4.8-(b), and $FWHM_{520}$ shows an upward trend with increasing IBE_{max}, with a threshold around ~45-55 eV. When IBE_{max} is below ~45-55 eV, $FWHM_{520}$ remains relative constant at low values. A sharp rise is observed when ion energy increases above ~45-55 eV. As shown in Figure 4.7-(b), this suggests that although similar crystalline volume fractions are obtained for all process conditions, high ion energy conditions can lead to the growth of smaller grained material[52].

Ellipsometry

Ellipsometry measurements have also been performed, and Figure 4.9 shows the comparison of the ellipsometry spectra for these films (only the "0-π" films are shown). The results confirm the crystalline phase dominant material as seen by Raman measurements.

The clear shoulder-like peaks at 3.4 eV and 4.2 eV are observed for all these films. However, one can see that the relative magnitude of the spectra at these points differs from each other. In Figure 4.9-(b), the comparison of the $\langle \varepsilon_i \rangle_{max}$ in the high energy portion for these films is presented. It shows a "M"-shape tendency with varying φ, with two minima at φ = 0 (*peaks*) and φ = π (*valleys*), and two maxima at φ = 0.5π (*sawtooth*) and φ = 1.5π (*sawtooth*). As mentioned in Section 3.4.2, a greater value of $\langle \varepsilon_i \rangle_{max}$ for μc-Si:H is usually an indication of improved material properties.

[52] M. N. Islam et al., *Appl. Phys. Lett.*, **78(6)**: 715 (2001).

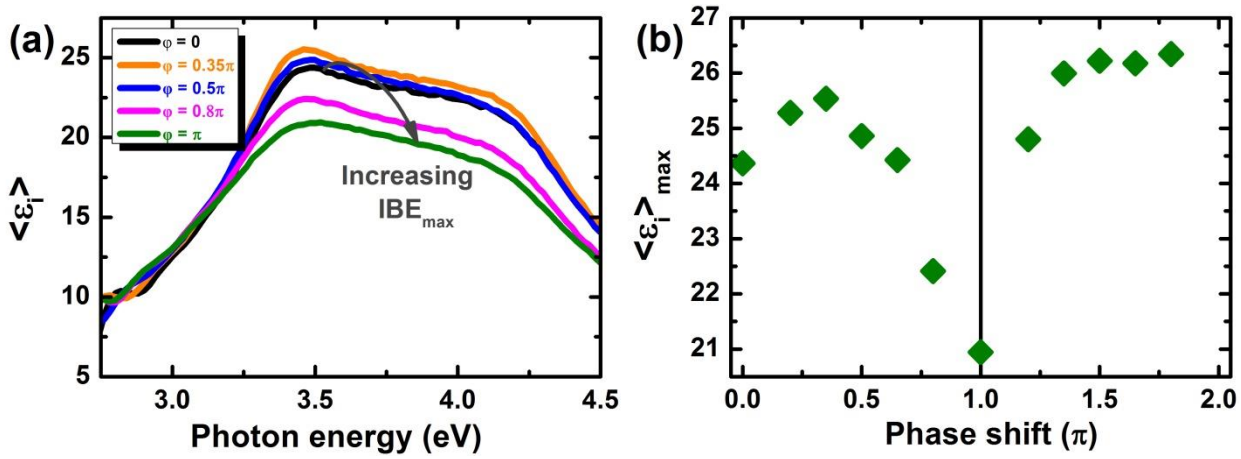

Figure 4.9 (a) Ellipsometry spectra in high energy portion for µc-Si:H films deposited using different TVW (only the "0-π" films are shown). (b) Variation of $\langle\varepsilon_i\rangle_{max}$ with varying φ.

In analogy to the results shown in Figure 4.8-(b), the $\langle\varepsilon_i\rangle_{max}$ is also plotted as a function of IBE_{max} (Figure 4.10). An increase with IBE_{max} is observed, up to values of ~45-55 eV. A monotonic decrease is then observed for higher ion energies (IBE_{max} > ~45-55 eV). It is worth noticing that this threshold coincides with the observation from Raman measurements. Interesting enough, one can note from the results that the "π-2π" films always present a higher value of $\langle\varepsilon_i\rangle_{max}$ than their counterparts, despite similar ion energy conditions. However, Raman measurements show that all these films present similar values of X_c^{Raman} (Figure 4.7-(b)), and no obvious distinction in the tendency of $FWHM_{520}$ with increasing IBE_{max} is observed between these two series (Figure 4.8-(b)). Therefore, it can be suggested that the difference in the ellipsometry spectra magnitude possibly does not originate from the films crystalline grain features (volume fraction and averaged grain size).

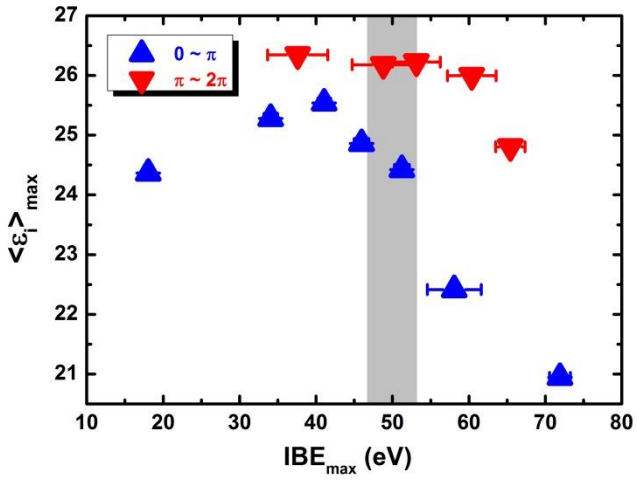

Figure 4.10 Variation of the $\langle\varepsilon_i\rangle_{max}$ at high energy portion with varying IBE_{max}.

In order to get further information from the spectra, ellipsometric modeling has been conducted. Figure 4.11 summaries the effect of ion energy conditions on the surface roughness, crystalline volume fraction (small and large grains) and void content in the bulk layer for the deposited films.

It can be noted from Figure 4.11-(a) that the surface roughness decreases slightly with increasing IBE_{max} up to ~45-55 eV, then increases for higher ion energies. However, one can see a striking difference between the two sets of films, namely a higher surface roughness is obtained for the "0-π" films. Although the surface roughness is not the only factor that determines the magnitude of ellipsometry spectra, the lower value of it for the "0-π" films can still partially explain the relatively lower $\langle \varepsilon_i \rangle_{max}$ observed in Figure 4.10[53,54].

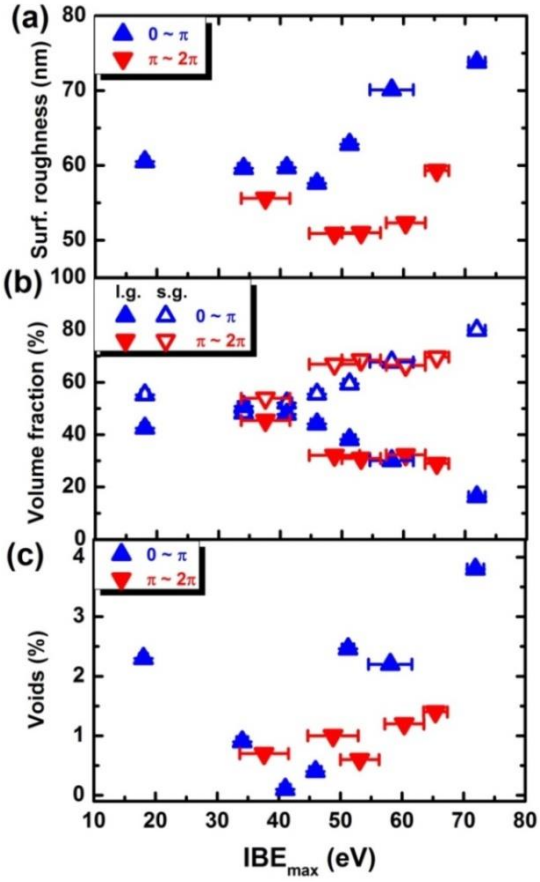

Figure 4.11 Variation of (a) surface roughness, (b) small and large grain volume fraction, i.e., X_{sg}^{ES} and X_{lg}^{ES}, and (c) void fraction X_v^{ES} in bulk layer with varying IBE_{max}.

In Figure 4.11-(b), the variation of small and large crystalline grains volume fraction (i.e., X_{sg}^{ES} and X_{lg}^{ES}) are presented. One can note that the total crystalline volume fraction ($X_c^{ES} = X_{sg}^{ES} + X_{lg}^{ES}$) deduced from the ellipsometric model is approaching 100 % ("fully crystallized"), which differs from that obtained from Raman measurements (X_c^{Raman} = ~70 %). Similar results have also been observed in Ref. 55. In that work, different process conditions lead to an increase of X_c^{Raman} from ~60 % up to ~80 %, while the X_c^{ES} stays roughly constant at 100 % (void content not considered, but is supposed to be at a low level). Such discrepancy from these two techniques could originate from the portion of small grains that are undistinguished from the amorphous phase by Raman

[53] A. Abramov, et al., *J. Non-Cryst. Solids*, **354**: 2218 (2008).
[54] Y. Djeridane, et al., *Thin Solid Films*, **515(19)**: 7451 (2007).
[55] A. Abramov, et al., *J. Non-Cryst. Solids*, **352**: 964 (2006).

scattering[56]. This underestimation of crystalline volume fraction for µc-Si:H film from Raman measurement has also been reported by a number of groups[57,58]. Limited by the fitting method, the presence of a broad tail at low wavenumber (by the a-Si:H tissue) for a µc-Si:H Raman spectra usually leads to X_c^{Raman} less than 90 %, even with a 100 % crystallinity from X-Ray Diffraction (XRD) measurement[59]. Therefore, XRD or high resolution TEM characterization should be performed for the precise determination of the crystalline volume fraction and the averaged grain sizes for the µc-Si:H film.

Nevertheless, one can see from Figure 4.11-(b) that the dependencies of X_{sg}^{ES} and X_{lg}^{ES} on IBE_{max} are similar for both sets of films, namely a continuous increase of X_{sg}^{ES} and decrease of X_{lg}^{ES} with increasing IBE_{max}. These results are consistent with the Raman analysis that smaller grained material is obtained at high ion energies (Figure 4.8-(b)), although the threshold values observed are not exactly the same. Such consistency can be even better revealed by studying correlations between the $FWHM_{520}$ from Raman spectra with the evolutions of X_{sg}^{ES} and X_{lg}^{ES}. As one can see in Figure 4.12, the values of X_{sg}^{ES}/X_{lg}^{ES} tend to split apart with increasing $FWHM_{520}$, namely the highest $FWHM_{520}$ and lowest X_{lg}^{ES} are obtained at the highest ion energy conditions.

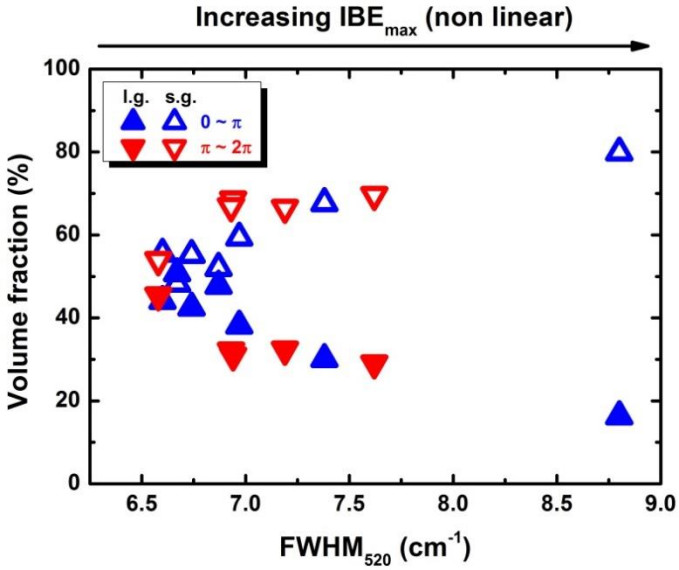

Figure 4.12 Correlation between fraction of small/large grain in bulk layer and $FWHM_{520}$.

Moreover, in Figure 4.11-(c), the variation of the void fraction (X_v^{ES}) in the bulk layer for these films deposited under different ion energy conditions are also presented. It shows that X_v^{ES} decreases simultaneously until IBE_{max} reaches ~45-55 eV, and after that it starts to increase again. Therefore, the moderate ion energy condition (IBE_{max} = ~45-55 eV) during processing can lead to the improvement of bulk layer density. Further support of this point will be provided by the following characterizations.

[56] G. Viera, et al., *J. Appl. Phys.*, **90**, 4175 (2001).
[57] L. Houben, et al., *Philos. Mag. A*, **77**: 1447 (1998).
[58] C. Ossadnik, et al., *Thin Solid Films*, **337**: 148 (1999).
[59] S. Klein, et al., *Thin Solid Films*, **430**: 202 (2003).

Infrared absorption

In addition to Raman and ellipsometry analysis, the film quality has been further examined by FTIR measurements. The films' microstructural properties (infrared absorption due to hydrides) have been studied. Basically, the peaks position of the hydride SMs for μc-Si:H film depend on the hydrogen configuration as well as the local network environments, and the assignment of the different SMs peaks have been discussed by a variety of research groups[60,61,62,63,64,65,66,67,68].

Figure 4.13 shows the FTIR spectra of a typical μc-Si:H film obtained in our work. It is generally believed that the SMs can be classified into two groups, namely the low SM (LSM, at ~1980-2030 cm^{-1}) and the high SM (HSM, at ~2060-2160 cm^{-1})[69]. Both of the LSM and HSM are related to the a-Si:H tissue in the material. Specifically, the LSM is assigned to hydrogen bonded in vacancies and that of the HSM to the hydrides group incorporated at the surface of internal nanosized voids. However, depending on the film microstructure (crystallinity, crystalline orientation, material density, etc.), more absorption peaks can be detected.

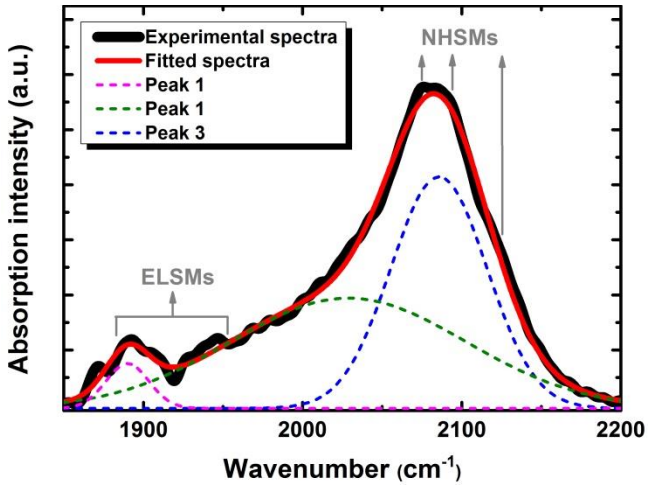

Figure 4.13 Fitting of FTIR spectra for μc-Si:H film. The ELSMs (~1850-1950 cm^{-1}) and NHSMs (~2083, ~2103 and ~2137 cm^{-1}) splitting from the HSM are indicated by the gray arrows.

In Figure 4.13, the spectra shows several additional absorption peaks in the extremely LSM (ELSM, at ~1850-1950 cm^{-1}). The assignment of these ELSMs is still under discussion, and one of the possibilities is proposed to be the (SiSi*d*)SiH group, where *d* represents a dangling bond[70,71].

[60] A. Hiraki, et al., *J. Phys. Colloq.*, **42**: C4 (1981).
[61] Y. J. Chabal, *Phys. Rev. Lett.*, **51**: 2233 (1983).
[62] M. A. Hachicha, et al., *MRS Online Proc. Libr. Arch.*, **164** (1989).
[63] N. Blayo, et al., *J. Non-Cryst. Solids*, **137**–**138**, **Part 2**: 775 (1991).
[64] U. Kroll, et al., *J. Appl. Phys.*, **80**: 4971 (1996).
[65] M. Scheib, et al., *J. Non-Cryst. Solids*, **198**: 895 (1996).
[66] J. K. Rath, et al., *MRS Online Proc. Libr. Arch.*, **452** (1996).
[67] H. Fujiwara, et al., *J. Non-Cryst. Solids*, **338**: 97 (2004).
[68] S. Lebib, et al., *J. Appl. Phys.*, **97**: 104310 (2005).
[69] A. H. M. Smets, et al., *Appl. Phys. Lett.*, **92**: 33503 (2008).
[70] G. Lucovsky, *Solid State Commun.*, **29**: 571 (1979).
[71] T. S. Shi, et al., *Phys. Status Solidi A*, **74(1)**: 329 (1982).

Besides, it shows a triplet of narrow peaks (~2083, ~2103 and ~2137 cm^{-1}) in the HSM range, which are called the narrow HSMs (NHSMs) peaks or high wavenumber (HWN) peaks. These peaks are typically observed for highly crystallized µc-Si:H films, for instance, in the case of deposition from the $SiF_4/H_2/Ar$ plasma chemistry. It has been pointed out that these narrow peaks are assigned to the absorption of mono-, di-, and trihydrides on the crystalline surface[72]. Then for the case of µc-Si:H, Smets *et al*[69] proposes that they are more likely associated with the crystalline grain boundaries. Furthermore, based on characterization using Polarized Raman Spectroscopy, Chaigneau *et al*[73] suggest that the origin of the twinned peak at ~2083 and ~2103 cm^{-1} can be attributed to the SiH_2 bonding configuration on the {110} interface between crystalline grains passivated by hydrogen rather than to amorphous tissue.

It has been experimentally confirmed that the presence of these NHSMs usually can be viewed as a signature of low material density for a µc-Si:H film. In fact, the consequence of high contribution from these NHSMs has already been observed in the study about the deposition of µc-Si:H film by using MDECR-PECVD presented in Section 3.4.2. The porous material (low ion energy condition) possessing obvious NHSMs in the spectra is more prone to be post-oxidized in ambient air. In contrast, less post-deposition oxidation is observed for denser films with less significant NHSMs absorption, indicating good passivation of the crystalline grain surfaces.

Figure 4.14 shows the comparison of the FTIR spectra for the co-deposited "0-π" films on c-Si wafers. It can be observed that the film deposited under a low ion energy condition ($\varphi = 0$, *peaks*) exhibits dominant HSM in the spectra, with the lesser existence of NHSMs. When slightly higher ion energy condition is used, the signature of LSM starts to show up ($\varphi = 0.35\pi$), and becomes more pronounced for further increased ion energy ($\varphi = 0.5\pi$, *sawtooth*). However, once even higher ion energy conditions are used ($\varphi > 0.5\pi$), the smaller grained material (observed from Raman and ellipsometry analysis) present prominent HSM again. Similar tendency is obtained for the "π-2π" films (not shown here).

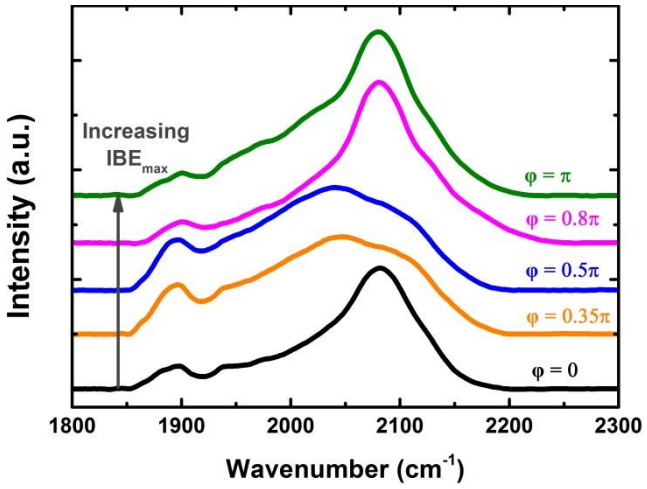

Figure 4.14 FTIR spectra in range from 1800 to 2300 cm^{-1} for µc-Si:H films deposited using different types of TVW (only the "0-π" films are shown).

[72] V. A. Burrows, et al., *Appl. Phys. Lett.*, **53**: 998 (1988).
[73] M. Chaigneau, et al., *Thin Solid Films*, **537**: 145 (2013).

In order to make a qualitative evaluation for the material microstructure, a microstructure parameter R^* can be derived from the FTIR spectra[74]. This R^* is defined by the ratio between the integrated absorption intensity of HSM and the sum of LSM and HSM as

$$R^* = \frac{I_{HSM}}{I_{LSM}+I_{HSM}} \tag{4.15}$$

The description of microstructure quality using parameter R^* originally comes from a-Si:H, and as said, a lower value of R^* indicates a denser material. However, for µc-Si:H the interpretation should be much more carefully treated due to the presence of additional peaks in some cases.

Figure 4.15 shows the variation of the R^* for this series of µc-Si:H films as a function of IBE_{max}, in which a clear transition can be noted: a moderate increase of IBE_{max} from ~20 eV up to ~50 eV leads to a continuous decrease from 0.75 down to 0.3; once the IBE_{max} is above this certain value, a dramatic increase of R^* back up to 0.8 at IBE_{max} = ~60 eV is observed. Again, this IBE_{max} threshold coincides with the values detected by Raman and ellipsometry measurements.

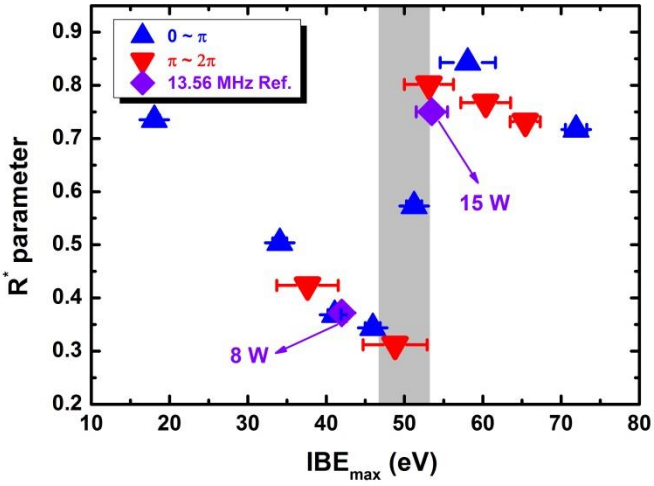

Figure 4.15 Variation of microstructure parameter R^* for µc-Si:H films deposited under varying ion energy conditions. Two reference films deposited using the standard 13.56 MHz excitation source with low (8 W) and high (15 W) power are shown by purple diamonds.

In addition, we have deposited two reference films using a standard single-frequency (13.56 MHz) excitation source. The process conditions are shown in Table 4.2: one of them (15W) is similar to the conditions used in Ref. 75 for the deposition of the intrinsic absorber layer for high efficiency µc-Si:H solar cell devices; for the other one, we attempted to decrease the RF power to achieve a lower ion energy during deposition. The V_{DC} has been recorded, and according to Equation (2.3), the IBE_{max} during the deposition of these two films are determined to be ~53.5 eV (15 W) and ~42 eV (8 W), respectively.

[74] E. Bhattacharya, et al., *Appl. Phys. Lett.*, **52(19)**: 1587 (1988).
[75] J.-C. Dornstetter, et al., *IEEE J. Photovolt.*, **3**: 581 (2013).

Table 4.2 Process conditions for two reference µc-Si:H films deposited using standard single-frequency (13.56 MHz) excitation source.

P_{RF}	V_{PP}	V_{DC}	IBE_{max}	t	X_c^{Raman}	r_d
W	V	V	eV	nm	%	Å/s
15	285	-35.5	~53.5	230	73	2.46
8	212	-22	~42	130	67	1.43

FTIR measurements have been conducted for these two films, and the corresponding spectra are shown in Figure 4.16. As one can see, the film deposited with IBE_{max} = ~53.5 eV shows a prominent HSM hydrides absorption. The decrease in IBE_{max} down to ~42 eV leads to a shift of the absorption peaks towards the LSM region.

The deduced R^* values are included in Figure 4.15 for comparison. It can be observed that, the results fit quite well in the trend with increasing IBE_{max}. Therefore, reducing the power injection could be a way to decrease the ion energy during deposition, thus making it possible to achieve improved material properties. However, one should note that this would probably lead to the sacrifice in deposition rate compared to the case of high power injection. As shown in Table 4.2, the deposition rate reduces from 2.46 Å/s at 15 W down to 1.43 Å/s at 8 W, showing an almost 40 % drop.

Therefore, these results remind one of the inadequacies of the standard single-frequency excitation in controlling the plasma properties for practical deposition processes. Provided one desires control over ion energy or ion flux in some cases, i.e., tunable ion energy condition with constant deposition rate (material quality), tunable deposition rate at similar ion energy conditions (process time), etc., the TVW technique can well satisfy these demands.

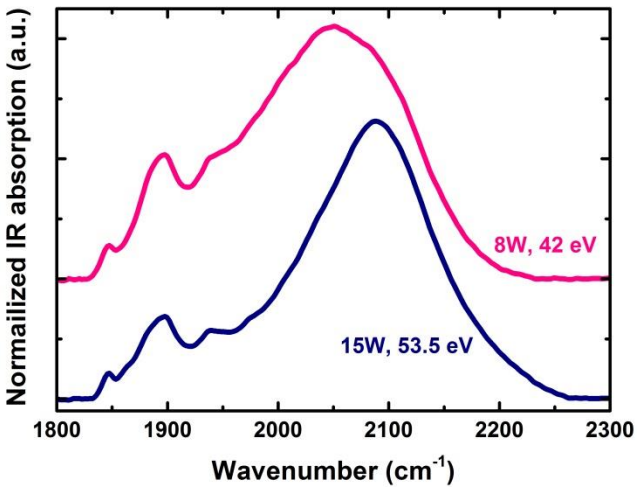

Figure 4.16 FTIR spectra in range from 1800 to 2300 cm^{-1} for two reference µc-Si:H films deposited using standard single-frequency (13.56 MHz) excitation source.

4.2.4. Transport properties

To examine the impact of ion energy on the films electronic properties, SSPG measurements have been carried out. In combination with the structural properties studied previously, these results can be useful to determine the most appropriate process conditions for active layer deposition in solar cell devices.

Herein, two sets of films with different thicknesses (0.5 μm and 1 μm) were deposited under different ion energy conditions. For comparison, reference films (13.56 MHz, 15W)[§] have also been deposited, and all the process conditions are shown in Table 4.3. For each sample, the measurement has been repeated five times at different characterization spots, and an averaging of the results has been taken.

Table 4.3 Process conditions for μc-Si:H film deposited using TVW with varying φ for electronic properties characterization. *t* represents the layer thickness.

Sources	IBE_{max}	P	d_i	T_{sub}	T_{rf}	SiF_4	H_2	Ar	t
	eV	Torr	mm	°C	°C	sccm	sccm	sccm	μm
13.56 MHz	~54	3	20	150	80	3.6	5	88	0.5
TVW	~18-65								1

The minority carrier diffusion length L_d for these two sets of films can be extracted from SSPG measurements, and the results are shown in Figure 4.17-(a). On the whole, the thicker films (1 μm) present a higher L_d than the thinner ones. This can be understood by considering the coplanar configuration of measurements and the columnar growth of μc-Si:H. Because of the material anisotropy along the growth direction, improved grain features (larger grain sizes) and less influence from the bottom part (amorphous incubation layer, or less crystallized layer in the early growth stage) for thicker films can reasonably have a better photoelectronic response. More interestingly, one can note from the results that the evolution of L_d with increasing IBE_{max} for both sets of films follows the tendencies observed in the material structural properties. Guided by the curves, L_d shows a continuous increase with increasing IBE_{max} up to moderate values (~45 eV), and then a decrease is observed for higher ion energies.

The measured value for the reference film is also shown in Figure 4.17-(a) (purple diamond). Notably, it fits quite well within the trend. Moreover, SSPG measurements allows for the determination of the ambipolar mobility-lifetime products (holes mobility-lifetime products, $\pi\tau_{min}$) through Equation (2.22). Figure 4.17-(b) presents the results of $\pi\tau_{min}$ plotted with increasing IBE_{max}. In line with L_d, similar variation trends of $\pi\tau_{min}$ are obtained.

These results can lead to the conclusion that the control over ion energy through TVW can give

[§] Reference sample with 0.5 μm and 1 μm thicknesses were both prepared, but thicker one peeled off after vacuum breaking.

some insights for the optimization of µc-Si:H film deposition using RF-PECVD. In the following section, possible interpretations for the consequence induced by those different ion energy conditions will be discussed.

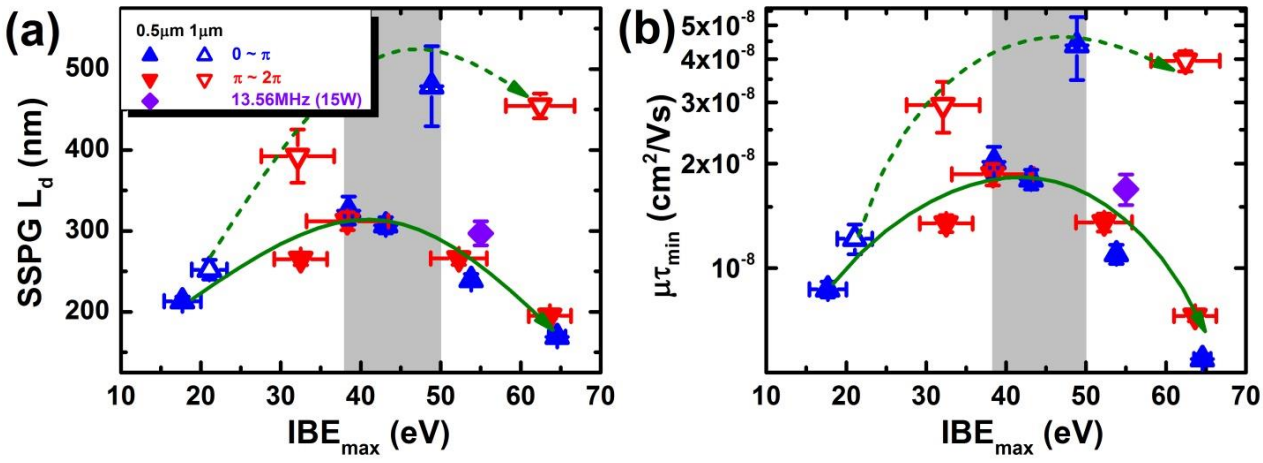

Figure 4.17 Variation of (a) L_d and (b) $\pi\tau_{min}$ at room temperature for two sets of µc-Si:H films with varying IBE_{max}The solid and open triangles correspond to films with 0.5 µm and 1 µm thickness, respectively. The purple diamond corresponds to the 0.5 µm thick reference film.

4.2.5. Ion-related interactions

As it has already been discussed in Section 3.4.3, energetic ions are of great importance for the PECVD of µc-Si:H film. Keeping in mind the IBE_{max} threshold for material properties, we again consider the mass-dependent ion-related interactions.

In line with the MDECR-PECVD process, H_x^+ (x = 0-3) and SiF_x^+ (x = 0-3) will still be the most probable candidates in the RF plasma to make effective ion-induced atomic displacements. The additional Ar^+ should also be considered, since Ar dominates the gas mixture. Moreover, large silicon-related ions containing more than one Si atoms ($Si_yF_x^+$, y > 1) cannot be ignored under such high process pressure. So, following the experimental observations, we try to make some arguments concerning the role of these different ions:

H_x^+: As it has been reported in Ref. 47, H_3^+-induced bulk displacement has a crucial impact on the µc-Si:H film growth dynamics as well as surface morphology. As a result, the nucleation process on the amorphous incubating layer is hindered, leading to the growth of smaller grained material. However, the ion energy threshold for this displacement process is around 65 eV, and it is well above the values found in our experiments (guided by the shadowed area in red). On the other hand, the threshold for the H_3^+-induced surface displacement is around 30 eV. Even though such surface displacement can be presented when the IBE_{max} is above this value, no obvious change is observed in the material properties.

Ar^+: The ion energy threshold for the Ar^+-induced surface displacement is around 12 eV, which means that this process is effectively triggered for all the deposition processes studied in our work. Therefore, this should not contribute to the sharp transitions in material properties. The bulk

displacement, however, can also be triggered if the ion energy is high enough (IBE_{max} > ~35 eV). As for the H_3^+-induced surface displacement, no obvious consequence is induced despite the occurrence of such effective interactions.

On the other hand, in the case of μc-Si:H film deposition from the Ar-diluted SiH_4 plasma, it has been shown that the density of Ar species in the metastable (Ar^*) increases sharply with Ar in an extremely high dilution case (> 90 %)[76]. In such a high Ar dilution case, Ar^* can provide an ample contribution to precursor dissociation via the fast quenching process[77,78]. Based on this argument, it has been pointed out that Ar^* plays a more important role than Ar^+ in determining the quality of the deposited films in this case[79]. In contrast to Ar^+ (which can be accelerated in the plasma sheath), the amount of energy transferred by Ar^* to the impinging sites is much lower, since it will just arrive at the growing surface with thermal velocity and relax to its ground state. Instead of inducing aggressive process on the growing surface, the energy released through the relaxation process could help to achieve a more compact atomic network. It should be noted that the gas mixture is our process is also highly diluted in Ar. In analogy with the discussion above, the observed transitions in material properties are not likely to be attributed to the increase of Ar^+ kinetic energy and the resulting atomic displacements.

SiF_x^+: Again, the SiF_x^+ species can be Si^+, SiF^+, SiF_2^+, and SiF_3^+, of which the ion energy thresholds to induce effective surface displacements are similar (~12-15 eV). Therefore, the same argument as Ar^+-induced surface displacement can be applied, these processes are not likely to induce significant change in the material properties. In terms of bulk displacement, the thresholds are 36 eV, 43 eV, 50 eV, and 55 eV respectively. It can be assumed that the Si^+ makes almost no contribution to the sharp change in material properties, since it has the similar threshold as Ar^+. However, all the other SiF_x^+ can be the possible candidates.

$Si_yF_x^+$ (y > 1): Doubtlessly, larger silicon-related ions with more than one Si atoms, i.e., $Si_yF_x^+$ (y > 1), can also be present in such high-pressure plasma processes, and we cannot ignore their impact on the film growth. However, one point to keep in mind is that higher numbers of atoms within the ions would favor elastic collisions upon contact with target atoms, thus the energy transfer could be much less effective. Moreover, we can try to make a reasonable assumption that, compared to the others, the amount of $Si_yF_x^+$ species with x, y > 3 are negligible. Concretely, the range of ion masses for $Si_yF_x^+$ is within 75-150 amu, as indicated by the shadowed area in gray. Considering the corresponding surface displacement, the required ion energies are all below ~20 eV. So for the surface displacement, the same arguments used for Ar^+ and SiF_x^+ can be used for the surface displacement induced by $Si_yF_x^+$ (not yet linked with the experimental observations). On the other hand, some of the $Si_yF_x^+$ species (like Si_2F^+ and $Si_2F_2^+$) can possibly lead to the effective bulk displacement, which might have some impact on the film growth.

[76] A. Kono, et al., *Jpn. J. Appl. Phys.*, **32(4)**: L543 (1993).
[77] D. Mataras, et al., *J. Appl. Phys.*, **66(1)**:119 (1989).
[78] L. Sansonnens, et al., *J. Phys. D: Appl. Phys.*, **27(7)**: 1406 (1994).
[79] U. K. Das, et al., *J. Appl. Phys.*, **80(9)**: 5389 (1996).

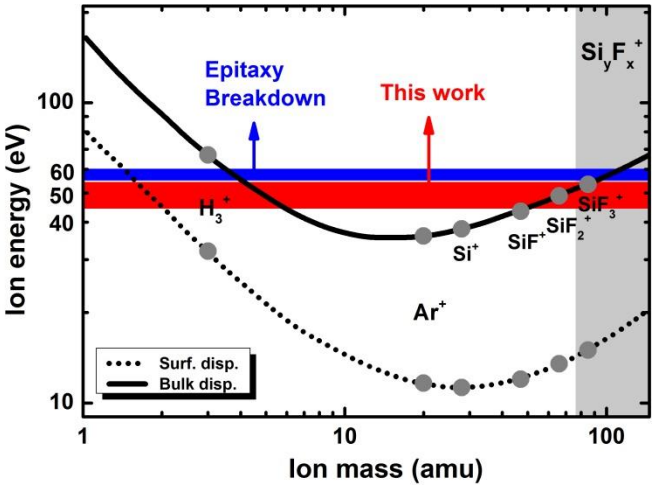

Figure 4.18 Energy threshold for ion-induced surface (dashed line) and bulk (solid line) atomic displacement on a silicon substrate versus impinging ion mass (calculated by Brice *et al*). The H_3^+, Ar^+ and SiF_x^+-induced displacements are highlighted (circles), and high order silicon-related ions ($Si_yF_x^+$, y > 1) are indicated by the shadow area in gray. The shadow areas in blue and red correspond to the upper limit of IBE_{max} to sustain the silicon epitaxial growth proposed in Ref. 80 and the experimental values found in this work.

In summary, µc-Si:H film deposition under moderate ion energy conditions with IBE_{max} = ~45-55 eV can be helpful to suppress the formation of nanovoids, as indicated by the reduction of X_v^{ES} and a drop of R^*. This can be understood by considering the different surface processes related to the impinging ions. Moderate ion energy conditions can be of great importance to deposit dense material. However, local defects and poor electronic properties will be induced if the ion energy is above a certain threshold. The experimentally observed material properties at transition are most likely to be associated with the silicon-related ion-induced bulk atomic displacements. As a consequence, crystallite growth is severely hindered, thus leading to the formation of smaller grained materials with deteriorated electronic properties.

Interestingly, in a previous work concerning the study of silicon epitaxy using similar process conditions on the same reactor, it has been proposed that stable epitaxial growth can be sustained only when IBE_{max} is below 58 eV, and epitaxy breakdown occurs instantly if it is above 60 eV (guided by the shadow area in blue)[80]. This critical value is in good agreement with the experimental observations in our work.

Based on these results, it can be concluded that the modification in ion energy conditions enabled through the use of TVW can indeed have a remarkable impact on the deposition of µc-Si:H films, even under high process pressures (3 Torr). The links between the ion-induced interactions and the material structural and electronic properties have been clearly established. In the following section, the performance of the resulting solar cell devices will be examined.

[80] R. Léal, et al., *42nd IEEE PVSC Proc.*, 1959 (2014).

4.2.6. µc-Si:H solar cell devices

Fabrication process flow

To test performance of the layers in devices, a series of substrate *n-i-p* structure single-junction solar cells were prepared, incorporating a TVW plasma-deposited intrinsic µc-Si:H film as the absorber layer. The device schematic is shown in Figure 4.19, and the order of fabrication is from bottom to top.

It should be noted that this study is only focused on the impact of the quality of intrinsic layer on the resulting device performance, and no special attention has been paid to the optimization of the doped layers. Moreover, the doped and intrinsic layers have been deposited in different PECVD reactors, necessitating vacuum breaks at both the *n*/*i* and *p*/*i* interfaces. A reference device has also been fabricated, with an intrinsic layer deposited using the process conditions shown in Table 4.3 (13.56 MHz, 15W). The detailed information of each layer is described in Table 4.4 (in the order of fabrication).

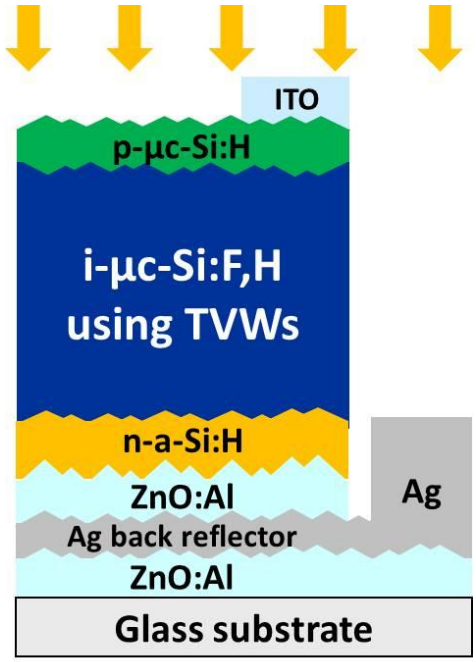

Figure 4.19 Schematic of substrate *n-i-p* µc-Si:H solar cell device.

Table 4.4 Process conditions for substrate *n-i-p* µc-Si:H solar cells.

1	substrate	1 inch ×1 inch Corning glass covered with 1 µm sputtered ZnO:Al (etched by 0.5 % HCl solution for 25 s).
2	back reflector and contact	Following the preparation of ZnO:Al, an Ag/ZnO:Al stack is sputtered with thicknesses around 200 nm and 100 nm respectively.
2	*n*-a-Si:H	The *n*-doped layer is made of amorphous silicon deposited from an $SiH_4/PH_3/H_2$ plasma chemistry in the "NEXTRAL" reactor. The thickness is around 20 nm.
3	*i*-µc-Si:H	The intrinsic µc-Si:H absorber layer is deposited from the $SiF_4/H_2/Ar$ plasma chemistry in the "PHILIX" reactor using TVW and the standard 13.56 MHz excitation source.
4	*p*-µc-Si:H	The *p*-doped layers is made of microcrystalline silicon deposited from an $SiH_4/B_2H_6/H_2$ plasma chemistry in the "NEXTRAL" reactor. The thickness is around 15 nm.
5	ITO	ITO of about 80 nm thickness is sputtered on the silicon stacks. A shadow mask composing of 6 circles with 4 mm diameter is used to define the surface area of each sub-cell.
6	front contact	Since the back contact is covered by these layers, scratches are made with a diamond pen on the edge of the samples. Ag paste is spread on the scratches to make electrical contact with the Ag underneath.
7	annealing	After preparation, all the solar cells are annealed at 125 ºC for one hour.

Solar cell performance

For these samples, the *p*-layer outside of the ITO contact for each sub-cell was not removed. Even though the *p*-layer is more resistive than the ITO, it can still lead to an increased collection area in the case of light *I-V* measurements. In order to minimize this impact and to better define the active area, the samples have been covered during light *I-V* measurements with the same type of shadow mask as was used for the deposition of ITO.

Figure 4.20 presents the light *I-V* characteristics for this series of solar cells, and detailed performance parameters (V_{OC}, J_{SC}, FF and η) are summarized in Table 4.5. Some trends can be noted from these results. Firstly, with the increase of ion energy, J_{SC} (from EQE) remains at a relative stable value around 23.0 mA/cm^2 up to IBE_{max} = ~55 eV (reference sample). However, it should be noticed that a thinner absorber layer is used at IBE_{max} = ~45 eV (see Table 4.5), thus a superior device quality can be assumed for this case. Afterwards, further increase in ion energy leads to a fast decay of device performance, indicated by the dramatic decrease of J_{SC} down to 4.3 mA/cm^2 at IBE_{max} = ~65 eV. In contrast to the sharp change in J_{SC}, V_{OC} shows a less dramatic but more sensitive dependence on the ion energy condition during processing. As shown in Table 4.5, with increasing ion energy, an increase in V_{OC} is observed, with an optimum value of 0.509 V occurring at IBE_{max} = ~45 eV. However, a decrease is observed for higher ion energies. Again, the result of the reference sample (IBE_{max} = ~55 eV) fits well within the tendency.

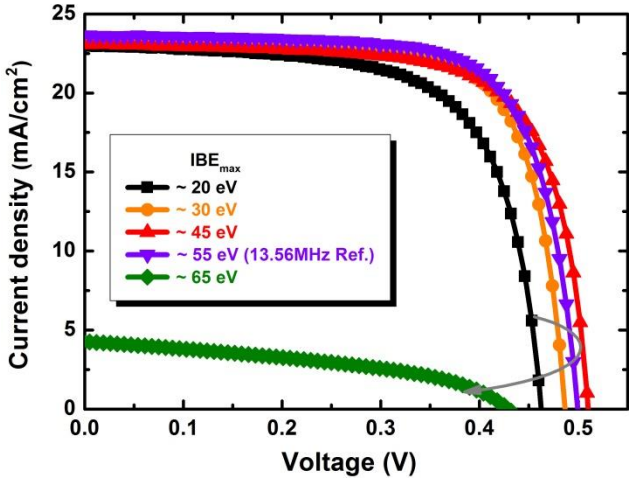

Figure 4.20 Light *I-V* curves of µc-Si:H solar cells with absorber layers deposited using TVW, and with reference sample deposited by standard 13.56 MHz excitation source shown in purple.

Table 4.5 *I-V* parameters of µc-Si:H solar cells with absorber layers deposited under different ion energy conditions using TVW, along with reference cell (IBE_{max} = ~55 eV) deposited by standard 13.56 MHz excitation source. t_i represents the thickness of absorber layer.

IBE_{max}	t_i	J_{SC}	V_{OC}	FF	η
eV	µm	mA/cm^2	V	%	%
~20	1.25 (±0.1)	23.0	0.460	68.0	7.19
~30	1.25 (±0.1)	23.5	0.488	72.6	8.32
~45	1.15 (±0.1)	23.1	0.509	71.6	8.42
~55 (Ref.)	1.45 (±0.1)	23.6	0.502	72.3	8.58
~65	1.45 (±0.1)	4.3	0.432	41.7	0.77

In order to access the physical properties of the photodiodes, *I-V* measurements have also been performed in the dark. Figure 4.21-(a) shows the semi-log plots of the dark *I-V* characteristics for these solar cells. In Figure 4.21-(b), one can note that the change of ion energy has a significant impact on the diode characteristics, since a lower magnitude of the dark current on almost the entire bias range is observed for the cell with an absorber layer deposited at IBE_{max} = ~45 eV.

According to Equation *(2.37)*, J_0 can be extracted from the dark *I-V* characteristics. The results are plotted as the evolution of J_0 as a function of IBE_{max} in Figure 4.21-(b). As can be seen, the improvement resulting from moderate ion energy conditions is rather noticeable. Lower values of J_0 around 2.5×10^{-4} mA/cm^{-2} are obtained with IBE_{max} at ~45-55 eV. This is in comparison to an order of magnitude higher value obtained at lower ion energy condition (IBE_{max} = ~20 eV) and the doubly greater value obtained at higher ion energy condition (IBE_{max} = ~65 eV). Therefore, this can partially explain the opposite trend of V_{OC}, which is also presented in Figure 4.21-(b).

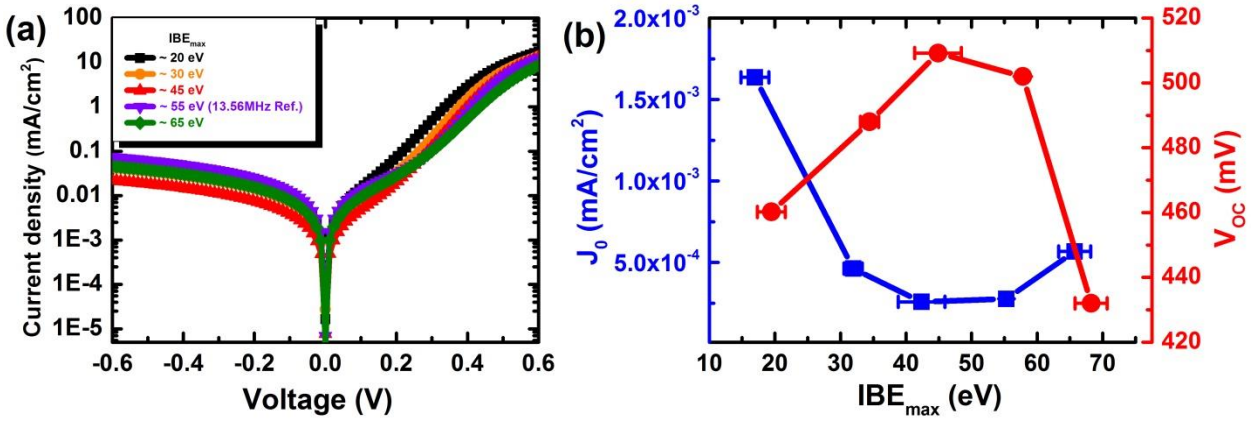

Figure 4.21 (a) Dark *I-V* curves of µc-Si:H solar cells with absorber layers deposited using TVW, with the reference cell shown in purple. (b) Variation of J_0 and V_{OC} with varying IBE_{max}.

In summary, the most interesting conclusion from this study is that the impact of energetic ion bombardment during the deposition of intrinsic µc-Si:H absorber layer can be reflected directly by the solar cell device performance. We have shown that the results are in line with the aforementioned material properties. Moderate ion bombardment during deposition is beneficial to the improvement of V_{OC}. However, solar cell devices with the absorber layer deposited under excessively high ion energy conditions present significantly degraded performance, and this can be correlated to the material deterioration induced by the bulk atomic displacement at high energies. One may also note that the reference process using the standard 13.56 MHz excitation source can lead to similar ion energy conditions and comparable device performance. However, the greater flexibility provided by the semi-independent control of plasma properties via TVW gives it an advantage, as it has the possibility to achieve higher deposition rates without sacrificing material properties.

4.3. Deposition of a-Si:H film using SiH_4/H_2 plasma chemistry

To advance knowledge on the further application of TVW in silicon thin film deposition, we now turn our attention to the deposition of a-Si:H. The impact of ion energy on the structural properties and the electronic stability of the resulting material and solar cell devices will be discussed.

Sample preparation

A series of a-Si:H films were deposited on both glass substrates and c-Si wafers using the SiH_4/H_2 plasma chemistry excited by different types of TVW with constant V_{PP} of 150 V. The process conditions are shown in Table 4.6. The deposition times were adjusted to produce films around 250 nm thick. For the electrical characterization, coplanar aluminum contacts with a 1 mm gap were evaporated on top of the films deposited on glass substrates. All the samples were annealed at 125 ºC for one hour after contact deposition.

Table 4.6 Process conditions for a-Si:H film deposition using TVW with varying φ.

φ	V_{PP}	P	d_i	T_{sub}	T_{rf}	SiH_4	H_2
π	V	mTorr	cm	ºC	ºC	sccm	sccm
0-2	150	120	2.8	200	100	5	10

To investigate the material stability under light exposure, a LID study has also been carried out. The light-soaking (LS) treatment for the samples is performed using Xe lamps (close to two sun intensity) over a period up to 224 hours. During LS, the system was fan-ventilated to minimize heating induced by illumination. All the following characterization data have been taken both in the initial state and after LS.

Ion energy and deposition rate

The value of V_{DC} measured during the a-Si:H film deposition is plotted as a function of φ in Figure 4.22-(a). In contrast to the µc-Si:H film deposition performed under much different process conditions (different plasma chemistry, process pressure, inter-electrode distance, etc.) in Section 4.2, a more symmetric trend of V_{DC} with φ is observed, implying a less significant slope asymmetry effect.

Again, the $\tilde{V}_{pl}$ during processing can be estimated using Equation (4.14), and thus a control over the IBE_{max} in the range of ~5-27 eV has been achieved[§], as shown in Figure 4.22-(b). In addition, Figure 4.22-(b) also provides the films deposition rates. A symmetric "W"-shape is observed, with two maxima of 0.85 Å/s at φ = 0 (*peaks*) and 1.14 Å/s at φ = π (*valleys*), and two minima of 0.60 Å/s at φ = 0.5π (*sawtooth*) and 0.53 Å/s at φ = 1.5π (*sawtooth*).

[§] As the plasma would not be sustained due to rapid electron leakage to the electrode if $\tilde{V}_{pl}$ is too low, one should note that the low IBE_{max} values (with φ close to 0 and 2π) might be underestimated. Therefore, depending on the electron temperature, a reasonable lower bound for IBE_{max} should rather be assumed.

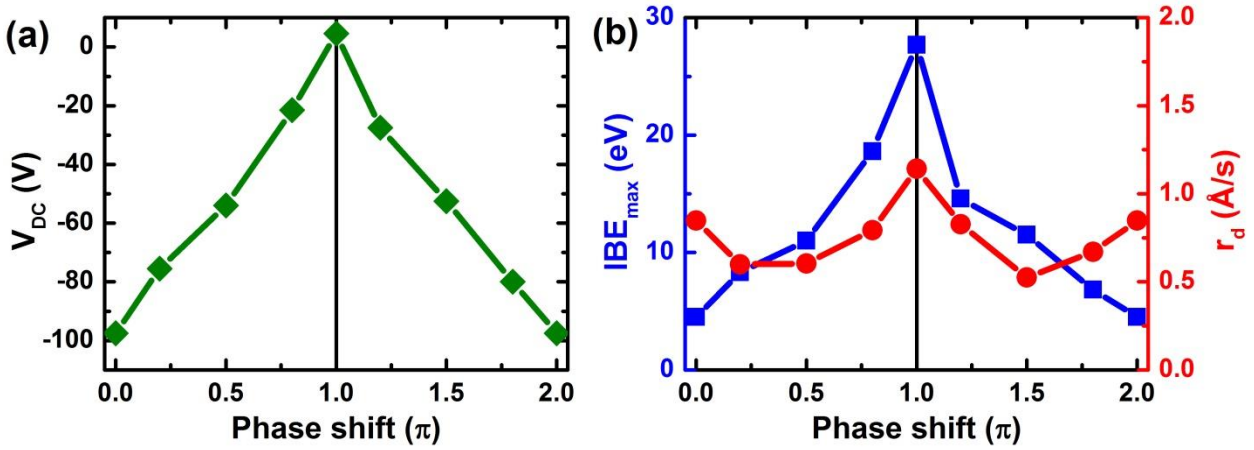

Figure 4.22 (a) Experimentally obtained V_{DC} as a function of φ during the a-Si:H film deposition. (b) Variation of the estimated IBE_{max} and r_d with varying φ.

4.3.1. Hydrogen bonding configuration

Infrared absorption

The films were first characterized using FTIR absorption measurements. Figure 4.23 shows the spectra for the films deposited under four different ion energy conditions. For the hydride stretching modes, not much difference is observed in the initial state, although the films deposited with φ = 0 (*peaks*) and φ = π (*valleys*) present a slightly lower and higher absorption intensity, respectively (Figure 4.23-(a)). In contrast, after LS (Figure 4.23-(b)), a significant difference is observed between the films; even without fitting the curves, one can see that the amplitude for the φ = 0 (*peaks*) film has visibly decreased.

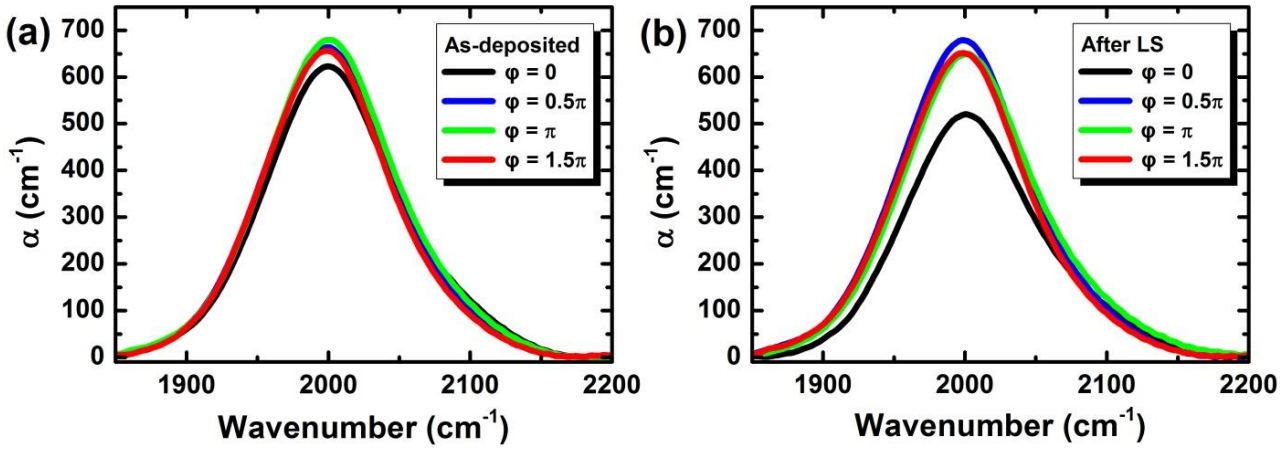

Figure 4.23 FTIR spectra for a-Si:H films deposited under low (φ = 0, *peaks*), moderate (φ = 0.5π or 1.5π, *sawtooth*) and high (φ = π, *valleys*) ion energy conditions measured (a) in their initial state and (b) after being light-soaked for 224 hours.

As shown in Figure 4.24, the FTIR spectra for a typical a-Si:H film can usually be deconvolved using two Gaussian absorption peaks, corresponding to the LSM and HSM, respectively. Relative

to case for µc-Si:H films, the characteristic absorptions in the infrared region for an a-Si:H film are less complex. Nevertheless, the exact assignment and interpretation of which hydride configurations contribute to the LSM and HSM is also an open question that is extensively discussed.

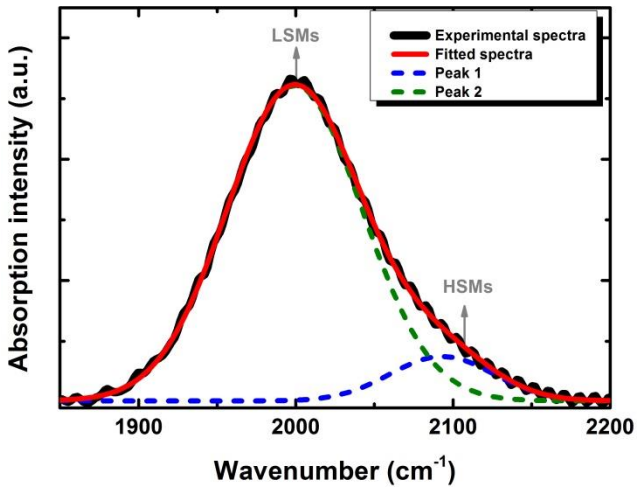

Figure 4.24 Fitting of FTIR spectra for a-Si:H film with two absorption peaks corresponding to LSM and HSM hydride vibrations.

It has been proposed that the SMs only depend on the hydride type, so that the monohydrides (SiH) and dihydrides (SiH_2) contribute to the LSM and HSM, respectively[70,81,82,83,84]. However, what the exact configurations are for these monohydrides and dihydrides is not clear[83,84]. Moreover, the distinction between LSM and HSM can also be influenced by the bulk environment, as some claim that the monohydrides on the internal voids surfaces can also contribute to the HSM[84]. In some cases, the monohydrides can even be responsible for an additional middle SM (MSM) at ~2030-2040 cm^{-1} (not observed in our case), when they are present at platelet surfaces[85,86,87].

A consistent conclusion on this topic is still lacking. Nevertheless, the most common argument suggests that the main contribution for the LSM and HSM absorption is attributed to the monohydrides in vacancies and the hydrides located on the internal voids surface, respectively[88], and a larger portion of LSM is usually viewed as a signature of a-Si:H film with higher density (higher R^* value, as discussed in Section 4.2.3).

Knowing the absorption intensities of the hydrides at LSM and HSM, the total hydrogen

[81] A. A. Langford, et al., *Phys. Rev. B*, **45**: 13367 (1992).
[82] R. J. Severens, et al., *Appl. Phys. Lett.*, **67**: 491 (1995).
[83] J. D. Ouwens, et al., *Phys. Rev. B*, **54**: 17759 (1996).
[84] W. Beyer, et al., *MRS Proc.*, **507**: 601 (1998).
[85] H. Fujiwara, et al., *Surf. Sci.*, **497**: 333 (2002).
[86] S. Vignoli, et al., *J. Non-Cryst. Solids*, **299-302**, **Part 1**: 220 (2002).
[87] S. Agarwal, et al., *J. Vac. Sci. Technol. B*, **22**: 2719 (2004).
[88] A. H. M. Smets, et al., *Appl. Phys. Lett.*, **82**: 1547 (2003).

amount N_H^T in the a-Si:H film can be estimated according to Brodsky *et al*[89] through

$$N_H^T = A_i \int \frac{\alpha}{\omega} d\omega \tag{4.16}$$

where A_i is the conversion factor that is proportional to the inverse of the oscillator strength of a given SM, for which 9.0×10^{19} cm^{-2} and 2.2×10^{20} cm^{-2} are used for the LSM and HSM, respectively[81], α is the absorption coefficient, and ω is the frequency in cm^{-1}. Then, the total hydrogen content C_H^T of the film is calculated by

$$C_H^T = \frac{N_H^T}{N_{Si}} \times 100\ \% \tag{4.17}$$

where N_{Si} = 5.0×10^{22} cm^{-3} is the atomic density of pure silicon. However, it should be noted that the actual atomic density of the a-Si:H film might slightly change, depending on the hydrogen incorporation. It has been proposed by Beyer[90] that N_{Si} can increase to a value of 5.8×10^{22} cm^{-3} for an a-Si:H film with C_H^T around 20 %. Therefore, limited by the atomic density variation and the method accuracy, a ±5 % uncertainty is assumed during the data treatment herein.

Figure 4.25 shows the variation of C_H^T for the a-Si:H films in both the as-deposited and LS states. The C_H^T values for these films show a slight dependency on φ in the initial state, varying between 7 % and 8 %, and most of them present almost no variation upon LS. Quite surprisingly, the film deposited at φ = 0 (*peaks*) is characterized by a significant decrease from 7.4 % down to 6.4 % when it is light-soaked.

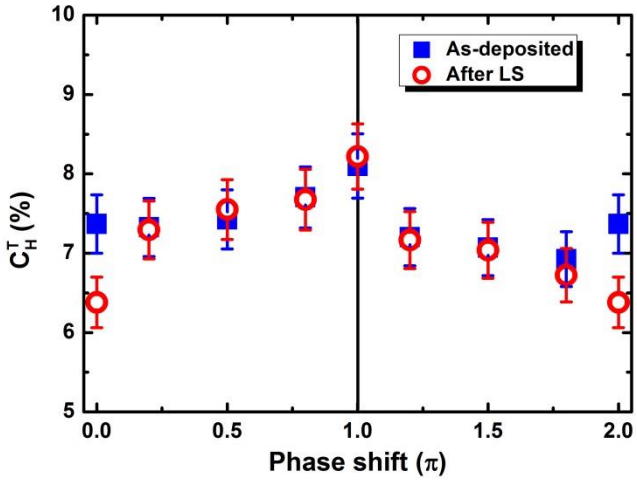

Figure 4.25 Total hydrogen content of a-Si:H films deposited using TVW with varying φ in their initial state and after being light-soaked for 224 hours.

Presented in Figure 4.26 is the variation of the R^* parameter as a function of φ. One can note from the results that the films can be classified into two sets in the initial state: films using waveforms with φ closer to 0 (or 2π, *peaks*) are characterized with higher R^* of about 0.07, and

[89] M. H. Brodsky, et al., *Phys. Rev. B*, **16**: 3556: (1977).
[90] W. Beyer, *Tetrahedrally-Bonded Amorphous Semiconductors*, D. Adler and H. Fritzsche (Ed.), Springer (1985).

those with φ closer to π with lower values of about 0.045. As seen in Figure 4.22-(b), plasmas excited by waveforms with φ closer to 0 (or 2π, *peaks*) have lower IBE_{max} values. Similar to the case observed for μc-Si:H film growth, the absence of sufficiently energetic ion bombardment during the a-Si:H film deposition can partially explain the low film density[91], thus leading to the high R^* values. However, if the films are deposited under reasonably higher ion energy conditions, i.e., using waveforms with φ closer to π (*valleys*) in our case, lower values of R^* can be obtained, suggesting a higher film density.

Remarkably, R^* for these films changes significantly upon LS, and presents different variations depending on phase shift, φ. A large increase of about 0.03 is observed for both the films deposited at φ = 0 (*peaks*) and φ = π (*valleys*). However, with φ close to 0.5π or 1.5π (*sawtooth*), the deposited films show almost no change, or even a slight decrease in the value of R^*. As a result, another "W"-shape tendency emerges, indicated by the red open circles in Figure 4.26.

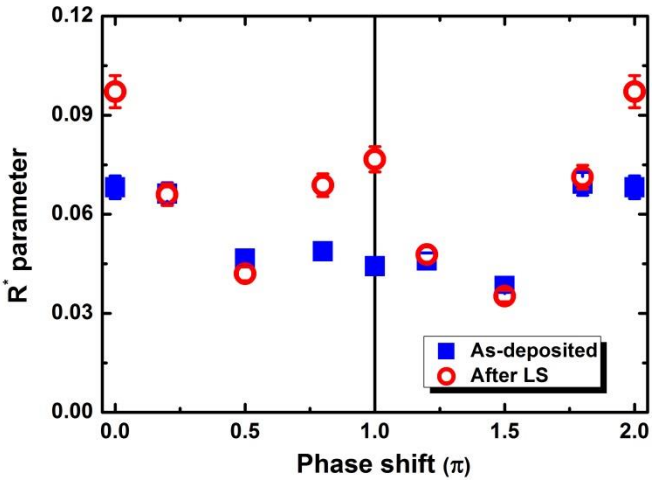

Figure 4.26 R^* for a-Si:H films deposited with varying φ, both in their initial state and after being light-soaked for 224 hours.

One may easily associate this "W"-shape tendency with the difference in films deposition rates, since it presents a similar dependency on φ as seen in Figure 4.22-(b). As proposed in Ref. 92, the increase in deposition rate can be accompanied by a deterioration of the film stability, and it was found to be closely correlated with the increase of dihydrides in the film. Accordingly, higher R^* values are obtained at higher deposition rates.

To examine this explanation, we chose to deposit another set of films at φ = 1.5π (*sawtooth*), the waveform giving the best R^* parameter. The same process conditions as in Table 4.6 were used, except higher values of V_{PP} were used (175 V and 200 V), to obtain higher deposition rates. Using Equation (4.14), the IBE_{max} during deposition for these two films have been estimated. As a comparison, all the details are summarized in Table 4.7. An increase of r_d from 0.53 Å/s at V_{PP} = 150 V up to 0.76 Å/s at V_{PP} = 200 V is observed, with all the IBE_{max} values staying roughly constant at ~12 eV.

[91] E. A. G. Hamers, et al., *J. Non-Cryst. Solids*, **226**: 205 (1998).
[92] T. Nishimoto, et al., *J. Non-Cryst. Solids*, **299**: 1116 (2002).

Table 4.7 Comparison of IBE_{max} and r_d for a-Si:H films deposited using *sawtooth* waveform at φ = 1.5π with different V_{PP}.

φ	V_{PP}	V_{DC}	IBE_{max}	r_d
π	V	V	eV	Å/s
1.5	150	-52.5	11.3	0.53
1.5	175	-64.5	11.5	0.69
1.5	200	-75.5	12.3	0.76

The hydrogen content and R^* parameter for these films have also been determined and are summarized in Figure 4.27. In the initial state, the C_H^T indeed shows an increase with increasing V_{PP}, and it is mainly contributed from the increase of hydrides in the HSM, i.e., C_H^{HSM} (Figure 4.27-(a)). Therefore, greater R^*values are obtained at higher V_{PP}, as shown by Figure 4.27-(b). However, after LS treatment, all these films present almost no change in C_H^T, but a slight decrease in C_H^{HSM} is observed, leading to a drop in the R^* parameter.

From this additional experiment, it can be concluded that despite the difference in deposition rates, the films deposited using *sawtooth* waveform at φ = 1.5π (which also have similar IBE_{max}) always stand out from the trend depicted in Figure 4.26. This phenomenon will be examined subsequently in more detail.

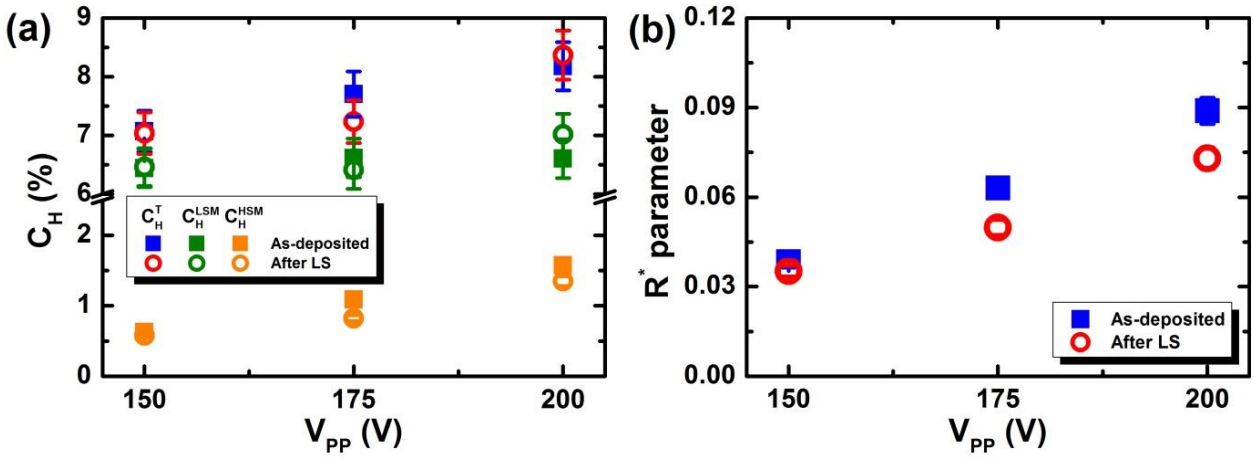

Figure 4.27 (a) C_H^T, C_H^{LSM}, and C_H^{HSM} for the a-Si:H films deposited using *sawtooth* waveform at φ = 1.5π with different V_{PP}. (b) Evolution of R^* for these films after LS.

Hydrogen exodiffusion

This series of a-Si:H films have been further characterized by performing exodiffusion measurements. Figure 4.28 depicts the comparison of the hydrogen effusion spectra for the films as seen in Figure 4.23 (deposited under typically different ion energy conditions). Generally, two hydrogen effusion peaks can be roughly identified in the spectra: one well-defined at ~300-350 °C

and one shoulder-like centered at ~450-500 °C. The presence of these two peaks has been attributed to hydrogen effusion from the internal cavities and from the bulk amorphous matrices, which are usually referred as the weakly and tightly bonded hydrogen, respectively[93].

It can be clearly seen that these films are indeed characterized by considerably different hydrogen bonding configurations. For the one deposited at φ = 0 (*peaks*), a large drop in P_{H_2} is seen after LS. This can be linked to a decrease in hydrogen content within the film as seen in Figure 4.25, since it can be qualitatively linked to the intensity of P_{H_2}. Moreover, the spectra measured after LS shows a downward shift of the effusion peaks, suggesting a portion of tightly bonded hydrogen is transformed to be weakly bonded. This implies that there is a significant reconstruction of film microstructure during LS, again in line with the results from FTIR measurements (Figure 4.26).

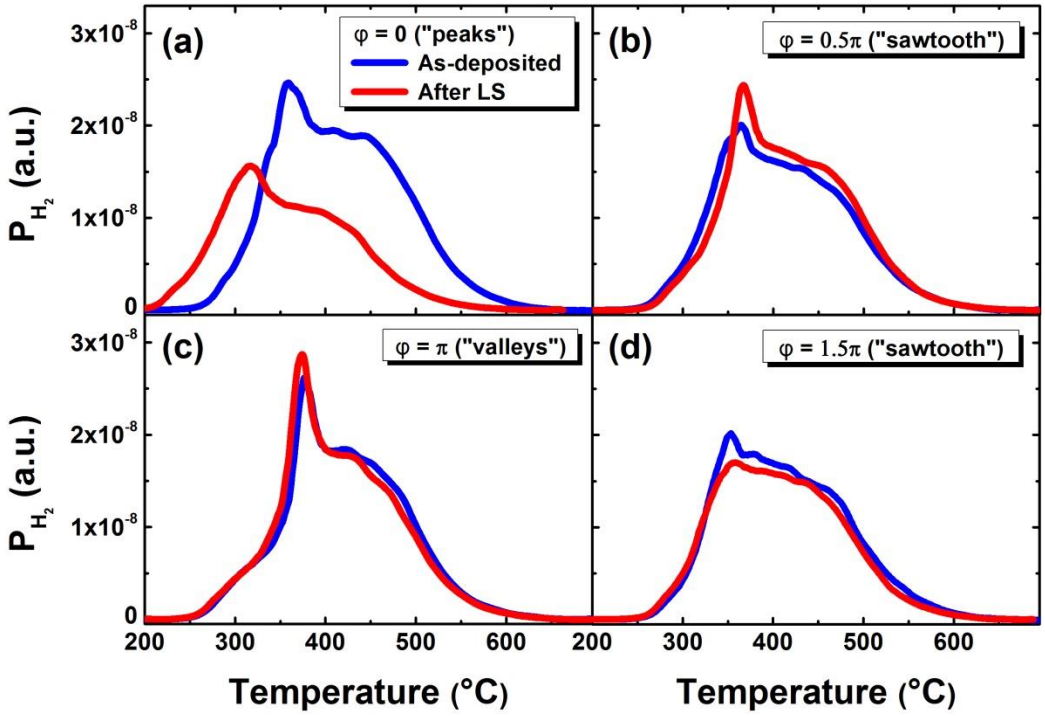

Figure 4.28 Comparison of hydrogen exodiffusion spectra for a-Si:H films deposited at (a) φ = 0 (*peaks*, low ion energy), (b) φ = 0.5π (*sawtooth*, moderate ion energy), (c) φ = π (*valleys*, high ion energy), and (d) φ = 1.5π (*sawtooth*, moderate ion energy). Both the spectra in their initial state and after LS are presented.

However, such dramatic evolution upon LS is not observed for films using the other types of waveforms. For instance, in Figure 4.28-(c) the film deposited at φ = π (*valleys*) presents a considerably higher fraction of weakly bonded hydrogen, but just a slight increase is shown after LS. The most interesting results are obtained for films deposited using the two types of *sawtooth* waveforms (φ = 0.5π or 1.5π) in Figure 4.28-(b) and (d). For these two films having both similar IBE_{max} during deposition and r_d, not much distinction can be noted from the hydrogen effusion spectra in the initial state, while significantly different evolution behaviors upon LS are observed. At φ = 0.5π, the deposited film appears to have more weakly bonded hydrogen after LS, as

[93] S. Lebib, et al., *Eur. Phys. J. - Appl. Phys.*, **26**: 17 (2004).

suggested by the increasing intensity for the low temperature effusion peak. However, its counterpart at φ = 1.5π shows a slight decrease of intensity for this low temperature effusion peak.

The cause of these different behaviors is not fully understood yet. One possible explanation could be the asymmetric plasma excitation produced by these *sawtooth* waveforms (through a slope asymmetry effect that will be introduced subsequently). Although it had little impact on the deposition rate and ion energy, the asymmetric plasma response may result in an asymmetric growth precursor distribution profile, with short lived precursors (SiH, SiH_2) more concentrated near one electrode. However, it should be noted that this speculation is based on previous investigations concerning the slope asymmetry effect and single-gas plasmas, in which no surface processes (deposition or etching) were considered. To better understand the impact of this effect on useful surface processing, further studies concerning multi-gas plasma are needed, and some extensive experimental work on this subject will be presented in Chapter 5.

4.3.2. Ion-related interactions

In order to have more detailed information about the impact of ion energy on the a-Si:H film deposition, ion-related interactions during processing are analyzed. In Figure 4.29 the R^* parameters for this series of films are replotted as a function of IBE_{max}.

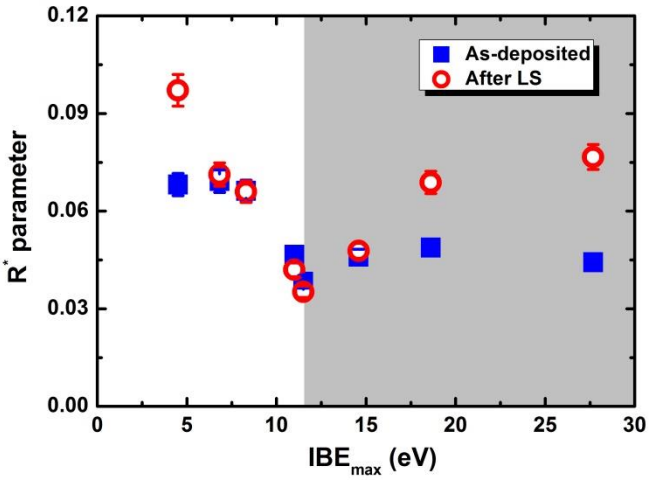

Figure 4.29 R^* for a-Si:H films in their initial state and after LS with varying IBE_{max}.

As one can see, some interesting trends are revealed. In the initial state, the R^* parameter decreases with increasing IBE_{max} up to ~12 eV, then stays relatively constant for further increased ion energies. However, due to differing evolution during LS (as observed in Figure 4.26), a "V" shape tendency with increasing IBE_{max} appears. The lowest R^* is still given by IBE_{max} at ~12 eV, but much higher values are observed at both low and high ion energies.

If we again consider the theoretical ion energy thresholds for ion-induced atomic displacement in this plasma, the most probable ion species to induce the interactions are H_3^+ and SiH_x^+ (x = 0-3). The corresponding ion energies for effective surface and bulk displacements are 30 eV and 65 eV for H_3^+, and 12 eV and 38 eV for SiH_x^+, respectively. Since the deposition process for this series of

films have been performed in a relative low pressure regime, $Si_yH_x^+$ (y > 1) ions that were considered in the study of µc-Si:H film deposition in Section 4.2.5 are not likely to be responsible. On the other hand, the IBE_{max} values for this series of depositions were all below ~30 eV. Therefore, the experimentally obtained threshold value of IBE_{max} at ~12 eV can be reasonably attributed to the SiH_x^+-induced surface displacement, as shown by Figure 4.30.

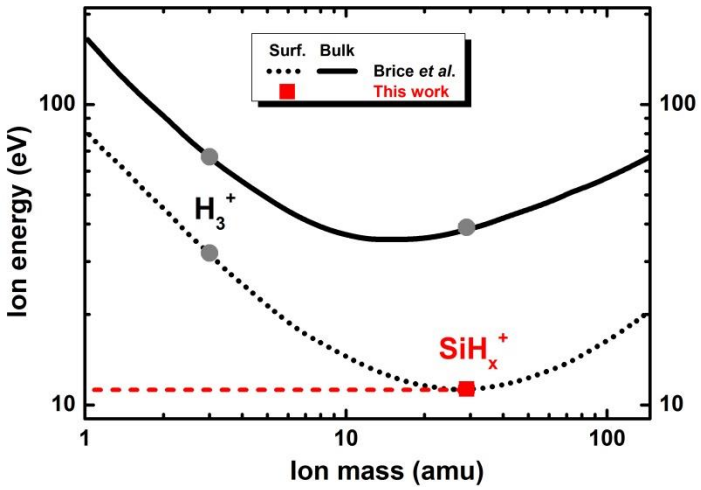

Figure 4.30 Energy threshold for ion-induced surface (dash line) and bulk (solid line) atomic displacement on a silicon substrate versus impinging ion mass (by Brice *et al*). The H_3^+ and SiH_x^+-induced displacements are highlighted (circles). The square presents the experimental value for SiH_x^+ found in this work.

It has been mentioned several times that a moderate ion energy condition during growth is of crucial importance in the reduction of nanosized voids, defect density and the improvement of material density for µc-Si:H, and this is also true for the case of a-Si:H. It should be noted that the R^* parameters for this series of a-Si:H films are all below 0.1. In the perspective of material density and defect states density, such low values of R^* can be a signature of "high" quality a-Si:H films[1,94,95], although it is not the only factor that guarantees high performance for the resulting solar cell device[96]. However, even among these "high" quality a-Si:H films, one can still note from these results that the hydrogen bonding configuration can be significantly impacted by the ion energy conditions. In particular, at low ion energies, insufficient ion bombardment during deposition will result in a less dense and unstable microstructural network with a high fraction of HSM hydrogen in the deposited material. At high ion energies, the occurrence of effective surface atomic displacements can also lead to reduced material stability under light exposure.

4.3.3. Transport properties

SSPG measurements were carried out for this series of a-Si:H films. In Figure 4.31 the evolution of L_d and $\pi\tau_{min}$ with varying φ is presented. As seen, both parameters show a monotonic decrease with increasing φ for the "0-π" films (or increase for the "π-2π" films) in both the initial state and after LS. However, standing out of the trend again is the film deposited at φ = 1.5π (*sawtooth*).

[94] U. Kroll, et al., *J. Non-Cryst. Solids*,**227**–**230**, **Part 1**: 68 (1998).
[95] A. H. M. Smets, et al., *J. Appl. Phys.*, **102**: 073523 (2007).
[96] G. Bugnon, et al., *Adv. Funct. Mater.*, **22(17)**: 3665 (2012).

Although it does not present the best properties in its initial state, the greatest values of L_d and $\pi\tau_{min}$ are observed after LS, suggesting a better electronic stability.

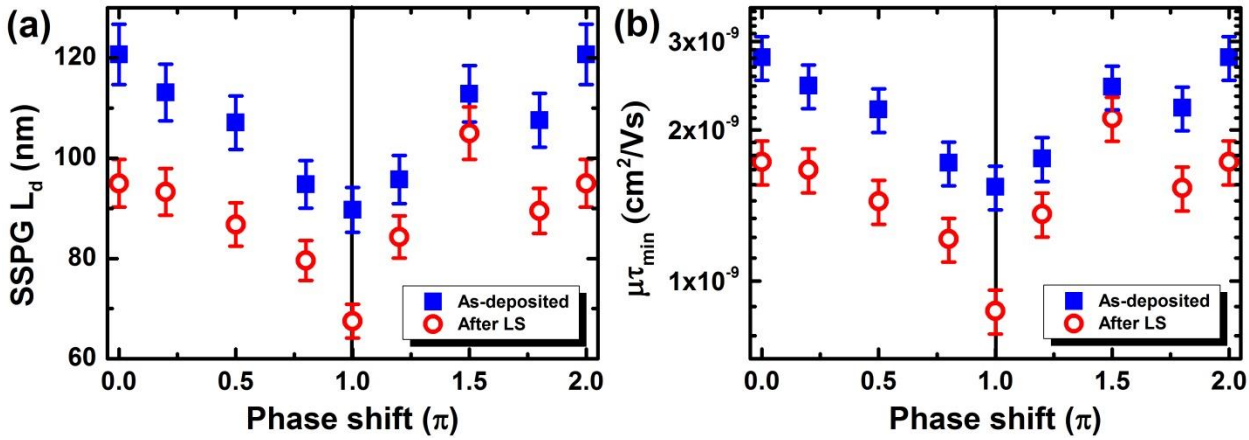

Figure 4.31 Variation of (a) L_d and (b) $\pi\tau_{min}$ with varying φ for a-Si:H films in initial state and after LS.

To have further information about the transport properties, we have conducted temperature-dependent dark conductivity and SSPC measurements. The measurements are performed for four films deposited at φ = 0 (*peaks*), 0.5π (*sawtooth*), π (*valleys*), and 1.5π (*sawtooth*), i.e., typically different ion energy conditions. The process conditions are the same as in Table 4.6, but here the film thickness is higher of about 380 nm. The deduced transport properties ($\pi\tau_{min}$, σ_{ph}, σ_{dark}, Φ ($= \sigma_{ph}/\sigma_{dark}$) and E_a) for these films in their initial state and after LS treatment are summarized in Table 4.8.

Table 4.8 Comparison of electronic properties (at 300 K) for a-Si:H films deposited under low (φ = 0, *peaks*), moderate (φ = 0.5π or 1.5π, *sawtooth*) and high (φ = π, *valleys*) ion energy conditions in their initial state and after LS.

φ	$\mu\tau_{maj}$		σ_{ph}		σ_d		Φ		E_a	
π	$cm^2\ V^{-1}\ s^{-1}$		$S\ cm^{-1}$		$S\ cm^{-1}$		-		eV	
	initial	LS	initial	LS	initial	LS	initial	LS (drop%)	initial	LS
0	6.8×10^{-7}	3.0×10^{-7}	1.6×10^{-5}	6.9×10^{-6}	2.7×10^{-10}	1.5×10^{-9}	5.7×10^{5}	0.46×10^{5} (92%)	0.96	0.68
0.5	7.5×10^{-7}	2.8×10^{-7}	1.7×10^{-5}	6.4×10^{-6}	5.8×10^{-10}	2.2×10^{-9}	2.9×10^{5}	0.30×10^{5} (90%)	0.93	0.67
1	4.5×10^{-7}	1.4×10^{-7}	1.5×10^{-5}	4.6×10^{-6}	7.2×10^{-10}	2.9×10^{-9}	2.0×10^{5}	0.16×10^{5} (92%)	0.90	0.66
1.5	6.7×10^{-7}	3.2×10^{-7}	1.5×10^{-5}	7.2×10^{-6}	2.1×10^{-9}	1.8×10^{-9}	0.7×10^{5}	0.39×10^{5} (44%)	0.83	0.71

One can easily note that, whatever the process conditions, all the films exhibit a degradation in electronic properties. However, the extent to which they degrade depends on the voltage waveforms used. In line with the results for minority carriers in Figure 4.31, the majority carrier transport properties are shown to be impacted by ion energy in the same manner. A $\pi\tau_{maj}$ value of 6.7×10^{-7} $cm^2\ V^{-1}\ s^{-1}$ for the film deposited at φ = 1.5π (*sawtooth*) is not the highest in the initial

state, but $\pi\tau_{maj}$ = 3.2×10^{-7} cm^2 V^{-1} s^{-1} after the LS treatment is more prominent compared to the others. Remarkably, all the other three films are shown to be rather more sensitive to the light-induced degradation, indicated by the tremendous drop of about 90 % in Φ after LS. However, the *sawtooth* film at φ = 1.5π is much less affected; the drop of 46% that it undergoes is considerably less, although it does show a lower initial value of Φ.

The measurement of MPC-DOS for these films has also been performed. To estimate the DOS, c = 4×10^{-8} cm^3 s^{-1} and μ_e = 10 cm^2 V^{-1} s^{-1} have been assumed herein. Figure 4.32 shows the comparison of the MPC-DOS for these four films, in both their initial state and after LS. Consistent with the transport properties, one can see that despite the difference in deposition conditions, all the a-Si:H films are characterized by similar DOS shape in the initial state, save for a slightly lower value displayed by the *sawtooth* film at φ = 1.5π.

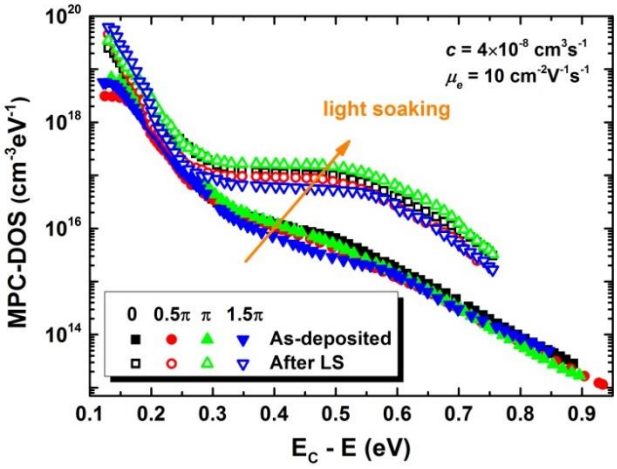

Figure 4.32 Comparison of MPC-DOS for the a-Si:H films deposited under low (φ = 0, *peaks*), moderate (φ = 0.5π or 1.5π, *sawtooth*) and high (φ = π, *valleys*) ion energy conditions in their initial state and after LS.

However, a critical difference is present after LS. All these films present an increase of both the deep defect density and band tail states. It has been proposed in Ref. 97 that the changes of deep defect states and band tail states are correlated. The creation of deep defects (dangling bonds) during LS is probably initiated by the tail-to-tail recombination. However, a lattice expansion induced by the creation of dangling bonds can also lead to the increase of band tail states, which in turn favors the creation of dangling bonds again.

Regardless of the defect generation mechanism, one can note from the results that compared to the *peaks* (φ = 0) and *valleys* (φ = π) films, the *sawtooth* (φ = 0.5π or 1.5π) films are characterized by a considerably lesser increase in the MPC-DOS after LS. Specifically, the *sawtooth* film at φ = 1.5π displays the lowest deep defects and band tail states. This is in good agreement with the results presented above concerning the material transport properties: the fast drop of $\pi\tau_{maj}$, $\pi\tau_{min}$, L_d and Φ after LS is in line with the high MPC-DOS. This is also consistent with the unstable hydrogen bonding configuration determined from FTIR analysis, and the greater values of R^* for

[97] C. Longeaud, et al., *Phys. Rev. B* **65**, 085206 (2002).

peaks (φ = 0) and *valleys* (φ = π) films may also be associated with the higher defect state density.

Similarly, if the results depicted in Figure 4.31 are plotted as a function of IBE_{max}, a more striking feature can be revealed. As one can see in Figure 4.33-(a), a continuous decrease of L_d is observed with increasing ion energy in both the initial state and after LS. However, it is more informative to study the relative evolution of L_d upon LS. In Figure 4.33-(b) the drops of L_d in percentage for these films are presented. After the LS treatment, the *peaks* (φ = 0) film deposited with the lowest ion energy shows a considerable reduction of L_d around 20 %. However, with a small increase of IBE_{max}, the films start to be less affected by the light-induced degradation. Indeed, with IBE_{max} around 12 eV (using *sawtooth* waveform at φ = 1.5π), it shows only about 7 % of reduction in L_d, suggesting a better stability for the deposited film. However, once higher ion energies are used, materials with worse stabilities are again obtained. For example, the *valleys* (φ = π) film deposited with the highest ion energy shows a reduction of around 25 % after LS.

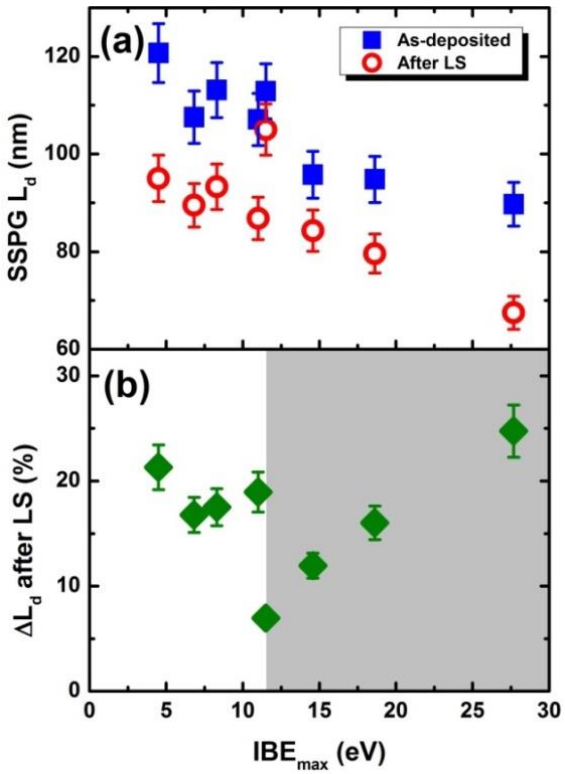

Figure 4.33 (a) L_d for a-Si:H films in their initial state and after LS, and (b) relative reduction of L_d upon LS with varying IBE_{max}.

To conclude, despite the fact that the intrinsic a-Si:H films deposited using different types of TVW all present a certain extent of light-induced degradation, the difference in ion energy conditions during processing indeed have remarkable impact on the evolution of material properties. As well, the differences between the two types of *sawtooth* waveforms (φ = 0.5π or 1.5π, with identical values of IBE_{max}) indicate that effects beyond ion bombardment may play a role. This motivates us to incorporate the TVW plasma-deposited a-Si:H films into solar cell devices, as discussed in the next section.

4.3.4. a-Si:H solar cell devices

Fabrication process flow

To test the resulting device performance, a series of superstrate *p*-*i*-*n* structure single-junction solar cells were prepared, incorporating TVW plasma-deposited intrinsic a-Si:H as the absorber layers. The device schematic is shown in Figure 4.34. As in the study of µc-Si:H solar cells in Section 4.2.6, we made no attempts for the optimization of doped layers, and the devices through vacuum breaks at both the *n*/*i* and *p*/*i* interfaces. The detailed information of each layer is described in Table 4.9 (in the order of fabrication).

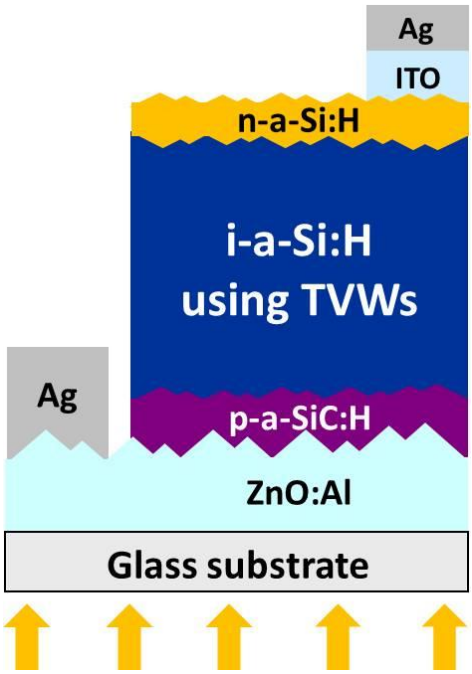

Figure 4.34 Schematic of superstrate *p*-*i*-*n* a-Si:H solar cell device.

Table 4.9 Process conditions for superstrate *p*-*i*-*n* a-Si:H solar cells.

1	superstrate	1 inch × 1 inch Corning glass covered with 1µm sputtered ZnO:Al (etched by 0.5 % HCl solution for 25s).
2	*p*-a-SiC:H	The *p*-doped layer is made of amorphous silicon carbide deposited from an $SiH_4/B_2H_6/CO_2/H_2$ gas mixture in the "NEXTRAL" reactor. The thickness is around 20 nm.
3	*n*-a-Si:H	The *n*-doped layer is made of amorphous silicon deposited from an $SiH_4/PH_3/H_2$ plasma chemistry in the "NEXTRAL" reactor. The thickness is around 20 nm.
4	*i*-a-Si:H	intrinsic a-Si:H absorber layer is deposited from the SiH_4/H_2 plasma chemistry in the "PHILIX" reactor using TVW. The phase shift is varied in range from 0 to 2π, and the film thickness is around 250 nm.

5	*n*-a-Si:H	The *n*-doped layers is made of amorphous silicon deposited from an $SiH_4/PH_3/H_2$ plasma chemistry in the "NEXTRAL" reactor. The thickness is around 20 nm.
6	back reflector and contact	ITO of about 80 nm thickness is sputtered on the silicon stacks. A shadow mask composing of 6 circles with 4 mm diameter is used to define the surface area of each sub-cell. Following the deposition of ITO, Ag is sputtered with a thickness around 400 nm using the same mask.
7	front contact	Since the ZnO:Al deposited on glass is covered by these layers, scratches are made with diamond pen on the edge of the samples. Ag paste is spread on the scratches to make electrical contact with the ZnO:Al underneath.
8	annealing	After preparation, all the solar cells are annealed at 125 ºC for one hour.

Solar cell characterization

The *I-V* characteristics of this series of solar cells were measured. In Figure 4.35 the photovoltaic parameters are plotted as a function of IBE_{max} during the absorber layer deposition. The measurements have been taken in the initial state and after being light-soaked for 1 and 244 hours.

In the initial state, it can be observed from Figure 4.35-(a) that J_{SC} shows a downward trend with increasing IBE_{max}. However, the variation is within a small range, showing by a slight decrease from 14.9 mA/cm^2 at lowest ion energy condition (*peaks* waveform, φ = 0) down to 14.1 mA/cm^2 at the highest ion energy condition (*valleys* waveform, φ = π). During the LS treatment, the devices underwent a considerable light-induced degradation. However, J_{SC} still presents a slightly downward and even more linear variation trend after 244 hours of LS: decreasing from 12.8 mA/cm^2 down to 12.1 mA/cm^2 with increasing IBE_{max}. A similar tendency has been observed for the V_{OC}. An almost linear decrease is observed in both states, but with a less scattered distribution of values after LS (Figure 4.35-(b)). As a result, a decrease from 0.860 V at the lowest ion energy condition down to 0.848 V at the highest ion energy condition is observed.

However, the striking behavior of V_{OC} is that it shows a moderate increase around 20 mV when it is only light-soaked for one hour. This is observed for all the studied films, regardless of the differences in process conditions. According to literature, such an increase in V_{OC} upon LS for a-Si:H solar cell with the absorber layer deposited from the SiH_4/H_2 plasma chemistry could result from a variety of possibilities. In some studies, it has been proposed that this is related to the activation of boron acceptors in the *p*-a-SiC:H layer via LS treatment[98,99,100]. While others claim that the decrease in valence band tail and states re-distribution at the *p*/*i* interface after LS can also be an underlying reason[101,102]. Moreover, such increase in V_{OC} could also reflect the evolution of the intrinsic layer properties, deducing from the shift of dark *I-V* characteristics to the higher voltage side[103]. In a more recent study, this phenomenon was also observed when the *p*-a-SiC:H

[98] M. Isomura, et al., *Appl. Phys. Lett.*, **69**: 1396 (1996).
[99] P. Roca i Cabarrocas, et al., *2nd IEEE PVSC Proc.*, 355 (1998).
[100] C. Longeaud, et al., *MRS Online Proc. Libr. Arch.*, **557** (1999).
[101] P. Siamchai, et al., *25th IEEE PVSC Proc.*, 1093 (1996).
[102] E. V. Johnson, et al., *Phys. Stat. Sol. (a)*, **207**: 691 (2010).
[103] M. Isomura, et al., *Jpn. J. Appl. Phys.*, **39**: 3339 (2000).

was capped by another *p*-µc-SiO:H layer[104]. The authors attributed the light-induced increase of V_{OC} to the creation of defects in the *p*-a-SiC:H layer. These defects can get charged and cause (via depletion of the *p*-µc-SiO:H layer) an increased negative space charge concentration. Therefore, the splitting of quasi-Fermi-level and thus the V_{OC} is enhanced. With longer duration of LS, a decrease of V_{OC} nevertheless occurs, presumably due to the creation of defect states through the *Staebler-Wronski Effect*. However, the values of V_{OC} for these films after being light-soaked for 244 hours are still higher than in their initial state.

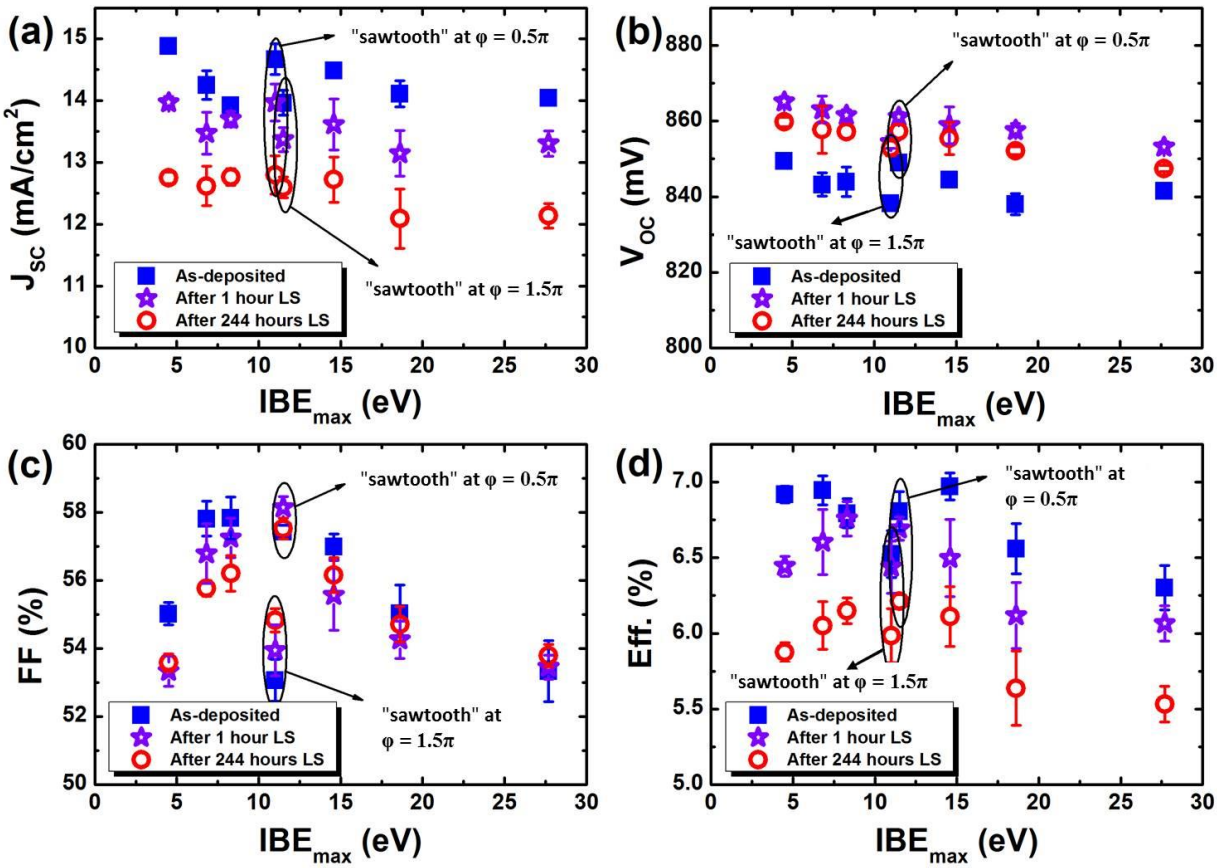

Figure 4.35 Variation of (a) J_{SC}, (b) V_{OC}, (c) FF, and (d) η for a-Si:H solar cells with intrinsic absorber layers deposited using TVW with varying IBE_{max}.

From Figure 4.35-(c), it can be noted that the impact of ion energy on the variation of FF is more dramatic. Both low and high ion energies lead to lower FF in the initial state, and higher values are obtained for moderate ion energy conditions. This trend is more obvious when the devices are light-soaked. A maximum value around 58 % is obtained with the intrinsic layer deposited at IBE_{max} = ~12 eV, using the *sawtooth* waveform at φ = 1.5π. This optimum can be attributed to several possible hypotheses. Although the "in-plane" coplanar transport properties studied in Section 4.3.3 generally present a linear downward trend with increasing IBE_{max}, the "out-of-plane" transport properties have a more crucial importance for the solar cell device. During processing, the effective energy transfer between the impinging ions with moderate kinetic energy may be beneficial for the material properties in the growth direction. Alternatively, a

[104] M. Stuckelberger, et al., *J. Appl. Phys.*, **116(9)**: 094503 (2014).

difference in the *p*/*i* interface properties (hydrogen incorporation, *p*-layer etching, etc.) resulting from different ion energy conditions in the early stage of intrinsic layer growth can also be an underlying reason. Either insufficient or excessive ion bombardment can possibly lead to interface problems that hinder carrier collection.

The net result of the different variations in the *I-V* characteristics (V_{OC}, J_{SC} and FF) is revealed by the conversion efficiency η in Figure 4.35-(d). It can be observed that there is strong coupling between the trends in FF and η (overwhelming the slight changes in V_{OC} and J_{SC}) suggesting that the impact of ion energy on FF is the main one in determining the overall performance for this series of a-Si:H solar cells. However, one can also note from the results that the LID in η is almost entirely due to the decrease in J_{SC}.

In Figure 4.36 the R_{SC} and R_{OC} [§] for these solar cells are presented, as extracted from the *I-V* curves. From this, the variation of solar cells performance and the distinct evolution behaviors upon LS can be better understood. Based on the improved equivalent circuit described in Section 2.4.3.1, it was suggested that the R_{SC} of an a-Si:H solar cell can serve as a quantifying tool for the device quality; the value of R_{SC} can be directly linked to the voltage dependent recombination effect in the *i*-layer resulting from degradation[105,106]. Based on this point, one can note that all the cells underwent a strong increase in voltage dependent recombination after LS treatment, indicated by the almost halved R_{SC} after just one hour of light exposure (Figure 4.36-(a)). On the other hand, at each stage of the measurements, an optimum (greater) value of R_{SC} is always obtained for the absorber layer deposited at IBE_{max} = ~12 eV (using *sawtooth* waveform at φ = 1.5π), which suggests better carrier collection properties compared to the "low and high ion energy" devices. The variation of R_{OC} is shown in Figure 4.36-(b), and one can note that not much difference is observed under such varying ion energy conditions (although lower values are obtained after LS at moderate ion energies).

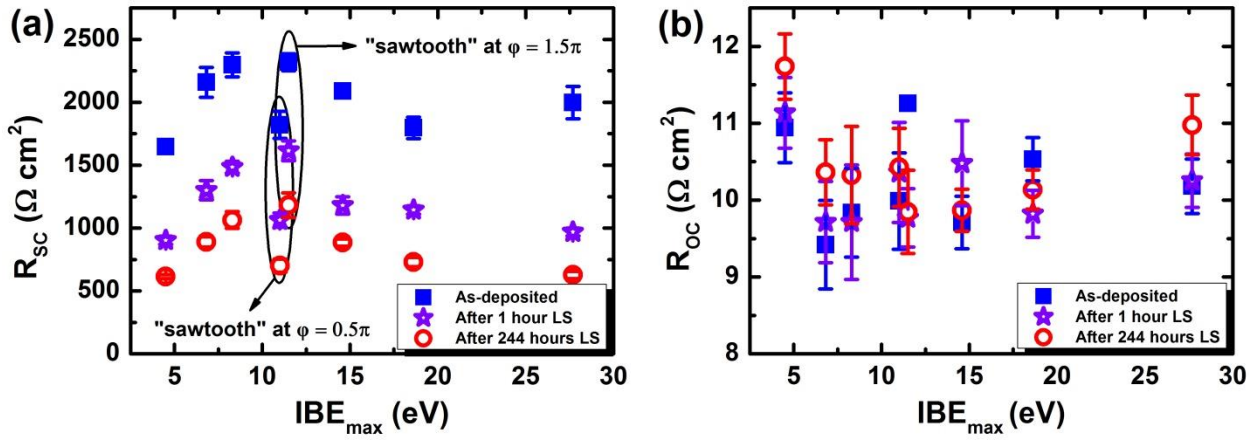

Figure 4.36 Variation of (a) R_{SC} and (b) R_{OC} for the a-Si:H solar cells with the intrinsic absorber layers deposited using TVW with varying IBE_{max}.

[§] Note that the R_{SC} and R_{OC} are the reciprocal slopes taken at the positions of zero-voltage and zero-current, respectively. As described in the literature[105], R_{SC} could be related to R_{SH}, and R_{OC} could be related to R_S.

[105] J. Merten, et al., *IEEE Trans. Electron Devices*, **45(2)**, 423 (1998).

[106] J. Hubin, et al., *Philos. Mag. Part B*, **72(6)**, 589 (1995).

However, one can note from the results in Figure 4.35 and Figure 4.36 that standing out from the trends is again the *sawtooth* film at φ = 0.5π, which actually has almost the same IBE_{max} as its counterpart using the *sawtooth* waveform at φ = 1.5π, but much lower values of FF and R_{SC}. As it has been mentioned in Section 4.3.1, such striking behavior could be attributed to the slope asymmetry effect induced by these special *sawtooth* waveforms.

In addition, the relative LID was also studied concerning all these *I-V* characteristics. Figure 4.37 shows the results estimated through the expression:

$$\Delta X = \frac{X^{as-dep.} - X^{after\ LS}}{X^{as-dep.}} \times 100\ \% \qquad (4.18)$$

where X corresponds to J_{SC}, V_{OC}, FF, or η. Surprisingly, the often observed drop in FF for a-Si:H solar cell upon LS is not obtained here, and some samples even present an enhancement after LS (negative values presented in Figure 4.37-(c)).

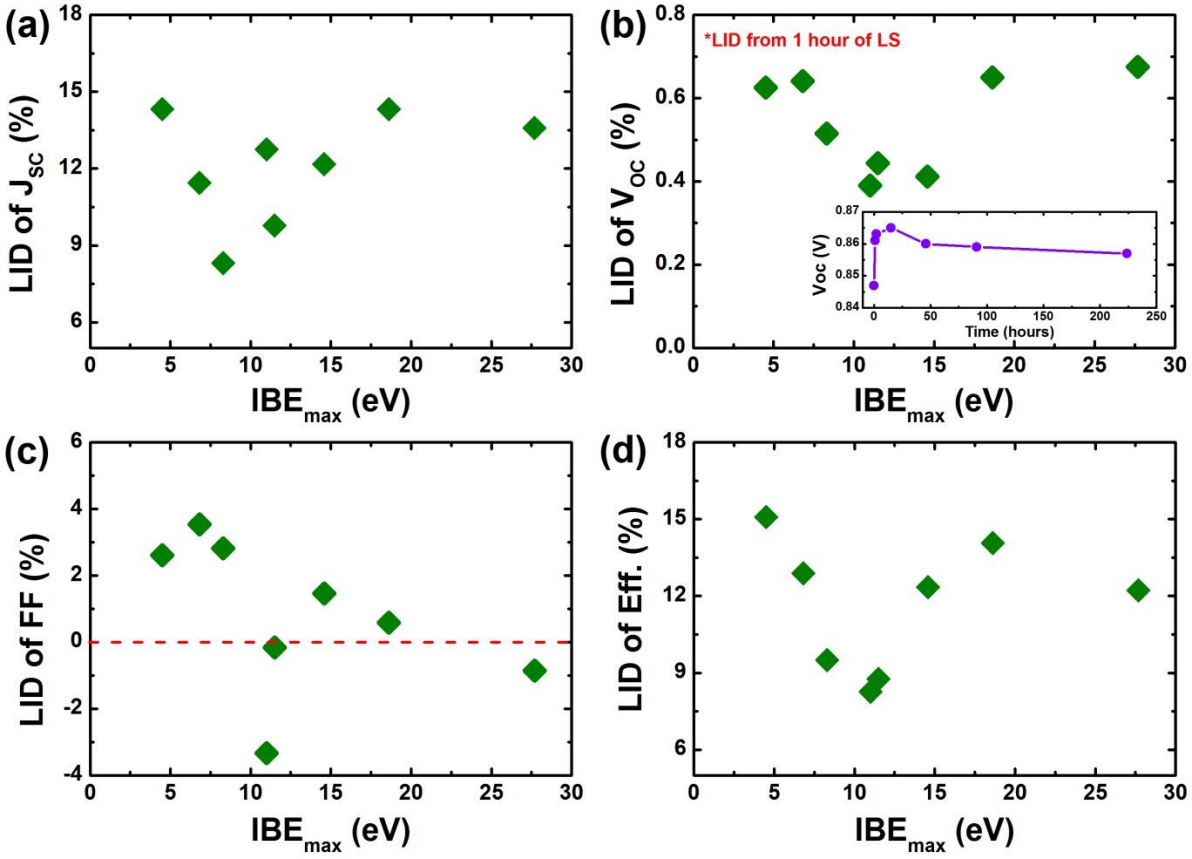

Figure 4.37 Relative LID of (a) J_{SC}, (b) V_{OC} (*using after one hour of LS as the initial state, the evolution of V_{OC} over time is shown in the inset), (c) FF, and (d) η for a-Si:H solar cells with absorber layers deposited at different ion energy conditions.

The reason for the unusually stable value of FF for this series of solar cells is not fully understood yet, although we recognize that they are all stable at quite poor values. Nevertheless, all the other parameters follow the trends of the variations in material transport properties. Note

that the LID of V_{OC} is estimated using the one hour light-soaked state as the "initial state", since it has been discussed above that a considerable increase in V_{OC} is seen upon LS for all the samples. The LID of V_{OC} for all these cells stays at a low level, as shown in Figure 4.37-(b). However, a minimum extent of degradation is still observed for the samples deposited with moderate ion energy conditions, and more specifically with IBE_{max} around 12 eV. In combination with the evolution of material properties studied above, one can naturally link these results with the ion-related interactions discussed in Section 4.3.2. Moderate ion energy conditions can be beneficial to achieve bulk material with greater quality as well as less defective *p*/*i* interface in the resulting solar cell device. However, excessive ion energies are highly undesirable, since the occurrence of effective atomic displacement on the growing surface can significantly impact the material properties and electronic stability under light exposure.

To sum up, these findings suggest that the performance of a-Si:H solar cells can indeed be impacted by the asymmetric plasma response through the use of TVW. With respect to the light-induced degradation, the results reinforce the capability of the semi-independently control in ion energy conditions during the intrinsic layer deposition for further process optimizations.

4.4. Summary

In this chapter, we have applied the multi-frequency TVW excitation technique to the RF-PECVD of silicon thin films. Making use of the amplitude asymmetry in the voltage waveforms, a semi-independent control over the IBE_{max} has been achieved. Based on the structural and electronic properties analyses, we find that a careful choice of the ion energy conditions during processing can be of vital importance to achieve high quality materials.

In the first part, concerning the μc-Si:H film deposition from the $SiF_4/H_2/Ar$ plasma chemistry, despite the relatively high process pressure (3 Torr), the impact of the small fraction of ions having IBE_{max} is revealed. Enhanced properties (crystalline grain features, material density and photoelectronic response) have been obtained with IBE_{max} around 45-55 eV. Higher ion energies above this range will induce some deterioration in the material quality, which can be attributed to silicon-related ion-induced bulk atomic displacement. When such TVW plasma-deposited intrinsic μc-Si:H films are incorporated into solar cell devices, the impact of ion energy is reflected directly by the *I-V* parameters. Single-junction μc-Si:H solar cells with an absorber layer deposited with IBE_{max} in the range of ~45-55 eV has shown an optimum performance, mainly attributed to the improvement of V_{OC}.

In the second part, the deposition of a-Si:H films from the SiH_4/H_2 plasma chemistry (at lower process pressure of 120 mTorr) has been studied. As for the conclusion of the study on μc-Si:H, a moderate increase in ion energy can result in a-Si:H film with improved material density and electronic stabilities. In analogy, an IBE_{max} threshold at ~12 eV, corresponding to the SiH_x^+-induced surface atomic displacement, has been determined to be responsible for the degradation in the material quality. As a result, single-junction a-Si:H solar cell device with better and more stable performance has been obtained by depositing its absorber layer with I_{max} around 12 eV during processing.

In addition to the crucial importance of ion energy, the effect of slope asymmetry through the utilization of the special group of *sawtooth* waveforms ($\varphi = 0.5\pi$ or 1.5π) has also been experimentally observed. Despite almost identical ion energy conditions, the asymmetric plasma response still leads to considerable differences in the material properties. Further studies focusing on this effect and its impact on surface processing will be presented in the following chapter.

Reference

[1] L. Martinu, J. Klemberg-Sapieha, O. Küttel, A. Raveh, and M. Wertheimer, "Critical ion energy and ion flux in the growth of films by plasma-enhanced chemical-vapor deposition", *J. Vac. Sci. Technol. A: Vac. Surf. Films*, vol. 12, no. 4, p. 1360, 1994.

[2] B. Kalache, A. I. Kosarev, R. Vanderhaghen, and P. Roca i Cabarrocas, "Ion bombardment effects on the microcrystalline silicon growth mechanisms and structure", *J. Non-Cryst. Solids*, vol. 299–302, Part 1, p. 63, 2002.

[3] J. Palmans, W. M. M. Kessels, and M. Creatore, "Plasma–surface interaction during low pressure microcrystalline silicon thin film growth", *J. Phys. D: Appl. Phys.*, vol. 47, no. 22, p. 224003, 2014.

[4] M. A. Lieberman and A. J. Lichtenberg, *Principles of Plasma Discharges and Materials Processing*, New Jersey: Wiley, 2005.

[5] P. Chabert and N. Braithwaite, *Physics of Radio-Frequency Plasmas*. Cambridge: Cambridge University Press, 2011.

[6] A. Matsuda, "Growth mechanism of microcrystalline silicon obtained from reactive plasmas", *Thin Solid Films*, vol. 337, no. 1-2, p. 1, 1999.

[7] A. Perret, P. Chabert, J. Jolly, and J.-P. Booth, "Ion energy uniformity in high-frequency capacitive discharges", *Appl. Phys. Lett.*, vol. 86, no. 2, p. 021501, 2005.

[8] P. Chabert, J. L. Raimbault, and J. M. Rax, "Self-consistent nonlinear transmission line model of standing wave effects in a capacitive discharge", *Phys. Plasmas*, vol. 11, no. 5, p. 1775, 2004.

[9] A. Shah, J. Dutta, N. Wyrsch, K. Prasad, H. Curtins, F. Finger, A. Howling, and C. Hollenstein, "VHF Plasma Deposition: A Comparative Overview", *MRS Online Proc. Libr. Arch.*, vol. 258, 1992.

[10] A. Perret, P. Chabert, J. Jolly, and J.-P. Booth, "Ion energy uniformity in high-frequency capacitive discharges", *Appl. Phys. Lett.*, vol. 86, no. 2, p. 021501, 2005.

[11] L. Sansonnens, A. Pletzer, D. Magni, A. A. Howling, C. Hollenstein, and J. P. M. Schmitt, "A voltage uniformity study in large-area reactors for RF plasma deposition", *Plasma Sources Sci. Technol.*, vol. 6, no. 2, p. 170, 1997.

[12] H. Goto, M. Sasaki, T. Ohmi, T. Shibata, A. Yamagami, N. Okamura, and O. Kamiya, "Minimizing Wafer Surface Damage and Chamber Material Contamination in New Plasma Processing Equipment", *Jpn. J. Appl. Phys.*, vol. 29, no. 12A, p. L2395, 1990.

[13] V. Georgieva, A. Bogaerts, and R. Gijbels, "Numerical investigation of ion-energy-distribution functions in single and dual frequency capacitively coupled plasma reactors", *Phys. Rev. E*, vol. 69, no. 2, p. 026406, 2004.

[14] H. Löwe, H. H. Goto, and T. Ohmi, "Control of ion energy and flux in a dual radio frequency excitation magnetron sputtering discharge", *J. Vac. Sci. Technol. A: Vac. Surf. Films*, vol. 9, no. 6, p. 3090, 1991.

[15] P. C. Boyle, A. R. Ellingboe, and M. M. Turner, "Independent control of ion current and

ion impact energy onto electrodes in dual frequency plasma devices", *J. Phys. D: Appl. Phys.*, vol. 37, no. 5, p. 697, 2004.

[16] Z. Donkó and Z. L. Petrović, "Analysis of a Capacitively Coupled Dual-Frequency CF_4 Discharge", *Jpn. J. Appl. Phys.*, vol. 45, no. 10S, p. 8151, 2006.

[17] M. M. Turner and P. Chabert, "Collisionless Heating in Capacitive Discharges Enhanced by Dual-Frequency Excitation", *Phys. Rev. Lett.*, vol. 96, no. 20, p. 205001, 2006.

[18] Z. Donkó, J. Schulze, P. Hartmann, I. Korolov, U. Czarnetzki, and E. Schungel, "The effect of secondary electrons on the separate control of ion energy and flux in dual-frequency capacitively coupled radio frequency discharges", *Appl. Phys. Lett.*, vol. 97, no. 8, p. 81501, 2010.

[19] A. Derzsi, Z. Donkó, and J. Schulze, "Coupling effects of driving frequencies on the electron heating in electronegative capacitive dual-frequency plasmas", *J. Phys. D: Appl. Phys.*, vol. 46, no. 48, p. 482001, 2013.

[20] D. O'Connell, T. Gans, E. Semmler, and P. Awakowicz, "The role of the relative voltage and phase for frequency coupling in a dual-frequency capacitively coupled plasma", *Appl. Phys. Lett.*, vol. 93, no. 8, p. 081502, 2008.

[21] J.-P. Booth, G. Curley, D. Marić, and P. Chabert, "Dual-frequency capacitive radiofrequency discharges: effect of low-frequency power on electron density and ion flux", *Plasma Sources Sci. Technol.*, vol. 19, no. 1, p. 015005, 2010.

[22] B. G. Heil, U. Czarnetzki, R. P. Brinkmann, and T. Mussenbrock, "On the possibility of making a geometrically symmetric RF-CCP discharge electrically asymmetric", *J. Phys. D: Appl. Phys.*, vol. 41, no. 16, p. 165202, 2008.

[23] J. Schulze, E. Schüngel, Z. Donkó, and U. Czarnetzki, "The electrical asymmetry effect in multi-frequency capacitively coupled radio frequency discharges", *Plasma Sources Sci. Technol.*, vol. 20, no. 1, p. 015017, 2011.

[24] T. Lafleur, "Tailored-waveform excitation of capacitively coupled plasmas and the electrical asymmetry effect", *Plasma Sources Sci. Technol.*, vol. 25, no. 1, p. 013001, 2016.

[25] B. Bruneau, "Control of radio frequency capacitively coupled plasma asymmetries using Tailored Voltage Waveforms", *PhD thesis*, École Polytechnique, 2015.

[26] Z. Donkó, J. Schulze, B. G. Heil, and U. Czarnetzki, "PIC simulations of the separate control of ion flux and energy in CCRF discharges via the electrical asymmetry effect", *J. Phys. D: Appl. Phys.*, vol. 42, no. 2, p. 025205, 2009.

[27] J. Schulze, E. Schüngel, and U. Czarnetzki, "The electrical asymmetry effect in capacitively coupled radio frequency discharges – measurements of dc self bias, ion energy and ion flux", *J. Phys. D: Appl. Phys.*, vol. 42, no. 9, p. 092005, 2009.

[28] E. V. Johnson, T. Verbeke, J.-C. Vanel, and J.-P. Booth, "Nanocrystalline silicon film growth morphology control through RF waveform tailoring", *J. Phys. D: Appl. Phys.*, vol. 43, no. 41, p. 412001, 2010.

[29] E. V. Johnson, S. Pouliquen, P. A. Delattre, and J.-P. Booth, "Control of Nanocrystalline

Silicon Growth Phase and Deposition Rate through Voltage Waveform Tailoring during PECVD", *MRS Online Proc. Libr. Arch.*, vol. 1339, 2011.

[30] E. V. Johnson, P. A. Delattre, and J.-P. Booth, "Microcrystalline silicon solar cells deposited using a plasma process excited by tailored voltage waveforms", *Appl. Phys. Lett.*, vol. 100, no. 13, p. 133503, 2012.

[31] E. V. Johnson, S. Pouliquen, P.-A. Delattre, and J.-P. Booth, "Tailored Voltage Waveform Deposition of Microcrystalline Silicon Thin Films from Hydrogen-Diluted Silane and Silicon Tetrafluoride: Optoelectronic Properties of Films", *Jpn. J. Appl. Phys.*, vol. 51, no. 8S1, p. 08HF01, 2012.

[32] E. V. Johnson, S. Pouliquen, P. A. Delattre, and J.-P. Booth, "Hydrogenated microcrystalline silicon thin films deposited by RF-PECVD under low ion bombardment energy using voltage waveform tailoring", *J. Non-Cryst. Solids*, vol. 358, no. 17, p. 1974, 2012.

[33] D. Hrunski, A. Janssen, T. Fritz, T. Hegemann, C. Clark, U. Schreiber, and G. Grabosch, "The influence of the electrical asymmetry effect on deposition uniformity of thin silicon film", *Thin Solid Films*, vol. 532, p. 56, 2013.

[34] D. Hrunski, F. Mootz, A. Zeuner, A. Janssen, H. Rost, R. Beckmann, S. Binder, E. Schüngel, S. Mohr, D. Luggenhölscher, U. Czarnetzki, and G. Grabosch, "Deposition of microcrystalline intrinsic silicon by the Electrical Asymmetry Effect technique", *Vacuum*, vol. 87, p. 114, 2013.

[35] E. Schüngel, R. Hofmann, S. Mohr, J. Schulze, J. Röpcke, and U. Czarnetzki, "Evaluation of the Electrical Asymmetry Effect by spectroscopic measurements of capacitively coupled discharges and silicon thin film depositions", *Thin Solid Films*, vol. 574, p. 60, 2015.

[36] M. M. Patterson, H. Y. Chu, and A. E. Wendt, "Arbitrary substrate voltage wave forms for manipulating energy distribution of bombarding ions during plasma processing", *Plasma Sources Sci. Technol.*, vol. 16, no. 2, p. 257, 2007.

[37] T. Lafleur, P. A. Delattre, J.-P. Booth, E. V. Johnson, and S. Dine, "Radio frequency current-voltage probe for impedance and power measurements in multi-frequency unmatched loads", *Rev. Sci. Instrum.*, vol. 84, no. 1, p. 015001, 2013.

[38] U. Czarnetzki, B. G. Heil, J. Schulze, Z. Donkó, T. Mussenbrock, and R. P. Brinkmann, "The Electrical Asymmetry Effect - A novel and simple method for separate control of ion energy and flux in capacitively coupled RF discharges", *J. Phys. Conf. Ser.*, vol. 162, no. 1, p. 12010, 2009.

[39] E. Schüngel, D. Eremin, J. Schulze, T. Mussenbrock, and U. Czarnetzki, "The electrical asymmetry effect in geometrically asymmetric capacitive radio frequency plasmas", *J. Appl. Phys.*, vol. 112, no. 5, p. 053302, 2012.

[40] A. Derzsi, I. Korolov, E. Schüngel, Z. Donkó, and J. Schulze, "Electron heating and control of ion properties in capacitive discharges driven by customized voltage waveforms", *Plasma Sources Sci. Technol.*, vol. 22, no. 6, p. 065009, 2013.

[41] J. Franek, S. Brandt, B. Berger, M. Liese, M. Barthel, E. Schüngel, and J. Schulze, "Power

supply and impedance matching to drive technological radio-frequency plasmas with customized voltage waveforms", *Rev. Sci. Instrum.*, vol. 86, no. 5, p. 053504, 2015.

[42] B. Berger, S. Brandt, J. Franek, E. Schüngel, M. Koepke, T. Mussenbrock, and J. Schulze, "Experimental investigations of electron heating dynamics and ion energy distributions in capacitive discharges driven by customized voltage waveforms", *J. Appl. Phys.*, vol. 118, no. 22, p. 223302, 2015.

[43] S. Brandt, B. Berger, E. Schüngel, I. Korolov, A. Derzsi, B. Bruneau, E. V. Johnson, T. Lafleur, D. O'Connell, M. Koepke, T Gans, J.-P. Booth, Z. Donkó, and J. Schulze, "Electron power absorption dynamics in capacitive radio frequency discharges driven by tailored voltage waveforms in CF_4", *Plasma Sources Sci. Technol.*, vol. 25, no. 4, p. 045015, 2016.

[44] E. V. Johnson and J.-P. Booth, "Circuit ´electrique pour adapter l'imp´edance d'une source et d'une charge sur une large gamme de fr´equences, proc´ed´e pour concevoir un tel circuit", *European patent*, EP 2675064 (A1), 2013.

[45] A. H. M. Smets and M. Kondo, "The role of ion-bulk interactions during high rate deposition of microcrystalline silicon by means of the multi-hole-cathode VHF plasma", *J. Non-Cryst. Solids*, vol. 352, no. 9-20, p. 937, 2006.

[46] A. C. Bronneberg, N. Cankoy, M. C. M. van de Sanden, and M. Creatore, "Ion-induced effects on grain boundaries and a-Si:H tissue quality in microcrystalline silicon films", *J. Vac. Sci. Technol. A: Vac. Surf. Films*, vol. 30, no. 6, p. 061512, 2012.

[47] B. Bruneau, J. K. Wang, J.-C. Dornstetter, and E. V. Johnson, "Growth mechanisms study of microcrystalline silicon deposited by SiH_4/H_2 plasma using tailored voltage waveforms", *J. Appl. Phys.*, vol. 115, p. 084901, 2014.

[48] B. Bruneau, M. Lepecq, J. K. Wang, J.-C. Dornstetter, J.-L. Maurice, and E. V. Johnson, "Effect of Ion Energy on Microcrystalline Silicon Material and Devices: A Study Using Tailored Voltage Waveforms", *IEEE J. Photovolt.*, vol. 4, no. 6, p. 1354, 2014.

[49] B. Bruneau, R. Cariou, J.-C. Dornstetter, M. Lepecq, J.-L. Maurice, P. Roca i Cabarrocas, and E. V. Johnson, "Ion Energy Threshold in Low-Temperature Silicon Epitaxy for Thin-Film Crystalline Photovoltaics", *IEEE J. Photovolt.*, vol. 4, no. 6, p. 1361, 2014.

[50] B. Bruneau, T. Novikova, T. Lafleur, J.-P. Booth, and E. V. Johnson, "Ion flux asymmetry in radiofrequency capacitively-coupled plasmas excited by *sawtooth*-like waveforms", *Plasma Sources Sci. Technol.*, vol. 23, no. 6, p. 065010, 2014.

[51] *Physical problems in microelectronics: Proceedings of the Fourth International School, ISPPM*, J. Kassabov (Ed.), Varna, Bulgaria, 1985.

[52] M. N. Islam and S. Kumar, "Influence of crystallite size distribution on the micro-Raman analysis of porous Si", *Appl. Phys. Lett.*, vol. 78, no. 6, p. 715, 2001.

[53] A. Abramov, D. Daineka, Y. Djeridane, and P. Roca i Cabarrocas, "Detailed study of surface and interface properties of μc-Si films", *J. Non-Cryst. Solids*, vol. 354, no. 19-25, p. 2218, 2008.

[54] Y. Djeridane, A. Abramov, and P. Roca i Cabarrocas, "Silane versus silicon tetrafluoride in the growth of microcrystalline silicon films by standard radio frequency glow discharge",

Thin Solid Films, vol. 515, no. 19, p. 7451, 2007.

[55] A. Abramov, Y. Djeridane, R. Vanderhaghen, and P. Roca i Cabarrocas, "Large grain μc-Si:H films deposited at low temperature: Growth process and electronic properties", *J. Non-Cryst. Solids*, vol. 352, no. 9-20, p. 964, 2006.

[56] G. Viera, S. Huet, and L. Boufendi, "Crystal size and temperature measurements in nanostructured silicon using Raman spectroscopy", *J. Appl. Phys.*, vol. 90, no. 8, p. 4175, 2001.

[57] L. Houben, M. Luysberg, P. Hapke, R. Carius, F. Finger, and H. Wagner, "Structural properties of microcrystalline silicon in the transition from highly crystalline to amorphous growth", *Philos. Mag. A*, vol. 77, no. 6, p. 1447, 1998.

[58] C. Ossadnik, S. Vepřek, and I. Gregora, "Applicability of Raman scattering for the characterization of nanocrystalline silicon", *Thin Solid Films*, vol. 337, no. 1-2, p. 148, 1999.

[59] S. Klein, F. Finger, R. Carius, T. Dylla, B. Rech, M. Grimm, L. Houben, and M. Stutzmann., "Intrinsic microcrystalline silicon prepared by hot-wire chemical vapour deposition for thin film solar cells", *Thin Solid Films*, vol. 430, no. 1-2, p. 202, 2003.

[60] A. Hiraki, T. Imura, K. Mogi, and M. Tashiro, "Si-H VIBRATIONAL PROPERTIES IN CRYSTALLIZED HYDROGENATED SILICON FABRICATED BY REACTIVE SPUTTERING IN H_2 ATMOSPHERE", *J. Phys. Colloq.*, vol. 42, no. C4, p. C4-277, 1981.

[61] Y. J. Chabal, "Hydrogen Vibration on Si(111)7x7: Evidence for a Unique Chemisorption Site.", *Phys. Rev. Lett.*, vol. 51, no. 24, p. 2233, 1983.

[62] M. A. Hachicha and E. Bustarret, "Transport Properties of B-, P-Doped and Undoped 50 kHz PECVD Microcrystalline Silicon", *MRS Online Proc. Libr. Arch.*, vol. 164, 1989.

[63] N. Blayo and B. Drevillon, "Infrared ellipsometry study of the vibrational properties of growing microcrystalline silicon thin films", *J. Non-Cryst. Solids*, vol. 137-138, Part 2, p. 775, 1991.

[64] U. Kroll, J. Meier, A. Shah, S. Mikhailov, and J. Weber, "Hydrogen in amorphous and microcrystalline silicon films prepared by hydrogen dilution", *J. Appl. Phys.*, vol. 80, no. 9, p. 4971, 1996.

[65] M. Scheib, B. Schröder, and H. Oechsner, "Deposition of nanocrystalline silicon films (nc-Si:H) from a pure ECWR-SiH_4 plasma", *J. Non-Cryst. Solids*, vol. 198, p. 895, 1996.

[66] J. K. Rath, K. F. Feenstra, D. Ruff, H. Meiling, and R. E. I. Schropp, "Purely Intrinsic Poly-Silicon Films by Hot Wire Chemical Vapor Deposition", *MRS Online Proc. Libr. Arch.*, vol. 452, 1996.

[67] H. Fujiwara, M. Kondo, and A. Matsuda, "Nucleation mechanism of microcrystalline silicon from the amorphous phase", *J. Non-Cryst. Solids*, vol. 338-340, p. 97, 2004.

[68] S. Lebib and P. Roca i Cabarrocas, "Effects of ion energy on the crystal size and hydrogen bonding in plasma-deposited nanocrystalline silicon thin films", *J. Appl. Phys.*, vol. 97, no. 10, p. 104310, 2005.

[69] A. H. M. Smets, T. Matsui, and M. Kondo, "Infrared analysis of the bulk silicon-hydrogen

bonds as an optimization tool for high-rate deposition of microcrystalline silicon solar cells", *Appl. Phys. Lett.*, vol. 92, no. 3, p. 33503, 2008.

[70] G. Lucovsky, "Chemical effects on the frequencies of Si-H vibrations in amorphous solids", *Solid State Commun.*, vol. 29, no. 8, p. 571, 1979.

[71] T. S. Shi, S. N. Sahu, G. S. Oehrlein, A. Hiraki, and J. W. Corbett, "Models for the Hydrogen-Related Defect-Impurity Complexes and Si-H Infrared Bands in Crystalline Silicon", *Phys. Status Solidi A*, vol. 74, no. 1, p. 329, 1982.

[72] V. A. Burrows, Y. J. Chabal, G. S. Higashi, K. Raghavachari, and S. B. Christman, "Infrared spectroscopy of Si(111) surfaces after HF treatment: Hydrogen termination and surface morphology", *Appl. Phys. Lett.*, vol. 53, no. 11, p. 998, 1988.

[73] M. Chaigneau, E. V. Johnson, L. Kroely, P. Roca i Cabarrocas, and R. Ossikovski, "Polarized Raman spectroscopy analysis of SiH_x bonds in nanocrystalline silicon thin films", *Thin Solid Films*, vol. 537, p. 145, 2013.

[74] E. Bhattacharya and A. H. Mahan, "Microstructure and the light-induced metastability in hydrogenated amorphous silicon", *Appl. Phys. Lett.*, vol. 52, no. 19, p. 1587, 1988.

[75] J.-C. Dornstetter, S. Kasouit, and P. Roca i Cabarrocas, "Deposition of High-Efficiency Microcrystalline Silicon Solar Cells Using SiF_4/H_2/Ar Mixtures", *IEEE J. Photovolt.*, vol. 3, no. 1, p. 581, 2013.

[76] A. Kono, N. Koike, K. Okuda, and T. Goto, "Laser-Induced-Fluorescence Detection of SiH_2 Radicals in a Radio-Frequency Silane Plasma", *Jpn. J. Appl. Phys.*, vol. 32, no. 4A, p. L543, 1993.

[77] D. Mataras, S. Cavadias, and D. Rapakoulias, "Spatial profiles of reactive intermediates in rf silane discharges", *J. Appl. Phys.*, vol. 66, no. 1, p. 119, 1989.

[78] L. Sansonnens, A. A. Howling, C. Hollenstein, J.-L. Dorier, and U. Kroll, "The role of metastable atoms in argon-diluted silane radiofrequency plasmas", *J. Phys. D: Appl. Phys.*, vol. 27, no. 7, p. 1406, 1994.

[79] U. K. Das, P. Chaudhuri, and S. T. Kshirsagar, "Effect of argon dilution on the structure of microcrystalline silicon deposited from silane", *J. Appl. Phys.*, vol. 80, no. 9, p. 5389, 1996.

[80] R. Léal, P. Roca i Cabarrocas, J.-L. Maurice, G. Poulain, I. Cosme Bolanos, W. Chen, R. Cariou, B. Bruneau, F. Haddad, and J.-C. Dornstetter, "Epitaxial Growth of Silicon Thin Films by Low Temperature RF-PECVD from SiF4/H2/Ar", *29th Proceedings of the 23th IEEE Photovoltaic Specialists Conference*, Amsterdam, p. 1959, 2014.

[81] A. A. Langford, M. L. Fleet, B. P. Nelson, W. A. Lanford, and N. Maley, "Infrared absorption strength and hydrogen content of hydrogenated amorphous silicon", *Phys. Rev. B*, vol. 45, no. 23, p. 13367, 1992.

[82] R. J. Severens, G. J. H. Brussaard, M. C. M. van de Sanden, and D. C. Schram, "Characterization of plasma beam deposited amorphous hydrogenated silicon", *Appl. Phys. Lett.*, vol. 67, no. 4, p. 491, 1995.

[83] J. D. Ouwens and R. E. I. Schropp, "Hydrogen microstructure in hydrogenated amorphous

silicon", *Phys. Rev. B*, vol. 54, no. 24, p. 17759, 1996.

[84] W. Beyer and M. S. A. Ghazala, "Absorption Strengths of Si-H Vibrational Modes in Hydrogenated Silicon", *MRS Online Proc. Libr. Arch.*, vol. 507, p. 601, 1998.

[85] H. Fujiwara, M. Kondo, and A. Matsuda, "Microcrystalline silicon nucleation sites in the sub-surface of hydrogenated amorphous silicon", *Surf. Sci.*, vol. 497, no. 1-3, p. 333, 2002.

[86] S. Vignoli, A. Fontcuberta i Morral, R. Butté, R. Meaudre, and M. Meaudre, "Hydrogen related bonding structure in hydrogenated polymorphous and microcrystalline silicon", *J. Non-Cryst. Solids*, vol. 299-302, Part 1, p. 220, 2002.

[87] S. Agarwal, B. Hoex, and M. C. M. van de Sanden, "Hydrogen in Si–Si bond center and platelet-like defect configurations in amorphous hydrogenated silicon", *J. Vac. Sci. Technol. B*, vol. 22, no. 6, p. 2719, 2004.

[88] A. H. M. Smets, W. M. M. Kessels, and M. C. M. van de Sanden, "Vacancies and voids in hydrogenated amorphous silicon", *Appl. Phys. Lett.*, vol. 82, no. 10, p. 1547, 2003.

[89] M. H. Brodsky, M. Cardona, and J. J. Cuomo, "Infrared and Raman spectra of the silicon-hydrogen bonds in amorphous silicon prepared by glow discharge and sputtering", *Phys. Rev. B*, vol. 16, no. 8, p. 3556, 1977.

[90] W. Beyer, "Hydrogen Incorporation in Amorphous Silicon and Processes of Its Release", in *Tetrahedrally-Bonded Amorphous Semiconductors*, D. Adler and H. Fritzsche, Eds. Springer US, p. 129, 1985.

[91] E. A. G. Hamers, W. G. J. H. M. van Sark, J. Bezemer, H. Meiling, and W. F. van der Weg, "Structural properties of a-Si:H related to ion energy distributions in VHF silane deposition plasmas", *J. Non-Cryst. Solids*, vol. 226, no. 3, p. 205, 1998.

[92] T. Nishimoto, M. Takai, H. Miyahara, M. Kondo, and A. Matsuda, "Amorphous silicon solar cells deposited at high growth rate", *J. Non-Cryst. Solids*, vol. 299-302, Part 2, p. 1116, 2002.

[93] S. Lebib and P. Roca i Cabarrocas, "Structure and hydrogen bonding in plasma deposited polymorphous silicon thin films", *Eur. Phys. J. - Appl. Phys.*, vol. 26, no. 1, p. 17, 2004.

[94] U. Kroll, J. Meier, P. Torres, J. Pohl, and A. Shah, "From amorphous to microcrystalline silicon films prepared by hydrogen dilution using the VHF (70 MHz) GD technique", *J. Non-Cryst. Solids*, vol. 227-230, Part 1, p. 68, 1998.

[95] A. H. M. Smets, W. M. M. Kessels, and M. C. M. van de Sanden, "The effect of ion-surface and ion-bulk interactions during hydrogenated amorphous silicon deposition", *J. Appl. Phys.*, vol. 102, no. 7, p. 073523, 2007.

[96] G. Bugnon, G. Bugnon, G. Parascandolo, T. Söderström, P. Cuony, M. Despeisse, S. Hänni, J. Holovský, F. Meillaud, and C. Ballif, "A New View of Microcrystalline Silicon: The Role of Plasma Processing in Achieving a Dense and Stable Absorber Material for Photovoltaic Applications", *Adv. Funct. Mater.*, vol. 22, no. 17, p. 3665, 2012.

[97] C. Longeaud, D. Roy, and O. Saadane, "Role of interstitial hydrogen and voids in light-induced metastable defect formation in hydrogenated amorphous silicon: A model", *Phys. Rev. B*, vol. 65, no. 8, p. 085206, 2002.

[98] M. Isomura, M. Tanaka, and S. Tsuda, “Two kinds of dopant activation in boron-doped hydrogenated amorphous silicon–carbon”, *Appl. Phys. Lett.*, vol. 69, no. 10, p. 1396, 1996.

[99] P. Roca i Cabarrocas, P. Stáhel, S. Hamma, and Y. Poissant, “Stable single junction P-I-N solar cells with efficiencies approaching 10%.”, *Proceedings of the 2nd World Conference and Exhibition on Photovoltaic Solar Energy Conversion*, p. 355, 1998.

[100] C. Longeaud, J. P. Kleider, M. Gauthier, R. Brtiggemann, Y. Poissant, and P. Roca i Cabarrocas, “Polymorphous Silicon: Transport Properties and Solar Cell Applications”, *MRS Online Proc. Libr. Arch.*, vol. 557, 1999.

[101] P. Siamchai and M. Konagai, “The role of H_2 dilution in the deposition of a-Si:H films and its effect on the solar cell degradation”, *Proceeding of the 25th IEEE Photovoltaic Specialists Conference*, Washington, p. 1093, 1996.

[102] E. V. Johnson, F. Dadouche, M. E. Gueunier-Farret, J. P. Kleider, and P. Roca i Cabarrocas, “Open-circuit voltage increase dynamics in high and low deposition rate polymorphous silicon solar cells”, *Phys. Status Solidi A*, vol. 207, no. 3, p. 691, 2010.

[103] M. Isomura, M. Kondo, and A. Matsuda, “Enhancement of Open Circuit Voltage via Light soaking in Amorphous Silicon Solar Cells”, *Jpn. J. Appl. Phys.*, vol. 39, no. 6R, p. 3339, 2000.

[104] M. Stuckelberger, Y. Riesen, M. Despeisse, J.-W. Schüttauf, F.-J. Haug, and C. Ballif, “Light-induced V_{OC} increase and decrease in high-efficiency amorphous silicon solar cells”, *J. Appl. Phys.*, vol. 116, no. 9, p. 094503, 2014.

[105] J. Merten, J. M. Asensi, C. Voz, A. V. Shah, R. Platz, and J. Andreu, “Improved equivalent circuit and analytical model for amorphous silicon solar cells and modules”, *IEEE Trans. Electron Devices*, vol. 45, no. 2, p. 423, 1998.

[106] J. Hubin and A. V. Shah, “Effect of the recombination function on the collection in a p-i-n solar cell”, *Philos. Mag. Part B*, vol. 72, no. 6, p. 589, 1995.

Chapter 5 "Electrode-Selective" processing using TVW plasmas

Contents

We have shown that the PECVD of silicon thin films can be significantly influenced by the amplitude asymmetry of the driving voltage waveforms. However, experimental results have shown that the film deposition (in particular deposition rate) can also be different when using waveforms with identical amplitude asymmetry. This effect has been explained through observing that such waveforms do not have time-reversal symmetry, and this has been called the slope asymmetry effect.

This slope asymmetry effect has been thoroughly studied and demonstrated to be useful to understand fundamental aspects of plasma physics. However, all previous work on this topic was based on single-gas plasmas, and studies about application-relevant processes have been rarely reported. A better understanding of such effect in reactive multi-gas plasmas would be of great use.

5.1. Slope asymmetry effect

We have already discussed and demonstrated in Chapter 4 that one may use TVW with different global voltage minima and maxima to generate a controllable DC self-bias in a geometrically symmetric reactor, i.e., the electrical asymmetry effect. However, in some earlier studies about the electrical asymmetry effect, it has been observed that for certain TVW-excited plasmas the symmetry parameter ε can be different from unity even if the driven waveforms present identical global extrema. Accordingly, a DC self-bias can be generated in this case[1,2,3,4]. At that time, this effect was attributed to kinetic effects and has received little attention. Later on, Bruneau *et al*[5,6,7] studied this effect thoroughly by using approximate *sawtooth*-shaped waveforms. A slope asymmetry effect arising from the temporal asymmetry in the rising (positive) and falling (negative) slopes of the applied voltage waveform was proposed. Through this effect, completely different sheath dynamics in front to each electrode can be achieved, thus leading to spatially localized electron power absorption and an independent control over ion flux on each electrode.

As one can see in Figure 5.1, this special group of *sawtooth* waveforms can be obtained by choosing φ to be either 0.5π or 1.5π in Equation (4.10). Such waveforms have no difference in the positive and negative excursions, but are distinguished by having differing rise and fall rates during each fundamental RF period. It can be observed that $\varphi = 0.5\pi$ gives a waveform comprising a slow rise and a fast fall (Figure 5.1-(a)), while an opposite situation is observed at $\varphi = 1.5\pi$, giving a waveform with a reversed rate of rise and fall (Figure 5.1-(b)). For the sake of clarification,

[1] Z. Donkó, et al., *J. Phys. D: Appl. Phys.*, **42(2)**: 025205 (2009).
[2] J. Schulze, et al., *J. Appl. Phys.*, **106(6)**: 063307 (2009).
[3] E. Schüngel, et al., *J. Phys. D: Appl. Phys.*, **44(28)**: 285205 (2011).
[4] I. Korolov, et al., *J. Phys. D: Appl. Phys.*, **45(46)**: 465205 (2012).
[5] B. Bruneau, et al., *Plasma Sources Sci. Technol.*, **23(6)**: 065010 (2014).
[6] B. Bruneau, et al., *Plasma Sources Sci. Technol.*, **24(1)**: 015021 (2015).
[7] B. Bruneau, et al., *Phys. Rev. Lett.*, **114(12)**: 125002 (2015).

we classify these two waveforms as the *sawtooth-up* waveform and the *sawtooth-down* waveform, and that of the so-excited plasma as the *sawtooth-up* plasma and the *sawtooth-down* plasma. Furthermore, it is worth noting that since these two types of voltage waveforms are mirror images of each other, switching between them simply results in reversing the role of each electrode in a geometrically symmetric reactor.

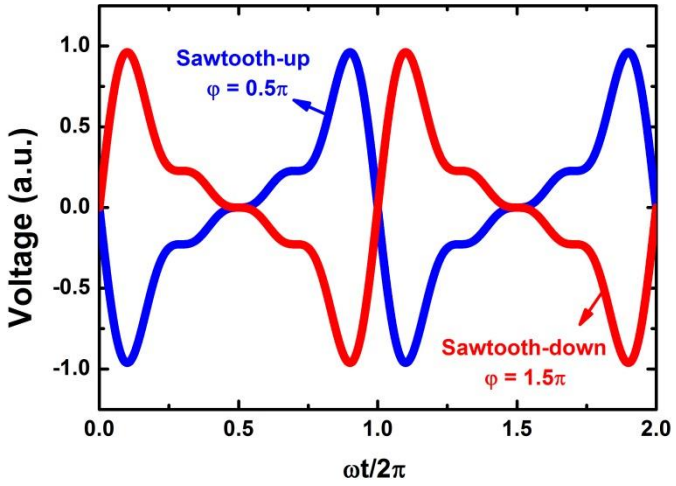

Figure 5.1 *Sawtooth-up* and *sawtooth-down* waveforms corresponding to φ = 0.5π and 1.5π, respectively.

As previously stated, an asymmetric plasma response (localized power absorption and differing ion flux on each electrode) can be observed when the plasma is driven by the *sawtooth* waveforms due to the slope asymmetry effect. However, a number of studies concerning single-gas plasmas (like Ar[1,2,4,5], H_2[8], O_2[3,9], and CF_4[10,11,12]) have shown that the difference in plasma chemistry can lead to fundamental differences in such discharge asymmetry, and the spatiotemporal distribution of the dominant plasma electron heating is identified as the main cause for these asymmetries[13].

Taking an Ar plasma excited by four-frequency TVW for instance, the normalized V_{DC} (to V_{PP}) and the ion flux ratio towards the powered electrode to that towards the grounded electrode as a function of φ is presented in Figure 5.2. As can be seen, it shows a positive value of V_{DC} in the case of *sawtooth-up* plasma at φ = 0.5π, but the sign inverts for the *sawtooth-down* plasma at φ = 1.5π. Moreover, a higher value of the ion flux ratio greater than unity is seen for the former, whereas less than unity for its counterpart. Such spatially different plasma properties can be of great interest for the CCP processes. For example, one can achieve a higher deposition (or etching) rate on the electrode of interest, without influence the IBE_{max} too much. Due to the accompanying low deposition/etching rate on the other electrode, the up-time of the reactor could be increased by keeping the maintenance-time low[13].

[8] B. Bruneau, et al., *Plasma Sources Sci. Technol.*, **25(4)**: 045019 (2016).
[9] A. Derzsi, et al., *Plasma Sources Sci. Technol.*, **26(3)**: 034002 (2017).
[10] E. Schüngel, et al., *J. Phys. D: Appl. Phys.*, **49(26)**: 265203 (2016).
[11] S. Brandt, et al., *Plasma Sources Sci. Technol.*, **25(4)**: 045015 (2016).
[12] B. Bruneau, et al., *J. Appl. Phys.*, **119(16)**: 163301 (2016).
[13] B. Bruneau, et al., *Plasma Sources Sci. Technol.*, **25(1)**: 01LT02 (2016).

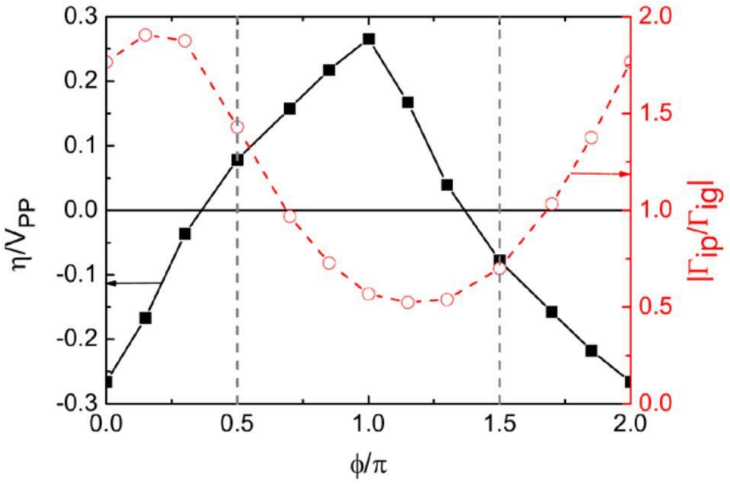

Figure 5.2 Normalized V_{DC} (left) and ion flux ratio (right) as a function of φ for an Ar plasma excited with TVW. The P, d_i, and V_{PP} are set to 0.4 Torr, 2.5 cm, and 200 V, respectively. Extracted from Ref. 5.

It is commonly believed that the sheath velocity plays an important role in the electron heating for CCP discharges[14,15,16]. Therefore, the asymmetric response observed in the Ar plasma above can be understood by considering the differing rise and fall rates of the applied voltage, since this can lead to the completely different sheath motions in front of each electrode. For the case of *sawtooth-down* plasma, the fast rise in voltage makes the sheath close to the grounded electrode expand rapidly, while the sheath close to the powered electrode contracts rapidly.

Figure 5.3 (first row) shows the comparison of the spatiotemporal profiles of electron impact excitation rates obtained from the PIC simulation and deduced from the experimentally measured emission intensity using phase resolved optical emission spectroscopy (PROES)[13]. The powered and grounded electrodes are located at x = 0 and 2.5 cm, respectively. As one can see, a good agreement is seen between simulation and experiment. A strong excitation peak is observed close to the grounded electrode right after the fast sheath expansion (the position of sheath edge is represented by the white lines). No peak is observed close to the powered electrode during the fast sheath contraction occurring at the same time, but several weaker excitation peaks are observed during the subsequent minor sheath expansions (due to the shape of the waveform). This behavior is consistent with the hard-wall model developed by Godyak[14].

Electropositive Ar plasmas, when operated in the α heating mode, are sustained by the electron energy gain in the oscillating sheath regions. Electrons are accelerated towards the quasi-neutral plasma bulk during the sheath expansion, and the faster the sheath expands, the higher energy they can gain. In this situation, a higher electron power absorption is expected at the rapidly expanding sheath edge, e.g., the sheath close to the grounded electrode in the case of *sawtooth-down* plasma seen in Figure 5.3. PIC simulation has shown that this asymmetric power absorption is attributed to a significant higher pressure heating where the fast sheath expansion occurs for the investigated Ar plasma[5,13]. As a result, a higher excitation rate close to the given electrode (grounded electrode

[14] V. A. Godyak, et al., *Sov. Phys. Tech. Phys.*, **16(7)**: 1073 (1972).
[15] M. A. Lieberman, et al., *Principles of Plasma Discharges and Materials Processing*, Wiley (2005).
[16] P. Chabert, et al., *Physics of Radio-Frequency Plasmas*, Cambridge University Press (2011).

in this case) is obtained, and accordingly a larger ion flux and a higher sheath density can be expected.

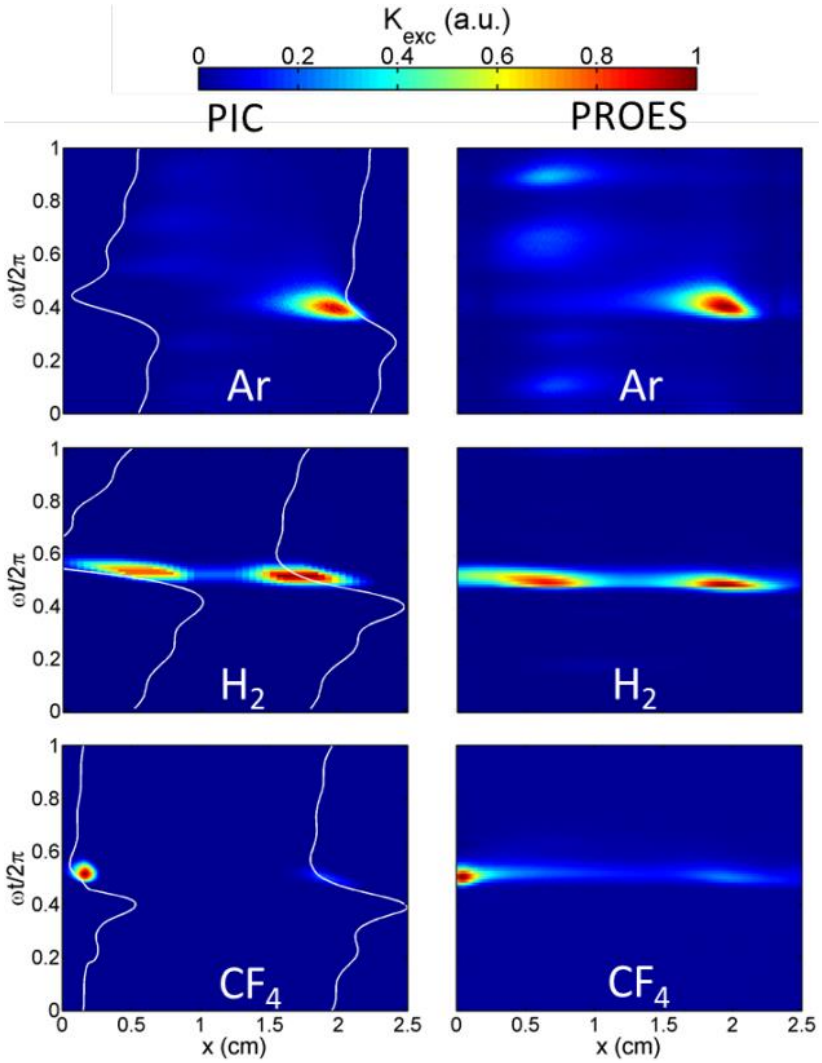

Figure 5.3 Excitation rate obtained from PROES measurements (left) and from PIC simulations (right) for an Ar (top row), H_2 (middle row), and CF_4 plasma (bottom row) excited with a *sawtooth-down* waveform in one RF period. The respective emission lines for Ar, H_2, and CF_4 are 750.4 nm, 656 nm (H_α), and 703.7 nm (F atom). Extracted from Ref. 13.

For an electronegative carbon tetrafluoride (CF_4), an inverted situation is observed (third row of Figure 5.3). In contrast to Ar, the most intense excitation is seen close to the powered electrode where a fast sheath contraction occurs. This is due to the fact that the electron heating for a CF_4 plasma can operate in a drift-ambipolar (DA) mode[17] depending on the process conditions. The collisional electron attachment process leads to the formation of a large amount of negative ions, causing a depletion of electron density and conductivity, so that a strong electric field forms in the plasma bulk. This can prevent electrons from instantaneously following the rapidly collapsing sheath close to the powered electrode by diffusion. Then, a local maxima in the electron density at

[17] J. Schulze, et al., *Phys. Rev. Lett.*, **107(27)**: 275001 (2011).

the electropositive edge region of the discharge pushes the electrons into the plasma bulk, and while positive ions continuously flow towards the electrode. Thus, an ambipolar electric field is built up at the sheath edge to couple the motions of electrons and positive ions, in order to accelerate electrons towards the electrode to compensate the ion flux. As a result, the electrons gain sufficient energy in this region, causing a higher production of negative ions. Then a local potential well is formed in front of the powered electrode, which traps these energetic electrons and reduces the possibility of their loss to the electrode[11]. This in turn increases the probability of the electron attachment process and negative ions generation. As a feedback, the local conductivity will be further reduced, leading to the enhancement of the reversed electric field. Therefore, this reversed electric field is the main power source for electrons, and such a positive feedback loop makes it self-sustaining until the plasma stabilizes. Consequently, the discharge symmetry is reversed compared to a plasma operated in the α-mode.

The results for a H_2 plasma is also presented in Figure 5.3 (middle row). As can be seen, excitation peaks with similar amplitudes are observed in front of both electrodes. This indicates that a hybrid combination of α- and DA-mode exists in the H_2 plasma, namely both the fast sheath expansion and the fast sheath contraction can lead to the intense electron power absorption (excitation).

To conclude, these results from the literature remind us that single-gas plasmas excited with temporally asymmetric *sawtooth* waveforms can have a local asymmetric response, and this asymmetry can actually help to identify specificities of the plasma chemistry. When the plasma heating operates in the α-mode (Ar), the most intense electron power absorption occurs close to the electrode experiencing a fast sheath expansion. Contrarily, for a highly electronegative plasma where the DA-mode dominates (CF_4), the fast sheath contraction will lead to the localized power absorption. While for the H_2 plasma operated under the investigated conditions, a hybrid α- and DA-mode has been found, thus leading to the observation of a more symmetric plasma response.

5.2. $SiF_4/H_2/Ar$ plasma chemistry

It has been discussed above that the asymmetric plasma response generated by *sawtooth* waveforms originates from the differing voltage rise and fall rates, hence a waveform composed of only two regions with different slopes can be viewed as a good candidate to the maximize this asymmetry. Accordingly, a certain type of "refined" *sawtooth* waveform has been proposed as[6]

$$\mathrm{V(t)} = \pm A \sum_{k=1}^{n} \frac{1}{k} sin(k\omega t) \tag{5.1}$$

in which the minus sign corresponds to the *sawtooth-up* waveform, and the plus sign corresponds to the *sawtooth-down* waveform. Presented in Figure 5.4 is the comparison of the two types of *sawtooth-down* waveforms based on Equation (4.10) and Equation (5.1). As one can see, the former waveform (red) shows two sharp voltage drops before and after the steep rise. It has been shown in an Ar plasma that these two voltage drops can actually lead to two small ionization peaks close to the grounded electrode, thus giving a reduced plasma asymmetry. This can be minimized by using the refined waveform (black). PIC simulations have confirmed that applying such a refined waveform allows one to maximize the ion flux asymmetry in the resulting plasma process[6].

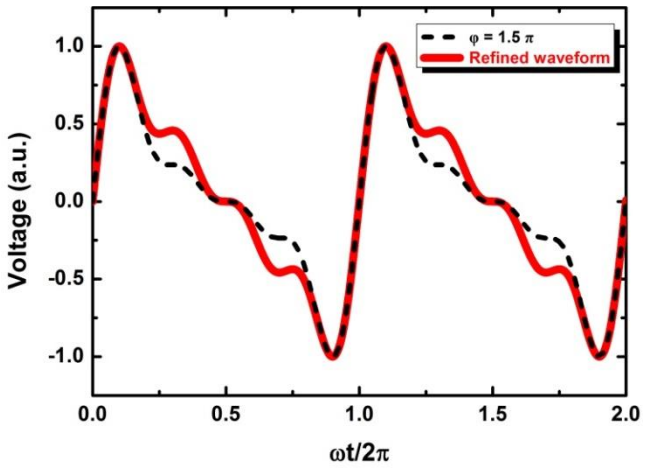

Figure 5.4 Comparison of initial *sawtooth-down* waveform based on Equation (4.10) and refined *sawtooth-down* waveform based on Equation (5.1) with *n* equals to four.

However, it should be noticed that this optimization is based on the assumption of a constant ion density in the plasma sheaths. Since the plasma current waveform and sheath densities are not known a priori for the case of voltage-driven discharges, these *sawtooth* waveforms might be different from the most optimized waveforms in reality. Nevertheless, the general idea of this optimization is trying to increase said asymmetry in the plasma response. For the following studies in this chapter, all the *sawtooth* waveforms will be generated based on Equation (5.1).

5.2.1. "Electrode-selective" processing using sawtooth waveforms

Based on the results in Section 4.2, one could expect that the slope asymmetry effect caused by the driving voltage waveform could have a strong impact on the resulting surface processes in an $SiF_4/H_2/Ar$ plasma chemistry. Extensive studies about the deposition and etching of silicon thin films have therefore been carried out on the PHILIX reactor.

5.2.1.1. Differing deposition rates

First of all, two sets of samples were deposited on glass substrates positioned on the grounded electrode. The H_2 flow rate was varied, and the two types of *sawtooth* waveforms were used, keeping V_{PP} constant at 285 V. The process conditions are described in Table 5.1. For the sake of brevity, samples deposited using the *sawtooth-up* waveform and the *sawtooth-down* waveform are named *sawtooth-up* sample and *sawtooth-down* sample.

Table 5.1 Process conditions for silicon thin film deposition using *sawtooth* waveforms with varying H_2 flow rate.

V_{PP}	P	d_i	T_{sub}	T_{rf}	SiF_4	H_2	Ar
V	Torr	cm	°C	°C	sccm	sccm	sccm
285	3	3	150	80	3.6	0-6	88

Figure 5.5 shows the variation of the deposition rate r_d as a function of H_2 flow rate for these two sets of samples. As can be seen in both cases, r_d increases with H_2 flow rate up to a value of 3 sccm, and then slightly decreases for greater H_2 flows. However, one can note that the *sawtooth-down* samples (shown in red) present a higher r_d than their counterparts (shown in blue) at low H_2 flow rates, and that the reverse situation is observed for H_2 flow rates above 3 sccm.

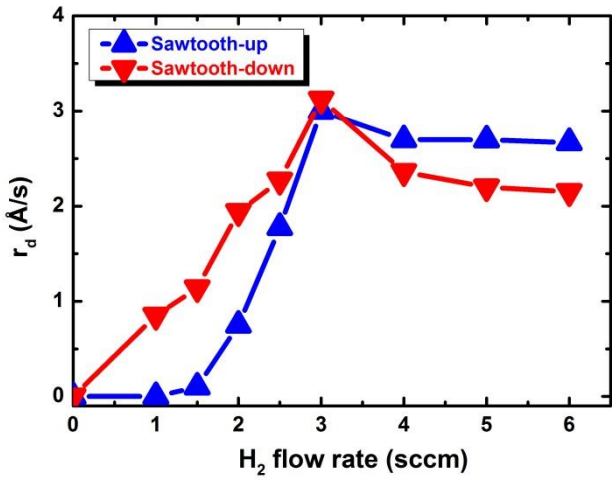

Figure 5.5 Variation of r_d of silicon thin films using *sawtooth-up* (blue) and *sawtooth-down* (red) waveforms with varying H_2 flow rate.

Most interestingly, the r_d for H_2 flow rates below 1.5 sccm is almost equal to zero in the case of the *sawtooth-up* waveform, while a deposition process is observed for its counterpart. To illustrate this result, images of the *sawtooth-up* and *-down* samples deposited at H_2 = 1 sccm are compared in Figure 5.6. Despite the presence of deposition inhomogeneity resulting from the plasma instability and geometrical limitations of the process chamber, one can clearly see that a deposition process is obtained from *sawtooth-down* plasma (Figure 5.6-(b)), but nothing from the *sawtooth-up* plasma (Figure 5.6-(a)).

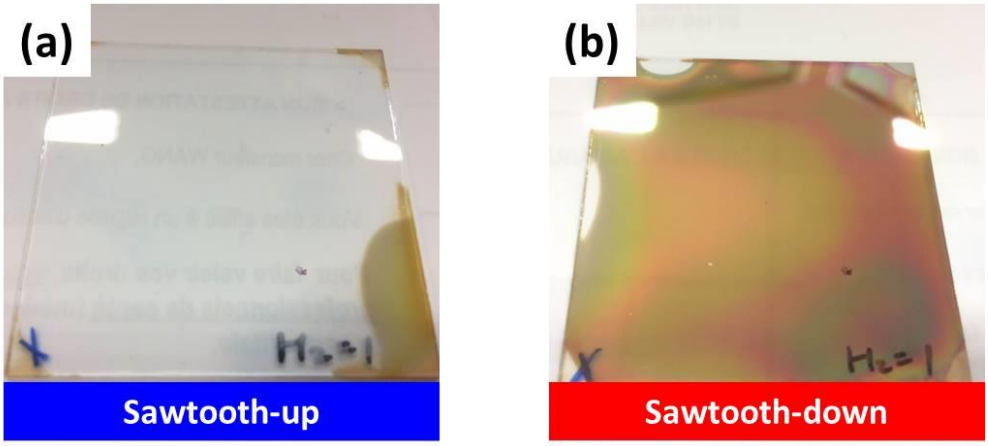

Figure 5.6 Images of samples deposited using (a) *sawtooth-up* and (b) *sawtooth-down* waveforms with H_2 flow rate set to 1 sccm.

5.2.1.2. Observation of etching

As discussed in Section 1.3, material growth from the $SiF_4/H_2/Ar$ plasma chemistry results from a competition between deposition and etching processes. Therefore, a second set of two-step depositions were carried out to allow us to see if etching is occurring. For these experiments, before the $SiF_4/H_2/Ar$ plasma processing (in the second step), an underlying a-Si:H layer was prepared using the standard 13.56 MHz RF source (in the first step). The plasma was stopped between these two steps, and the process conditions for this sublayer of a-Si:H are shown in Table 5.2.

Table 5.2 Process conditions for a-Si:H underlying layer in two-step deposition study.

V_{PP}	P	d_i	T_{sub}	T_{rf}	SiH_4	H_2
V	Torr	cm	°C	°C	sccm	sccm
385	0.4	3	150	80	10	20

To evaluate the resulting surface processes, *in-situ* ellipsometry measurements have been performed during processing. Figure 5.7-(a) shows the evolution of the value of $\langle\varepsilon_i\rangle$ at 3.6 eV ($\langle\varepsilon_i\rangle_{3.6}$) over time during the second processing step. Curves are shown for each of the two types of *sawtooth* waveform, and both with H_2 flow rate at 1.5 sccm. Note that the thickness of the underlying a-Si:H layer in these two processes were slightly different: ~60 nm and ~100 nm were used for the *sawtooth-up* process and *sawtooth-down* process, respectively.

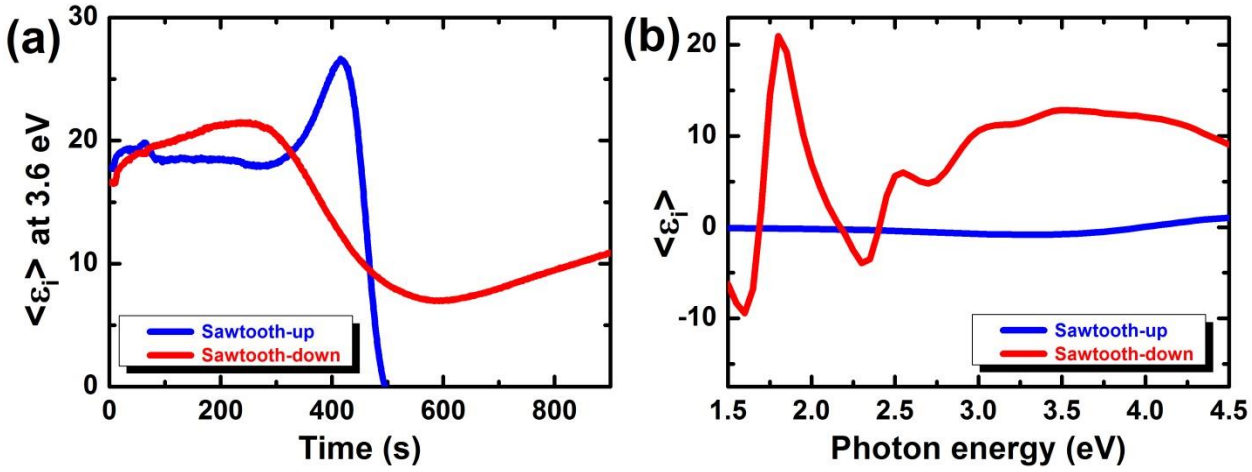

Figure 5.7 (a) Evolution of $\langle\varepsilon_i\rangle$ at 3.6 eV over time in the second step for the two-step deposited films. (b) Ellipsometry spectra for the films after the plasma processing using the *sawtooth-up* (blue) and *sawtooth-down* (red) waveforms. H_2 flow rate is set to 1.5 sccm.

As can be seen, this sublayer allows us to observe that indeed, an etching of the underlying a-Si:H layer is occurring at such low H_2 injection. The *sawtooth-up* sample shows a slow increase in $\langle\varepsilon_i\rangle_{3.6}$ after ~275 s. A sharp decrease is observed starting at ~420 s, and then $\langle\varepsilon_i\rangle_{3.6}$ goes to zero at ~500 s. This indicates that the a-Si:H layer deposited in the first step has been effectively etched during the plasma processing in the second step (the increase is due to an interference fringe). The

ellipsometry spectra of the resulting samples are presented in Figure 5.7-(b). A different situation is observed in the case of the *sawtooth-down* process. In the second step, $\langle \varepsilon_i \rangle_{3.6}$ goes from the value expected for a-Si:H (~20), and then decreases as a microcrystalline phase forms on the surface. From the ellipsometry measurements, the films' thicknesses before and after the plasma treatment can be estimated. Although a precise ellipsometric modeling for the plasma-treated layer is difficult due to the complex stack, one can still get some insights about the thickness by using a simplified model, as shown in Figure 5.8. In doing so, one can see that after 900 s of plasma treatment, a thicker layer with a thickness of ~173 nm is obtained.

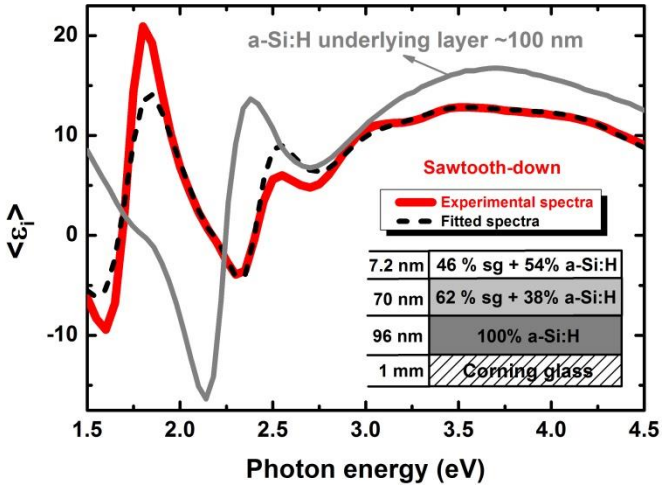

Figure 5.8 Comparison of ellipsometry spectra for film before (gray) and after (red) the *sawtooth-down* plasma treatment for 900 s. The fitted spectra for the film after treatment is shown in dashed.

Based on this ellipsometric modeling, the variation of r_d (in the second step) as a function of H_2 flow rate for all this series of films is shown in Figure 5.9. To keep it simple, we classify all these results by a net deposition rate $r_{d,net}$. In this sense, a negative value of $r_{d,net}$ indicates the occurrence of a net etching process, as indicated by the shaded region.

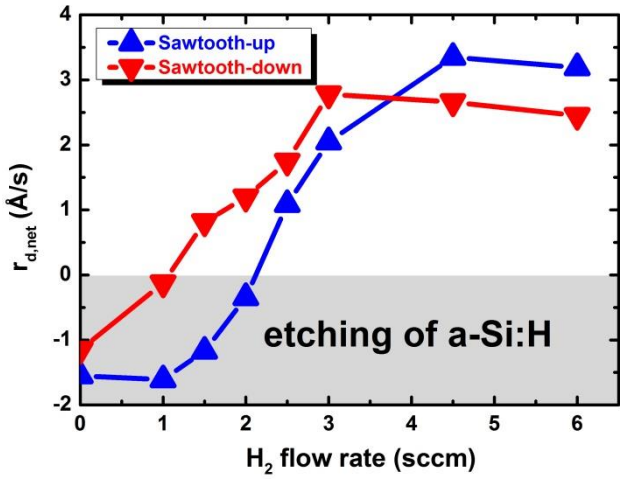

Figure 5.9 Variation of $r_{d,net}$ of silicon thin films deposited on the underlying a-Si:H layer using the *sawtooth-up* (blue) and *sawtooth-down* (red) waveforms with varying H_2 flow rate.

As in the results of the one-step deposition in Figure 5.5, $r_{d,net}$ increases with the H_2 flow rate initially, followed by a slight decrease at higher flows. It can be observed that when there is no H_2 injection, etching processes are obtained in both cases. However, once a small amount of H_2 is added to the mixture, completely different surface processes for the *sawtooth-up* and *-down* plasmas are observed. In the case of only 1 sccm H_2, the *sawtooth-up* plasma leads to a strong etching effect, while almost no thickness variation of the underlying a-Si:H layer is observed for the *sawtooth-down* plasma. When the H_2 flow is increased to 1.5 sccm, an etching process ($r_{d,net}$ = -1.2 Å/s) is still observed for the *sawtooth-up* plasma, whereas a deposition process with ($r_{d,net}$ = 0.82 Å/s) is observed for its counterpart, as shown in Figure 5.7. By further increasing the H_2 flow rate up to 2 sccm, the etching effect is essentially suppressed for the *sawtooth-up* plasma, while for the *sawtooth-down* plasma, a further increase in $r_{d,net}$ up to 1.2 Å/s is seen.

In brief, by applying the two types of *sawtooth* waveforms, conspicuously different surface processes are observed during $SiF_4/H_2/Ar$ plasma processing, despite the fact that all other process conditions are kept constant. Recalling that **in a geometrically symmetric reactor**, **switching between these two waveforms is equivalent to reversing the roles of two electrodes**, the results in Figure 5.5 and Figure 5.9 therefore indicate that differing deposition or etching process could be achieved on each electrode of a CCP system, as determined by the relative H_2 flow rate. In short, one can realize an "electrode-selective" process in a CCP reactor, namely achieving either a deposition or etching process on one electrode (or substrate) without influencing the other, or even a deposition process on one electrode but an etching process on the other.

Gas molecule consumption

As discussed in Section 2.4.1, the use of RGA allows one to quantify the gas molecule consumption in a plasma process. Therefore, verify that changes in gas consumption are not responsible for the selective processing shown above, as well as to further understand the changes in the plasma that enable such electrode-selective processing, complementary measurements have been performed by analyzing the effluent gas composition by RGA.

Figure 5.10 shows the deduced results plotted as a function of H_2 flow rate. As one can see, the *sawtooth-up* and *-down* plasmas present almost identical results. This indicates that changes in gas consumption are not responsible for the appearance of this selective processing. When no H_2 is injected, SiF_4 is barely consumed at all, relative to its actual flow (3.6 sccm). For low values of H_2 flow, H_2 is essentially fully consumed, while the depletion of SiF_4 increases with H_2 flow rate and is consumed at about half the rate of H_2. When the H_2 flow increases above about 3 sccm, the consumption of H_2 remains constant, as does that of SiF_4.

These results can help us to make some assertions about what is occurring in the plasma with increasing H_2 injection. As can be seen in Figure 5.10, at low H_2 flow rates, the consumption of SiF_4 increases with H_2. This is consistent with the *phenomenological model* described in Section 1.3, which states that the role of H_2 is to remove the fluorine produced by the SiF_4 dissociation via the formation of HF molecules. Without the scavenging of fluorine via this process, atomic fluorine etches any silicon surface. Therefore, the presence of H_2 is the limiting factor in the consumption of SiF_4. However, due to the slope asymmetry effect caused by the *sawtooth* waveforms, the asymmetric electron power absorption entails additional complexity in this

experiment. The resulting local variations in gas dissociation are therefore responsible for the spatial variation in the fluorine removal process.

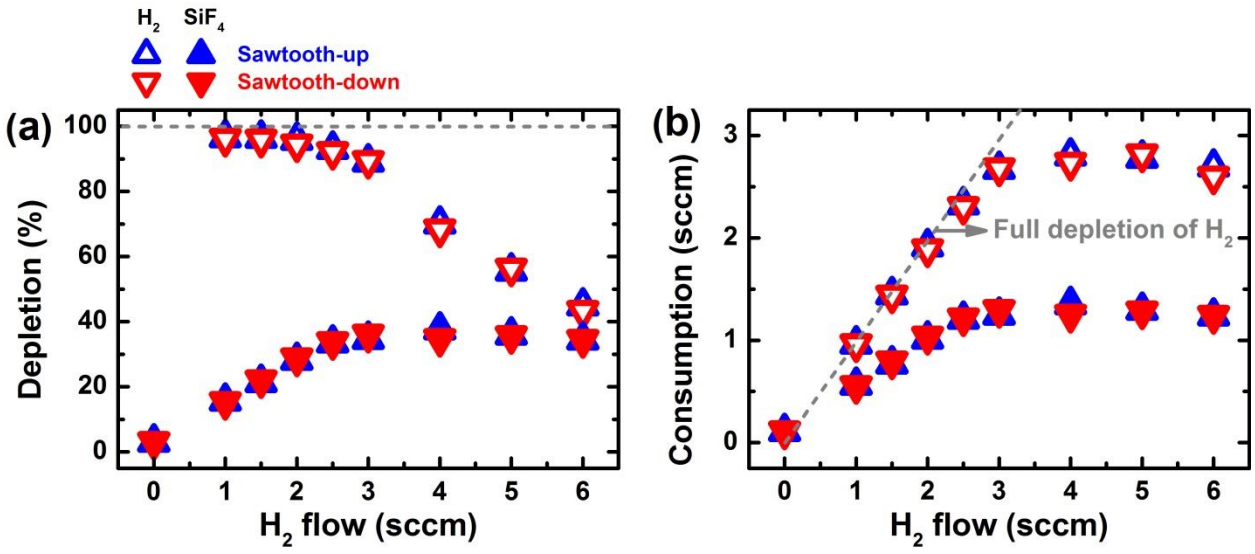

Figure 5.10 (a) Depletion and (b) consumption of H_2 (open symbols) and SiF_4 (solid symbols) as a function of H_2 flow rate, as measured using RGA. The dashed line in (b) indicates the full depletion of H_2.

DC self-bias as an indicator

According to the analytical model concerning the generation of V_{DC} through the electrical asymmetry effect (presented in Section 4.1.2), a modified version of Equation (4.7) for the situation of *sawtooth* waveforms ($V_{max} = -V_{min}$) can be expressed as[13]

$$V_{DC} = -\frac{V_{PP}}{2} \times \frac{1-\varepsilon}{1+\varepsilon} \tag{5.2}$$

Knowing the definition of ε, Equation (5.2) states that for a plasma operated in a geometrically symmetric reactor, the V_{DC} that forms can be directly linked with the mean ion density in the sheath (or ion fluxes). Therefore, for the electropositive Ar plasma shown in Figure 5.3, a higher sheath density close to the **grounded** electrode ($\varepsilon < 1$) will lead to a **negative** V_{DC} to equalize the period-averaged electron and ion fluxes, as shown in Figure 5.11. However, for the electronegative CF_4 plasma having an inverted discharge asymmetry, a higher sheath density close to the **powered** electrode ($\varepsilon > 1$) is expected. As a consequence, one will observe **positive** values of V_{DC}. Furthermore, for the H_2 plasma operated in a hybrid α-DA electron heating mode, V_{DC} values close to zero are obtained.

Thinking in the opposite way, for a plasma excited by *sawtooth* waveforms, the sign of V_{DC} can therefore be used to determining the dominant electron heating mechanism (and thus the discharge asymmetry) during processing. However, it would be difficult to use this technique directly for our experiments, as a non-zero V_{DC} will always exist due to the geometrical asymmetry of the reactor. However, we can still use the experimentally obtained V_{DC} values as an indicator for the discharge asymmetry by comparing the **relative** values for *sawtooth-up* and *-down* waveforms, since the

geometrical asymmetry will just lead to an offset of the V_{DC} values. In the following work, particular attention was paid to the relative values of V_{DC} during processing for both *sawtooth-up* and *-down* waveforms.

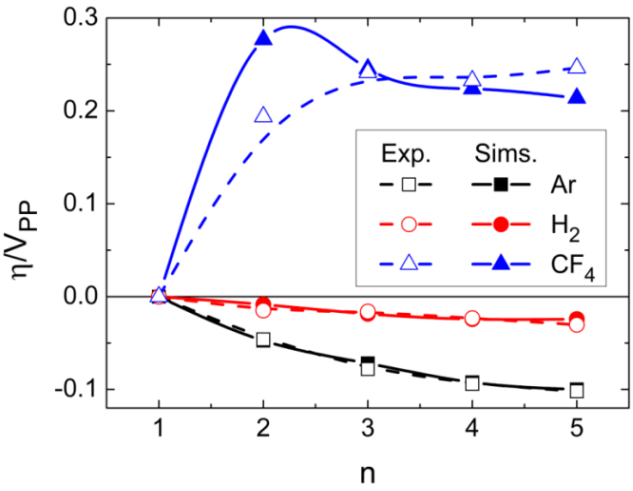

Figure 5.11 Normalized V_{DC} obtained from experiments (empty symbols) and from PIC simulations (solid symbols) obtained for Ar (black), H_2 (red), and CF_4 (blue) plasmas excited with *sawtooth-down* waveform composed of *n* frequencies. Extracted from Ref. 13.

Figure 5.12-(a) shows the experimentally measured V_{DC} as a function of H_2 flow rate. For both types of *sawtooth* plasma processes, V_{DC} decreases in absolute value (less negative) with increasing H_2 flow up to 3 sccm, and then stays roughly constant at a lower level at higher flow rates. This trend has also been reported in previous work for the same plasma chemistry excited with a single-frequency (13.56 MHz) waveform[18]. However, the absolute values of V_{DC} for each *sawtooth* plasma process remain quite different. As one can see, a significant decrease (in absolute value) of V_{DC} is found for *sawtooth-down* plasma, while less so for the *sawtooth-up* plasma. Significantly, a reverse in the relative magnitudes is observed at 1 sccm.

Again, using Equation (4.14), the IBE_{max} during the deposition of these two sets of films can be determined, and the results are shown in Figure 5.12-(b). Except for the case of H_2 = 1 sccm, all these processes present a difference in ion energy conditions between *sawtooth-up* and *-down*. Taking the case of no H_2 injection for example (although almost no deposition occurs), a value of IBE_{max} around 29 eV is obtained for the *sawtooth-down* process but around 40 eV for *sawtooth-up*. Then, the increase of H_2 flow rate leads to a greater increase in ion energy for *sawtooth-down* compared to its counterpart, saturating at an IBE_{max} around 63 eV for the former and around 45 eV for the latter with H_2 flow above 3 sccm.

Using results already shown in this thesis, one can easily eliminate the explanation that different ion energy conditions may alone be the cause of the selective processing observed. Recalling the results presented in Section 4.2, one can note that although variations in IBE_{max} in the same range as seen here can modify the film quality, they are not likely to be the underlying reason for switching between deposition and etching. In addition, as the reactor used here is geometrically asymmetric, the IBE_{max} observed on the substrate for both types of *sawtooth*

[18] J.-C. Dornstetter, et al., *J. Chem. Phys.*, **140**: 234706 (2014).

plasma processes is lower than in a symmetric reactor. However, as ion energy alone is not a determining factor for deposition rate[19,20], this would at most result in a shifted process window for selective processing when transferring this process from a small, asymmetric reactor to a large, symmetric one.

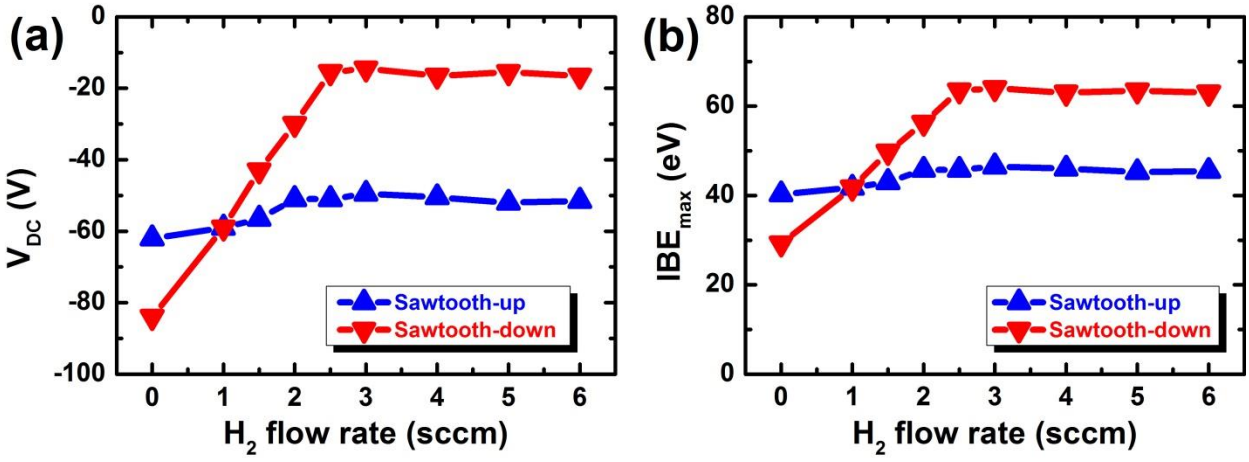

Figure 5.12 Variation of (a) V_{DC} and (b) estimated IBE_{max} with varying H_2 flow rate.

On the other hand, looking more closely at the results of Figure 5.11, one can notice that the reverse in the relative values of V_{DC} indicates a change in the plasma electronegativity with increasing H_2 flow rate. When there is no H_2, the V_{DC} value for the *sawtooth-down* plasma is more negative than that for the *sawtooth-up*. This indicates that for this condition, the plasma acts as more like an electropositive one, analogous to the Ar plasma of Figure 5.3. With increasing H_2 flow rate, the relative values of V_{DC} for the two types of *sawtooth* plasmas switch places, and the *sawtooth-up* waveform takes on the more negative value. This indicates that the plasma takes on a more electronegative character, which means that the most intense power absorption switches close to the electrode where a fast sheath contraction occurs. We can now use these results and the plasma behavior they suggest to establish a consistent link with the processing results they produce.

Plasma species spatial distribution & surface process

To understand the selective processing results, we present an explanation based on the expected concentration of hydrogen and fluorinated species near each electrode for different H_2 flows, using the case of a *sawtooth-up* plasma (the situation will simply be reversed for the case of *sawtooth-down* plasma). The relative species concentrations will be determined both by the gas flows, and by the plasma asymmetry (deduced from the relative values of V_{DC}). In addition, we assume that the available hydrogen will be identical near both electrodes during processing, and therefore focus only on differences in the much heavier fluorinated species concentration.

When there is no H_2, the plasma electron heating operates in the α-mode, so more intense power absorption occurs close to the powered electrode experiencing the fast sheath expansion, represented by the darker pink shade in Figure 5.13. However, net etching processes can be

[19] M. Hayama, et al., *J. Appl. Phys.*, **67**: 1356 (1990).
[20] A. H. M. Smets, et al., *J. Non-Cryst. Solids*, **352**: 937 (2006).

observed on both electrodes since there are no H_2 molecules to scavenge the active fluorinated species.

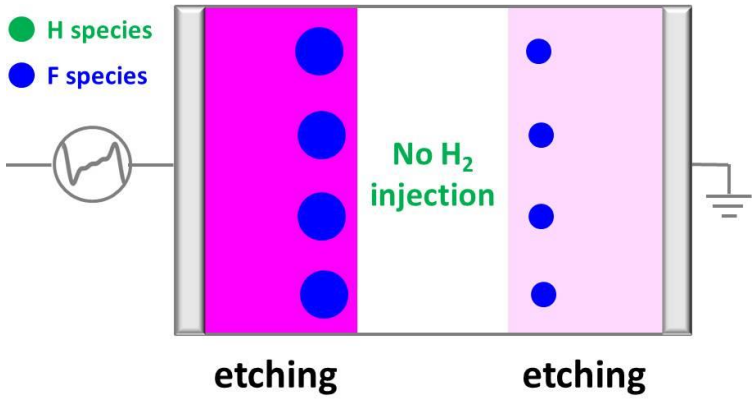

Figure 5.13 Qualitative comparison of hydrogen (green circles, not present in this case) and active fluorinated (blue circles) species concentration distribution in the *sawtooth-up* waveform excited plasma (i): no H_2. The strength of local electron power absorption is represented by the color shades of the two sheaths.

Once H_2 is injected, such as for the condition of H_2 = 1 sccm, the plasma switches to behaving like a more electronegative one. The plasma electron heating starts to be dominated by the DA-mode, and thus the intense power absorption occurs close to the grounded electrode that experiences a fast sheath contraction, as shown in Figure 5.14. As a consequence, a higher active fluorinated species concentration would be found in front of the grounded substrate. However, the injected H_2 is still not enough to scavenge these species, thus leading to either no deposition (Figure 5.5) or an intense chemical etching (Figure 5.9).

In contrast, due to weaker electron power absorption, a lower fluorinated species concentration is present near the powered electrode. This amount of fluorinated species **can** be easily scavenged by the available hydrogen. Therefore, the etching effect will be much weaker, resulting in either deposition (Figure 5.5) or at least the absence of net etching process (Figure 5.9) at low H_2 flow rates.

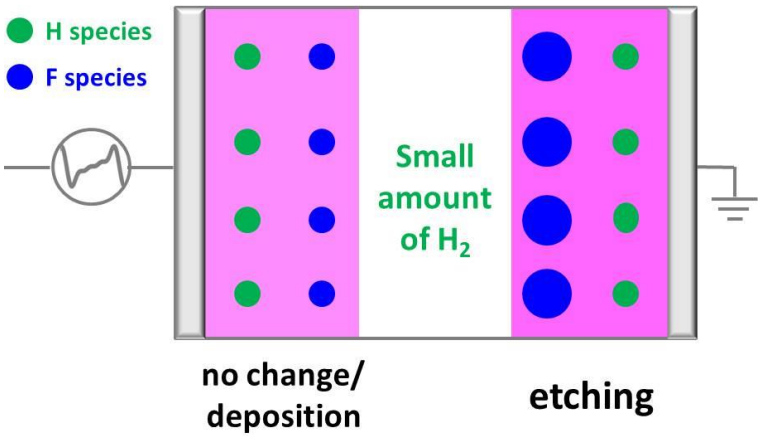

Figure 5.14 Qualitative comparison of hydrogen and active fluorinated concentration (ii): little H_2 flow.

With increasing H_2 injection, the etching effect will be gradually reduced. As shown in Figure 5.15, the provided amount of H_2 can eliminate not only the active fluorinated species in front of the powered electrode, but also those in front of the grounded electrode. Therefore, as seen at H_2 = 1.5 or 2 sccm, we can either achieve a deposition process on the grounded electrode (with low r_d, Figure 5.5) or at least a much weaker etching process (less negative $r_{d,net}$, Figure 5.9).

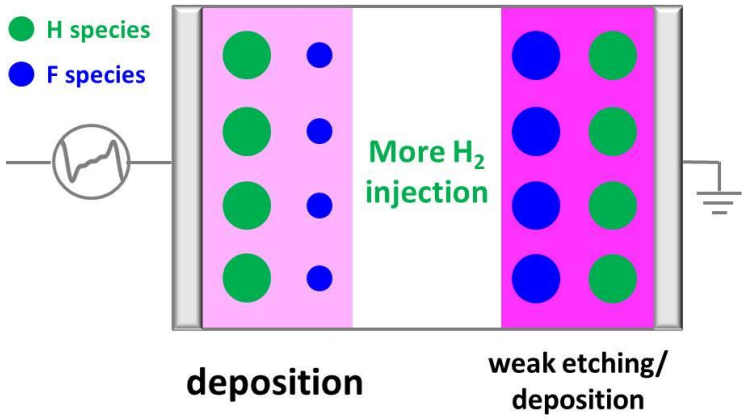

Figure 5.15 Qualitative comparison of hydrogen and active fluorinated concentration (iii): low H_2 flow.

When H_2 injection is more than enough, i.e., higher than 2 sccm in this study, deposition processes can be observed on both electrodes, even with the a-Si:H layer underneath (Figure 5.9). As shown in Figure 5.16, the resulting surface process is no longer limited by the presence of H_2, but by the dissociation of the feed gas for growth precursors – SiF_4. In this case, the more intense dissociation of SiF_4 close to the grounded electrode will now lead to a higher deposition rate for this electrode, which previously observed a lower r_d (Figure 5.5) or $r_{d,net}$ (Figure 5.9).

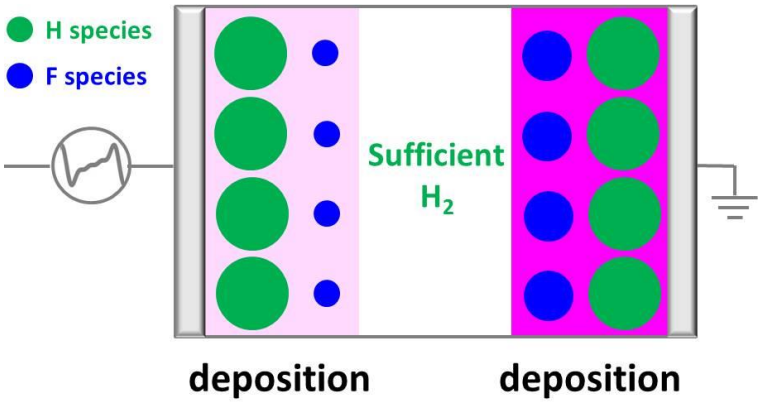

Figure 5.16 Qualitative comparison of hydrogen and active fluorinated concentration (iv): high H_2 flow.

To conclude, these experimental results have shown that the use of *sawtooth* waveforms can result in controllably differing deposition or etching processes on each electrode from the $SiF_4/H_2/Ar$ plasma chemistry in a CCP chamber. This is due to two effects: the multi-precursor nature of the deposition/etching process for such plasma chemistry and the localized electron power absorption caused by the slope asymmetry effect. Figure 5.17 summarizes all these

processes presented from Figure 5.13 to Figure 5.16 with varying H_2 injections, in which the strength of local electron power absorption is represented by the color shades of the two sheaths.

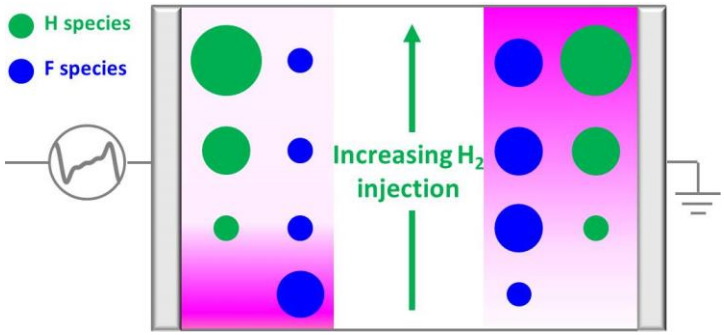

Figure 5.17 Qualitative comparison of hydrogen and active fluorinated concentration (v): varying H_2 flow.

The injection of H_2 results in a transition of the electron heating mode from the α-mode to the DA-mode (under the process conditions investigated in this work), and a reverse of the localized power absorption is expected. The further increase in H_2 flow rate can lead to the increase of plasma electronegativity, and as a consequence, completely different surface processes will be obtained. At low H_2 flow rates, when processing identical a-Si:H layers but with the opposite *sawtooth* waveforms, one can achieve a deposition process on the electrode where the weak electron power absorption occurs during the fast sheath expansion, and an etching process on the other electrode that experiencing a fast sheath contraction. Moreover, this deposition/etching balance on each electrode can be directly controlled by the H_2 flow rate. At higher H_2 flow rates, the deposition processes are obtained on both electrodes. As limited by the dissociation of SiF_4, the relative net deposition rate on each electrode is now reversed. As a matter of fact, the transition of electron heating dynamics as well as the resulting surface processes can be simply indicated by measuring the values of V_{DC} during experiments.

5.2.2. Effect of gas pressure

The above selective processing results are shown for a single total process pressure. However, the process gas composition and pressure can significantly impact the plasma response asymmetry, and thus the resulting surface processes on each electrode. To advance knowledge on this topic, in this section we study the impact of process pressure on the resulting plasma process while building up the complexity of the gas composition.

5.2.2.1. Single-gas plasma

Ar plasma

As first experiment, electropositive Ar plasmas excited by *sawtooth* waveforms under different pressures were investigated. Due to the practical pumping ability, lower process pressures are achieved by reducing feed gas flow. Details about the process conditions are shown in Table 5.3.

Table 5.3 Process conditions for Ar plasma study with different pressure.

V_{PP}	P	d_i	T_{sub}	T_{rf}	Ar
V	Torr	cm	°C	°C	sccm
130-290	0.15-1	3	150	80	10, 15, and 88

Figure 5.18 shows the experimentally measured V_{DC} with V_{PP} ranging from 130 V to 290 V. Since the discharge reactor is geometrically asymmetric, the values of V_{DC} are always negative. As can be seen, the V_{DC} presents a downward trend (more negative) with increasing V_{PP} regardless of the process pressure. This can be easily understood by considering Equation (5.2), which states that a greater V_{PP} leads to greater V_{DC} (in absolute value). One may also note from the results that slightly more negative values of V_{DC} are observed for the case of *sawtooth-down* plasma than its counterpart, which is consistent with the results shown in Figure 5.2.

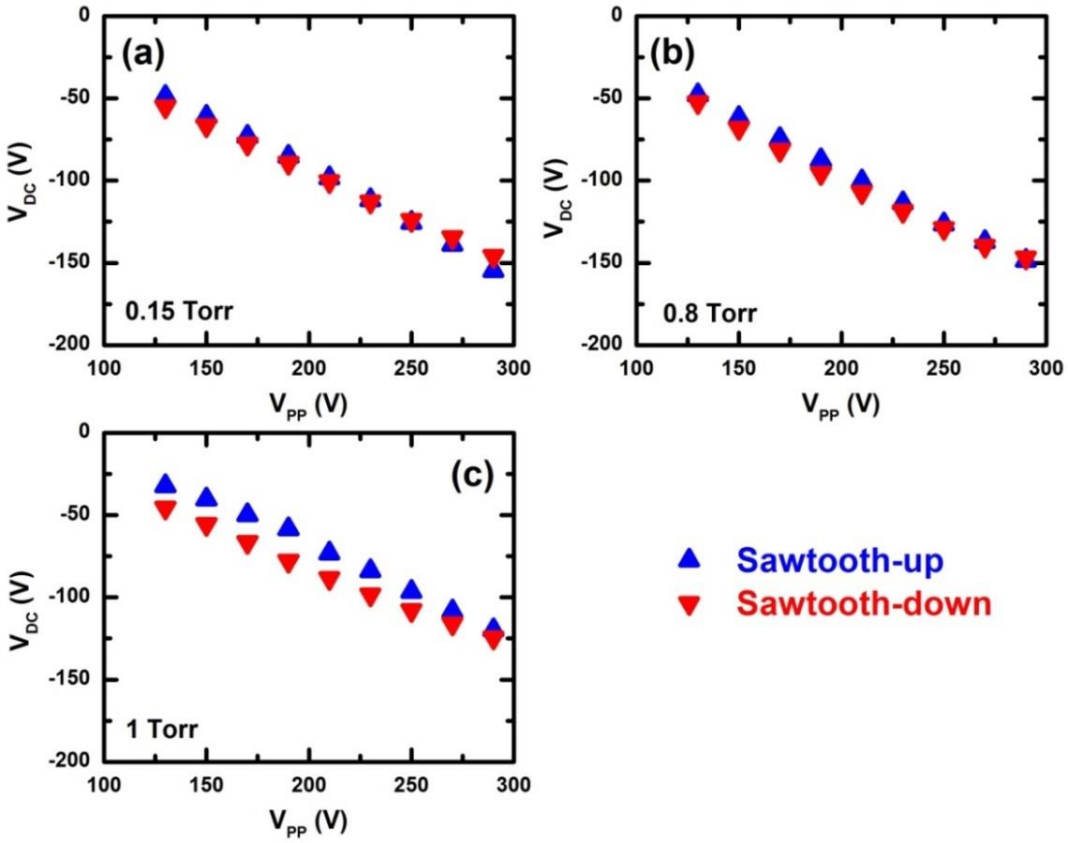

Figure 5.18 Experimentally obtained V_{DC} for Ar plasma excited by *sawtooth* waveforms at (a) 0.15 Torr, (b) 0.8 Torr, and (c) 1 Torr, with Ar flow rates set to 10 sccm, 15 sccm, and 88 sccm, respectively.

Moreover, the difference between these two cases is slightly enlarged when operating at higher pressures. As previously shown in Ref. 5 through PIC simulation, increased pressure can lead to an increasing asymmetry in the localized ionization at two sheath edges. This spatial variation in the electron power absorption comes from the inverse dependency of mean free path (between

collisions for the energetic electrons) with pressure. At low pressures, electrons tend to travel longer before through the discharge before suffering a collision, resulting in a more uniform ionization between two electrodes. At high pressures, electrons cannot travel far from the heating region due to the shorter mean free path, and thus the ionization process occurs closer to the sheath region and will be more localized near the rapidly expanded sheath edge[13,21]. Therefore, for the case of *sawtooth-down* plasma, a higher mean sheath ion density close to the grounded electrode ($\bar{n}_{sp} < \bar{n}_{sg}$) is expected, and thus a more negative values of V_{DC}.

SiF_4 plasma

The impact of process pressure was also studied for an electronegative plasma, namely when SiF_4 is used as the feed gas. Details about the process conditions are shown in Table 5.4.

Table 5.4 Process conditions for SiF_4 plasma study with different pressure.

V_{PP}	P	d_i	T_{sub}	T_{rf}	SiF_4
V	Torr	cm	°C	°C	sccm
150-310	0.2-1	3	150	80	30

It has been extensively reported that the electron power absorption dynamics of an electronegative plasma (depending on the gas) can be impacted by the gas pressure[22,23,24]. Due to the special waveshape, this effect can be even more obvious when the *sawtooth* waveform is employed as the excitation source. For instance, the transition of electron heating for an O_2 plasma from the DA-mode to the α-mode is found by increasing the pressure[9], while an opposite situation, i.e., transition from the α-mode to the DA-mode with increasing pressure, is observed for the CF_4 plasma[10,12]. As aforementioned, the electron heating mode can strongly affect the absolute value of V_{DC} through the electrical asymmetry effect. This is even more obvious for *sawtooth* plasmas, since the generation of V_{DC} is only determined by the slope asymmetry of the waveform in a geometrically symmetric reactor. Due to the strongly localized, asymmetric plasma response, a sign reversal of V_{DC} can be expected by switching the electron heating from the α-mode to the DA-mode, or vice versa.

As discussed in Section 5.2.1, in a geometrically asymmetric reactor such as the one used in our experiments (which usually gives negative values of V_{DC}), such gas pressure-impact heating mode transitions are more clearly determined by comparing the relative magnitude of V_{DC} for *sawtooth-up* and *-down* waveforms. The experimentally obtained results for the SiF_4 plasma are shown in Figure 5.19.

[21] T. Lafleur, et al., *J. Phys. D: Appl. Phys.*, **45(39)**: 395203 (2012).
[22] K. Denpoh, et al., *Jpn. J. Appl. Phys.*, **39(5R)**: 2804 (2000).
[23] O. V. Proshina, et al., *Plasma Sources Sci. Technol.*, **19(6)**: 065013 (2010).
[24] G. H. Liu, et al., *Plasma Sources Sci. Technol.*, **24(3)**: 034006 (2015).

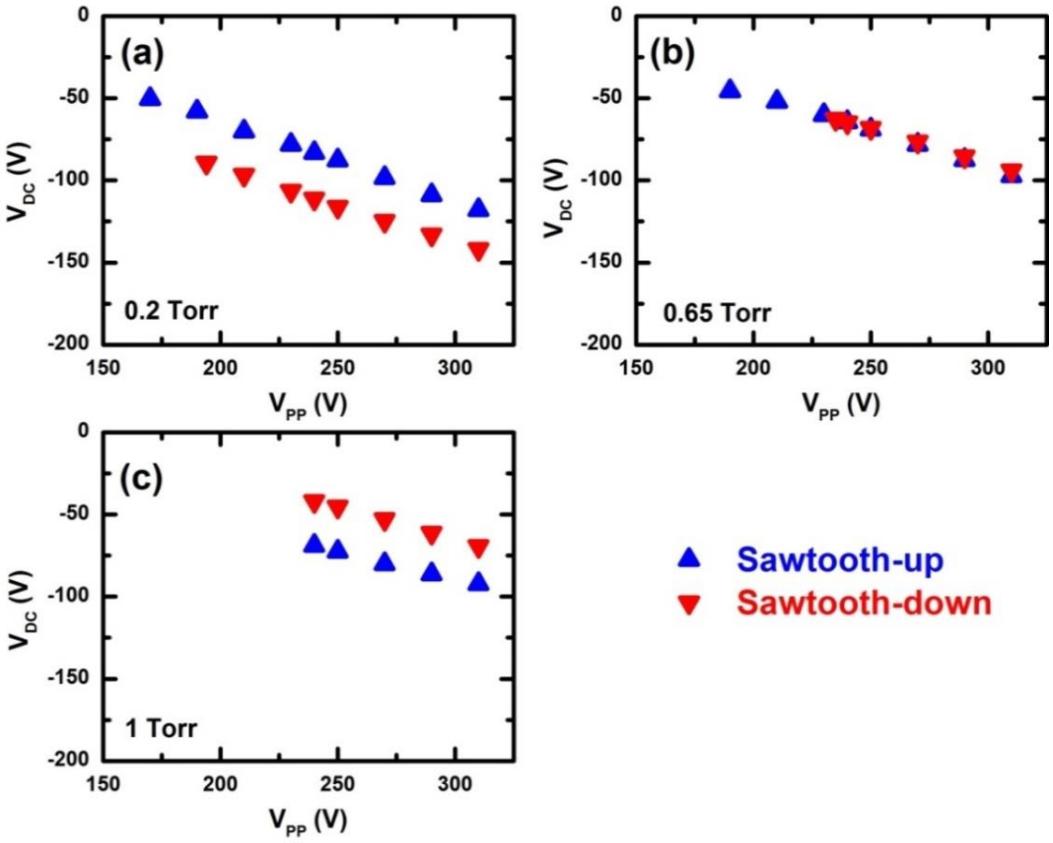

Figure 5.19 Experimentally obtained V_{DC} for SiF_4 plasma excited by *sawtooth* waveforms at (a) 0.2 Torr, (b) 0.65 Torr, and (c) 1 Torr.

As one can see, the magnitude of V_{DC} increases with increasing V_{PP} for all the investigated pressures. However, the absolute values of V_{DC} for the *sawtooth-up* and *-down* plasmas remain quite different, and a reversal of the relative magnitude is seen with increasing gas pressure. These results indicate that the increase of gas pressure lead to a transition of the electron heating mode. In analogy with CF_4 plasma[10,12], the SiF_4 plasma operates in the α-mode at low pressure (0.2 Torr, Figure 5.19-(a)). As a result, the *sawtooth-down* plasma takes on the more negative values based on Equation (4.8) and (5.2), since the most intense power absorption occurs close to the rapidly expanding grounded sheath ($\bar{n}_{sp} < \bar{n}_{sg}$).

At medium pressure (0.65 Torr, Figure 5.19-(b)), similar values of V_{DC} are observed in both cases. This suggests a transition of the plasma operation mode from the α-mode to a hybrid α-DA mode, presumably due to the increase of plasma electronegativity resulting from the enhanced electron attachment process at high pressure.

When the gas pressure is high enough (1 Torr, Figure 5.19-(c)), the relative of values of V_{DC} switch places compared to the process operated at low pressure. For the *sawtooth-down* plasma, the self-sustaining effect in the DA-mode described above leads to a higher sheath density close to the powered electrode experiencing a rapid sheath contraction ($\bar{n}_{sp} > \bar{n}_{sg}$). Therefore, less negative values of V_{DC} are observed in this case.

H_2 plasma

The H_2 plasma operated under different pressure was also studied. Here, a higher gas injection is used to achieve higher gas pressure. Details about the process conditions are shown in Table 5.5.

Table 5.5 Process conditions for H_2 plasma study with different pressure.

V_{PP}	P	d_i	T_{sub}	T_{rf}	H_2
V	Torr	cm	°C	°C	sccm
200-360	0.2 and 1	3	150	80	50 and 100

The results are shown in Figure 5.20. As can be seen, comparable values of V_{DC} are obtained for both waveforms at both low and high gas pressures, which can be viewed as a sign that these *sawtooth* waveform excited H_2 plasmas are operated in a hybrid α-DA mode throughout the investigated pressure and V_{PP} range. This is consistent with the results obtained in a geometrically symmetric reactor showing V_{DC} values close to zero, as seen in Figure 5.11.

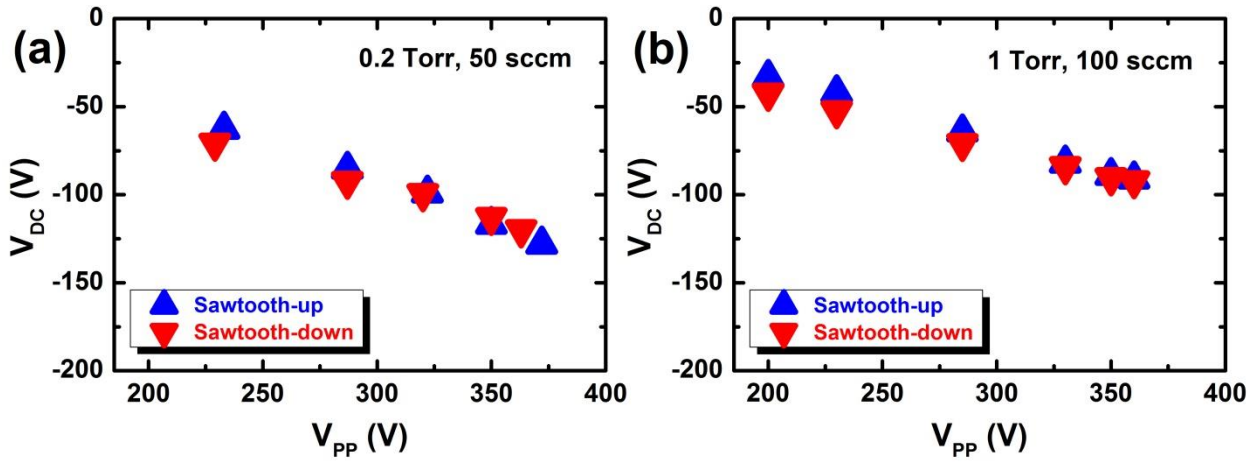

Figure 5.20 Experimentally obtained V_{DC} for H_2 plasma excited by *sawtooth* waveforms at (a) 0.2 Torr and (b) 1 Torr, with H_2 flow rates set to 50 sccm and 100 sccm, respectively.

5.2.2.2. Multi-gas plasma

$SiF_4/H_2/Ar$ plasma

Application relevant processes usually deal with multi-gas plasmas with more complex chemical and physical features. This motivates us to study the impact of the pressure on the discharge asymmetry of the $SiF_4/H_2/Ar$ plasma employed in our work. Following the study presented in Section 4.2 about the deposition of μc-Si:H films, the H_2 and SiF_4 flow rates were set to 3.6 sccm and 5 sccm, respectively. Two gas pressure ranges have been investigated by employing different levels of Ar dilution, and details about the process conditions are shown in Table 5.6.

Table 5.6 Process conditions for SiF_4/H_2/Ar plasma study with different pressure.

V_{PP}	P	d_i	T_{sub}	T_{rf}	SiF_4	H_2	Ar
V	Torr	cm	°C	°C	sccm	sccm	sccm
285	1.25-3	3	150	80	3.6	5	88
260	0.25-1						11

The experimentally obtained V_{DC} as a function of increasing gas pressure is shown in Figure 5.21. It can be seen that increasing the gas pressure leads to a less negative values of V_{DC} for both sets of processes. In a previous study about the deposition of amorphous hydrogenated carbon from a methane, benzene, and helium plasma chemistry [25], the authors described the experimentally obtained V_{DC} using the model (considering the CCP-plasma as two capacitive sheath and one resistive bulk) described in Section 0. They have proposed an inversely proportional relationship between V_{DC} and gas pressure P, i.e., $V_{DC} \propto P^{-1/2}$. The validity of this relationship have been examined in a large variety of plasma processes[26,27,28,29]. Therefore, the lower values of V_{DC} (in absolute value) at higher pressures observed in our study can be expected.

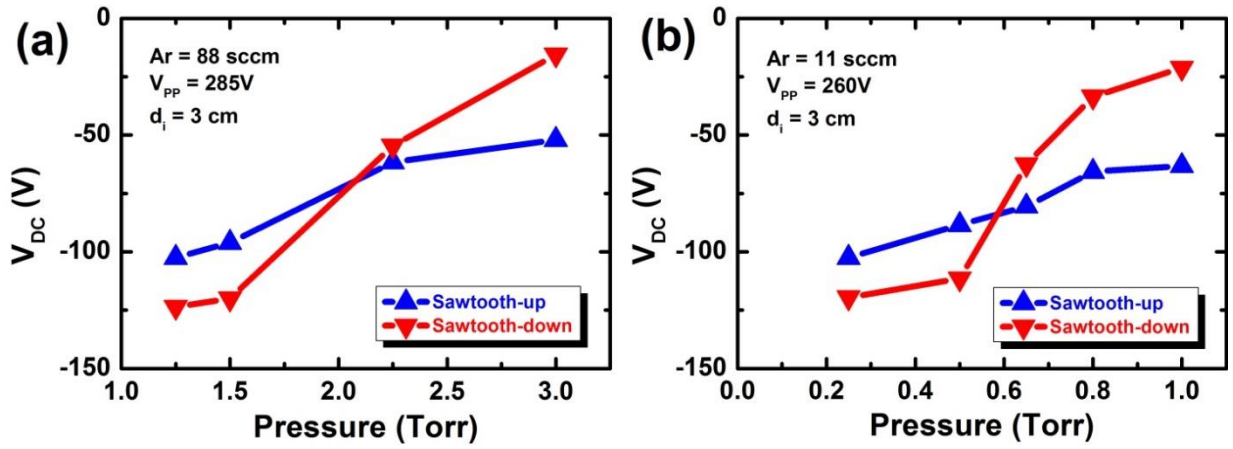

Figure 5.21 Experimentally obtained V_{DC} for SiF_4/H_2/Ar plasma excited by the *sawtooth* waveforms at different pressure ranging (a) from 1.25 Torr to 3 Torr and (b) from 0.2 Torr to 1 Torr, with the Ar flow rate set to 88 sccm and 11 sccm, respectively.

As one can see in Figure 5.21-(a), the *sawtooth-up* plasma takes a less negative value of V_{DC} at low pressures (1.25 Torr and 1.5 Torr), indicating a dominant α-mode electron heating for these conditions. However, as seen for the pure SiF_4 plasma above, increasing the pressure leads to a reversal in the relative values of V_{DC} for these two waveforms. After crossing at ~2.25 Torr, V_{DC} = ~-52 V for the *sawtooth-up* plasma and V_{DC} = ~-15.5 V for *sawtooth-down* at 3 Torr. This indicates

[25] Y. Catherine, et al., *Thin Solid Films*, **144(2)**: 265 (1986).
[26] N. Mutsukura, et al., *J. Appl. Phys.*, **66(10)**: 4688 (1989).
[27] J. Robertson, *Mater. Sci. Eng. R Rep.*, **37(4-6)**: 129 (2002).
[28] K. Bewilogua, et al., *Surf. Coat. Technol.*, **242**: 214 (2014).
[29] G. Alexiou, et al., *J. Phys. Conf. Ser.*, **700(1)**: 012038 (2016).

that under the investigated process conditions, the $SiF_4/H_2/Ar$ plasma undergoes an electron heating mode transition from a dominant α-mode at low pressure, through a hybrid α-DA mode at medium pressure, then to a dominant DA-mode at high pressure.

A similar phenomenon is observed for the plasma processes with lower Ar flow rate, i.e., the plasma operated at lower pressure range. An electron heating mode transition and the resulting reversal of V_{DC} relative magnitude are also observed. The transition point is found to drop down to a lower pressure value around 0.6 Torr. This will be discussed in more detail subsequently.

5.2.3. Effect of geometric asymmetry

The generation of V_{DC} is an overall characteristic feature of the discharge asymmetry regardless of its origin, either geometrical, electrical, or both. In a previous study about a TVW-excited Ar plasma[30], it has been reported that although the geometrical asymmetry parameter (varied by changing the electrode surface ratio via the inter-electrode distance d_i) has little impact on the form of the dependence of V_{DC} on φ, it indeed affects the V_{DC} in absolute value via the amplitude asymmetry effect.

However, the impact of geometrical asymmetry on the slope asymmetry effect has received little attention, especially for multi-gas plasmas. In this section, the influence of such geometrical asymmetry on *sawtooth* waveform excited single-gas and multi-gas plasmas are studied, as well as the resulting surface processes.

5.2.3.1. Single-gas plasma

Ar plasma

Firstly, Ar plasmas excited by the *sawtooth* waveforms under different d_i conditions ranging from 2 cm to 5 cm were studied. Details about the process conditions are shown in Table 5.7.

Table 5.7 Process conditions for Ar plasma study with varying d_i.

V_{PP}	P	d_i	T_{sub}	T_{rf}	Ar
V	Torr	cm	°C	°C	sccm
120 and 220	1	2-5	150	100	20

In Figure 5.22, the experimentally obtained V_{DC} is plotted as a function of d_i. At V_{PP} = 120 V (Figure 5.22-(a)), a slight increase of V_{DC} (more negative values) with increasing d_i is seen for both sets of plasma processes. This can be partially explained by the increasing geometrical asymmetry, i.e., higher values of A_p/A_g, when d_i increases. Accordingly, more negative values of V_{DC} are expected at higher d_i values. Again, since the plasma heating operates in the α-mode, the *sawtooth-down* plasma show more negative values compared to its counterpart. When V_{PP}

[30] E. Schüngel, et al., *J. Appl. Phys.*, **112(5)**: 053302 (2012).

increases up to 220 V as Figure 5.22-(b) shows, more negative values of V_{DC} are observed for both cases, because higher V_{PP} leads to greater magnitudes of V_{DC} (Equation (4.8)).

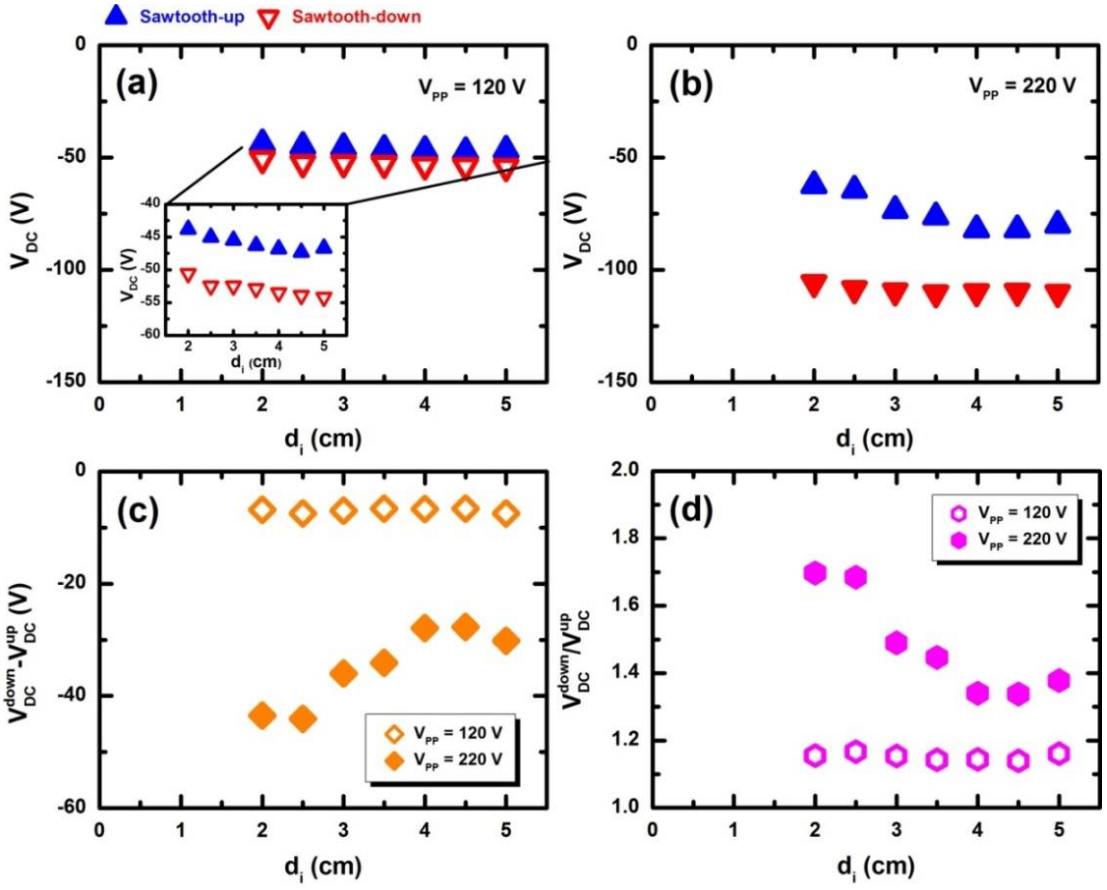

Figure 5.22 Evolutions of V_{DC}^{up} and V_{DC}^{down} with varying d_i for Ar plasma, with V_{PP} set to (a) 120 V and (b) 220 V. The corresponding evolution of (c) $V_{DC}^{down} - V_{DC}^{up}$ and (d) $V_{DC}^{down}/V_{DC}^{up}$.

These results can be better illustrated if we consider the relative magnitude of V_{DC} values. For the sake of clarity, we denote the V_{DC} measured for the *sawtooth-up* and *-down* plasma processes as V_{DC}^{up} and V_{DC}^{down}, respectively. Figure 5.22-(c) and (d) depict the variation of $V_{DC}^{down} - V_{DC}^{up}$ and $V_{DC}^{down}/V_{DC}^{up}$ as a function of d_i. For the case of V_{PP} = 120 V, $V_{DC}^{down} - V_{DC}^{up}$ stays rather low and constant at around 7 V for all the d_i conditions, and that of $V_{DC}^{down}/V_{DC}^{up}$ stays constant around 1.15. However, the situation is different for V_{PP} = 220 V. A larger discrepancy is now present between V_{DC}^{up} and V_{DC}^{down}, generating considerably higher values of $V_{DC}^{down} - V_{DC}^{up}$ and $V_{DC}^{down}/V_{DC}^{up}$. This may be interpreted as a sign of stronger slope asymmetry effect in plasma under these conditions.

H_2 plasma

H_2 plasmas excited by *sawtooth* waveforms under different d_i conditions ranging from 2 cm to 5 cm were also studied. Details about the process conditions are shown in Table 5.8, and Figure 5.23 shows the variation of V_{DC} with increasing d_i.

Table 5.8 Process conditions for H_2 plasma with varying d_i.

V_{PP}	P	d_i	T_{sub}	T_{rf}	H_2
V	Torr	cm	°C	°C	sccm
215, 285, and 340	1 and 1.13	2-5	150	100	100

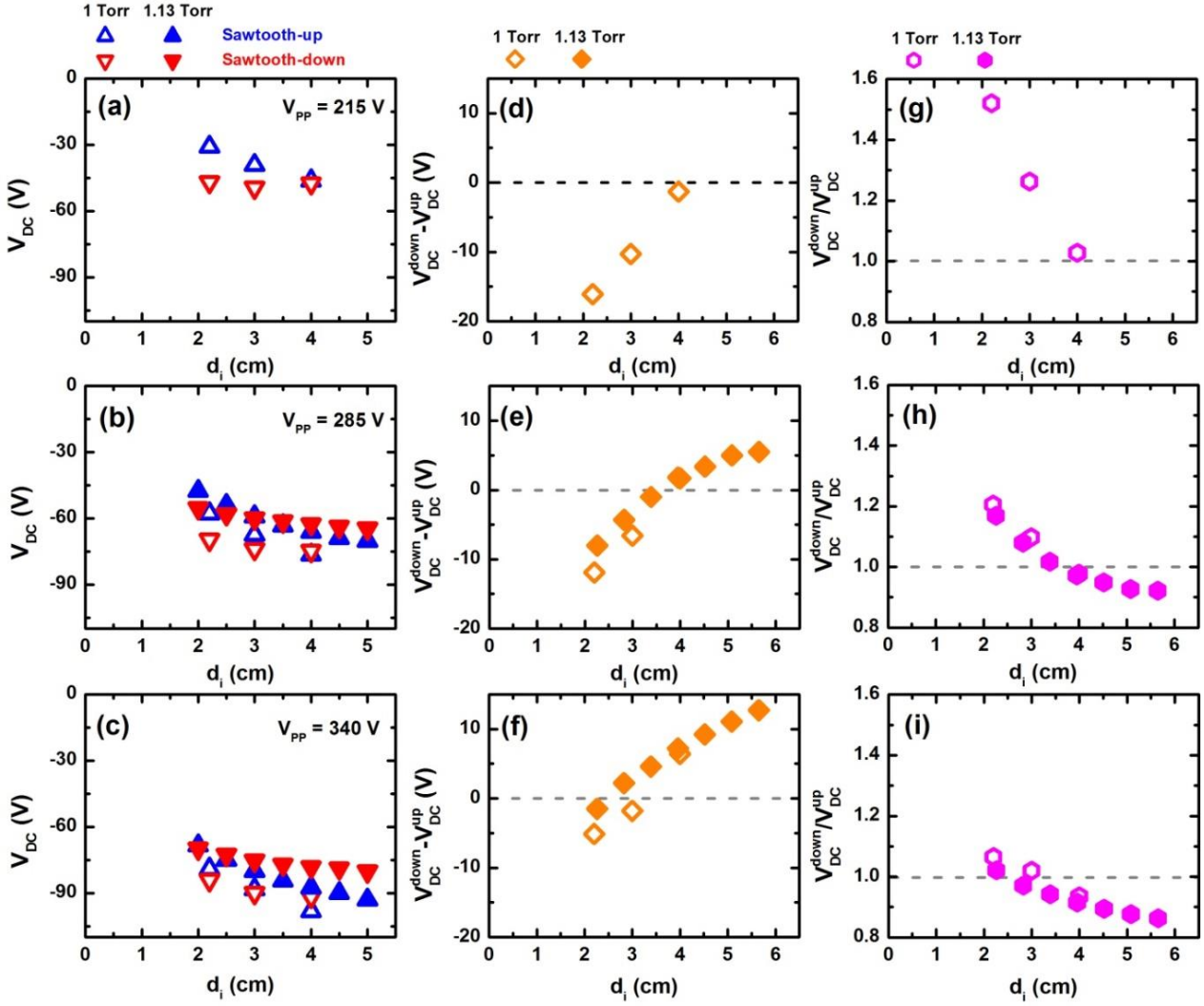

Figure 5.23 (a)/(b)/(c) Evolution of V_{DC}^{up} and V_{DC}^{down} and (d)/(e)/(f) $V_{DC}^{down}/V_{DC}^{up}$ as a function of d_i for a H_2 plasma, with V_{PP} set to 215 V/285 V/340 V, respectively. The open and solid symbols correspond to 1 Torr and 1.13 Torr, respectively.

Again, one can note from Figure 5.23-(a) ~ (c) in the first column that V_{DC} shows a downward trend for all the investigated process conditions. Both an increase of V_{PP} and pressure can lead to an increase of V_{DC} (more negative values), as has already been observed for the Ar plasma in Figure 5.21 and Figure 5.22.

More interestingly, a reverse of the relative magnitude of V_{DC}^{up} and V_{DC}^{down} is observed for the H_2 plasma when d_i is changed. In Figure 5.23-(a), the plasma heating operates in a dominant α-mode at low d_i conditions with V_{PP} = 215 V, since more negative values of V_{DC}^{down} are observed compared to V_{DC}^{up}, and thus giving negative values of $V_{DC}^{down} - V_{DC}^{up}$ in Figure 5.23-(d). However, the magnitude of $V_{DC}^{down} - V_{DC}^{up}$ decreases with increasing d_i, and a value around zero is observed at 4 cm. This suggests that the plasma response is more symmetric compared to the former cases, presumably due to a hybrid α-DA mode electron heating under this condition. Then, the increase of V_{PP} up to 285 V allows one to observe the sign reverse for $V_{DC}^{down} - V_{DC}^{up}$ at certain d_i values (Figure 5.23-(g)). This indicates an electron heating transition from α-mode to DA-mode is achieved when d_i is high enough. Furthermore, V_{PP} = 315 V also leads to the observation of such transition, but at even lower d_i values as seen in Figure 5.23-(f).

Similar conclusion can be deduced from the results presented from Figure 5.23-(g) ~ (i) about the evolution of $V_{DC}^{down}/V_{DC}^{up}$. The electron heating mode transition is reflected by the variation of $V_{DC}^{down}/V_{DC}^{up}$ value from less than unity (α-mode dominated) to greater than unity (DA-mode dominated) with increasing d_i.

5.2.3.2. Multi-gas plasma

It has been shown above that, depending on the gas property, the plasma response asymmetry (dominant heating mode) can be significantly impacted by the reactor geometry in a *sawtooth* waveform excited single-gas plasma. In this part, such geometry-impacted electron heating dynamics is further investigated for the case of multi-gas plasma.

$SiF_4/H_2/Ar$ plasma with constant H_2 flow rate

$SiF_4/H_2/Ar$ plasmas excited by the *sawtooth* waveforms were studied under different d_i conditions ranging from 0.5 cm to 4.5 cm. Following the study presented in Section 5.2.2, different pressure conditions were also considered. Details about the process conditions are shown in Table 5.9.

Table 5.9 Process conditions for $SiF_4/H_2/Ar$ plasma study under different pressure with varying d_i.

V_{PP}	P	d_i	T_{sub}	T_{rf}	SiF_4	H_2	Ar
V	Torr	mm	°C	°C	sccm	sccm	sccm
285	1.25-3	5-45	150	80	3.6	5	88

The variations of V_{DC} with increasing gas pressure are shown in Figure 5.24, with (a) ~ (i) representing the results for increasing d_i. As in the results seen in Figure 5.21, the absolute value of V_{DC} shows an upward trend (less negative) with increasing pressure.

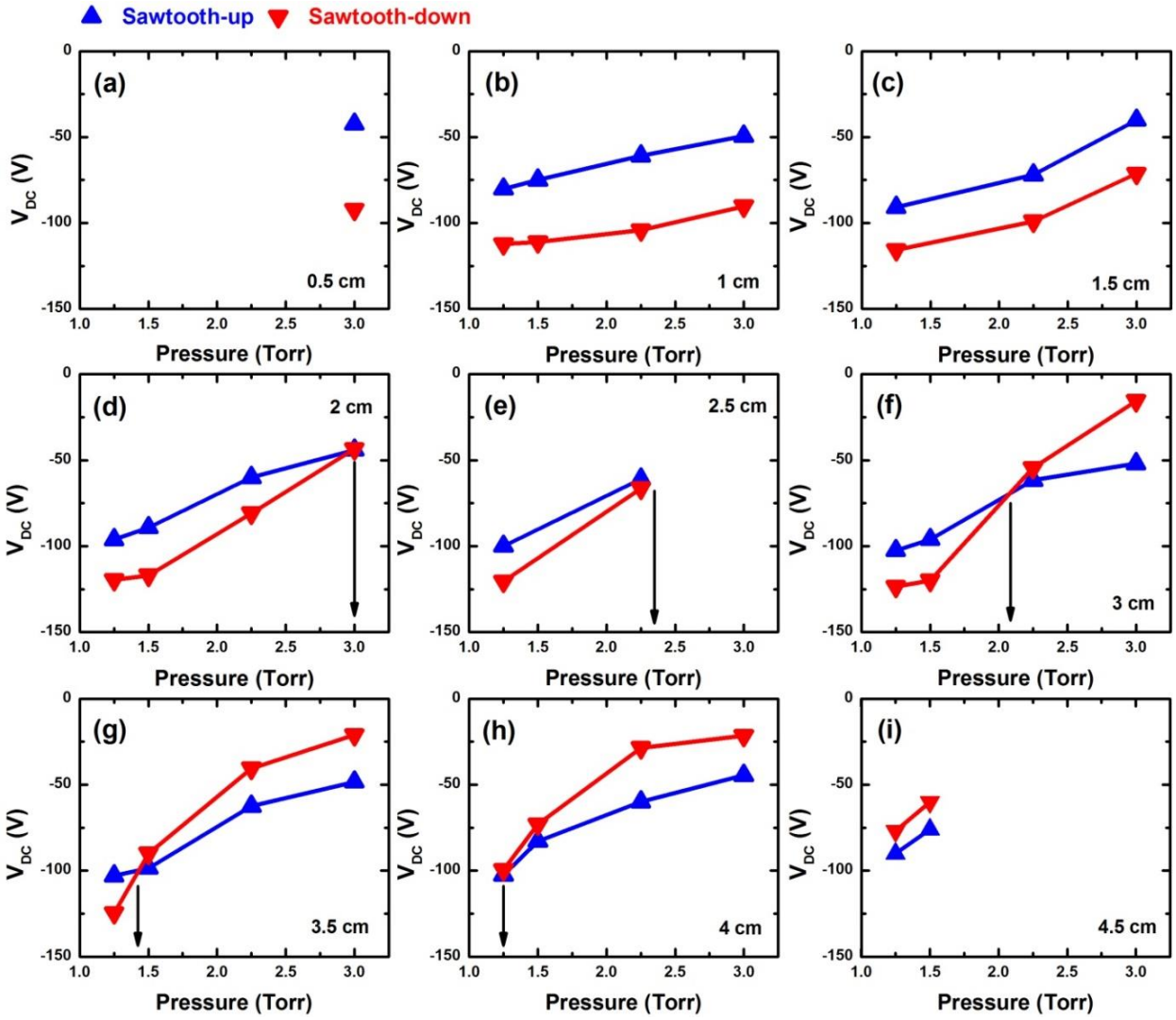

Figure 5.24 Variation of V_{DC} for $SiF_4/H_2/Ar$ plasma excited by *sawtooth* waveforms at pressures ranging from 1.25 Torr to 3 Torr, with (a) to (i) representing d_i from 0.5 cm to 4.5 cm.

Since the product of pressure and inter-electrode distance ($P{\cdot}d_i$ product) is known to be a crucial parameter in determining the properties of PECVD-deposited silicon thin films[31,32], we choose to describe the evolution of V_{DC} as a function of $P{\cdot}d_i$ in Figure 5.25. It can be observed that $V_{DC}^{down}/V_{DC}^{up}$ presents a general downward trend with increasing $P{\cdot}d_i$ values. To make a further analysis, we classify the results into group A, B, and C, as depicted by the three ellipses.

Zone A corresponds to plasmas operated at low d_i ($\leq$ 1.5 cm) or medium d_i (2-3 cm) conditions but with relatively low pressure, and as a result, the all $P{\cdot}d_i$ products are lower than ~5-6 Torr·cm. Taking a detailed look at the results at each specific value of d_i in this zone, one can note that the value of $V_{DC}^{down}/V_{DC}^{up}$ increases with increasing pressure. For instance, at d_i = 1 cm, a ratio of 1.4 is obtained at 1.25 Torr while that of 1.8 is obtained at 3 Torr. This is consistent with the argument

[31] Y. Djeridane, et al., *Thin Solid Films*, **515(19)**: 7451 (2007).
[32] P. Roca i Cabarrocas, et al., *Solid-State Electron.*, **52(3)**: 422 (2008).

discussed concerning the electropositive plasma (in Figure 5.18). For a plasma operated in the dominant α-mode, the increase of pressure leads to an enhancement of asymmetric plasma response via the slope asymmetry effect. Therefore, larger discrepancies between V_{DC}^{up} and V_{DC}^{down}, i.e., higher $V_{DC}^{down}/V_{DC}^{up}$ values, are expected at higher pressures. In this Zone, the value of d_i seems to take precedence over the quantity $P{\cdot}d_i$.

The situation is different for zone B, which extends over a higher range of $P{\cdot}d_i$ values. The value of $V_{DC}^{down}/V_{DC}^{up}$ decreases with increasing $P{\cdot}d_i$, and becomes less than unity above ~5-6 Torr·cm. As previously discussed, this variation reflects a plasma heating transition from the α-mode to the DA-mode, thus producing more negative values of V_{DC}^{up}. Interesting enough, one can note from the results that the transition point for different process conditions coincide at the similar $P{\cdot}d_i$ value at ~5-6 Torr·cm. For further increased $P{\cdot}d_i$ values (> ~9 Torr·cm) in zone C, the $V_{DC}^{down}/V_{DC}^{up}$ seems to saturate.

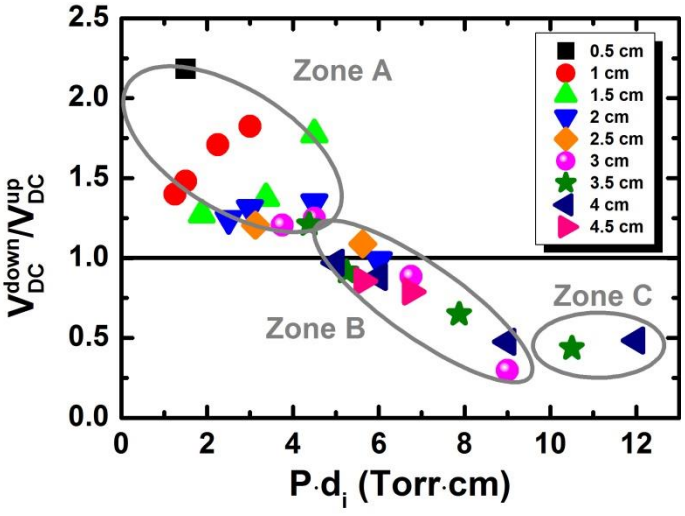

Figure 5.25 Evolution of $V_{DC}^{down}/V_{DC}^{up}$ with varying $P{\cdot}d_i$. The ellipses indicate the zone A, B, and C as described in the text.

To better understand the data concerning electron heating transition shown above, we refer to a previous RGA measurement study performed on the same PECVD reactor but with the standard 13.56 MHz excitation source[33]. In that work, the H_2 depletion in $SiF_4/H_2/Ar$ (slightly more H_2 flow rate at 5.3 sccm) plasma processes operated under different gas pressure (1.7. 2.5, and 3.8 Torr) and d_i conditions (0.5-4.5 cm) was deduced from RGA measurements. We have extracted these experimental results and re-plotted them as a function of $P{\cdot}d_i$ in Figure 5.26.

As one can see, all three sets of plasma processes (in terms of pressure) show an increase of H_2 depletion at low $P{\cdot}d_i$ values. Then, for further increased $P{\cdot}d_i$ above ~5-6 Torr·cm, the depletion stays roughly constant at a relatively high value. Note that the H_2 flow rate is kept constant at 5.3 sccm (SiF_4-limited regime), therefore the gas molecule depletion and consumption are proportional. Due to the similar reasoning, a similar trend can be expected for SiF_4.

[33] J.-C. Dornstetter, *PhD thesis*, École Polytechnique (2015).

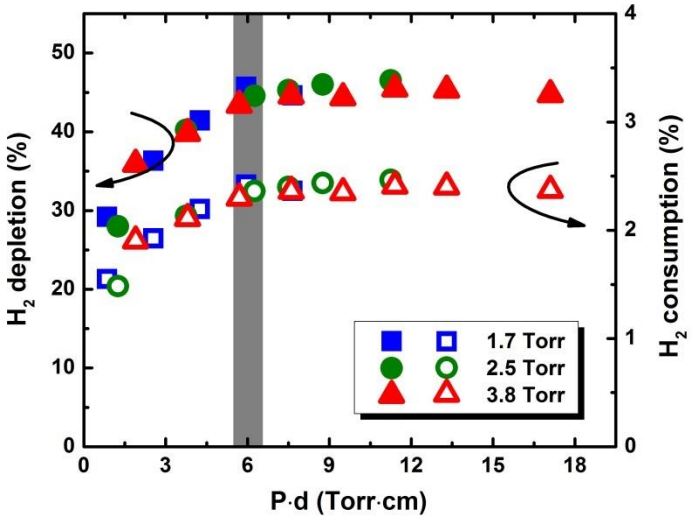

Figure 5.26 H_2 molecule depletion (solid symbols, left axis) and consumption (open symbols, right axis) for $SiF_4/H_2/Ar$ plasma excited by standard 13.56 MHz excitation source with varying $P{\cdot}d_i$. The $SiF_4/H_2/Ar$ flow rates were set to 3.6/5.3/88 sccm. The temperatures of the powered and grounded electrode were set to 70 °C and 150 °C, respectively. Updated from Ref. 33.

All three trends overlap, which suggests that the $P{\cdot}d_i$ product is a key parameter in determining the H_2 depletion in the $SiF_4/H_2/Ar$ plasma under these conditions. According to the discussion in Section 5.2.1, a high dissociation of SiF_4 leads to a stronger electronegative characteristic of the plasma, therefore a transition from the α-mode to the DA-mode and a resulting $V_{DC}^{down}/V_{DC}^{up}$ less than unity can be expected. Considering the dusty nature of such plasma process, the density of larger silicon molecules, plasma-generated nanoparticles, and large agglomerates (powders) is known to increase with pressure and electrode distance[32, 34]. These nanoparticles and large agglomerates (powders) will be negatively charged and trapped within the plasma before being pumped away when it is large enough. Accordingly, the electron density will be considerably reduced. This provides an explanation for the more electronegative character of the plasma. For the case of *sawtooth-down* plasma, this largely enhances the reverse electric field close to the fast contracting powered sheath. As a consequence, the mean ion density in said sheath will be even higher, therefore an even less negative value of V_{DC}^{down} is observed.

To understand the saturation in zone C, one should consider the combination of the following two effects: i) the formation and elimination (through pumping) of the large agglomerates (powders) approaching a dynamic equilibrium at high $P{\cdot}d_i$ conditions, and ii) higher d_i might lead to the fact that the discharge symmetry is more geometrically determined. Therefore, the enhancement of the asymmetric plasma response via the slope asymmetry effect is reduced.

$SiF_4/H_2/Ar$ plasma with varying H_2 flow rate

As shown previously in Section 5.2.1, a small variation of gas ratio can significantly influence the electron heating dynamics for the $SiF_4/H_2/Ar$ plasma. To further explore this effect, we examine the impact of the geometrical asymmetry on plasma properties under different gas ratio conditions.

[34] P. Roca i Cabarrocas, et al., *J. Phys. D: Appl. Phys.*, **40(8)**: 2258 (2007).

Therefore, a complementary plasma study varying H_2 flow rate was performed at different d_i values. Details about the process conditions are shown in Table 5.10. Figure 5.27 shows the experimentally obtained V_{DC} plotted as a function of H_2 flow rate, with (a), (b), and (c) corresponding to 3 cm, 2 cm, and 1 cm of d_i.

Table 5.10 Process conditions for SiF_4/H_2/Ar plasma study under different pressure with varying H_2 flow.

V_{PP}	P	d_i	T_{sub}	T_{rf}	SiF_4	H_2	Ar
V	Torr	cm	°C	°C	sccm	sccm	sccm
285	3	1-3	150	80	3.6	0-10	88

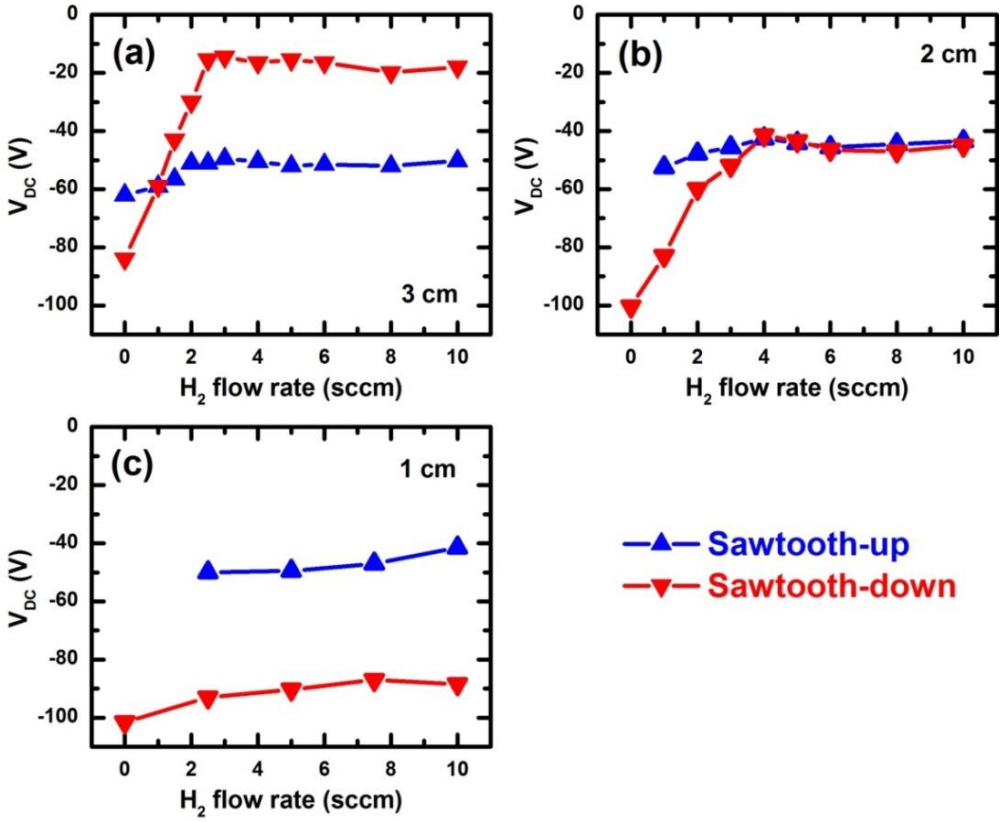

Figure 5.27 Variation of V_{DC} for SiF_4/H_2/Ar plasma excited by *sawtooth* waveforms using varying H_2 flow rate with d_i set to (a) 3 cm, (b) 2 cm, and (c) 1 cm.

In fact, Figure 5.27-(a) just shows the results at d_i = 3 cm as seen in Figure 5.12-(c), but with additional data points at higher H_2 flow rates (up to 10 sccm, for which no change in the trend is seen). However, something different can be noticed at lower d_i values. At d_i = 2 cm, the increase of H_2 flow rate also leads to the decrease (in absolute value) in both V_{DC}^{up} and V_{DC}^{down}, but the latter presents a variation in a larger range as shown in Figure 5.27-(b). Therefore, identical values of V_{DC} are seen at a certain H_2 flow rate around 4 sccm, which actually is higher than that around 1.5 sccm in the case of d_i = 3 cm. This can be understood by combining the results shown in Figure 5.10 and Figure 5.26. Plasma with less electronegative characteristic is expected for d_i = 2 cm

(lower $P{\cdot}d_i$ value), so that higher H_2 flow rate is needed to promote the dissociation of SiF_4 to achieve greater electronegativity (more negative ions or negatively charged nanoparticles).

However, further increase of H_2 flow rate does not lead to the occurrence of a reversal in the relative magnitude of V_{DC}. This can be attributed to the saturation of gas consumption at high H_2 flow rates (Figure 5.10). When d_i is decreased down to 1 cm, V_{DC}^{up} presents less negative values than V_{DC}^{down} for all the investigated H_2 flow rates as shown in Figure 5.27-(c), indicating that the plasma always operates in the α-mode under these conditions.

5.2.3.3. Silicon thin film deposition

Although the transitions observed above are helpful to understand the plasma physics, it could be of interest to see the resulting surface processes. Therefore, a set of silicon thin film depositions have been performed using the $SiF_4/H_2/Ar$ plasma chemistry with different $P{\cdot}d_i$ values. Details about the process conditions are shown in Table 5.11.

Table 5.11 Process conditions for silicon thin film deposition using $SiF_4/H_2/Ar$ plasma chemistry using *sawtooth* waveforms with varying $P{\cdot}d_i$.

V_{PP}	P	d_i	T_{sub}	T_{rf}	SiF_4	H_2	Ar
V	Torr	cm	°C	°C	sccm	sccm	sccm
285	2-3.5	1-3	150	80	3.6	5	88

Figure 5.28-(a) shows the evolution of $V_{DC}^{down}/V_{DC}^{up}$ under these different process conditions. Again, the reversal of the relative magnitudes of V_{DC} is observed when $P{\cdot}d_i$ at ~5-6 Torr·cm. The resulting film deposition rates are also presented in Figure 5.28-(b), expressed as the ratio of the rate for film deposited using *sawtooth-down* waveform over that of its counterpart, i.e., r_d^{down}/r_d^{up}.

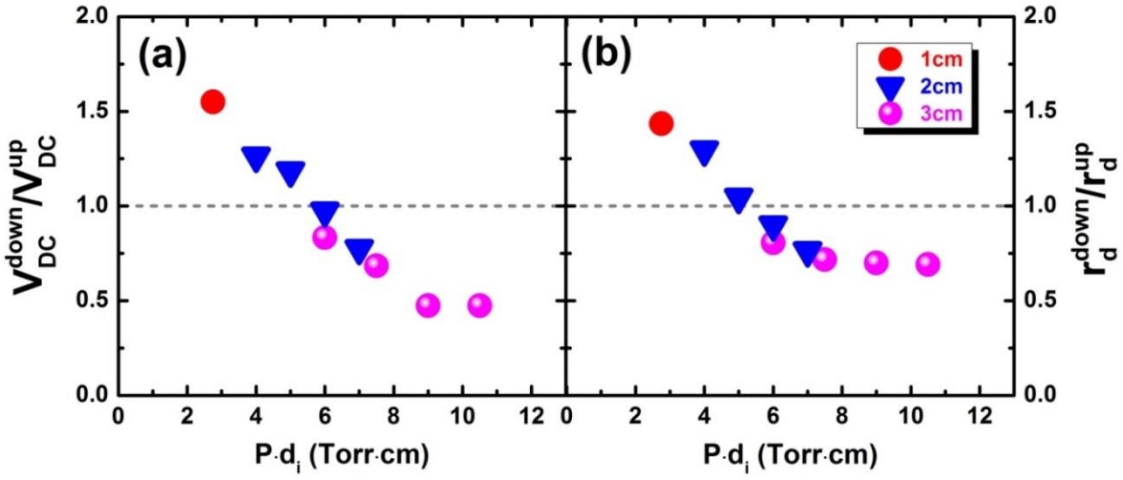

Figure 5.28 (a) Evolution of $V_{DC}^{down}/V_{DC}^{up}$ and (b) the r_d ratio between the *sawtooth-down* sample and the *sawtooth-up* sample, i.e., r_d^{down}/r_d^{up}, with varying $P{\cdot}d_i$.

As one can see, the material deposition properties correlate with the plasma results. At low $P{\cdot}d_i$ values, the plasma heating operates in the α-mode. Since the surface process is limited by the presence of growth precursors (SiF_x), the localized power absorption close to the grounded electrode experiencing a fast sheath expansion for the *sawtooth-down* plasma process gives a higher deposition rate than its counterpart, i.e., r_d^{down}/r_d^{up} greater than unity. The transition of heating mode induced by the increasing $P{\cdot}d_i$ leads to a spatially re-distributed profile of plasma species, so that a r_d^{down}/r_d^{up} close to unity at medium $P{\cdot}d_i$ values and less than unity at high $P{\cdot}d_i$ values are expected. Interesting enough, not only are the trends similar, but as indicated by the dashed line, $V_{DC}^{down}/V_{DC}^{up}$ and r_d^{down}/r_d^{up} share the same transition point in terms of $P{\cdot}d_i$.

5.3. SiH_4/H_2 plasma chemistry

It has been shown in previous sections that the asymmetric plasma response for a *sawtooth* waveform excited $SiF_4/H_2/Ar$ plasma can be controlled by the process parameters (pressure, geometric asymmetry), and through this, asymmetric processing can be achieved. In this section, we explore the analogous experiments but for the more frequently used SiH_4/H_2 plasma chemistry.

5.3.1. Without Ar

As it has been observed in the $SiF_4/H_2/Ar$ plasma, the $P{\cdot}d_i$ product is proved to be a crucial parameter in determining the dominant electron heating mode, and thus the relative film deposition rates on two electrodes. In this section, another set of a-Si:H films have been deposited using an SiH_4/H_2 plasma excited by *sawtooth* waveforms. Different pressures and inter-electrode distances are employed to achieve varying $P{\cdot}d_i$ conditions, and details about the process conditions are shown in Table 5.12.

Table 5.12 Process conditions for silicon thin film deposition using SiH_4/H_2 plasma chemistry using *sawtooth* waveforms with varying $P{\cdot}d_i$.

V_{PP}	P	d_i	T_{sub}	T_{rf}	SiH_4	H_2
V	Torr	cm	°C	°C	sccm	sccm
285	0.65-1.35	2-4	150	100	10	100

Figure 5.29-(a) and (b) show the evolution of $V_{DC}^{down}/V_{DC}^{up}$ and r_d^{down}/r_d^{up} under these different process conditions, respectively. As in the results for the $SiF_4/H_2/Ar$ plasma shown in Figure 5.25-(a), three zones can be roughly identified for the SiH_4/H_2 plasma regarding the values of $V_{DC}^{down}/V_{DC}^{up}$ with varying $P{\cdot}d_i$. In zone A, the plasmas heating operate in the α-mode, leading to $V_{DC}^{down}/V_{DC}^{up}$ values greater than unity and increasing with pressure. However, the increase of $P{\cdot}d_i$ in zone B leads to the heating transition from the α-mode, then a hybrid α-DA mode, finally into the dominant DA-mode. As a consequence, $V_{DC}^{down}/V_{DC}^{up}$ reverses to less than unity at high $P{\cdot}d_i$ (> ~3 Torr·cm) conditions. Eventually, $V_{DC}^{down}/V_{DC}^{up}$ stabilizes around a relatively low value in zone C with further increased $P{\cdot}d_i$ values.

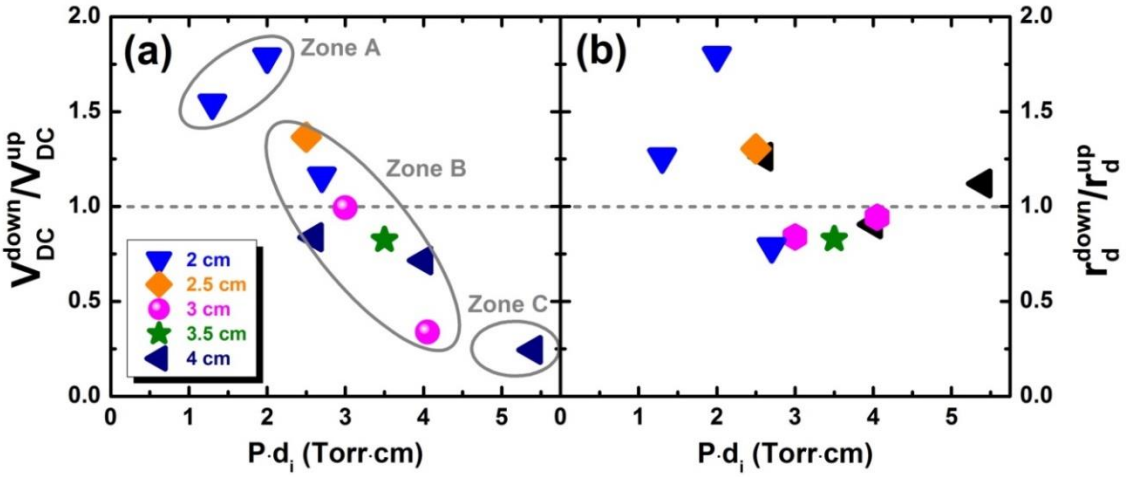

Figure 5.29 Evolution of (a) $V_{DC}^{down}/V_{DC}^{up}$ and (b) r_d^{down}/r_d^{up} with varying $P{\cdot}d_i$ for the SiH_4/H_2 plasma. The ellipses indicate the zone A, B, and C as described in the text.

The resulting relative deposition rates are presented in Figure 5.29-(b). In contrast with the case for $SiF_4/H_2/Ar$, the process results do not correlate as strong as the plasma results. However, transition of the relative magnitude of deposition rate at higher $P{\cdot}d_i$ value (~3 Torr·cm) is also seen in zone B, close to where the values of V_{DC} are reversed. However, further increase of $P{\cdot}d_i$ does not lead to further decrease of r_d^{down}/r_d^{up} as it has been observed in the case of $SiF_4/H_2/Ar$ plasma processes. On the contrary, an increase of r_d^{down}/r_d^{up} up to ~1.1 is seen at $P{\cdot}d_i$ = 5.4 Torr·cm.

To understand this point, one should consider the hydrogen dominated plasma in this series of experiments. For the case of *sawtooth-up* plasma, the transition of electron heating from the α-mode into the DA-mode leads to a more intense dissociation of SiH_4 (accumulation of growth precursors) in front the grounded electrode experiencing a fast sheath contraction, thus resulting in a higher deposition rate. However, as opposed to material growth from the $SiF_4/H_2/Ar$ plasma chemistry studied in Section 5.2.1, the SiH_4/H_2 chemistry does require hydrogen to eliminate by-products. Therefore, all the available hydrogen species have the possibility to participate in the material deposition and etching processes. In this case, the effect of spatial localization of hydrogen species, especially at high $P{\cdot}d_i$ conditions (as suggested by the results in Section 5.2.3), becomes more important in determining the processing results. Since hydrogen species are much more effective at etching a-Si:H compared to µc-Si:H material,[35,36], a stronger etching effect can also be expected during processing at high $P{\cdot}d_i$ conditions. Therefore, the further increase in $P{\cdot}d_i$ does not lead to a continuous decrease of r_d^{down}/r_d^{up}, and even an increase is observed for $P{\cdot}d_i$ above 5 Torr·cm (Figure 5.29-(b)).

For the *sawtooth-down* plasma process, although the concentration of the growth precursors is lower in front of the grounded electrode due to the slow sheath contraction, the hydrogen species concentration is also lower. This means that a weaker etching effect would also be expected during processing. Therefore, the "transfer" of the discharge asymmetry via the slope asymmetry effect to a film deposition rate asymmetry will be less effective in the SiH_4/H_2 plasma chemistry.

[35] R. C. van Oort, et al., *Electron. Lett.*, **23(18)**: 967 (1987).
[36] B. Giovanni, et al., *Philos. Mag.*, **89(28-30)**: 2469 (2009).

5.3.2. With Ar

Similar studies were taken with additional Ar injection in the gas mixture, i.e., using an $SiH_4/H_2/Ar$ plasma chemistry. In this case, higher gas pressures can be achieved, thus leading to a control over the $P{\cdot}d_i$ values in a larger range. Details about the process conditions are shown in Table 5.13.

Table 5.13 Process conditions for silicon thin film deposition from $SiH_4/H_2/Ar$ gas mixture using *sawtooth* waveforms with varying $P{\cdot}d_i$.

V_{PP}	P	d_i	T_{sub}	T_{rf}	SiH_4	H_2	Ar
V	Torr	cm	°C	°C	sccm	sccm	sccm
285	1.39 and 2	2.5-4	150	100	2.5	100	20

Figure 5.30-(a) and (b) show the evolution of $V_{DC}^{down}/V_{DC}^{up}$ and r_d^{down}/r_d^{up} under these different process conditions, respectively. Due to inadequate data points, zone A and C cannot be well illustrated in the results. However, one can still find a clear transition of electron heating mode (in zone B) at a certain $P{\cdot}d_i$ value.

However, the link with the resulting deposition process (as seen in Figure 5.30-(b)) is now even less clear. A higher relative deposition rate for *sawtooth-down* samples is indeed obtained at a low $P{\cdot}d_i$ value around 2.8 Torr·cm. However, although the transition is again observed at the same $P{\cdot}d_i$, value, the relative deposition rate r_d^{down}/r_d^{up} reverses trend and again becomes greater than unity. The explanation for this behavior may be similar to that for the case without Ar, but useful and predictable trends are not as clear as for the SiF_4 case.

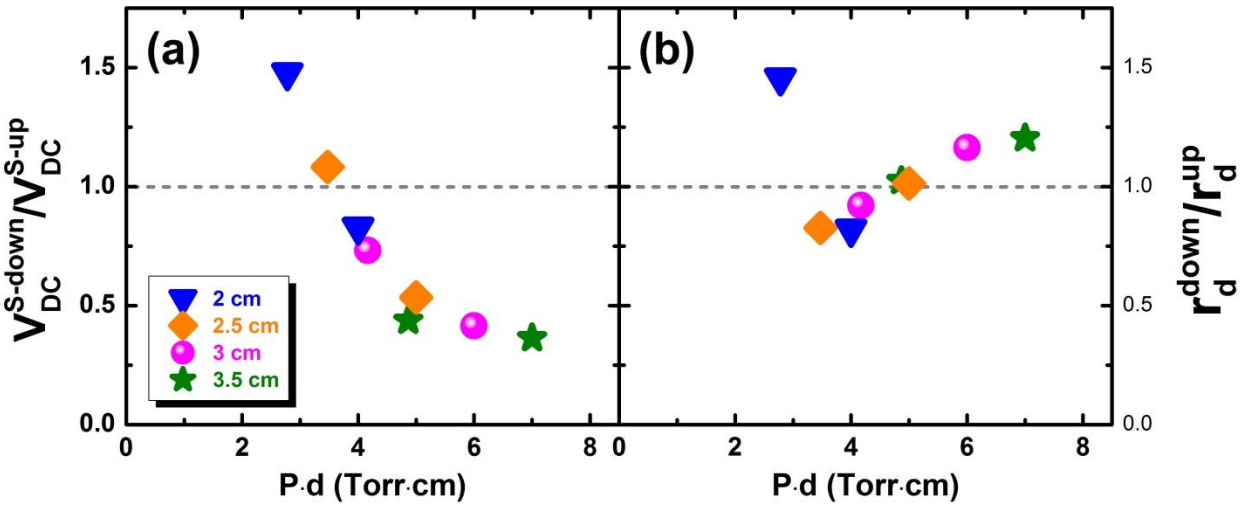

Figure 5.30 Evolution of (a) $V_{DC}^{down}/V_{DC}^{up}$ and (b) r_d^{down}/r_d^{up} with varying $P{\cdot}d_i$ for the $SiH_4/H_2/Ar$ plasma.

5.4. The possibility of "electrode-selective" processing using peaks/valleys waveform

To maximize and study the slope asymmetry effect separately from the amplitude asymmetry, the work presented in the previous section exclusively focused on the use of *sawtooth* waveforms having identical minimum and maximum excursions in the applied voltage. In this section, we present a study using another set of TVW, namely *peaks* and *valleys* waveforms, which are normally dedicated to maximize the amplitude asymmetry. As depicted in Figure 5.31, such voltage waveforms have significantly different minima and maxima, and are obtained by choosing $\varphi = 0$ and π for Equation (4.10).

The sheath motion dynamics for *peaks* and *valleys* waveform excited plasmas are very different from that for the *sawtooth* plasmas. Both fast sheath expansion **and** contraction can happen close to **both** electrodes. However, as for *sawtooth* plasmas, localized electron heating dynamics and the reversal of discharge asymmetry (depending on pressure, fundamental driving frequency, number of harmonics, etc.) play a large role, especially for electronegative O_2[9,10] and CF_4[11,12] plasmas excited by the *peaks* and *valleys* waveforms.

Taking a CF_4 plasma operating in the DA-mode for instance[11], the fast voltage drop for the *peaks* waveform leads to the sheath close to the grounded electrode collapsing rapidly, but also remaining collapsed for most of the time during one fundamental RF period. In this case, negative ions can enter the sheath region in front of the grounded electrode due to the weak time-averaged electric field. Then, because of the similar self-sustaining effect described in Section 5.1, the accumulation of negative ions can lead to a reduction of local electron density and conductivity, causing the formation of a strong reversed electric field at the edge of the collapsing sheath close to the given electrode. However, this does not happen for the sheath close to the powered electrode, where the fast sheath contraction is immediately followed by a fast sheath expansion. Therefore, in such cases, an ionization asymmetry can even occur for the case of *peaks* and *valleys* waveforms.

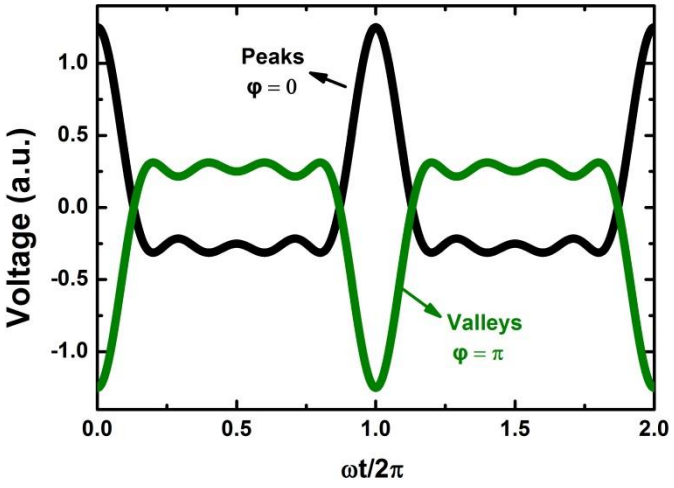

Figure 5.31 *Peaks* and *valleys* waveforms corresponding to $\varphi = 0$ and π, respectively.

Intrigued by these results, a further investigation on the "electrode-selective" effect was carried out using *peaks* and *valleys* waveforms as the driving sources for an $SiF_4/H_2/Ar$ plasma. As a

comparison, plasma processes using the *sawtooth* waveforms were also studied. Herein, the underlying a-Si:H layers were all kept at ~60 nm thick. Details about the process conditions are shown in Table 5.14.

Table 5.14 Process conditions for the two-step deposition using the *sawtooth*, *peaks* and *valleys* waveforms.

Waveform	Time	V_{PP}	V_{DC}	IBE_{max}	P	d_i	SiF_4	H_2	Ar	Depletion	
										H_2	SiF_4
	s	V	V	V	Torr	cm	sccm	sccm	sccm	%	%
Sawtooth-up	555	285	-54	~44	3	3	10	2.5	88	-	-
Sawtooth-down			-18	~62						-	-
Peaks	1020	240	-80	~22						96.0	8.7
Valleys			20	~54						97.2	8.4

Note that although different SiF_4 and H_2 gas flows of 10 and 2.5 sccm were used in the second step for this study, the processes were still operated in the H_2-limited regime. As shown in Table 5.14, the H_2 is almost fully depleted in both plasma processes.

The ellipsometry spectra for the samples after the SiF_4/H_2/Ar plasma treatment in the second step are presented in Figure 5.32. Consistent with the results of Section 5.2.1, the *sawtooth-up* plasma treatment causes a strong etching of the underlying layer, whereas a net deposition process is observed for the case of *sawtooth-down*, as seen in Figure 5.32-(a).

Interestingly, similar results are also observed when the *peaks* or *valleys* waveform was applied. As seen in Figure 5.32-(b), a net etching process is caused by the *peaks* plasma, while a net deposition process is given by its counterpart.

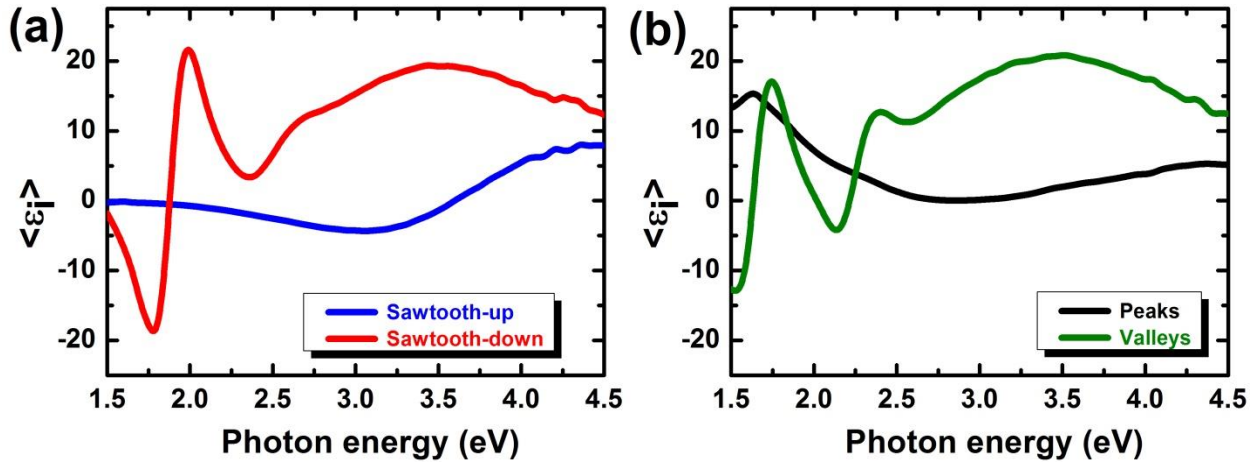

Figure 5.32 Ellipsometry spectra for two-step deposited films using (a) *sawtooth-up* (blue), *sawtooth-down* (red), and (b) *peaks* (black), *valleys* (green) waveforms.

The corresponding ellipsometric modeling for the two deposition plasmas (*sawtooth up* and

valleys) are presented in Figure 5.33, with the underlying a-Si:H layer deposited in the first step shown in gray. For the *sawtooth-up* waveform, as shown in Figure 5.33-(a), after 555 s of plasma treatment, a layer with a thickness of ~128 nm is obtained. As modelled in Figure 5.33-(b), a thicker layer with a thickness of ~157 nm is obtained after 1020 s of *valleys* plasma treatment.

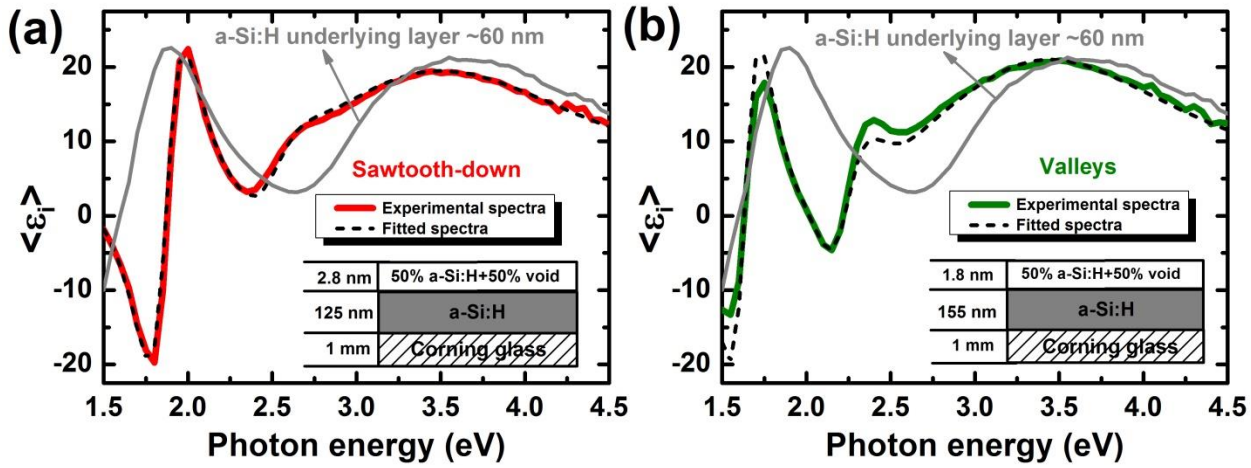

Figure 5.33 Comparison of ellipsometric spectra for films before (gray) and after (red) the (a) *sawtooth-down* and (b) *peaks* plasma treatment for 555 s and 1020 s, respectively. The fitted spectra for the layer after treatment is shown in dashed.

As for the origin of such different deposition/etching processes in the case of *peaks* and *valleys* plasmas, first of all, one can easily eliminate the possible contribution of sputtering by the impinging ions. The ion energy conditions for the *peaks* plasma is typically low, indicated by a IBE_{max} value of ~22 eV compared to that of ~54 eV for the *valleys* plasma in this study. Therefore, we should rather consider the effect of discharge asymmetry in such processes. In the case of a *peaks* plasma (in analogy with the CF_4 plasma in Ref. 11), the electron power absorption is spatially localized near the fast shrinking grounded sheath (remaining to be collapsed for most of the RF cycle), and thus a higher concentration of fluorinated species can accumulate in front of the grounded electrode. Since the process is operated in the H_2-limited regime, such an elevated amount of fluorinated species cannot be easily scavenged by the available hydrogen, and a strong etching effect on the grounded electrode is therefore expected.

However, the situation is different for the *valleys* plasma, since the discharge asymmetry is reversed. The fast collapsing sheath close to the powered electrode leads to an accumulation of fluorinated species, while not for the grounded electrode. Therefore, instead of having a strong etching effect, a deposition process is obtained therein.

5.5. Summary

In this chapter, we have explored the application of the slope asymmetry effect to multi-gas plasmas. Studies on silicon thin film deposition have been carried out by using *sawtooth* voltage waveforms as the driving source. The *sawtooth* waveform presents different rising and falling rates over one fundamental period, and accordingly, differing plasma sheath motion close to each electrode can be achieved. Either the *sawtooth-up* (fast rise and slow fall) or the *sawtooth-down* (slow rise and fast fall) waveform can induce a fast sheath expansion followed by a slow contraction close to one electrode, while the opposite for the other electrode. Because of the difference in sheath dynamics, the discharge power absorption becomes spatially asymmetric (discharge asymmetry) depending on the electron heating mode. Such discharge asymmetry can simply be reflected by measuring the DC self-bias.

By combining this effect with a multi-precursor deposition/etching process (namely the $SiF_4/H_2/Ar$ plasma chemistry), the discharge asymmetry can result in differing deposition or etching processes on each electrode. This kind of "electrode-selective" processing can be directly controlled by the gas flow ratio. By increasing the H_2 flow, the enhancement of plasma electronegativity triggers a transition of plasma electron heating from a dominant α-mode into a dominant DA-mode, which leads to a reverse in the discharge asymmetry. As a consequence, one electrode experiences a greater precursor generation than the other. Taking the *sawtooth-up* waveform excited plasma for example, at low H_2 flows, high concentrations of fluorinated species at the grounded electrode cannot be easily scavenged by the available hydrogen. This will lead to a strong etching effect or a lower deposition rate at the grounded electrode compared to the powered electrode. However, at high H_2 flows, the surface process is not limited by the presence of H_2, and deposition can be achieved on both electrodes. As the spatially asymmetric excitation of the plasma now creates an asymmetric distribution of growth precursors, a reverse of the net deposition rate on each electrode is now observed.

In addition, the impact of pressure P and inter-electrode distance d_i on the slope asymmetry effect for both single-gas and multi-gas plasmas have been studied. Depending on the gas property, changes in P and d_i can induce an enhancement or a reduction of the discharge asymmetry, or even a transition of the electron heating mode. For the electronegative $SiF_4/H_2/Ar$ plasma under the investigated process conditions, the discharge operates in a dominant α-mode at low $P \cdot d_i$ conditions, while above certain $P \cdot d_i$ values (~5-6 Torr·cm), the DA-mode becomes prevalent. This means that the discharge asymmetry can be modified by the $P \cdot d_i$ conditions, and a more flexible control over the balance of the above "electrode-selective" processing is therefore expected. This scenario is further explored for the SiH_4/H_2 plasma chemistry; for this chemistry, the etching effect of hydrogen significantly modifies the surface processing balance.

Further experimental results have shown that such discharge asymmetry and therefore "electrode-selective" processing can also be achieved in an electronegative plasma by using the *peaks* and *valleys* waveforms, which are rather designed to maximize the amplitude asymmetry effect (control over the ion energy). Although the resulting plasma has identical sheath expansion and contraction rates, one of the sheaths remains collapsed for most of the RF cycle. For an electronegative plasma, such sheath motion also causes a localized power absorption occurring near the collapsing sheath edge. Thus, for certain process conditions (with not enough H_2), a strong etching effect can be observed at the given electrode, while a deposition is seen at the other one.

Reference

[1] Z. Donkó, J. Schulze, B. G. Heil, and U. Czarnetzki, “PIC simulations of the separate control of ion flux and energy in CCRF discharges via the electrical asymmetry effect”, *J. Phys. D: Appl. Phys.*, vol. 42, no. 2, p. 025205, 2009.

[2] J. Schulze, E. Schüngel, U. Czarnetzki, and Z. Donkó, “Optimization of the electrical asymmetry effect in dual-frequency capacitively coupled radio frequency discharges: Experiment, simulation, and model”, *J. Appl. Phys.*, vol. 106, no. 6, p. 063307, 2009.

[3] E. Schüngel, Q. Z. Zhang, S. Iwashita, J. Schulze, L. J. Hou, Y. N. Wang, and U. Czarnetzki, “Control of plasma properties in capacitively coupled oxygen discharges via the electrical asymmetry effect”, *J. Phys. D: Appl. Phys.*, vol. 44, no. 28, p. 285205, 2011.

[4] I. Korolov, Z. Donkó, U. Czarnetzki, and J. Schulze, “The effect of the driving frequencies on the electrical asymmetry of dual-frequency capacitively coupled plasmas”, *J. Phys. D: Appl. Phys.*, vol. 45, no. 46, p. 465205, 2012.

[5] B. Bruneau, T. Novikova, T. Lafleur, J.-P. Booth, and E. V. Johnson, “Ion flux asymmetry in radiofrequency capacitively-coupled plasmas excited by *sawtooth*-like waveforms”, *Plasma Sources Sci. Technol.*, vol. 23, no. 6, p. 065010, 2014.

[6] B. Bruneau, T. Gans, D. O’Connell, A. Greb, E. V. Johnson, and J.-P. Booth, “Strong Ionization Asymmetry in a Geometrically Symmetric Radio Frequency Capacitively Coupled Plasma Induced by Sawtooth Voltage Waveforms”, *Phys. Rev. Lett.*, vol. 114, no. 12, p. 125002, 2015.

[7] B. Bruneau, T. Novikova, T. Lafleur, J.-P. Booth, and E. V. Johnson, “Control and optimization of the slope asymmetry effect in tailored voltage waveforms for capacitively coupled plasmas”, *Plasma Sources Sci. Technol.*, vol. 24, no. 1, p. 015021, 2015.

[8] B. Bruneau, P. Diomede, D.J. Economou, S. Longo, T. Gans, D. O’Connell, A. Greb, E. V. Johnson, and J.-P. Booth, “Capacitively coupled hydrogen plasmas sustained by tailored voltage waveforms: excitation dynamics and ion flux asymmetry”, *Plasma Sources Sci. Technol.*, vol. 25, no. 4, p. 045019, 2016.

[9] A. Derzsi, B. Bruneau, A.R. Gibson, E. V. Johnson, D. O’Connell, T. Gans, J.-P. Booth, and Z. Donkó, “Power coupling mode transitions induced by tailored voltage waveforms in capacitive oxygen discharges”, *Plasma Sources Sci. Technol.*, vol. 26, no. 3, p. 034002, 2017.

[10] E. Schüngel, I. Korolov, B. Bruneau, A. Derzsi, E. V. Johnson, D. O’Connell, T. Gans, J.-P. Booth, Z. Donkó, and J. Schulze, “Tailored voltage waveform capacitively coupled plasmas in electronegative gases: frequency dependence of asymmetry effects”, *J. Phys. D: Appl. Phys.*, vol. 49, no. 26, p. 265203, 2016.

[11] S. Brandt, B. Berger, E. Schüngel, I. Korolov, A. Derzsi, B. Bruneau, E. V. Johnson, T. Lafleur, D. O’Connell, M. Koepke, T Gans, J.-P. Booth, Z. Donkó, and J. Schulze, “Electron power absorption dynamics in capacitive radio frequency discharges driven by tailored voltage waveforms in CF_4”, *Plasma Sources Sci. Technol.*, vol. 25, no. 4, p. 045015, 2016.

[12] B. Bruneau, I. Korolov, T. Lafleur, T. Gans, D. O'Connell, A. Greb, A. Derzsi, Z. Donkó, S. Brandt, E. Schüngel, J. Schulze, E. V. Johnson, and J.-P. Booth, "Slope and amplitude asymmetry effects on low frequency capacitively coupled carbon tetrafluoride plasmas", *J. Appl. Phys.*, vol. 119, no. 16, p. 163301, 2016.

[13] B. Bruneau, T. Lafleur, T. Gans, D. O'Connell, A. Greb, I. Korolov, A. Derzsi, Z. Donkó, S. Brandt, E. Schüngel, J Schulze, P. Diomede, D.J. Economou, S. Longo, E. V. Johnson, and J.-P. Booth, "Effect of gas properties on the dynamics of the electrical slope asymmetry effect in capacitive plasmas: comparison of Ar, H_2 and CF_4", *Plasma Sources Sci. Technol.*, vol. 25, no. 1, p. 01LT02, 2016.

[14] V. A. Godyak, "Statistical Heating of Electrons at an Oscillating Plasma Boundary", *Sov. Phys. Tech. Phys.*, vol. 16, p. 1073, 1972.

[15] M. A. Lieberman and A. J. Lichtenberg, *Principles of Plasma Discharges and Materials Processing* (second edition), New Jersey: Wiley, 2005.

[16] P. Chabert and N. Braithwaite, *Physics of Radio-Frequency Plasmas*, Cambridge: Cambridge University Press, 2011.

[17] J. Schulze, Z. Donkó, B.G. Heil, D. Luggenhölscher, T. Mussenbrock, R.P. Brinkmann, and U. Czarnetzki, "Electric field reversals in the sheath region of capacitively coupled radio frequency discharges at different pressures", *J. Phys. D: Appl. Phys.*, vol. 41, no. 10, p. 105214, 2008.

[18] J.-C. Dornstetter, B. Bruneau, P. Bulkin, E. V. Johnson, and P. Roca i Cabarrocas, "Understanding the amorphous-to-microcrystalline silicon transition in SiF_4/H_2/Ar gas mixtures", *J. Chem. Phys.*, vol. 140, no. 23, p. 234706, 2014.

[19] M. Hayama, H. Murai, and K. Kobayashi, "Ion bombardment effects on undoped hydrogenated amorphous silicon films deposited by the electron cyclotron resonance plasma chemical vapor deposition method", *J. Appl. Phys.*, vol. 67, no. 3, p. 1356, 1990.

[20] A. H. M. Smets and M. Kondo, "The role of ion-bulk interactions during high rate deposition of microcrystalline silicon by means of the multi-hole-cathode VHF plasma", *J. Non-Cryst. Solids*, vol. 352, no. 9-20, p. 937, 2006.

[21] T. Lafleur and J.-P. Booth, "Control of the ion flux and ion energy in CCP discharges using non-sinusoidal voltage waveforms", *J. Phys. D: Appl. Phys.*, vol. 45, no. 39, p. 395203, 2012.

[22] K. Denpoh and K. Nanbu, "Self-Consistent Particle Simulation of Radio Frequency CF_4 Discharge: Effect of Gas Pressure", *Jpn. J. Appl. Phys.*, vol. 39, no. 5R, p. 2804, 2000.

[23] O. V. Proshina, T. V. Rakhimova, A. T. Rakhimov, and D. G. Voloshin, "Two modes of capacitively coupled rf discharge in CF_4", *Plasma Sources Sci. Technol.*, vol. 19, no. 6, p. 065013, 2010.

[24] G. H. Liu, Y. X. Liu, D. Q. Wen, and Y. N. Wang, "Heating mode transition in capacitively coupled CF_4 discharges: comparison of experiments with simulations", *Plasma Sources Sci. Technol.*, vol. 24, no. 3, p. 034006, 2015.

[25] Y. Catherine and P. Couderc, "Electrical characteristics and growth kinetics in discharges used for plasma deposition of amorphous carbon", *Thin Solid Films*, vol. 144, no. 2, p. 265,

1986.

[26] N. Mutsukura, K. Kobayashi, and Y. Machi, "Monitoring of radio-frequency glow-discharge plasma", *J. Appl. Phys.*, vol. 66, no. 10, p. 4688, 1989.

[27] J. Robertson, "Diamond-like amorphous carbon", *Mater. Sci. Eng. R Rep.*, vol. 37, no. 4-6, p. 129, 2002.

[28] K. Bewilogua and D. Hofmann, "History of diamond-like carbon films - From first experiments to worldwide applications", *Surf. Coat. Technol.*, vol. 242, p. 214, 2014.

[29] G. Alexiou, G. Tsigaras, E. Amanatides, and D. Mataras, "Detection of powder formation in SiH_4/H_2 glow discharges", *J. Phys. Conf. Ser.*, vol. 700, no. 1, p. 012038, 2016.

[30] E. Schüngel, D. Eremin, J. Schulze, T. Mussenbrock, and U. Czarnetzki, "The electrical asymmetry effect in geometrically asymmetric capacitive radio frequency plasmas", *J. Appl. Phys.*, vol. 112, no. 5, p. 053302, 2012.

[31] Y. Djeridane, A. Abramov, and P. Roca i Cabarrocas, "Silane versus silicon tetrafluoride in the growth of microcrystalline silicon films by standard radio frequency glow discharge", *Thin Solid Films*, vol. 515, no. 19, p. 7451, 2007.

[32] P. Roca i Cabarrocas, Y. Djeridane, V. D. Bui, Y. Bonnassieux, and A. Abramov, "Critical issues in plasma deposition of microcrystalline silicon for thin film transistors", *Solid-State Electron.*, vol. 52, no. 3, p. 422, 2008.

[33] J.-C. Dornstetter, "Microcrystalline silicon deposited from $SiF_4/H_2/Ar$ plasmas and its application to photovoltaics", *PhD thesis*, École Polytechnique, 2014.

[34] P. Roca i Cabarrocas, T. Nguyen-Tran, Y. Djeridane, A. Abramov, E. V. Johnson, and G. Patriarche, "Synthesis of silicon nanocrystals in silane plasmas for nanoelectronics and large area electronic devices", *J. Phys. D: Appl. Phys.*, vol. 40, no. 8, p. 2258, 2007.

[35] R. C. van Oort, M. J. Geerts, J. C. van den Heuvel, and J. W. Metselaar, "Hydrogen plasma etching of amorphous and microcrystalline silicon", *Electron. Lett.*, vol. 23, no. 18, p. 967, 1987.

[36] B. Giovanni, C. Pio, G. Maria M., and L. Maria, "From amorphous to microcrystalline silicon: Moving from one to the other by halogenated silicon plasma chemistry", *Philos. Mag.*, vol. 89, no. 28-30, p. 2469, 2009.

Chapter 6 Conclusions and Highlights

In the first and second parts of this thesis, great effort has been dedicated to studying the process optimization of silicon thin film materials deposition and photovoltaic devices fabrication using different types of PECVD techniques, and specifically the impact of ion energy on the processing results. In the third part, as an application of the multi-frequency TVW excitation technique, we discovered an "electrode-selective" effect using a CCP process.

MDECR-PECVD of μc-Si:H

In order to obtain high growth rate μc-Si:H, we combined the MDECR-PECVD technique and a halogenated plasma chemistry using an SiF_4/H_2 gas mixture. Substrate temperature is demonstrated to be essential for achieving high crystalline volume fraction under such high density and low pressure plasma conditions, due to the thermally-induced enhancement of surface species diffusion. On the other hand, due to the specific design of the MDECR system, we performed a careful investigation of the impact of ion energy conditions to the material deposition. We found that a moderate ion energy condition is beneficial to achieve a significant drop in the density of nano-voids, and thus a higher quality material with better stability can be obtained. By increasing the ion energy during deposition, two IBE thresholds at ~12 eV and ~43 eV are detected, corresponding to the effects of SiF^+-induced surface and bulk atomic displacements. The smaller grain sizes and rougher surface layers observed are qualitatively linked to the SiF^+-induced surface displacement. At higher energies, bulk displacement induced by SiF^+ ions can severely suppress the nucleation process, leading to a local amorphization effect on the growing film.

Furthermore, we found that the incubation process is the most challenging step of μc-Si:H growth for this technology. A two-step deposition method is introduced as an alternative way to eliminate the existence of amorphous incubation layer. By preparing a highly crystallized seed layer (can be as thin as ~4 nm) at a rather low process pressure, the subsequently deposited high growth rate μc-Si:H main layer at high process pressure can proceed into the crystalline phase growth directly. These results all suggest that the use of MDECR-PECVD and the SiF_4/H_2 plasma chemistry for the growth of μc-Si:H film result in relaxed requirements on process parameters for device quality material.

Application of TVW in silicon thin film deposition

We have explored the application of the TVW excitation technique for CCP processes. As an advantage over the conventional single-frequency excitations, the non-sinusoidal TVW provide an elegant solution for ion flux-energy decoupling in CCP discharges through the electrical asymmetry effect. Based on this insight, we studied the impact of ion energy on CCP-PECVD μc-Si:H using an $SiF_4/H_2/Ar$ plasma chemistry. A semi-independent control over the ion energy has been achieved, as a little-varying film growth rate allows us to focus on ion effects.

We find that a variation of ion energy, or precisely speaking the maximum IBE (IBE_{max}) at

relatively high pressure conditions, can be directly translated into the material quality. Through structural and electronic analysis, we found that the material with optimum properties is obtained with moderate IBE_{max} values in the range of ~45-55 eV. Beyond this range, a reduction in the material properties showing by smaller crystallite features and higher density deficiency is observed, which corresponds to the effect of bulk atomic displacements induced by silicon-related ions during processing. Such effectiveness of TVW in process control is further confirmed by studying the deposition of a-Si:H from an SiH_4/H_2 plasma chemistry. Under the investigated ion energy conditions, we found that moderate IBE_{max} values can lead to an improved material density as well as better stability under illumination. An IBE_{max} threshold at ~12 eV, corresponding to the SiH_x^+-induced surface displacement, has been determined to be responsible for the material quality degradation. We further applied these results to photovoltaic applications (both µc-Si:H and a-Si:H) and established comprehensive links from the controllable plasma parameters via TVW to the properties of deposited materials, and eventually to the performance of resulting devices.

"Electrode-selective" surface process

In this part, the slope asymmetry effect caused by the use of *sawtooth* TVW has been studied. Due to the strong asymmetry of the rising and falling slopes in the applied voltage, spatially asymmetric sheath dynamics and electron power absorption close to each electrode can be generated, even in a geometrically symmetric reactor. In analogy with single-gas plasmas, such discharge asymmetry depends on the dominant plasma heating mechanism and can be simply reflected through the measurements of DC self-bias. By coupling this effect with the multi-precursor $SiF_4/H_2/Ar$ plasma, we observed the occurrence of an "electrode-selective" effect in a CCP process. For certain gas flow ratios, we can obtain a deposition process on one electrode, while at the same time either no deposition or an etching process on the other electrode. Furthermore, such deposition/etching balance can be controlled through the H_2 injection.

The impact of pressure and reactor geometry on the slope asymmetry effect for both the single-gas and multi-gas plasmas has also been studied. The product of pressure and inter-electrode distance $P{\cdot}d_i$ is deduced to be a crucial parameter in determine the plasma heating mode, as deduced by the experimentally obtained DC self-bias, especially the relative values for *sawtooth-up* and *-down* waveforms. This has also been observed in the SiH_4/H_2 plasma chemistry, with similar conclusions. This means that the discharge asymmetry can be switched by changing the $P{\cdot}d_i$ conditions, and thus a more flexible control over the "electrode-selective" process can be expected.

Surprisingly, such "electrode-selective" processes have also been identified when using *peaks* or *valleys* waveforms, typically used to maximize the amplitude asymmetry effect (control over the ion energy). We propose that this is caused by one of the sheaths shrinking rapidly and remaining collapsed for most of one fundamental period. Such unique sheath dynamics can also cause localized plasma heating near a collapsing sheath edge.

In short, these results reinforce the flexibility of the TVW technique for optimizing RF-CCP related processes. The possibility of achieving controllable discharge asymmetry and the

discovery of “electrode-selective” processes encourage the prospect that one could choose a set of process conditions to achieve a wide variety of desired depositions on one electrode, while leaving the other pristine.

Appendix

Another initial target of this thesis work is dedicated to the fabrication of high-efficiency single-junction µc-Si:H solar cells based on the $SiF_4/H_2/Ar$ plasma chemistry. But due to the planned works in our group, only some preliminary work will be presented here. Again, this part of work mainly focuses on the process optimization of intrinsic absorber layer in the device, and it has been carried out only using the standard single-frequency (13.56 MHz) excitation source.

Based on of the perspectives from the recent PhD thesis work[1] relating with this topic, a $P{\cdot}d_i$ value of 6 Torr·cm is used for all the processes herein ($P{\cdot}d_i$ = 12 Torr·cm was used in former work), since it has been suggested in Ref. 2 that an optimum for both deposition rate and electronic properties can be achieved under such condition. Moreover, as it has been done in Section 4.2, all the solar cell devices are in a substrate *n-i-p* configuration (a superstrate *p-i-n* configuration was used in Ref. 1).

A.1. Effect of H_2 flow rate

First of all, a series of µc-Si:H films were deposited at a constant SiF_4 flow rate of 3.6 sccm and Ar dilution of 88 sccm, while the H_2 flow rate was varied from 2.5 sccm up to 7 sccm. The detailed information is shown in Table A.1. All the films are kept around 500 nm (±50 nm) thick.

Table A.1 Process conditions for µc-Si:H film deposition with varying H_2 flow rate.

P_{RF}	P	d_i	T_{sub}	T_{rf}	SiF_4	H_2	Ar
W	T	cm	°C	°C	sccm	sccm	sccm
15	3	2	150	80	3.6	2.5-7	88

Instead of keeping the V_{PP} of excitation source constant, we used a constant RF power at 15 W for this series of deposition. However, the IBE_{max} values for these processes only vary in a small range around 55 eV (±2 eV), which does not exceed the ion energy threshold relating with the material properties transition observed in Section 4.2. Therefore, one can neglect the difference of ion energy conditions during processing and their impact to the resulting materials that have been extensively discussed in this work.

Ellipsometry and Raman measurements were performed for the samples, and the results are presented in Figure A.1. One can note from both characterizations that the increase of H_2 flow rate

[1] J.-C. Dornstetter, "Microcrystalline silicon deposited from $SiF_4/H_2/Ar$ plasmas and its application to photovoltaics", *PhD thesis*, École Polytechnique (2014).
[2] P. Roca i Cabarrocas, T. Nguyen-Tran, Y. Djeridane, A. Abramov, E. V. Johnson, and G. Patriarche, "Synthesis of silicon nanocrystals in silane plasmas for nanoelectronics and large area electronic devices", *J. Phys. D: Appl. Phys.*, vol. 40, no. 8, p. 2258, 2007.

gives rise to an increase of the film crystallinity, indicated by the more pronounced should-like peaks in ellipsometry spectra (Figure A.1-(a)) and the less intensity of the broad amorphous peak in Raman spectra (Figure A.1-(b)). What are also included in Figure A.1-(b) are the corresponding X_c^{Raman} values. For H_2 flow rate at 2.5 sccm, the film is in the amorphous-to-microcrystalline transition regime with comparable contents of materials in both phase. By increasing H_2 to 3 sccm, X_c^{Raman} sharply increases to ~61 %, which is then followed by a continuous increase up to ~80 % at H_2 = 7 sccm.

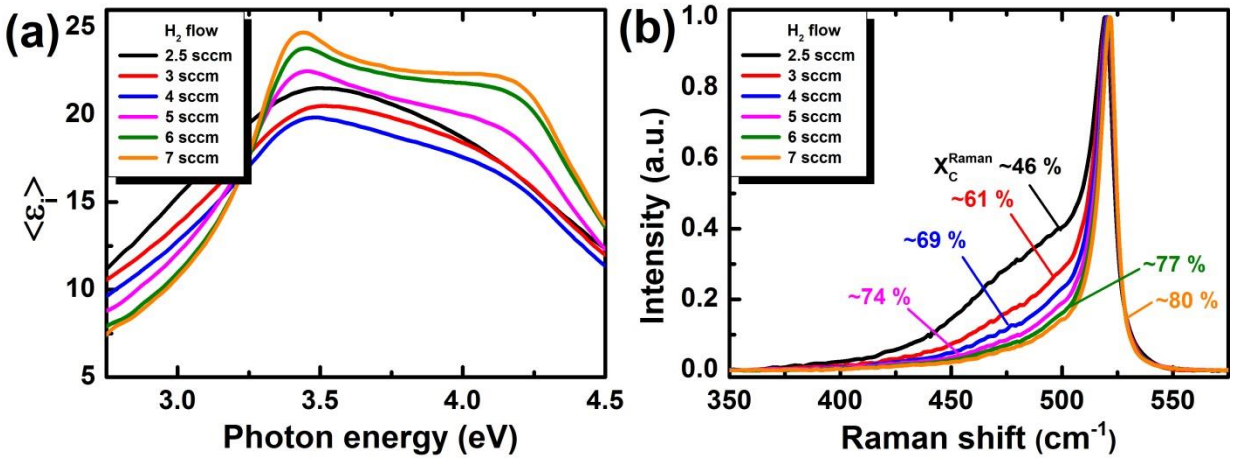

Figure A.1 (a) Ellipsometry spectra in high energy portion and (b) Normalized Raman spectra for µc-Si:H films deposited using different H_2 flow rates.

In order to examine the resulting device performance, a set of single-junction solar cells with the same structure as seen in Figure 4.19 were fabricated by using the above µc-Si:H films as the absorber layers. Here, only H_2 flow rates in the range of 3-6 sccm were tested, and the thicknesses of the absorber layers were kept around 1.5 µm. Table A.2 summaries the *I-V* parameters for these solar cells, and the corresponding EQE spectra is shown in Figure A.2. An optimum device performance is obtained at H_2 = 4 sscm, showing the highest η = 9.61 % with J_{SC} = 25.2 % (from EQE), V_{OC} = 0.530 V, and FF = 72.0 %.

Table A.2 *I-V* parameters of the substrate *n-i-p* µc-Si:H solar cells with absorber layers deposited using different H_2 flow rates.

H_2 sccm	t_i µm	J_{SC} mA/cm^2	V_{OC} V	FF %	η %
3	~1.5 (±0.1)	23.4	0.509	51.6	6.15
4		25.2	0.530	72.0	9.61
5		24.2	0.523	73.1	9.24
6		23.9	0.524	74.0	9.26

Due to the inadequate experimental data, it would be difficult for one to make some solid conclusions about the impact of H_2 flow rate to the resulting device performance, for which further

experiments as well as complementary characterizations should be performed. Nevertheless, one can still deduce some useful hints from the existing results. Although, in terms of crystallinity, such variation in H_2 flow rate do not bring too much influence for the resulting µc-Si:H films (from ~61 % to ~77 %), an appropriate choice can still lead to a better performance of the solar cell device: too low H_2 flow rate (at 3 sccm, X_c^{Raman} = 61 %) would bring some negative impact to the device quality, especially the much lower value of FF; a medium H_2 flow rate (at 4 sccm, X_c^{Raman} = 69 %) is shown be a better choice, since it gives a broader spectral absorption.

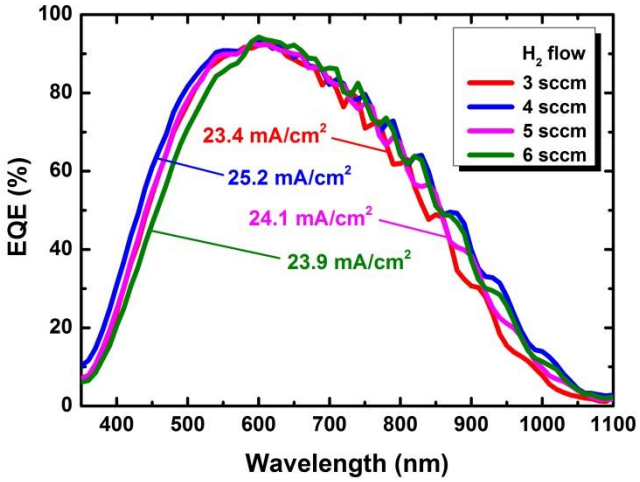

Figure A.2 EQE spectra of µc-Si:H solar cells with absorber layers deposited using different H_2 flow rates.

At this point, a quite reasonable baseline can be obtained. For further improvement, one can naturally have the ideas to use thicker absorber layer, to insert buffer layers between *p*/*i* and *i*/*n* layers, to optimize the doped layers, to use one pump down process during the deposition of silicon stacks, to use novel back reflector, to use anti-reflection coating, etc. In this preliminary work, we will only present the results by using thicker absorber layer.

A.2. Effect of absorber layer thickness

We fabricated a set of solar cells with different absorber layer thicknesses at 1.5 µm, 3.0 µm, and 4.5 µm (H_2 flow rate set to 6 sccm). Moreover, to make a better comparison, another set of solar cells using the same process conditions but in a superstrate *p*-*i*-*n* configuration (as seen in Figure 4.34) were also prepared. The *I*-*V* characteristics for these devices are summaries in Figure A.3[§]. As one can see, thicker intrinsic layers indeed lead to a considerable enhancement in the device performance, in particular the J_{SC}. For the *p*-*i*-*n* devices, an approximately 20 % of increase from 18.0 mA/cm^2 at 1.5 µm up to 21.4 mA/cm^2 at 4.5 µm is observed. While at the same time, the variation of V_{OC} still stays in a small range. Similar situation is observed for the *n*-*i*-*p* devices. By increasing the absorber layer from 1.5 µm to 3.0 µm, J_{SC} presents a ~10 % enhancement from 23.6 mA/cm^2 up to 25.9 mA/cm^2. Unfortunately, the 4.5 µm sample peeled off upon the vacuum break

[§] Note that due to the reproducibility issue of doped layers (especially the *p*-µc-Si:H layers), the solar cells studied herein are not comparable to the previous ones in Section A.1.

after intrinsic layer deposition[§]. However, in analogy with the results from *p-i-n* devices, further improvement can still be reasonably expected.

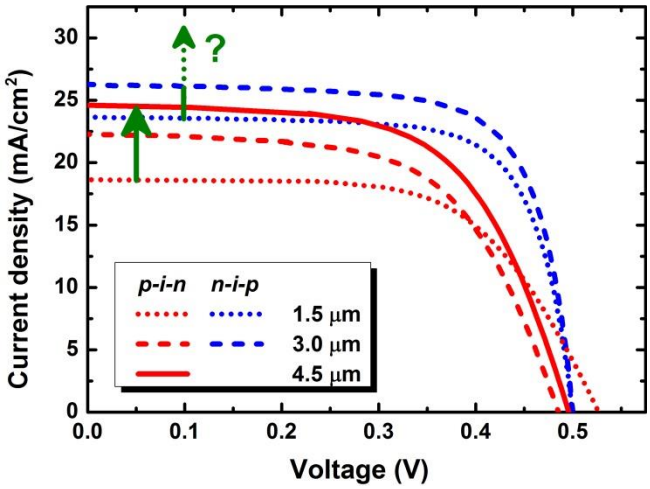

Figure A.3 Light *I-V* curves of the superstrate *p-i-n* (blue) and substrate *n-i-p* (red) μc-Si:H solar cells with absorber layers of 1.5 μm (dot), 3.0 μm (dash), 4.5 μm (solid) thick.

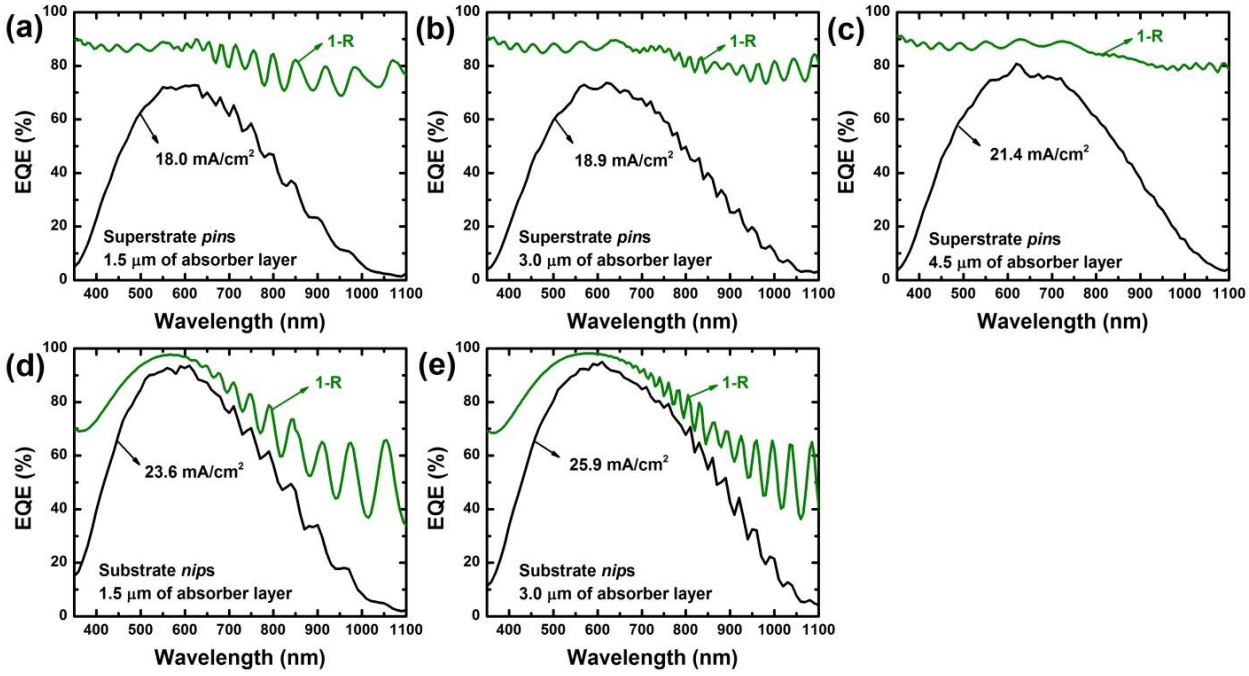

Figure A.4. EQE spectra of the (a), (b), (c) substrate *n-i-p* and (d), (e) superstrate *p-i-n* μc-Si:H solar cells with different absorber layer thicknesses. The green spectra indicates the corresponding information of light reflection *R* from the device surface.

[§] This was realized to be associated with the delamination of silver layer from the textured ZnO:Al after long time processing, since silver has low adhesion to ZnO:Al. For purpose of improving the interface adhesion, one can deposit a thin "adhesive metal layer" (like chromium, titanium or other active metals) after the texturation of ZnO:Al.

By further looking at the corresponding EQE spectra shown in Figure A.4, the improvement is more conspicuous. Taking the EQE at 800 nm/1000 nm for example (Table A.3), *p-i-n* devices present an increase from ~43 %/~6 % at 1.5 µm up to ~59 %/~15 % at 4.5 µm, and that of *n-i-p* devices from ~57 %/~9 % at 1.5 µm up to ~70 %/~ 18 % at 3.0 µm are observed. Such enhancement of spectral response in the infrared region can be favorable for the case of tandem or multi-junction devices, since this part light absorption will be more contributed by the µc-Si:H bottom sub-cell.

Table A.3. Example of the improvement of solar cell spectral response in the infrared region by increasing the absorber layer thickness, shown by the EQE at 800 nm and 1000 nm for both substrate *p-i-n* and substrate *n-i-p* devices.

t_i	**superstrate *p-i-n***		**substrate *n-i-p***	
µm	800 nm	1000 nm	800 nm	1000 nm
1.5	~43 %	~6 %	~57 %	~9 %
3.0	~49 %	~11 %	~70 %	~18 %
4.5	~59 %	~15 %	-	-

List of publication

Peer reviewed journals

- **J. Wang**, D. Daineka, M. Elyaakoubi, and E. V. Johnson, "Control of microcrystalline silicon thin film deposition for the application to photovoltaics using Tailored Voltage Waveforms: key roles of ion energy" (Manuscript prepared to be submitted).
- Z. Li, C. Lu, Rusli, M. Foldyna, R. Khoury, P. Bulkin, **J. Wang**, W. Chen, A. B. Prakoso, E. V. Johnson, P. R. i Cabarrocas, "Optical Study of Nanostructured Back Reflectors for Enhanced Light Trapping and Parasitic Loss in Silicon Thin Film Solar" (Manuscript prepared to be submitted).
- Z. Li, Rusli, M. Foldyna, **J. Wang**, W. Chen, A. B. Prakoso, C. Lu, and P. R. i Cabarrocas, "Nanostructured Back Reflectors produced using Polystyrene Assisted Lithography for Enhanced Light Trapping in Silicon Thin Film Solar Cells" (Manuscript prepared to be submitted).
- **J. Wang**, and E. V. Johnson, "Electrode-selective surface processes from $SiF_4/H_2/Ar$ chemistry using Tailored Voltage Waveforms plasmas", *Plasma Sources Science and Technology*, **26**: 01LT01 (2017). (**Featured article**).
- J. Kim, **J. Wang**, D. Daineka, and E. V. Johnson, "Improvement of near-infrared diffuse reflectance of silver back reflectors through Ag_2O formation by a UV-ozone exposure process", *Solar Energy Materials and Solar Cells*, **170**: 114 (2017).
- **J. Wang**, P. Bulkin, I. Florea, J.-L. Maurice, and E. V. Johnson, "Microcrystalline Silicon Thin Films deposited by Matrix-Distributed Electron Cyclotron Resonance Plasma Enhanced Chemical Vapor Deposition using an SiF_4/H_2 Chemistry", *Journal of Physics D: Applied Physics*, **49**: 285203 (2016).
- **J. Wang**, I. Florea, P. Bulkin, J.-L. Maurice, and E. V. Johnson, "Using MDECR-PECVD to study the impact of ion bombardment energy on microstructural properties of μc-Si:H thin film grown from an SiF_4/H_2 chemistry", *Physica Statues Solidi C*, **13(10-12)**: 782 (2016).
- **J. Wang**, C. Longeaud, F. Ventosinos, D. Daineka, M. Elyaakoubi, and E. V. Johnson, "Deposition of a-Si:H thin films using tailored voltage waveform plasmas: impact on microstructure and stability", *Physica Statues Solidi C*, **13(10-12)**: 735 (2016).

Conference proceedings

- **J. Wang**, and E. V. Johnson, "Selective deposition for "chamber clean-free" processes using tailored voltage waveform plasmas", *Bulletin of the American Physical Society*, **61(9)** (2016).

Conference oral presentations

- **Invited talk,** 6th Workshop on Radio Frequency Discharges, May 2017, Presqu'île de Giens, France.
- **Contributed talk**, 63rd AVS, November 2016, Nashville, USA.
- **Contributed talk**, 69th GEC, October 2016, Bochum, Germany.
- **Contributed talk**, E-MRS spring meeting, May 2016, Lille, France.
- **Contributed talk,** 62nd AVS, October 2015, San Jose, USA.

Conference poster presentations

- E-MRS spring meeting, May 2016, Lille, France.
- Journées Nationales du PhotoVoltaïque (JNPV), November 2016, Dourdan, France.
- 26th ICANS, September 2015, Aachen, Germany.
- JNPV, December 2015, Dourdan, France.

université PARIS-SACLAY
ÉCOLE DOCTORALE
INTERFACES
Approches Interdisciplinaires : Fondements, Applications et Innovation

Titre : Nouveaux concepts dans le dépôt de couches minces de silicium par PECVD: de la chimie du plasma aux applications de dispositifs photovoltaïques

Mots clés : Couche mince de silicium, Dépôt chimique en phase vapeur assisté par plasma, Résonance cyclotron électronique, Effet d'asymétrie électrique, Tailored voltage waveform, Énergie ionique

Résumé : Ce manuscrit présente l'étude de la fabrication de couches minces de silicium basée sur des différents types de dépôt chimique en phase vapeur assisté par plasma (PECVD) pour des applications dans le photovoltaïque.
Tout d'abord, nous avons combiné une chimie du plasma halogéné en utilisant un mélange de SiF_4/H_2 et la technique plasmas distributés matriciellement à résonance cyclotronique électronique (MDECR) PECVD pour le dépôt de µc-Si:H à grande vitesse. Nous trouvons que les conditions d'énergie ionique modérée sont bénéfiques pour obtenir une diminution significative de la densité des nano-vides, et ainis nous pouvons obtenir un matériaux de meilleure qualité avec une meilleure stabilité. Une méthode de dépôt en deux étapes a été introduite comme moyen alternatif d'éliminer la formation d'une couche d'incubation amorphe pendant la croissance du film.
Ensuite, nous avons exploré la technique d'excitation Tailored Voltage Waveform (TVW) pour les processus plasma radiofréquence capacitivement couplé (RF-CCP). Grâce à l'utilisation de TVW, il est possible d'étudier indépendamment l'influence de l'énergie ionique sur le dépôt de matériaux à une pression de processus relativement élevée. Basé sur ce point, nous avons étudié le dépôt de µc-Si:H et a-Si:H à partir des plasma de $SiF_4/H_2/Ar$ et de SiH_4/H_2, respectivement. A partir d'une analyse des propriétés structurelles et électroniques, nous constatons que la variation de l'énergie ionique peut directement traduite dans la qualité du matériaux. Les résultats se sont appliqués aux dispositifs photovoltaïques et ont établi des liens complets entre les paramètres de plasma contrôlables par TVW et les propriétés de matériaux déposé, et finalement, les performances du dispositif photovoltaïque correspondant.
Enfin, nous avons trouvé que dans le cas du dépôt de couches minces de silicium à partir du plasma de $SiF_4/H_2/Ar$ à l'aide de *sawtooth* TVW, on peut réaliser un processus de dépôt sur une électrode, sans aucun dépôt ou gravure. contre-électrode. Ceci est dû à deux effets: la nature multi-précurseur du processus de surface résultant et la réponse de plasma spatiale asymétrique par l'effet d'asymétrie de pente de la *sawtooth* TVW. La découverte de tels procédés "electrode-selective" encourage la perspective que l'on puisse choisir un ensemble de conditions de traitement pour obtenir une grande variété de dépôts désirés sur une électrode, tout en laissant l'autre vierge.

Title : Novel concepts in the PECVD of silicon thin films: from plasma chemistry to photovoltaic device applications

Keywords : Silicon thin film, Plasma-enhanced chemical vapour deposition, Electron cyclotron resonance, Electrical asymmetry effect, Tailored voltage waveform, Ion energy

Abstract: This manuscript presents the study of silicon thin film materials fabrication using different plasma-enhanced chemical vapour deposition (PECVD) techniques for applications in photovoltaics.
First, we have combined a halogenated process chemistry using an SiF_4/H_2 gas mixture with the matrix-distributed electron cyclotron resonance (MDECR) PECVD technique for the growth of µc-Si:H at high rate. We find that moderate ion energy conditions are beneficial to achieve a significant drop in the density of nano-voids, and thus a higher quality material with better stability can be obtained. A two-step deposition method has been introduced as an alternative way to eliminate the formation of an amorphous incubation layer during film growth.
Then, we have explored the Tailored Voltage Waveform (TVW) excitation technique for capacitively coupled plasma (CCP) processes. Through the utilization of TVW, it is possible to independently study the impact of ion energy on material deposition at relatively high process pressure. Based on this insight, we have studied the deposition of µc-Si:H and a-Si:H from the $SiF_4/H_2/Ar$ and SiH_4/H_2 plasma chemistries, respectively. From an analysis of the structural and electronic properties, we find that the variation of ion energy can be directly translated into the material quality. The results have applied to photovoltaic devices and have established comprehensive links between the controllable plasma parameters via TVW, the deposited material properties, and, finally, the resulting device quality.
Finally, we have found that in the case of silicon thin film deposition from the $SiF_4/H_2/Ar$ plasma chemistry using the sawtooth TVW, one can achieve a deposition process on one electrode, while at the same time either no deposition or an etching process on the counter electrode. This is due to two effects: the multi-precursor nature of the resulting surface process and the spatially asymmetric plasma response through the slope asymmetry effect of sawtooth TVW. The discovery of such "electrode-selective" processes encourage the prospect that one could choose a set of process conditions to achieve a wide variety of desired depositions on one electrode, while leaving the other pristine.

Université Paris-Saclay
Espace Technologique / Immeuble Discovery
Route de l'Orme aux Merisiers RD 128 / 91190 Saint-Aubin, France